



Politechnika Wroclawska

Field of Science: Engineering and Technical Sciences

Discipline of Science: Civil Engineering, Geodesy and Transport

DOCTORAL DISSERTATION

Numerical modeling of soil-steel composite structures behavior under ultimate loads

Raport serii PRE nr 5 /2024

Alemu Mosisa Legese

Supervisor: Dr. hab. inż. Adrian Róžański

Assistant supervisor: Dr. inż. Maciej Sobótka

Keywords:

corrugated steel plate;
failure mode;
geotextile reinforcement;
moving load;
shell spacing;
ultimate load.

Wrocław, June 2024

Autor (Autorzy):

1. mgr inż. Alemu Mosisa Legese

Politechnika Wrocławska
Wydział Budownictwa Lądowego i Wodnego
Katedra Geotechniki, Hydrotechniki, Budownictwa Podziemnego i Wodnego
Wybrzeże Wyspiańskiego 27, 50-370 Wrocław
tel. +48 517 639 094
e-mail: alemu.legese@pwr.edu.pl

Raport został złożony w Redakcji Wydawnictw Wydziału Budownictwa Lądowego i Wodnego Politechniki Wrocławskiej w czerwcu 2024 r.

Lista odbiorców:	Recenzenci	3 egz.
	Promotor	1 egz.
	Promotor pomocniczy	1 egz.
	Autor	1 egz.
	Archiwum W-2	1 egz.
	<hr/>	
	Razem	7 egz.

Acknowledgment

First and foremost, I thank God for his many graces and blessings.

I would like to express my gratitude to all those who have made this work possible. In particular, I extend my deepest gratitude to Professor Adrian Róžański, my supervisor, for imparting his knowledge and guidance throughout my research. I also wish to thank Dr. Maciej Sobótka, my assistant supervisor, for inspiring my research, assisting in planning simulations, and providing invaluable help in editing this thesis. Additionally, I would like to express my deep appreciation to Professor Adam Wysokowski for his help and support during my research by sharing valuable data.

I am also grateful to Michał Pachnicz and Yada Boru for their valuable comments and motivation.

Finally, I would like to express my heartfelt thanks to my family for their unwavering support and encouragement throughout this journey. Specifically, I am deeply grateful to my wife, Banchiayehu Aga, and my daughters, Naif and Siana for the support and patience through the ups and downs, the sleepless nights and hard times throughout this long but rewarding journey. Special thanks to my father, mother and all my family members for their continuous prayers and motivation.

Table of Contents

List of Tables	8
List of Figures	9
List of Abbreviations	15
List of Symbols	16
1. Introduction	17
1.1. Soil-steel composite structure.....	17
1.2. Structure of the work.....	18
1.2.1. The layout of the thesis.....	18
1.2.2. List of publications.....	20
2. Theoretical and experimental research on SSCS made of corrugated steel plate.....	22
2.1. Construction of SSCSs	22
2.1.1. Corrugated steel plate.....	22
2.1.2. Foundation.....	27
2.1.3. Engineered backfill.....	29
2.2. Design of the SSCSs	31
2.3. Behavior of SSCS under different loading conditions	34
2.3.1. Construction stage	34
2.3.2. Under static and semi-static load.....	36
2.3.3. Under ultimate load.....	39
2.4. Behavior of multi-span SSCS.....	42
2.5. Behavior of geosynthetic reinforced SSCS under different loading conditions	43
2.6. Selected studies of flexible culverts on a natural scale	45
2.6.1. Full-scale test on box type	45
2.6.2. Full-scale test on pipe arch CSP structure	49
2.6.3. Full-scale laboratory test on geotextile reinforced SSCS	51
2.7. Summary of the state of research.....	56
3. Purpose of the research.....	58
3.1. Specific objectives.....	58
3.2. Scope of the Research	58
4. Stability of engineering structures.....	59

4.1.	Elastic and plastic behavior of structural steel.....	60
4.2.	Yielding of a cross-section	61
4.2.1.	Stage 1 – Elastic stage	61
4.2.2.	Stage 2 – Yielding stage	63
4.2.3.	Stage 3 – Elasto-plastic stage	65
4.2.4.	Stage 4 – fully plastic stage	65
4.3.	Influence of axial forces on plastic moment capacity	66
4.3.1.	Design Codes and Standards	69
4.3.1.1.	CHBDC (CSA, 2019) and AASHTO (AASHTO, 2019)	69
4.3.1.2.	Swedish design method	70
4.4.	Buckling mechanism	70
4.4.1.	Buckling of the flexible culvert wall	71
4.4.2.	Buckling according to Swedish design method	73
5.	Soil-steel composite structures under ultimate load: effects of stiffening ribs and geotextile	75
5.1.	Experimental detail	75
5.2.	Numerical modelling	77
5.3.	Numerical model validation	80
5.3.1.	Simulation of construction stage.....	80
5.3.2.	Simulation of ultimate load test	85
5.4.	Effects of stiffening ribs	89
5.5.	Behavior of geotextile reinforced SSCS under ultimate load.....	97
6.	Influence of geotextile soil reinforcement layout on the deformation of a model SSCSs	107
6.1.	Numerical Modelling	108
6.3.	Effect of geotextile subjected to external load.....	116
6.4.	Effect of double layer of geotextile subjected to external load.	119
6.5.	Summary	125
7.	Behavior of multi-span SSCS under ultimate load: effect of shell spacing.....	127
7.1.	Spacing and load configuration	128
7.2.	Analysis and behavior of a SSCS during backfilling	138
7.3.	Analysis and behavior of multi-span SSCS under ultimate load (Model-C).....	145

7.3.1.	Load displacement curve	146
7.3.2.	Bending moment	151
7.3.3.	Axial force.....	155
7.3.4.	Failure mode of the SSCSs under Model-C loading position	159
7.4.	Analysis and Behavior of multi-span SSCS under ultimate load (Model-R)	164
7.4.1.	Load displacement curve	164
7.4.2.	Bending moment	169
7.4.3.	Axial force.....	172
7.4.4.	Failure mode of the SSCSs under model-R loading condition.....	176
7.5.	Behavior of multi-span SSCS under ultimate load (Model-LR)	178
7.5.1.	Load displacement curve	178
7.5.2.	Bending moment	182
7.5.3.	Axial force.....	185
7.5.4.	Failure mode of the SSCSs under Model-LR loading condition.....	189
7.6.	Stability of multi-span soil-steel composite structures.....	191
7.7.	Summary	192
8.	Effect of shell spacing on mechanical behavior of multi-span soil-steel composite structure under moving load.....	194
8.1.	The behavior of the structure under live load	196
8.1.1.	Testing procedure	197
8.1.2.	Testing results	198
8.2.	Formulation of computational model	200
8.2.1.	Parametric analysis.....	202
8.2.2.	Validation of numerical model	204
8.2.2.1.	Simulation results	204
8.3.	Numerical results.....	207
8.4.	Discussions.....	219
8.5.	Summary	224
9.	Summary and final conclusions.....	226
9.1.	Evaluation of ultimate load: effects of stiffening ribs and geotextile.....	226
9.2.	Influence of geotextile soil reinforcement layout on the deformation of a model SSCSs	227

9.3. Behavior of multi-span SSCS under ultimate load: effect of shell spacing..... 227

9.4. Behavior of multi-span SSCS under moving load: effect of shell spacing..... 228

References..... 229

List of Tables

Table 2.1: Profiles of SSCSs [26].	23
Table 2.2: Structural properties of 152×51 mm corrugated plates [31].	25
Table 2.3: Structural properties of deep corrugated plate (SuperCor) plates [31].	25
Table 2.4: Section properties of Multiplate MP200 plate [6].	26
Table 2.5: Section properties of SuperCor plate [6].	26
Table 2.6: Section properties of UltraCor plate [6].	26
Table 2.7: Stiffening of CSPs with additional ribs [32].	27
Table 5.1: The summary of the material parameters used in the computations.	87
Table 6.1: The position of geotextile in the soil above the crown of the shell.	109
Table 7.1: Summary of maximum vertical displacement in the shells after backfilling	142
Table 7.2: Comparison of bending moment and axial force of central and lateral shells for different S/D ratios under Model-C at peak load.	159
Table 7.3: Summary of critical location and failure mode for all models under loading position – Model-C	164
Table 7.4: Comparison of bending moment and axial force of central and lateral shells for different S/D ratios under Model-R at peak load.	175
Table 7.5: Summary of critical location and failure mode for all models under loading position – Model-R	177
Table 7.6: Comparison of bending moment and axial force of central and lateral shells for different S/D ratios under Model-LR at ultimate load.	188
Table 7.7: Summary of critical location and failure mode for all models under loading position – Model-LR.	190
Table 8.1: The material parameters used in the computations.	206

List of Figures

Figure 1.1: Crossing for animals over a road constructed as the SSCS.....	17
Figure 1.2: Pressure transferring within a soil-arch system [17].....	18
Figure 1.3: outline of the thesis.....	21
Figure 2.1:Geometry and terminology of corrugation profiles.....	24
Figure 2.2: Comparison of various CSP profiles (a) and their corrugation types (b).	24
Figure 2.3: a) Young’s modulus of the CSP and orthotropic plate with equivalent modulus [35] b) stiffness of corrugation profile for stiffened and unstiffened CSP [27].....	27
Figure 2.4: Assembly of CSP: a) closed profile on the ground, b) open profile on the RC strip footings, c) open profile on the CSP [36]	28
Figure 2.5: Backfilling stages: a) completed assembly of the shell, b), c), and d) laying and compaction of subsequent layers of backfill, e) completed backfilling.....	29
Figure 2.6: The height of cover definition for the cases of a) car traffic pavement on the surface, b) railway road, and c) sloped surface.	33
Figure 2.7:Vertical displacement of the shell crown point: a) result of real scale test, b) result of the simulation (based on [73])	37
Figure 2.8: Models: (a) model I (shell made of CSPs); (b) model II (shell made of CSPs with additional CSP ribs); (c) model III (shell made of CSPs with CSP ribs and filling with C25/30 concrete), (Source: Maleska and Beben [33]).....	38
Figure 2.9: A summary of failure loads from 3D model [45].....	40
Figure 2.10: Bending moment resulting from dead load of soil and live load at tandem loads just before the first yield of the steel material as calculated from the 3D models [45].	41
Figure 2.11: a) Cross-section of the tested structure b) after soil backfill c)general view of the tested structure [98].....	46
Figure 2.12: Measuring points with arrangement of displacement and strain gauges (After [98])	47
Figure 2.13: Deformation of the shell during consecutive backfilling[99]	48
Figure 2.14: a) Displacement under destructive load for shell b) View of damage under destructive load[98].	48
Figure 2.15: General view of the structure a) after backfilling b) the plate to transfer the load to the ground [98][99].	49
Figure 2.16: Location of strain gauges and sensors[98]	50
Figure 2.17: Maximum stress values in the shell[98]	51
Figure 2.18: Cross-section of the tested structure after reinforcing with the geosynthetic material[94].....	52
Figure 2.19: The measured results at the crown of the shell under class “A” Load a) Vertical displacement b) stress values[94]	53
Figure 2.20: The measured results at the crown of the shell under class “B” Load a) Vertical displacement b) stress values[94]	54

Figure 2.21: The measured results at the crown of the shell under class “C” Load a) Vertical displacement b) stress values[94]	55
Figure 4.1: Stress-strain curve for steel structure (a) Real, (b) Ideal[107] [108].....	60
Figure 4.2: Elastic, plastic, and total stress-strain curve [109].	62
Figure 4.3: Stress distribution a) elastic b) yield c) elastoplastic d) fully plastic (Modified from [110]).....	62
Figure 4.4: Von Mises Yield Surface for Plain Stress	65
Figure 4.5: Typical axial force-bending moment interaction curve.	68
Figure 4.6: Adjustment of the critical normal force depending on the stiffness and length of the reinforced section of a reinforced member (Source: Pettersson [16])	73
Figure 4.7: The ratio $M_{u,cr} / M_u$ as a function of corrugated steel sheet thickness for the selected profiles [57].....	74
Figure 5.1: Model of the soil steel composite structure in laboratory test: a) general view of the assembled corrugated steel structure, b) after backfill model prepared for ultimate loading test [98]	76
Figure 5.2: Geometry of the tested structure.	77
Figure 5.3: Model of considered SSCS: finite element mesh and boundary conditions adopted in the numerical model.....	78
Figure 5.4: Corrugated steel plate model a) main shell b) main shell with stiffening rib.	79
Figure 5.5: Diagram of practical procedures for compaction models of a backfill layer placed adjacent to a the shell: (a) new layer of backfill; (b) vertical surface load on new layer;(c) loads that squeeze the new layer; (d) the third approach is application of horizontal loads to shell [130].	82
Figure 5.6: Successive backfilling and compaction process.....	83
Figure 5.7: Comparison of measurements and numerical modeling results for the crown displacement during backfilling.....	85
Figure 5.8: The SSCS model with reduced soil height of cover.....	86
Figure 5.9: Load-displacement curve.	87
Figure 5.10: Schematic presentation of reinforcement in the models: a) Model-I, b) Model-II, c) Model-III, d) Model-IV (all dimensions are in millimeter).....	88
Figure 5.11: Load displacement curve for the model with and without additional rib at the crown.	90
Figure 5.12:: Bending moment vs vertical displacement curve for a) Model-I b) Model-II.....	93
Figure 5.13: Bending moment distribution on the shell of SSCS for a) Model-I b) Model- II....	95
Figure 5.14: Maximum axial thrust distribution on the shell of SSCS under ultimate load; a) Model-I b) Model -II.....	96
Figure 5.15: Load-Displacement curve at crown.....	98
Figure 5.16: Bending moment displacement curve at the crown and shoulder for Model -III....	99
Figure 5.17: Bending moment displacement curve at the crown of the shell for Model -IV	101

Figure 5.18: Bending moment distribution on the shell of geotextile reinforced SSCS under ultimate load for a) Model-III b) Model- IV.....	102
Figure 5.19: Maximum axial thrust distribution on the shell of geotextile reinforced SSCS under ultimate load; a) Model-III b) Model-IV.	103
Figure 6.1: Model of SSCS a) without reinforcement, b) with geotextile at the centre of the soil cover.....	108
Figure 6.2: Position of geotextile: a) Model I, b) Model II, c) Model III, d) Model IV, e) Model V, f) Model VI.....	109
Figure 6.3: Backfill and compaction load in the fifth layer of the model.....	110
Figure 6.4: Vertical displacement at the crown of the shell during backfilling by placing geotextile at different position above the crown of the shell.....	111
Figure 6.5: Effect of double membrane on the vertical displacement of the shell at the crown during backfilling.	112
Figure 6.6: Distribution of vertical deformation of the soil: a) Reference, b) Model I, c) Model II, d) Model III, e) Model IV, f) Model V g) Model VI.	116
Figure 6.7: Vertical displacement at the crown of the shell by placing geotextile at different positions.....	118
Figure 6.8: Stresses at the crown of the shell by placing geotextile at different positions.....	119
Figure 6.9: The influence of single and double layers geotextile on vertical displacement of the shell at crown.....	120
Figure 6.10: Distribution of vertical deformation of the soil: a) unreinforced, b) reinforced (Model I), c) reinforced (Model II), d) reinforced (Model III), e) reinforced (Model IV), f) reinforced (Model V) g) double reinforced (Model VI).....	124
Figure 7.1: Geometry of box-type SSCS considered as the reference model in the study.....	128
Figure 7.2: Finite element mesh and boundary condition for a reference model (single span)..	128
Figure 7.3: Geometry of three span box-type SSCS with span (D) and spacing (S).....	129
Figure 7.4: Loading position and location of characteristic points for Model-C.....	129
Figure 7.5: Finite element model for Model-C (S/D=0.04).....	130
Figure 7.6: Finite element model for Model-C (S/D=0.1).....	130
Figure 7.7: Finite element model for Model-C (S/D=0.25).....	131
Figure 7.8: Finite element model for Model-C (S/D=0.5).....	131
Figure 7.9: Finite element model for Model-C (S/D=1.0).....	132
Figure 7.10: Loading position Case-II and location of characteristic points.....	132
Figure 7.11: Finite element model for Model-R (S/D=0.04).....	133
Figure 7.12: Finite element model for Model-R (S/D=0.10).....	133
Figure 7.13: Finite element model for Model-R (S/D=0.25).....	134
Figure 7.14: Finite element model for Model-R (S/D=0.50).....	134
Figure 7.15: Finite element model for Model-R (S/D=1.0).....	135
Figure 7.16: Loading position and location of characteristic points for Model-LR.....	135
Figure 7.17: Finite element model for Model-LR (S/D=0.04).....	136

Figure 7.18: Finite element model for Model-LR (S/D=0.10)	136
Figure 7.19: Finite element model for Model-LR (S/D=0.25)	137
Figure 7.20: Finite element model for Model-LR (S/D=0.50)	137
Figure 7.21: Finite element model for Model-LR (S/D=1.0)	138
Figure 7.22: The vertical deformation distribution of the shell (Reference model)	139
Figure 7.23: Deformation of the crown of the central shell during construction stage at different shell spacing for Model-C.....	140
Figure 7.24: Deformation of the crown of the lateral shell during construction stage	141
Figure 7.25: The vertical deformation distribution of the shell for S/D=0.04.....	143
Figure 7.26: The vertical deformation distribution of the shell for S/D=0.10.....	143
Figure 7.27: The vertical deformation distribution of the shell for S/D=0.25	144
Figure 7.28: The vertical deformation distribution of the shell for S/D=0.50.....	144
Figure 7.29: The vertical deformation distribution of the shell for S/D=1.0.....	145
Figure 7.30: Load displacement curve at the crown of central shell	147
Figure 7.31: Load displacement curve at the crown of lateral shell	149
Figure 7.32: Load displacement curve at the haunch of central shell.....	150
Figure 7.33: Load displacement curve at the haunch of lateral shell.....	151
Figure 7.34: Bending moment distribution at failure load for reference model	152
Figure 7.35: Bending moment distribution at failure load for S/D=0.04	152
Figure 7.36: Bending moment distribution at failure load for S/D=0.10	153
Figure 7.37: Bending moment distribution at failure load for S/D=0.25	154
Figure 7.38: Bending moment distribution at failure load for S/D=0.50	154
Figure 7.39: Bending moment distribution at failure load for (S/D=1.0).....	155
Figure 7.40: Axial force at failure load for reference model	156
Figure 7.41: Axial force at failure load for model S/D=0.04	157
Figure 7.42: Axial force at failure load for model S/D=0.10	157
Figure 7.43: Axial force at failure load for model S/D=0.25	157
Figure 7.44: Axial force at failure load for model S/D=0.50	158
Figure 7.45: Axial force at failure load for model S/D=1.0	158
Figure 7.46: Bending moment–vertical displacement curve for central shell (S/D=0.10)	161
Figure 7.47: Bending moment–vertical displacement curve for Lateral shell (S/D=0.10).....	162
Figure 7.48: Load displacement curve at the crown of central shell.	166
Figure 7.49: Load displacement curve at the crown of the loaded lateral shell.....	167
Figure 7.50: Load displacement curve at the haunch of central shell.....	168
Figure 7.51: Load displacement curve at the haunch of the loaded lateral shell.	169
Figure 7.52: Bending moment distribution at failure load for (S/D=0.04).....	170
Figure 7.53: Bending moment distribution at failure load for (S/D=0.1).....	170
Figure 7.54: Bending moment distribution at failure load for (S/D=0.25).....	171
Figure 7.55: Bending moment distribution at failure load for (S/D=0.5).....	171
Figure 7.56: Bending moment distribution at failure load for (S/D=1.0).....	172

Figure 7.57: Axial force distribution at failure load for (S/D=0.04)	173
Figure 7.58: Axial force distribution at failure load for (S/D=0.10)	173
Figure 7.59: Axial force distribution at failure load for (S/D=0.25)	174
Figure 7.60: Axial force distribution at failure load for (S/D=0.50)	174
Figure 7.61: Axial force distribution at failure load for (S/D=1.0)	175
Figure 7.62: Load displacement curve at the crown of central shell.	179
Figure 7.63: Load displacement curve at the crown of the loaded lateral shell.....	180
Figure 7.64: Load displacement curve at the haunch of central shell.....	181
Figure 7.65: Load displacement curve at the haunch of the loaded lateral shell	182
Figure 7.66: Bending moment distribution at failure load for (S/D=0.04).....	183
Figure 7.67: Bending moment distribution at failure load for (S/D=0.10).....	183
Figure 7.68: Bending moment distribution at failure load for (S/D=0.25).....	184
Figure 7.69: Bending moment distribution at failure load for (S/D=0.50).....	184
Figure 7.70: Bending moment distribution at failure load for (S/D=1.0).....	185
Figure 7.71: Axial force distribution at failure load for (S/D=0.04)	186
Figure 7.72: Axial force distribution at failure load for (S/D=0.10)	186
Figure 7.73: Axial force distribution at failure load for (S/D=0.25)	187
Figure 7.74: Axial force distribution at failure load for (S/D=0.50)	187
Figure 7.75: Axial force distribution at failure load for (S/D=1.0)	188
Figure 7.76: Comparing the failure load in three loading conditions.	191
Figure 8.1: Example of multi-span soil steel composite structure; a) open profile [6] b) closed profile [147]	195
Figure 8.2: Cross section of the tested structure [8].	196
Figure 8.3: Loading arrangement, for test.	197
Figure 8.4: Results from the field measurement at the crown of the shell a) vertical displacement b) stress [8].....	200
Figure 8.5: Geometry of numerical models: a) no space between the shells b) 0.6 m spacing c) half of the span spacing d) spacing equal to span e) twice of span spacing f) three-time span spacing g) infinite spacing or reference bridge.	202
Figure 8.6: Equivalent nodal forces from truck loads.....	203
Figure 8.7: Vertical displacement curve at the crown of the shell during consecutive truck crossings.....	205
Figure 8.8: Circumferential stress at the crown of the shell during consecutive truck crossings.	205
Figure 8.9: Vertical displacement at the crown of the central shell during consecutive truck crossings: (a) reference (b) central shell at 0.0m distance from lateral shell (c) at 0.6m (d) at 2.625m (e) at 5.25m (f) at 10.5 m (g) at 15.75 m	211
Figure 8.10: Horizontal displacement in the central shell crown during consecutive truck crossings: (a) reference, (b) central shell at 0.0m distance of 0.0 m from the lateral shell (c) at 0.6m (d) at 2.625m (e) at 5.25m (f) at 10.5 m (g) at 15.75 m.	215

Figure 8.11: Stress in the crown of the central shell during consecutive truck crossings: (a) reference (b) central shell at 0.0m distance of 0.0 m from the lateral shell (c) at 0.6m (d) at 2.625m (e) at 5.25m (f) at 10.5 m (g) at 15.75 m 219

Figure 8.12: Displacements at the crown of the central shell vs. shell spacing during truck crossings (a) vertical and (b) horizontal. 223

Figure 8.13: Stress at the Crown of the Central Shell vs. Shell Spacing During Truck Crossings 224

List of Abbreviations

AASHTO	American association of state highway and transportation officials
CSA	Canadian Standards Association
CSP	Corrugated steel plate
FEA	Finite element analysis
RC	Reinforced concrete
SLS	Serviceability limit state
SSI	Soil-steel interaction
SSCS	Soil-steel composite structures
SDM	Swedish design method
ULS	Ultimate limit state

List of Symbols

A_{sI}	Area of the cross section of the CSP shell
c	Cohesion
γ	Dynamic factor
E	Young's modulus of steel
E_{soil}	Design tangent modulus for the soil
h_c	Soil height of cover depth
I	Moment of inertia
K_n	Normal stiffness of contact interface
K_t	Tangential stiffness of contact interface
M_p	Plastic moment capacity
M_u	Ultimate moment capacity
N	Normal force
N_p	Maximum capacity of the shell wall against normal force
$N_{d,s}$	Axial force due to backfilling
$N_{cr,el}$	Buckling load for a buried pipe under ideal elastic conditions
ν	Poisson's ratio
W_I	Section modulus
Z	Plastic section modulus
σ	Stresses in the CSP
σ_y	Yield tensile stress
ψ	Dilation angle of soil
φ	Internal friction angle
ϵ^{total}	total strain
$\epsilon^{elastic}$	elastic strain
$\epsilon^{plastic}$	plastic strain
$u_{d,y}$	Distortion energy at yielding in a uniaxial tensile test
f_b	Buckling critical stress
e	Modulus of soil resistance,

1. Introduction

1.1. Soil-steel composite structure

With the rapid expansion of transport infrastructure, modern solutions like flexible structures are gaining popularity in civil engineering. Soil-steel composite structures (SSCSs) refer to a technology of constructing engineering objects in which a flexible shell works in mutual interaction with the surrounding soil backfill. SSCSs are most often made of corrugated steel plates (CSPs) joined by high-strength screws. The main concept of the SSCS consists of constructing the engineering objects in such a way to take advantage of soil backfill in transmitting service loads to the subsoil. Due to the phenomenon of arching in the backfill, the composite structure is capable of carrying large loads despite the use of much lighter structural elements compared to other types of bridges [1] [2] [3] [4].

Helically corrugated steel pipes can be used for constructing culverts. Plate thickness falls usually within the range of 1.50-12.50 mm [5] [6] [7]. Flat steel sheets [6][8] or plastic pipes [9] [10] [11] [12] are used less frequently. Today, this type of structure is being increasingly used in road, railway, tunneling, and animal overpass projects as an alternative to conventional type bridges, for example, reinforced concrete (RC) slab bridges [13] [14] [15] [16]. An example of an animal overpass constructed as SSCS is shown in Fig. 1.1.



Figure 1.1: Crossing for animals over a road constructed as the SSCS.

The interaction between the shell and the soil is consistently a significant concern when estimating the load-bearing capacity of SSCSs. It has been demonstrated that the stiffness ratio between the shell and the soil exerts a significant influence on the soil pressure applied onto the shell [17][18][19]. When the shell has relatively great stiffness, a negative arching action is induced, which leads to an enhanced soil pressure on the arch (shown in Fig.1.2(a)). If the shell has relatively weaker stiffness, a positive arching action will be induced, and the soil pressure applied over the steel arch will be decreased significantly (shown in Fig. 1.2(b)) [20] [21]. Due to the flexible features of SSCSs, the soil pressure over the shell is significantly decreased [21].

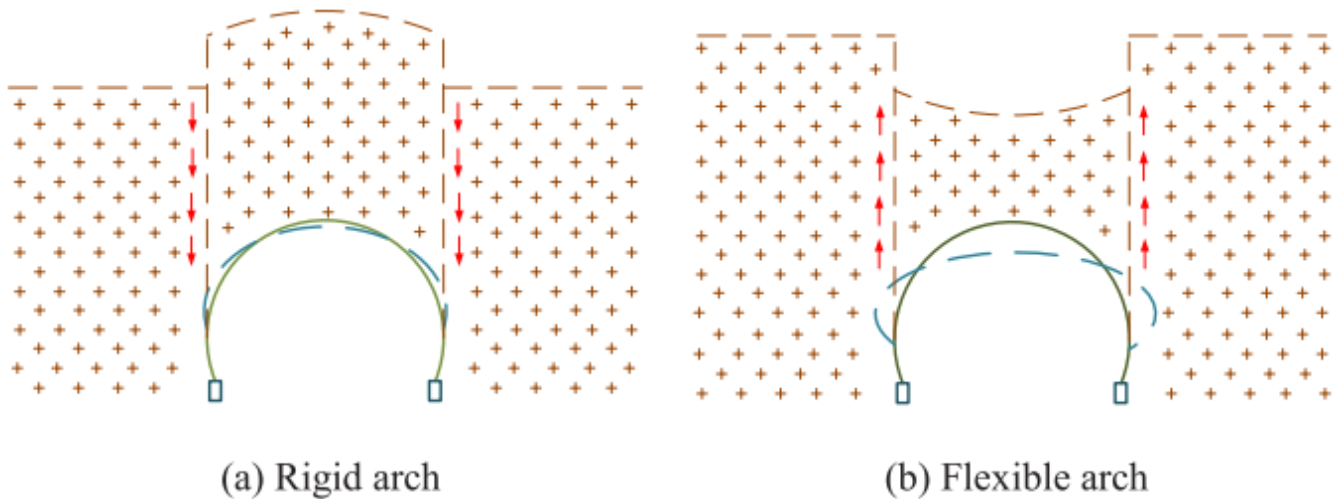


Figure 1.2: Pressure transferring within a soil-arch system [17]

1.2. Structure of the work

1.2.1. The layout of the thesis

Chapter 1 presents the general introduction of the thesis.

Chapter 2 presents first basic information on the construction of soil-steel composite structures. Then review the current state of knowledge regarding the research on this type of structure, in particular their behavior under static, semi-static, and ultimate loads. Subsequently focused on reviewing the full-scale tests conducted in laboratory. At the end the chapter highlights the gap in the current state of knowledge and the motivation for the current research. The findings outlined in this chapter have been disseminated through journal publication (#1), as listed in section 1.2.2.

Chapter 3 presents the objectives of this research. The chapter also provides the scope and significance of this research.

Chapter 4 presents the stability of engineering structures, specifically focusing on soil-steel composite structures as per established standards and existing literature. It extensively reviews the various failure modes encountered in engineering structures particularly, soil-steel composite structures.

Chapters 5 constituting the main part of the work, it is presented original results of numerical analyses of the behaviour of the structure under failure load. A two-dimensional nonlinear finite element model is developed and validated by the measured deformations during backfilling and under external load after backfilling is completed. The validated model is used to investigate the ultimate load bearing capacity of the structure and investigate the failure mode of the shell. The findings outlined in this chapter have been disseminated through journal publication (#2), as listed in section 1.2.2.

Chapters 6 presents the influence of placing a geotextile at different positions within the soil cover above the crown of the shell on the mechanical behaviour of SSCSs subjected to different static loads. The chapter also examines the impact of using a double layer of the membrane. The findings outlined in this chapter have been disseminated through journal publication (#3), as listed in section 1.2.2.

Chapter 7 presents the preparation of computational models for multi-span soil-steel composite structures and analyses their behavior under loading to failure. This chapter also examines the influence of spacing on the bearing capacity and the failure mode of the shell. The findings outlined in this chapter have been accepted for conference presentation and will be disseminated through a conference publication (#5), as listed in section 1.2.2.

Chapter 8 in this chapter, the computational models for multi-span soil-steel composite structure (flat shell) are prepared and their behaviour under the influence of moving load is analysed considering the direction of load movement. The findings outlined in this chapter have been disseminated through journal publication (#4), as listed in section 1.2.2.

The work ends with Chapter 9, which contains a summary and conclusions of the results obtained in the thesis. The general outline of the thesis is presented in Fig. 1.3.

1.2.2. List of publications

Some results presented in the thesis were already published and the publications were drafted by the author; supervised, reviewed and edited by dr hab. inż. Adrian Róžański and dr inż. Maciej Sobótka. The following is a list of publications published and under review.

Journal Publications

1. **Alemu Mosisa Legese**, Maciej Sobótka, Czesław Machelski, and Adrian Róžański (2023). "Behavior of soil-steel composite structures during construction and service: a review. " *Archives of Civil Engineering*, 263-292. <http://dx.doi.org/10.24425/ace.2023.147659>.
2. **Alemu Mosisa Legese**, Adrian Róžański, Maciej Sobótka and Adam Wysokowski (2024). "Soil-steel composite structures under ultimate load: effects of stiffening ribs and geotextile reinforcement of backfill soil." *Archives of Civil and Mechanical Engineering*. 24 (3). <https://doi.org/10.1007/s43452-024-00986-7>.
3. **Alemu Mosisa Legese**, Adam Wysokowski, Adrian Róžański, and Maciej Sobótka (2024). " Influence of geotextile soil reinforcement layout on the deformation of a model soil-steel composite structure. *Engineering Structures*, 312, 118196. <https://doi.org/10.1016/j.engstruct.2024.118196>.
4. **Alemu Mosisa Legese**, Adrian Róžański, and Maciej Sobótka (2024). Effect of Shell Spacing on Mechanical Behavior of Multi-Span Soil-Steel Composite Structure. *Heliyon*, 10(1) <https://doi.org/10.1016/j.heliyon.2023.e23376>.

Conference Proceedings

5. **Alemu Mosisa Legese**, Adrian Róžański, Maciej Sobótka and Adam Wysokowski (2024) "Effects of shell spacing and loading positions on the behavior of multi-span SSCS." *Buried Metal Bridges Symposium, Ohio State University, USA*. **Accepted** for presentation in October 2024

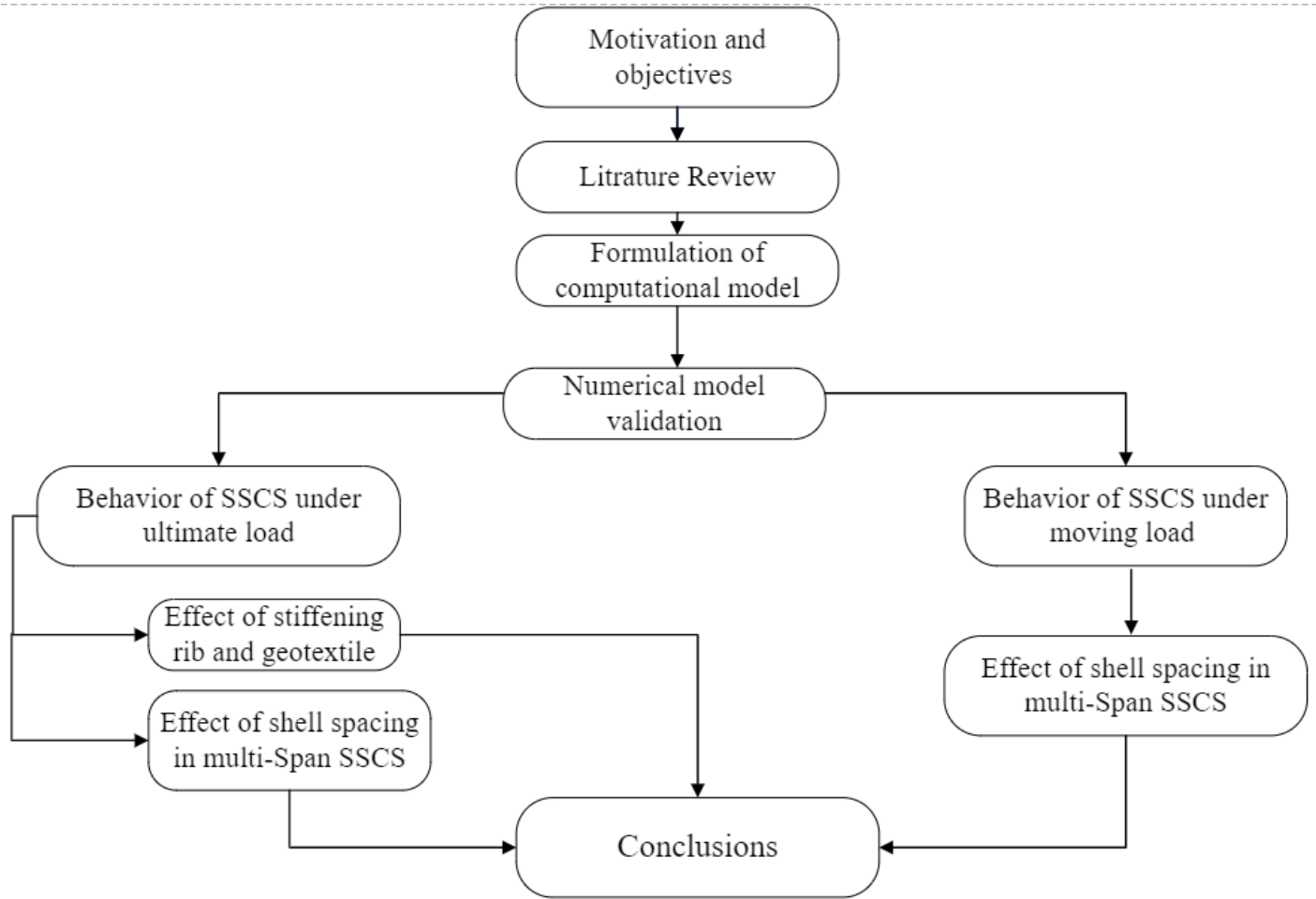


Figure 1.3: outline of the thesis.

2. Theoretical and experimental research on SSCS made of corrugated steel plate.

2.1. Construction of SSCSs

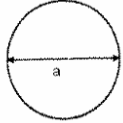
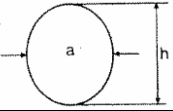
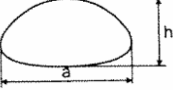
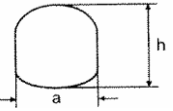
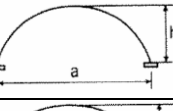
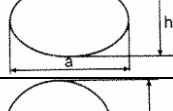
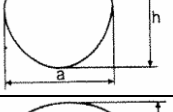
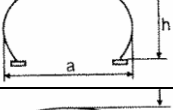
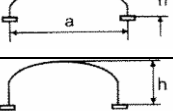
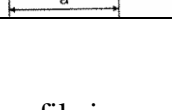
The practical applications of flexible structures started in the end of the 19th century. In Europe, flexible corrugated steel culverts have been used since the mid-1950s. Initially, the spans have been moderate and the heights of the backfill cover over the steel shell have been chosen with great care [7] [2] [13]. The practical applications of flexible structures started at the end of the 19th century. In Europe, flexible corrugated steel culverts have been used since the mid-1950s. Initially, the spans have been moderate and the heights of the backfill cover over the steel shell have been chosen with great care [2] [13]. To design such structures simple diagrams, the so-called standard drawings, have been used. They covered two types of profiles: low-rise culverts, and vertical ellipses. These standard drawings were prepared for spans up to 5 m [14]. Up to now, the construction and modernization of bridge structures using CSPs has been known and widely used in Europe, Canada, and USA. Usually, the span length of SSCSs ranges from 3 to 25 m, and it can be used as an effective alternative for short-span bridges and culverts [4]. However, larger structures are also possible to construct. For example, the SSCS having a span of 32.5 m was recently built in the United Arab Emirates [3], [15]. According to [4], span lengths of SSCSs can reach up to 40 m in the future. Conceptually, there is no limit to the structure's width. If it is much greater than the span, the object is considered to be a tunnel. There are tunnels made of CSPs that exceed the length of 100 m [7]. In addition to the construction of new bridges, CSPs can be used to reinforce old ones because they enable to carry construction works to be carried out in normal (or timely limited) traffic and to achieve effects in a very short time [7]. The details on the response of these structures to applied load and the full-scale test conducted at natural scale are addressed in the following subsections.

2.1.1. Corrugated steel plate

SSCS shells are made most often of corrugated steel plates due to increased flexural stiffness compared to flat sheets [22] [23]. They are produced in a wide range of cross-section and corrugation types [7] [24] [25]. In general, the SSCS cross-section can be closed or open. If open, the edges of the shell need to be supported on continuous RC or steel footings; otherwise, the structure can be placed directly on the ground without additional support. The selection of a shell

shape and size depends on the function of the structure and local conditions [26]. The manufacturer's catalog, for example [6], can be used to choose a particular one. The most commonly used profiles of CSP are depicted in Table 2.1 that include both open and closed shapes.

Table 2.1: Profiles of SSCSs [26].

Shape		Range of the span (mm)	Applications
Round		150 – 15,800	Culverts, drainage pipeline bridges, rainwater sewage system, retention reservoirs, service tunnels
Vertical ellipse		1,500 – 6,700	Culverts, service tunnels, sewage system, relining
Pipe-arch		1,200 – 12,000	Culverts, bridges and crossing for animals, relining
Tunnel		1,700 – 12,000	Underpasses, relining
Arched profile		1,500 – 21,000	Bridges and viaducts
Horizontal ellipse		1,600 – 12,000	Culverts, bridges, tunnel, crossing for animals, viaducts
Pear		7,200 – 8,600	Viaducts, tunnel (railway), underpasses or large clearance areas
High arched profile		6,300 – 23,000	Bridges, crossing for animals, viaducts, tunnels
Low hatch profile		6,100 – 23,000	Bridges, crossing for animals, viaducts, tunnels
Box		3,200 – 15,700	Bridges, viaducts, relining

A corrugation profile is usually described by its pitch and depth, as well as the thickness of the shell itself. Classic corrugations consist of a series of crests and valleys formed by straight tangent sections connecting smooth, single radius arcs [27]. The nomenclature utilized to describe corrugated profiles is presented in Fig. 2.1.

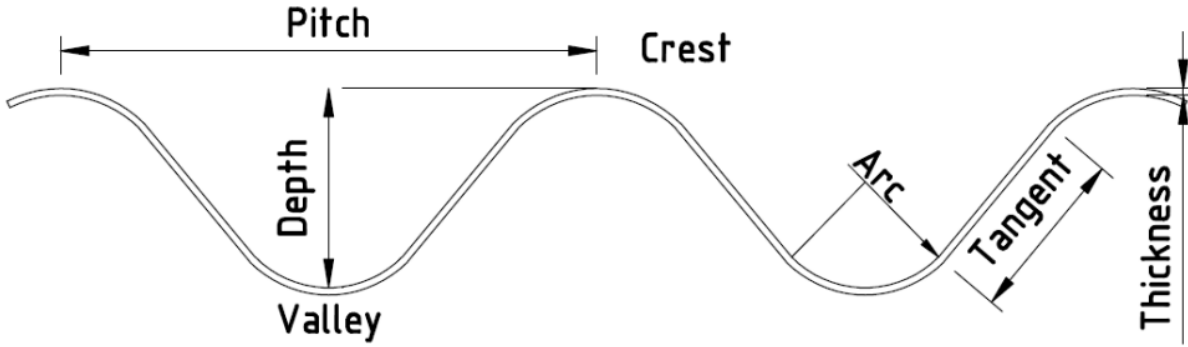


Figure 2.1: Geometry and terminology of corrugation profiles.

The corrugation profiles are classified as shallow, deep, or deeper [25] [28] as shown in Fig. 2.2b. The deepest corrugation profile (at the bottom of Fig.2.2b) was developed in 2011. It has a pitch of 500 mm and a rise of 237 mm [28]. The first structure built with this profile was constructed in 2011 for a highway underpass in eastern Canada with a span of 13.3 m and a rise of 5.3 m [29]. Work [28] states that the largest flexible buried structure in Europe was constructed in Ostróda Town, Poland, using a 500 x 237 mm corrugation profile. It has a span of 25.5 m and a rise of 9.0 m. At the time of completion, it was the largest flexible buried structure in the world.

Today, there is a huge evolution in the technology of the corrugated steel plate profile. As shown in Fig. 2.2 (adopted from [6]) it is possible to construct the bridge with a span of more than 30 m. In 2019, the largest steel buried structure in the world was built for a transportation application in United Arab Emirates. Utilizing the UltraCor corrugation, the structure has a span of 32.42 m and a rise of 9.57 m [29].

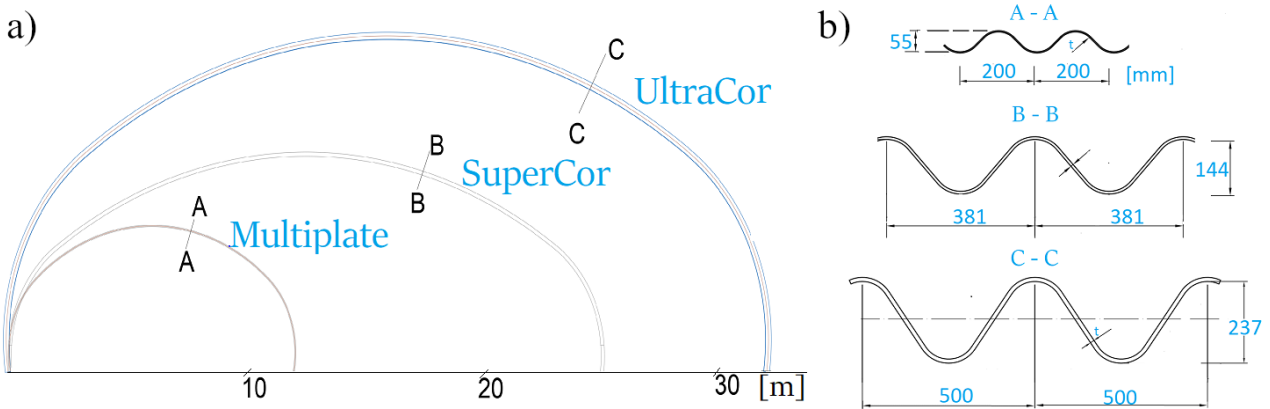


Figure 2.2: Comparison of various CSP profiles (a) and their corrugation types (b).

Corrugated plates are categorized based on the corrugation depth, pitch, width, and thickness [30]. A comparison of deep corrugation (SuperCor) and shallow corrugation was done by [31] and it is summarized in Tables 2.2 and 2.3. The shallow corrugated plate has a cross-sectional area A of $8.29 \text{ mm}^2/\text{mm}$, while the deep corrugated plate with almost the same thickness has the area of $9.8 \text{ mm}^2/\text{mm}$, representing an increase in volume or weight of only $\sim 13\%$. However, the moment of inertia I_s of the deep corrugated plate ($24,164 \text{ mm}^4/\text{mm}$) is more than 9 times of the shallow corrugated plate ($3,213.2 \text{ mm}^4/\text{mm}$). The radius of gyration, the property of the plate that governs the buckling strength of the deep corrugated plate, is about 2.8 times that of the shallow corrugated plate. Thus, it can be concluded that deeper corrugations are very efficient in improving the flexural properties of the corrugated plates.

Table 2.2: Structural properties of $152 \times 51\text{mm}$ corrugated plates [31].

Nominal plate thickness (uncoated)	Area	Moment of inertia	Radius of gyration
[mm]	$[\text{mm}^2/\text{mm}]$	$[\text{mm}^4/\text{mm}]$	[mm]
3.00	3.522	1057	17.33
4.00	4.828	1458	17.38
5.00	6.149	1867	17.43
6.00	7.461	2278	17.48
7.00	8.712	2675	17.52

Table 2.3: Structural properties of deep corrugated plate (SuperCor) plates [31].

Nominal plate thickness (uncoated)	Area	Moment of inertia	radius of gyration
[mm]	$[\text{mm}^2/\text{mm}]$	$[\text{mm}^4/\text{mm}]$	[mm]
3.50	4.784	11,710	49.48
4.20	5.846	14,332	49.52
4.80	6.536	16.037	49.54
5.50	7.628	18,740	49.57
6.30	8.716	21,441	49.60
7.10	9.807	24,125	49.64
8.10	11.06	27,259	49.65

A comparison of section properties of Multiplate MP200, SuperCor and UltraCor plates based on [3] is presented in Tables 2.4, 2.5 and 2.6.

Table 2.4: Section properties of Multiplate MP200 plate [6].

Plate thickness	Yield stress	Area	Moment of inertia	Section modulus
[mm]	[MPa]	[mm ² /mm]	[mm ⁴ /mm]	[mm ³ /mm]
3.00	235 / 355	3.54	1 356.36	46.77
4.00	235 / 355	4.74	1 813.80	61.49
5.00	235 / 355	5.93	2 316.15	77.20
6.00	235 / 355	7.11	2 787.57	91.40
7.00	235 / 355	8.29	3 213.20	103.65
8.00	235 / 355	9.37	3 616.77	114.82

Table 2.5: Section properties of SuperCor plate [6].

Plate thickness	Yield stress	Area	Moment of inertia	Section modulus	Plastic section modulus
[mm]	[MPa]	[mm ² /mm]	[mm ⁴ /mm]	[mm ³ /mm]	[mm ³ /mm]
5.50	Minimum 315	6.968	17,141.15	235.62	607.80
7.00		8.867	21,897.45	297.92	710.15

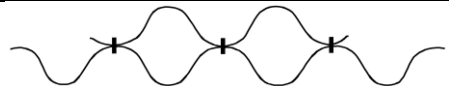
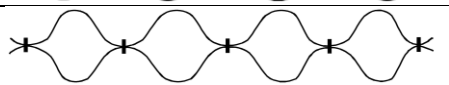
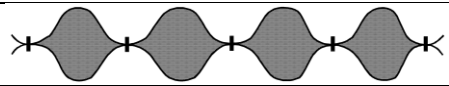
Table 2.6: Section properties of UltraCor plate [6].

Plate thickness	Yield stress	Area	Moment of inertia	Section modulus	Plastic section modulus
[mm]	[MPa]	[mm ² /mm]	[mm ⁴ /mm]	[mm ³ /mm]	[mm ³ /mm]
6.00	355 / 420 / 500	8.662	54,849	451.43	607.80
7.00	355 / 420 / 500	10.110	64,131	525.67	710.15
8.00	355 / 420 / 500	11.559	73,457	599.65	812.81
9.00	355 / 420 / 500	13.009	82,827	673.39	915.79
10.00	355 / 420 / 500	14.460	92,243	746.91	1019.09
11.00	355 / 420 / 500	15.913	101,706	820.21	1122.72
12.00	355 / 420 / 500	17.366	111,217	893.31	1226.68

Reinforcing (stiffening) can be used if the flexural capacity of a single CSP is exceeded [6]. Stiffening consists of additional corrugated ribs installed over the shell. According to [31] the flexural rigidity of two 7.1 mm thick, fully composite deep corrugated plates is almost equivalent to that of a 200 mm thick concrete shell. However, since the connection of the stiffening ribs to the base shell is never perfect, paper [32] proposed a practical method to calculating the sectional properties of the reinforced shell. The stiffening can be used along the entire perimeter, or its selected sections based on the shape of the shell and the span of the structure. Typically, the stiffening ribs are utilized in the crown and haunches for box-shaped shells. Moreover, to get a greater capacity, space between the main shell and reinforcing ribs can be filled with concrete.

Stiffening methods are depicted in Table 7 (adapted from [32]). The use of filled ribs can be necessary for large span structures [33]. Usually, C25/30 concrete is used [34] for this purpose.

Table 2.7: Stiffening of CSPs with additional ribs [32].

No.	Designation of the sheet arrangement	Scheme of the shell with the overlay
1	SC + SC/2	
2	SC + SC	
3	SC + SC + concrete fill	

MacDonald [27] presented the mechanical response of stiffened and non-stiffened CSP determining the equivalent transverse stiffness of corrugated sheets. The figure Fig.2.3(a) show simple diagram used to determine the effective parameters of the corrugated steel plate with appropriate stiffnesses in the transverse direction [35]. The diagram on Fig.2.3(b) shows the shell stiffened and unstiffened corrugated steel plate. The stiffening of CSP significantly enhances the mechanical performance of the shell.

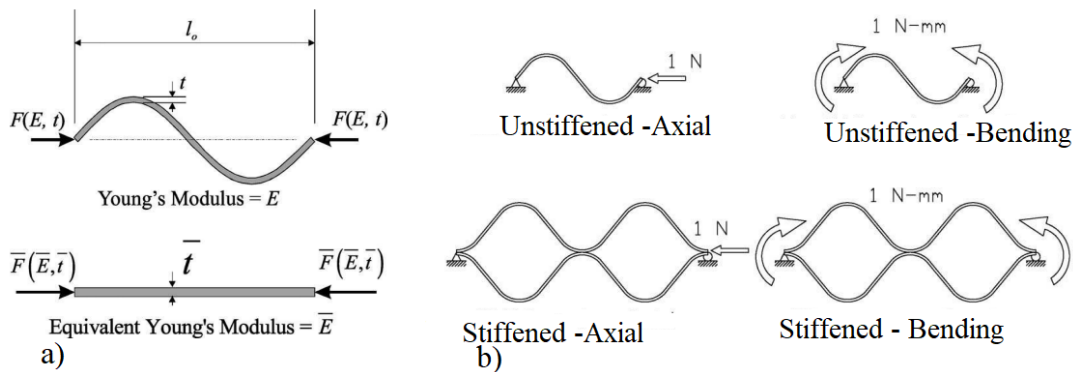


Figure 2.3: a) Young's modulus of the CSP and orthotropic plate with equivalent modulus [35] b) stiffness of corrugation profile for stiffened and unstiffened CSP [27].

2.1.2. Foundation

CSP with closed profile are placed directly on the ballast from aggregate [53] [82] as shown in Fig.2.4(a). On the other hand, for the opened profile there are two fundamental types of foundations employed to provide essential structural support. The first type consists of rigid

concrete foundations. The second type of foundation is constructed using corrugated steel plates. Comprising corrugated steel sheets, these foundations are designed to adapt to limited ground movement and deformation. The choice between these foundation types of hinges on project-specific criteria, necessitating a careful engineering analysis to ensure an optimal fit for soil steel composite structures. The assembly of CSP shells is shown in Fig.2.4 for both cases.



Figure 2.4: Assembly of CSP: a) closed profile on the ground, b) open profile on the RC strip footings, c) open profile on the CSP [36]

Within SSCS technology, the use of a buried soil-steel structure eliminates the need to construct the bridge deck, approach slabs, and expansion joints that are necessary in traditional bridge design. This significantly reduces maintenance and total life cycle costs [37]. One of the important issues of the design and construction of the SSCS is finishing the headwalls. It is recommended to use a concrete collar around the edges of a CSP. This serves to stiffen the edges, protecting them from localized damage and deformation, while improving their structural integrity. Square or beveled ends are most often used. Alternatively, headwall solutions such as mechanically stabilized earth (MSE) wire mesh face, bin-wall, and steel face tie-back walls can be considered. Additionally, for water crossings, it is necessary to construct impervious headwalls and wingwalls to protect the structure against piping and erosion [38].

2.1.3. Engineered backfill

All the engineered soil around the structure is called a backfill [39]. The design of SSCS requires consideration of the interaction between the corrugated steel structure and the surrounding soil. This interaction is the key factor for the high bearing capacity of the flexible buried structure [40], [41] [42] [43] [44]. The CSP sheet is flexible, and in fact, the load carrying capacity of the composite structure depends on the quality of the backfill. It should be composed of well-graded soils, whose properties do not change with time [31]. The quality of the backfill soil, built at the early stage of filling, has a great impact on the durability of the entire soil-steel composite bridge [25]. It is important to execute backfilling in a symmetric way on both sides of the structure with layers of 150-300 mm thickness. The backfill surface should be at the same level on both sides of the shell [40] [45] [46]. The correct way of backfilling is depicted in Fig.2.5.

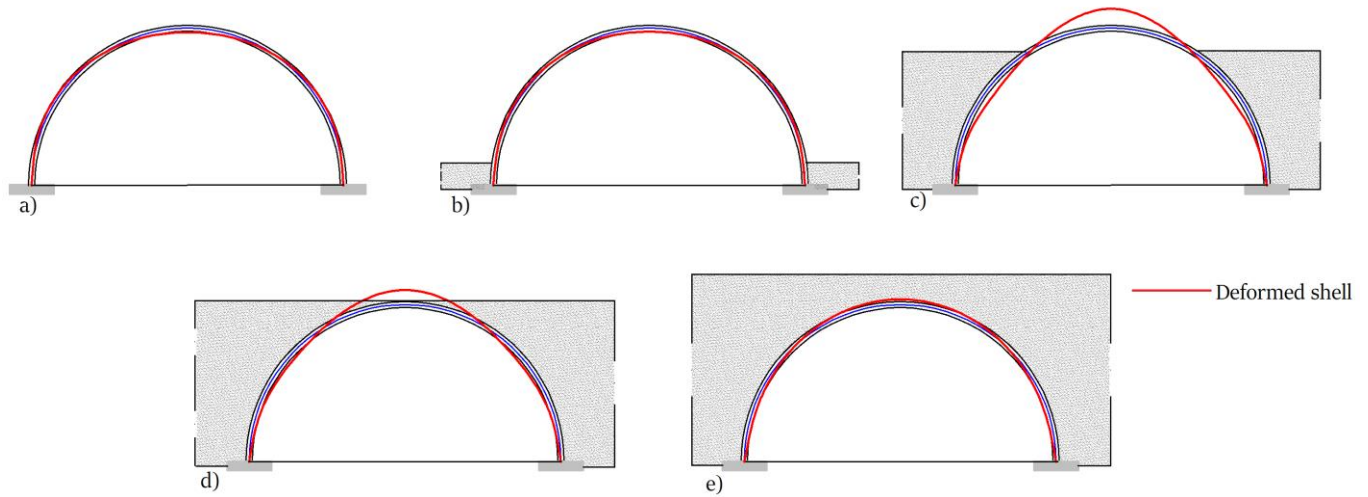


Figure 2.5: Backfilling stages: a) completed assembly of the shell, b), c), and d) laying and compaction of subsequent layers of backfill, e) completed backfilling.

Proper control and avoiding excessively large deformation of the CSP during backfilling is one of the difficulties to overcome in the construction process. The major problem that may affect correct execution of backfilling is buckling and loss of stability, which is not observed in typical arch or box RC structures [7] [45] [47]. A regular deformation of the shell is depicted schematically in Fig.2.5 with the red line. During the initial stages of backfilling, the soil exerts lateral pressure on the sides of the shell. As a result, it is narrowing. At the same time, CSP rises at the crown. Typically, the maximum upward deflection is observed when the backfill level reaches the crown point [48]. Next, the top of the shell moves downward with increasing backfill height. As a result,

the sides of the shell press against the backfill [49]. This, in turn, generates an increase in lateral pressure in the adjacent backfill soil. Usually, the crown point does not return to the initial level after completion of backfilling even when completely backfilled. In other words, the final displacement of the shell at the crown is upward. This can be considered as an advantageous effect of shell pre-stressing. Since the vertical deflection of the shell top induced during construction is opposite to the direction of service loads (e.g., transmitted from vehicles), at least a part of the load contributes to the reduction of the above-mentioned upward displacement. However, this effect applies mostly to circular or arched shells.

Since shell deformation during backfilling is a significant issue, it should be controlled using geodetic techniques [31]. The vertical displacement at crown as well as shell narrowing at predefined height are to be observed. For the SSCSs, the upward or downward crown during construction is required to be limited to 2% of the rise [31]. If the uplift of the crown point during backfilling reaches a value greater than designed, ballasting of the shell can be utilized [50]. The term ballasting here means an additional load on the top of the shell, e.g., using soil or concrete slabs. This additional load aims to prevent excessive uplift of the shell in the intermediate stages of backfilling. According to the work [25] circular and arched cross-sections are characterized by high susceptibility to horizontal deformation in the case of unsymmetrical laying and compaction of the backfill, while vertical deformation is observed in a situation when the backfill is placed symmetrically on both sides of the structure.

Typical mistakes made in the construction phase of SSCS include: incorrect execution of joints between CSPs, damage of anti-corrosion protection during assembly (this may lead to the appearance of corrosion spots and their development at service phase), the use of heavy construction vehicles, like excavators and rollers too close to the shell (the actions of great magnitude can cause damage to the steel structure), improper backfilling (this can cause loss in shear strength of soil and deformations of the shell which may lead to loss of stability) [7]. To overcome such mistakes, special attention must be paid to both the design and the construction that should be performed by professionals having reliable experience.

The correct execution of backfilling is of particular importance because it determines the performance of completed SSCS under service loads. Its behavior significantly depends on the characteristics of the backfill soil, such as its density index, type of soil, the grain size distribution,

maximum dry density, the thickness of the compacted layers, and height of soil cover[33]. Soil parameters such as internal friction angle, cohesion, modulus of elasticity, Poisson ratio, unit weight, and coefficient of lateral earth pressure determine the overall stiffness and load bearing capacity of the backfill. Furthermore, the strength parameters of the backfill affect the behavior of the structure in both quantitative and qualitative sense. The effect of backfill material parameters on soil-structure interaction (SSI) of a buried corrugated steel arch bridge was analyzed in [51]. Numerical analysis was performed by changing parameters such as cross-section of the CSP, as well as elastic modulus, internal friction angle and Poisson's ratio of the backfill. The results of the analysis showed that the incorporation of SSI in the calculation contributed to a significant reduction in the adverse influence of excessive structural displacement and redistributed stresses in the surrounding soil. The increase of elastic modulus of backfill soil leads to decrease in the pressure exerted on the steel arch by the soil. Furthermore, the higher the value of the internal friction angle, the higher the pressure within the soil. With decreasing Poisson's ratio, soil displacements increase slightly, but it has a positive effect on reducing soil pressure on the shell. Generally, the authors of [51] conclude that increasing the modulus of elasticity has a positive impact on the SSI, while increasing internal friction has slightly adverse effect on structure performance.

2.2. Design of the SSCSs

The design methods for soil steel composite structures are generally based on both theoretical and experimental tests [52]. The theoretical design method was initially based on the basic concept of compression theory developed by White and Layer [53] which entails that the flexible culverts are designed simply for a prevailing normal force in the circumferential band. Nowadays, this method of design may not be effective, since the SSCSs' span lengths become larger, and the design demands heavier concentrated loads at shallow depths of soil cover. Therefore, it needs detailed analysis and investigation by developing a 2D and 3D finite element (FE) models to understand the effect of service live load and soil dead load on the soil-culvert interaction (SCI) [52] [54].

The American standard AASHTO LRFD [55] has provided the design procedure and specification for soil-steel composite structures. It utilizes the concept of ring compression for the relatively small span culverts. For large span structures, AASHTO proposes a design specification

based on the research output of a field testing of a 9.5 m span metal arch supported with finite element analysis (FEA) [23][52]. However, the Canadian highway bridge design code (CHBDC) [56] does not involve soil-steel interaction (SSI) effects for box culverts of the span greater than 8.0 m.

The design method by Pettersson and Sundquist [57] has been used in Sweden as well as in the other Nordic and some of the Baltic countries. The design loads (forces and moments) of SSCS in this handbook are approached mainly using the principles of the soil-culvert interaction (SCI) method by [43] with some modifications made to the calculation of the modulus of elasticity of the backfill soil and load distributions. In the principle of SCI, most of the load is carried by soil, of course, it depends on shape of the shell, load position, and other factors. The engineered backfill soil as a load-carrying element affects the bridge/culvert behavior depending on the deformation modulus, which results from the soil type used and its degree of compaction. In particular, careful compaction of the backfill soil in the vicinity of the corrugated steel plate is important to attain the desired interaction between the steel and the soil [26]. Generally, as stated in the AASHTO LFRD (2017) [55] code, the backfill should meet the requirements of AASHTO M145:1991 (2012) [58]. In the case of structures with deep corrugation, the backfill soil should meet the unified American soil classification provided by ASTM D-2487-11 (2011) [59][56]. It boils down to groups I and II of density index not less than 0.90 [7].

Both the Canadian and American codes (CHBDC, [56] and AASHTO LFRD (2017) [55]) consider the interaction between CSP and the soil to determine the strength of the SSCS. Since the CSP is flexible, allowing excessive deformation to occur can easily cause its failure. To avoid this, structural reinforcement can be added to increase the stiffness and, thus, to restrain deflection [51]. According to Pettersson [16] as well as Wadi and Pettersson [60] the bearing capacity of the soil-steel composite culvert or bridge is highly dependent on soil compaction.

The height of the backfill cover above the shell, denoted as h_c , is a significant design factor with regard to the behavior of the SSCSs at the operational phase. According to Pettersson [16], Pettersson *et al.* [40] and Bęben [7] the height of cover is defined as the distance between the top of the corrugation and the road surface as shown in Fig. 2.6a. For railways, the live load is assumed to be transferred to the soil at the underside of the sleepers. Therefore, as presented in Fig. 2.6b, in this case the height of cover is the distance from the top of the shell to the bottom of the sleepers

[16]. The height of cover is usually measured along the center line of the structure but a sloped surface shift this location towards downhill slope [61] [62] – see h_c^{slope} in Fig.2.6c.

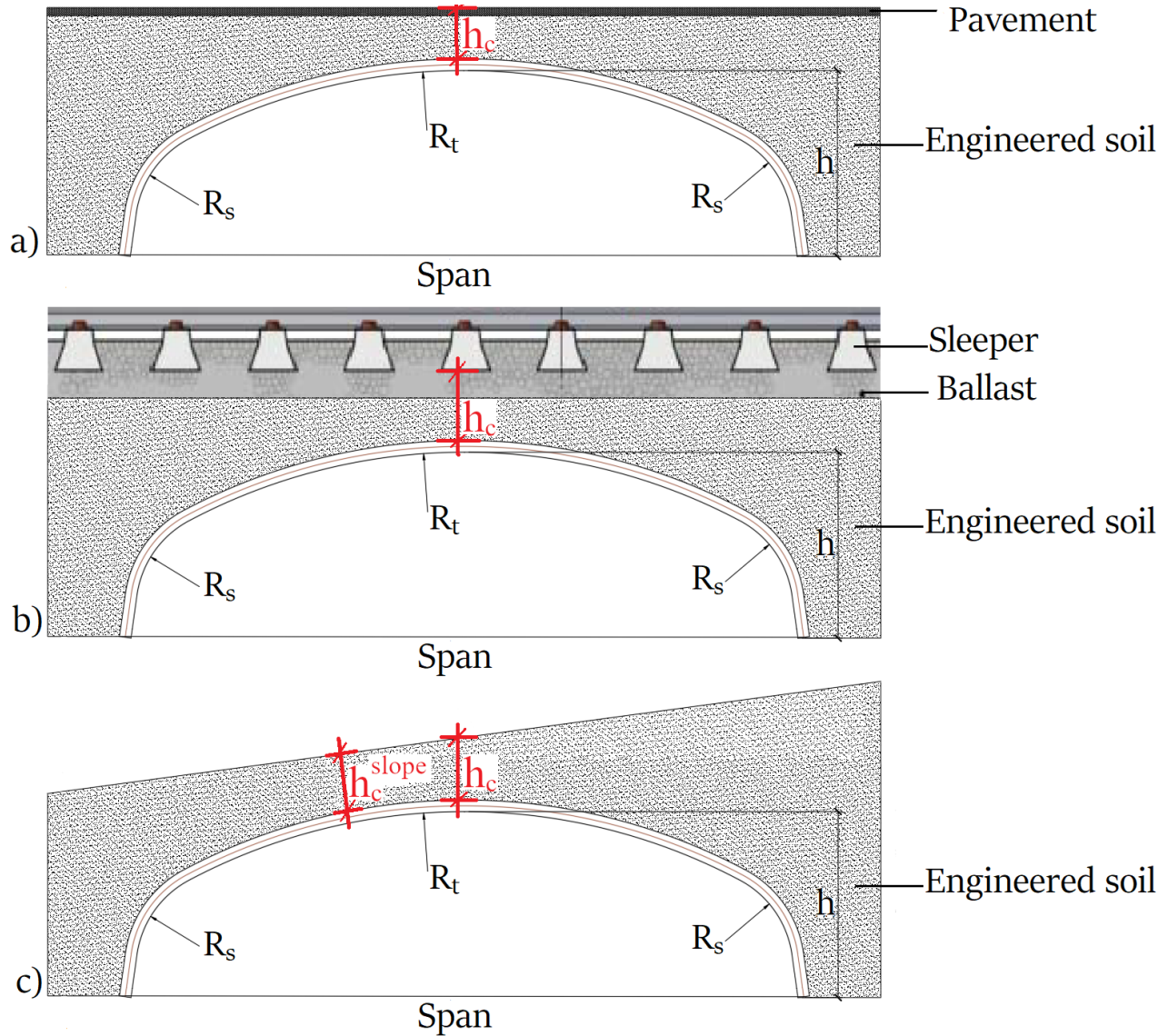


Figure 2.6: The height of cover definition for the cases of a) car traffic pavement on the surface, b) railway road, and c) sloped surface.

The cover depth h_c must be carefully designed. Especially in the case of low cover, a slight change in its height may be critical for the load-bearing capacity. SSCSs are sensitive to this design parameter. Therefore, this problem has been thoroughly studied by different authors [7] [54] [45] [63]. Furthermore, it is important to note that the height of the cover should be taken as the net distance after the backfill completion. In particular, the vertical deflection at the crown of the shell due to backfilling has to be taken into account [57].

A minimum of one eighth of the bridge span or 0.6 m soil depth of cover is required to achieve well compaction of the backfill soil above the crown. However, as revealed before, in cases of large magnitudes of live loads, the above-set criteria may not be good enough for shallow cover design [16].

The cover-to-span ratio is the best way to deal with a low height of the cover. At the same time, it is a way to define whether the structure is at a low height of cover or not. Pettersson *et al* [40] conclude that using a similar truck for the test, the bending moment at the crown increased by 75% by reducing height of cover from 0.9 m to 0.75 m. This indicates how the SSCS is sensitive to the cover depth hc . According to [7], the minimum soil cover shall not be less than:

- $S/8 \geq 0.3$ m for corrugated metal pipe and structural plate pipe structures,
- 0.61-1.22 m for long-span structural plate (this depends on the top radius and steel thickness (without ribs)),
- $S/4 \geq 0.3$ m for spiral metal pipe,
- 0.43 m for metal box structures,
- 0.91 m or the limits for long-span structural plate structures based on the top radius and plate thickness for structure with deep corrugations (according to AASHTO LFRD (2017) [55] requirements).

Above all, a properly designed height of cover should ensure the stability of the structure. If the backfill thickness is too low, a potential failure can be initiated by excessive tension and/or shear within the soil cover and, eventually, result in buckling of the structure. This can usually be avoided by applying a minimum depth of soil cover specified in the design codes [63] [64]. It is, however, also determined by correct and careful execution of backfilling. These issues become especially important in the cases of large span and low cover depth. Then the risk of soil failure must be checked, and efforts are to be made to avoid it by using good quality, well-graded soil and rigorous control of its compaction.

2.3. Behavior of SSCS under different loading conditions

2.3.1. Construction stage

In SSCS, corrugated steel plates are usually under maximum stress during backfilling [65]. The forces acting on the shell and the resultant shell displacements change during backfilling. Extreme

values of both strains and displacements, are obtained once the backfill level reaches the crown [48] [66] [65] [67].

Seed and Ou [68] studied the effects of compaction on a long span culvert. They measured the deformations of a structure during backfilling. The measured data were compared with the FEA output and a good agreement between both results was observed. From the finite element analysis, the authors conclude that the structural deformation was significantly increased during compaction of the backfill and the bending moments within the culvert were also significantly affected. However, the effect of compaction-induced earth pressures on the axial thrust around the culvert perimeter was not significant.

Korusiewicz and Kunecki [67] conducted full-scale tests on the corrugated steel box-type culvert with a span of 3.55 m and a height of 1.62 m. They observed the behavior of the structure during the backfilling process. Furthermore, the authors compared the numerical simulation output with the experimental results, and they found that the FE model was incapable of determining internal forces and displacements in the steel structure at the initial stages of backfilling since it did not take soil compacting forces into account. However, the model output agrees with the experimental results once the backfilling is complete. It also remains true when one assumes a pavement model. However, the output from numerical simulation is still overestimated.

Mańko and Bęben [69] analyzed the behavior of SuperCor road bridge located in Gimán, Sweden under backfill load during construction. They compared the displacements obtained from the measurements and calculations. The average strain and displacement values were lower than the calculated values in nearly all the points examined in the CSP sections. The displacement comparison indicates significant differences between these values (measured and calculated) and are in the range of 55 to 85 %. The authors conclude that the reason for such differences was the interaction between the shell structure elements and the surrounding soil.

Embaby et al. [70] investigated the structural behavior as well as the soil-structure interaction of a large arched SSCS constructed using CSP with a deep corrugation profile, 500 mm x 237 mm, during the construction and operation phase. The investigated structure had a span of 32.40 m and a vertical height of 9.57 m. From the numerical analysis, they observed that due to the reinforcement of the CSP, the strain in the buried structure was reduced by 50%, while the circumferential steel bar stiffeners reduced the crown vertical deformations to 0.5% of the structure

rise. The reduction in vertical displacement was observed due to the fact that circumferential steel bar stiffeners enhance the performance of the CSP against downward deformations after adding the soil cover above the structure.

The behavior of the SSCS under backfill was analyzed by Machelski *et al.* [28]. The bridge had a span of 25.5 m and a rise of 9.00 m. The CSP had a thickness of 9.5 mm and UltraCor corrugation (500 x 237 mm) was used. The bridge carried the heavy traffic of the S7 express road. The authors observed maximum vertical deflection during the test, reaching 2.3% of the rise. This exceeded the limit value of 2% defined by the code CAN/CSA-S6-14 [56]. The authors suggested that the deflection limit in CAN/CSA-S6-14 needs to be revised for such structures. The new limit value of 2.5% of the rise was recommended, provided that field measurements and/or finite element analysis were used. For large-span SSCS, these challenges can be alleviated by using additional stiffening materials such as ribs, relieving slabs, longitudinal beams, steel ribs and steel ribs filled with concrete [33] and EPS geof foam [71]. These issues are addressed further in the next Section

2.3.2. Under static and semi-static load

As the main function of a bridge structure is to carry the service loads transmitted from a road or railway, the analysis and testing structures under mechanical actions is one of the main research topics. SSCSs exhibit a number of unique features to this group of engineering structures. In the tests described in [8] [49] [72] [73] [74] [75] [76] changes in the displacement and strains at selected points of the shell due to the moving loads were analyzed. These studies were conducted in a quasi-static manner. In addition, the tests analyzed at least one load cycle consisting of a vehicle crossing the bridge in one direction and then returning in reverse gear. In this way, the settings of the vehicle (or vehicles) were repeated on the return. One fundamental conclusion emerges from these studies: the mechanical response of the SSCS subjected to semi-static moving load is affected not only by the location and intensity of the load but also by the direction of its movement. This effect is exhibited by distinct hysteresis loops in plots of either stress or displacement of the shell versus vehicle position along the bridge in a passage and return loading cycle [77]. In general, it is assumed to be a result of frictional contact at the soil-steel interface [72] [73] as well as non-linear, namely plastic behavior of backfill soil itself [64] [72]. The effect of live hysteretic load effect in SSCS has been reconstructed using numerical simulation in [72] [73] [75]. Fig. 2.7 (adopted from [73]) shows the comparison of the results of the real-scale test

and numerical simulation of an SSCS along railway road in Świdnica, Poland. In the test, the ST43-type locomotive was crossing the bridge one way and then back along the same track. The plots in Fig.2.7 show the vertical displacement of the shell's crown in the course of passage and return loading cycle. The initial passage from left to right is plotted with a red line, while the subsequent return – from right to left – with a blue one. The x-axis values correspond to the locomotive position along the track. As it can be apparently seen, both plots form hysteresis loops.

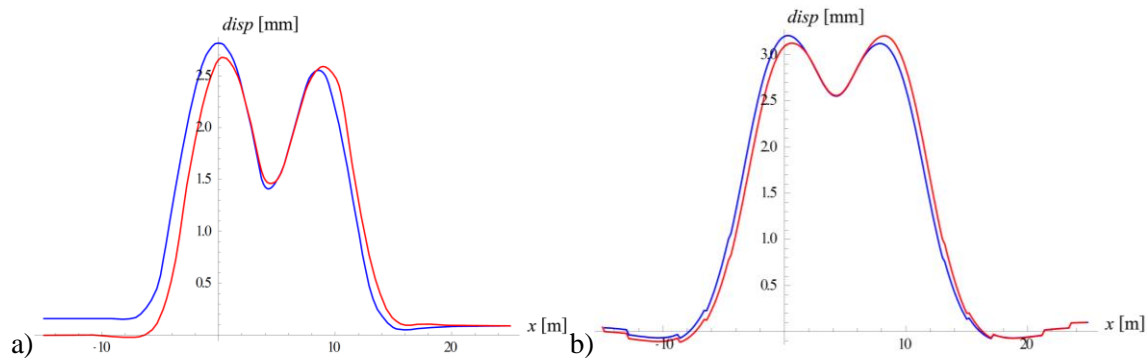


Figure 2.7: Vertical displacement of the shell crown point: a) result of real scale test, b) result of the simulation (based on [73])

Nowacka *et al.* [78] analyzed the impact of expanded polystyrene (EPS) geofoam on the behavior of SSCS under static loads. The authors observed that the application of EPS geofoam in SSCS reduced vertical displacement, stress in the steel shell, axial forces, and the bending moment by 41, 24, 30 and 30%, respectively, compared to the model in which relieving element was not used. The authors also compared the EPS geofoam with the RC relieving slab and the former one is more effective and economical. It was also noted that the level of bending moment in all considered models (without relieving slab, with 0.2m thick RC slab and with EPS blocks) was low, showing that SSCS carries load more due to the axial forces than bending moments.

Maleska and Bęben [33] conducted numerical analyzes of SSCS with a span length of 17 m using the 3D DIANA program, based on FEM. They explored three models for shell structure. The first model did not incorporate stiffening, the second model considered steel ribs, and the third model employed steel ribs filled with C25/30 concrete as shown in Fig.2.8. The response of the CSP shell during backfilling was numerically verified. As a result, the numerical analysis revealed a reduction in maximum displacement, as well as in stresses, bending moments, and axial forces when stiffening elements were introduced into the CSP shell.

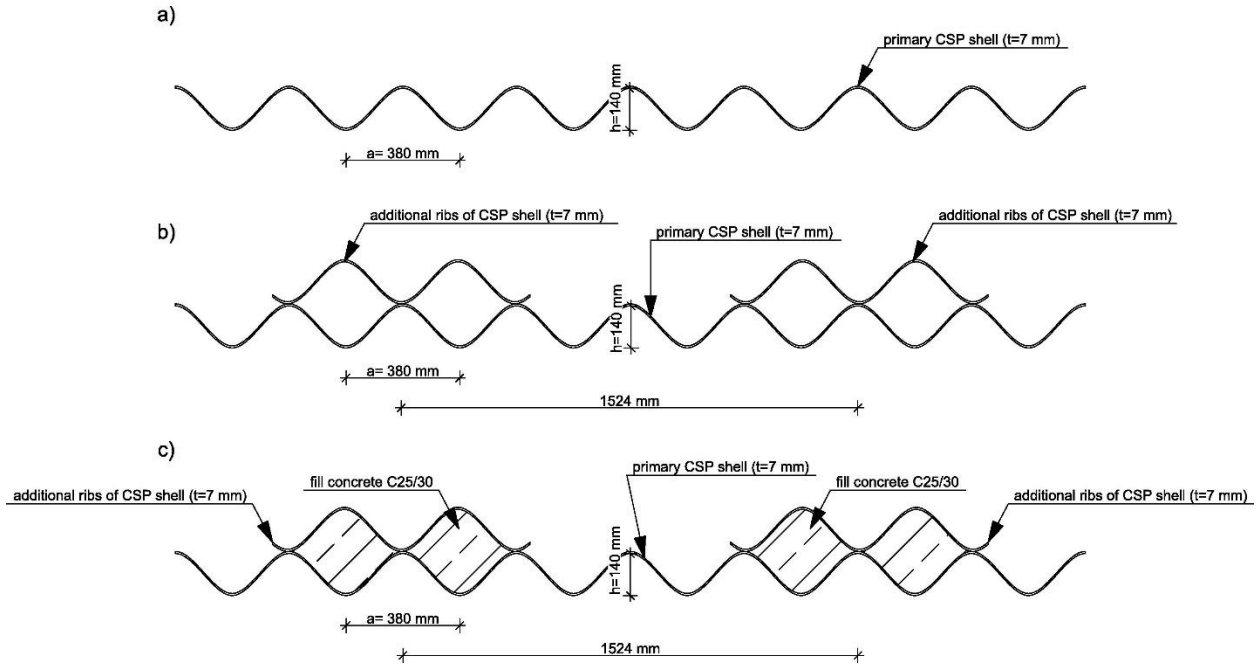


Figure 2.8: Models: (a) model I (shell made of CSPs); (b) model II (shell made of CSPs with additional CSP ribs); (c) model III (shell made of CSPs with CSP ribs and filling with C25/30 concrete), (Source: Maleska and Bęben [33]).

The authors [33], compared the combined stress resulting from axial force and bending moment calculated numerically with the maximum stress in the shell based on Eq (1). They observed that the stress calculated from the numerical simulation was lower than the stress calculated using Eq (2.1). The maximum stress in the shell determined by the formula [24] [56]:

$$\sigma = \frac{N_{d,s}}{A_{s1}} + \frac{M_{d,s}}{W_1}, \quad (2.1)$$

where:

σ – maximum stresses in the CSP shell (kPa),

$N_{d,s}$ – axial force due to backfilling (kN/m),

$M_{d,s}$ – bending moment due to backfilling (kNm/m),

W_1 – section modulus (m^3/m),

A_{s1} – area of the cross section of the CSP shell (m^2/m).

The use of additional stiffening did not yield a significant advantage in stress reduction within the shell [33]. Furthermore, in the model without stiffening, the allowable stresses and displacements were not exceeded, indicating that the CSP could support the loads resulting from

backfilling. Flener [49] also conducted analyses to explore the effects of stiffening. The results indicated a 50% reduction in crown rise when the culvert was stiffened with ribs.

2.3.3. Under ultimate load

The capacity of the SSCS should be checked in the serviceability limit state (SLS) and the ultimate limit state (ULS) [16]. Furthermore it is suggested by [16] that fatigue tests should be a part of the ultimate limit state verification. Numerous field and laboratory tests have been conducted throughout the recent decades to realize the behavior of the SSCSs, and their performance under different conditions has been analyzed. Full-scale tests were carried out together with computer simulations, most frequently using FEM. This helped researchers and practitioners realize the structural behavior of SSCSs and develop efficient design methods.

Since the formulation of the ring compression theory [53], different design methods have been developed to account for the various design conditions and facilitate the use of larger spans. For example, the research done by Duncan [43] on SCI has utilized 2D FEM results to propose a set of design equations, which became the basis for the Canadian Highway Bridge Design Code (CHBDC) of the Canadian Standards Association (CSA) 2014 [79]. Similarly, the research conducted by Pettersson and Sundquist [24] based on full-scale tests set the foundation for Swedish design method (SDM). Also, research presented by Moore and Taleb [80] was used for the AASHTO design method which compiled the study of a 9.5 m span metal arch culvert field test together with FEA, given the opportunity to provide recommended specifications for large-span culverts.

Today, researchers are focusing on the use of numerous materials to alleviate and strengthening the performance of SSCSs. To increase the load capacity and reduce deformation of CSP structures, in addition to a basic shell, extra stiffening methods are used, for example: additional steel ribs [33], concrete or steel beams, RC relieving slabs, filling the ribs with concrete, and expanded polystyrene (EPS) geof foam [13] [71], and geo-synthetic materials strengthening the backfill [13] [33] [81].

Flener [54] conducted a full-scale test to observe the response of large span soil steel composite structure under ultimate loading tests. The structures with 14 m and 8 m span lengths and different crown stiffness were investigated assuming different cover depths. The author observed that the load-bearing capacity of the structure increased linearly with an increasing soil depth of cover. The

ultimate load carrying capacity increases significantly with the use of crown stiffeners and the load resistance of the composite structures is doubled at the crown level with this crown stiffening. The author concludes that the ultimate loading tests performed on the 14 m span showed that the loading was kept in elastic range. Therefore, the maximum loads applied to the structures do not necessarily represent the ultimate load.

Brachman et al. [82] tested a deep corrugated steel box culvert with a span of 10 m and a rise of 2.4 m to its limit load capacity under controlled experimental conditions. The structure was subjected to a vertical force applied to a tandem axle frame centered on the box culvert with a soil cover depth of 0.45 m. The ULS of the box culvert was reached with an applied force of 1,100 kN. The authors observed that the force required to reach the ULS was 1.8 times greater than the factored tandem axle load from the AASHTO bridge design specifications. Similarly, the factored resistance in the ULS was 1.7 times larger than the factored CL-625-ONT tandem axle load from the Canadian Highway Bridge Design Code.

Wadi *et al.* [45] investigated the effect of the different loading positions on the maximum load capacity of SSCS having 18.1 m. It was observed that the failure load was reduced by loading the structure in an asymmetrical manner. From the 3D simulation, they predicted a failure load of at least 1.5 times the standard tandem loads, as it was shown in Fig. 2.9. (adopted from [45]).

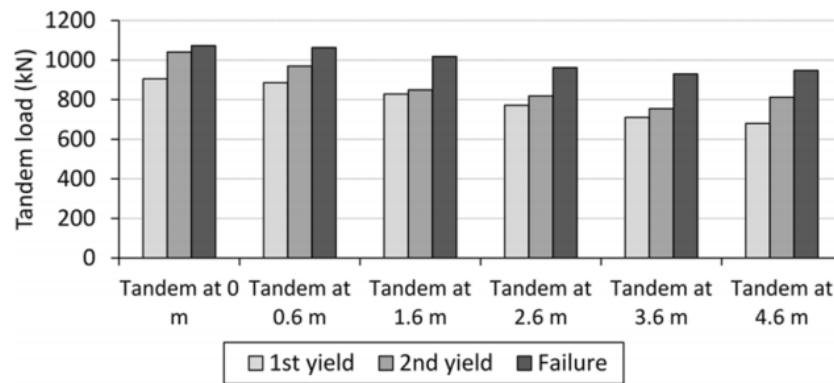


Figure 2.9: A summary of failure loads from 3D model [45].

The authors of [45] concluded that the maximum values of bending moments were observed when the tandem was centrally located above the crown point – tandem at 0 according to Fig. 2.10 (adopted from [45]). Furthermore, the impact of bending moments from the backfill soil causes the first yield of the steel to be seen at a lower load when the tandem is located away from the crown. This prediction was made by assuming a Mohr-Coulomb material model for the backfill

and frictional interface in the soil-steel contact zone. The following backfill parameters were adopted: elastic modulus $E = 60 \text{ MPa}$, internal friction angle $\phi = 45^\circ$, cohesion $c = 5 \text{ kPa}$, Poisson's ratio $\nu = 0.3$, depth of cover $h_c = 70 \text{ cm}$.

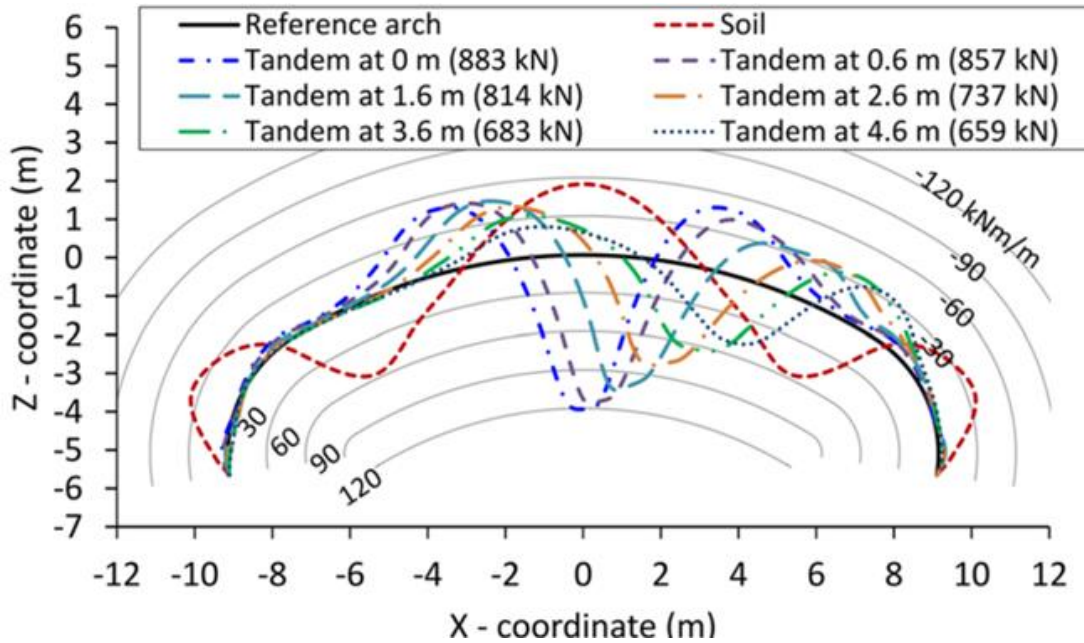


Figure 2.10: Bending moment resulting from dead load of soil and live load at tandem loads just before the first yield of the steel material as calculated from the 3D models [45].

Wadi *et al.* [83] conducted a numerical simulation to determine the ultimate bearing capacity of a 6.1m span soil-steel culvert under live load. The results of the computation, namely deformation, normal forces, and bending moments, were compared with the results of the field measurement. The authors noted that the developed model overestimated the ultimate load in comparison to the field test data.

Regier *et al.* [63] have conducted an experimental study to observe the behavior of a horizontal ellipse culvert with a cover depth of 0.45 m during backfilling. The structure failed at the maximum load of 1,324 kN. The limit state was reached due to the formation of three plastic hinges within the CSP shell.

Pettersson [16] performed ultimate load tests on flexible culverts and concluded that if the degree of compaction was increased by 3% (from 92% to 95% modified Proctor density), the maximum axle load was increased by approximately 30%. This indicated a significant dependence of compaction on the load bearing capacity of the composite structure. Moreover, Loughed [84]

observed the significant impact of geometrical non-linearity on mechanical behavior of SSCS subjected to ultimate load.

According to the work of Wysokowski [25], the reinforcement of a backfill soil with a geogrid contributes to increasing the loading bearing capacity of the entire facility by approximately 30%. From the tests, the author concluded that the values obtained for the stresses and displacements for the steel shell structure were relatively small, even at loads that far exceeded the standard loads.

Based on the reviewed works, the following general remarks on the assessment of ultimate load bearing capacity of soil-steel bridges and culverts can be formulated. Generally, it can be investigated through a full-scale test and evaluated through numerical simulation. The former is believed to be the most reliable approach. However, it is obvious that direct testing of the ultimate load bearing capacity is very expensive, and, above all, it is destructive to the structure that must be then dismantled. In addition, such tests have further limitations, e.g., they are conducted for a single, predefined load configuration. For these reasons, regarding the load capacity, the full-scale tests can only be treated as a verification of design or modeling methods. On the other hand, the costs of numerical simulations are relatively low. Furthermore, computational analyses make it possible to perform parametric analyses by checking multiple cases of design assumptions (e.g., cover depth) or load configuration. This approach is obviously much more credible if the model is calibrated on the field measured data. In summary, both approaches are of unquestionable practical importance. They should be used in parallel, taking advantage of the specifics of each of them.

2.4. Behavior of multi-span SSCS

The behavior of multi-span SSCS during construction and service stages has been studied by many scholars. Bao et al [85], conducted a numerical simulation on performance of multi-span SSCS during construction and operation stage under vehicle load and concludes that stress and deformation initially increase rapidly with load cycles, stabilizing afterward. Sawamura et al. [86] conducted a study on the influence of multi-arch culvert spacing and mechanical behavior under seismic conditions through numerical analysis. The results indicate that with narrow element spacing, the overall stiffness of the soil and culvert increases. Hwang et al. [87] investigated the influence of multi-arch culvert spacing through dynamic finite-element analysis and found that when the spacing between arch culverts is close, the increase in ground stress is observed while volumetric strain is limited.

Urbański et al [88], conducted numerical analysis on two span SSCS under railway load. In their analysis, the influence of interactions between adjacent shells on the values of internal forces was demonstrated. In the study, three different structural models were prepared, each with varying spacings between adjacent shells: 0.72 meters, 1.3 meters, and a model without an adjacent shell (single shell). The analysis aimed to investigate how these different configurations influence the cross-sectional forces and stress levels within the structure. The authors' findings unequivocally confirm that the spacing between adjacent shells has a substantial impact on reducing cross-sectional forces occurring in the structure. This result underscores the importance of considering the arrangement of adjacent shells in the design and analysis of shell structures. When comparing the first model (0.72 meters spacing) with the second model (1.3 meters spacing), it becomes evident that significantly lower values of forces were obtained as the spacing increased. This trend suggests that a greater distance between adjacent shells leads to a more efficient distribution of loads and consequently reduces the cross-sectional forces experienced by the structure. Furthermore, the authors compared the models with adjacent shells at different spacings to a model with a single shell, where there is no adjacent shell. The results revealed that the stress levels in the structure were significantly impacted by the presence and spacing of the adjacent shell: When the adjacent shell was spaced at 0.72 m, the stress increased by a substantial 90% compared to the single-shell configuration. This indicates that a closer spacing between shells can lead to higher stress levels, potentially affecting the structural integrity. Similarly, when the adjacent shell was spaced at 1.3 meters, the stress increased by 30% compared to the single-shell configuration. While this increase is less pronounced than in the closer spacing scenario, it still highlights the importance of considering the spacing between adjacent shells in structural analysis and design. These findings have practical implications for the design and engineering of shell structures. They emphasize the significance of optimizing the spacing between adjacent shells to achieve desired structural performance, minimize forces, and ensure structural stability. The choice of shell spacing should be carefully considered based on the specific requirements and loading conditions of the structure.

2.5. Behavior of geosynthetic reinforced SSCS under different loading conditions

A substantial portion of the load-bearing capacity and stiffness of these types of structure is through interaction with the backfill. This indicates that the quality of the surrounding backfill will determine the performance of this structure under external load [70]. Since the soil is weak against

tensile stress, it is important to improve the bearing capacity of the soil in order to improve its stability by reducing the lateral displacement and settlement under different loading conditions.

Geotextile has become a subject of significant scientific research in recent years. Moreover, they have gained widespread use as reinforcements in stabilizing various engineering structures, including buried structures like soil- steel composite structures [89] [90].

Adding a layer of geosynthetics to the backfill can significantly increase the stiffness of the composite structure. Thus, stress and displacement in the shell can be reduced. Geomembrane act as a stress-distributing layer, dispersing the applied service loads more evenly across the SSCS. This helps prevent localized points of stress concentration that could lead to premature failures. By mitigating stress concentrations, geotextiles enhance the overall durability of the structure during routine.

The effect of the geomembrane on the behavior of SSCS is evaluated at field tests [91][92] and numerical simulations [93]. Wysokowski [94] conducted a full-scale test and investigated the influence of single-layer geotextile on the mechanical behavior of SSCS subjected to different types of static loads (See section 2.4.3 for the details of the test and findings) . A single layer of geotextile contributes to reducing displacement and stresses in the shell. Moreover, the vertical displacement at the crown of the shell was reduced by 30%, and a slight stress reduction was observed.

Maleska et al. [93] addressed a redistribution of the applied load over the shell due to using a geomembrane above the shell of SSCS. In the model, the single-layer geotextile was placed in the middle of the height of the soil cover above the crown of the shell. They reported that the vertical displacement at the crown of the shell is reduced by 28% compared with a model without Geotextile reinforced structure.

El-Sakhawy et al. [92] conducted a numerical simulation to investigate the effect of geogrids in a soil-steel culvert. Their analysis showed that the bending moment in the corrugated steel plate is significantly reduced.

Bathurst et al. [95] analyzed the geocell-reinforced large-span SSCSs. From their analysis, they observed that thinner layers of geocell-reinforced soil height of cover could be used to provide the same or enhanced load-deflection response the same as a 1 m thick unreinforced soil cover.

Vaslestad et al [96] conducted full-scale test on geogrid reinforced corrugated steel box culvert. The maximum deflection of the geogrid reinforced shell subjected to static traffic load was reduced with 29.5 %. Furthermore, the deflection at the crown of the shell was reduced by 17.8 % under dynamic load.

Jeyapalan, and Lytton [97] conducted a numerical simulation on geosynthetics reinforced box culvert. The analysis showed that the vertical displacement at the crown of the shell was reduced by 30% for the geosynthetics-reinforced culvert. The effect was analyzed within the serviceability limit state in the laboratory test and numerical simulation.

Few works [94] [96] investigate the behavior of membrane-reinforced SSCS under load beyond service load. Under ultimate load, geomembrane plays a critical role in reinforcing the soil mass. Geomembrane are engineered to have high tensile strength, and they interact with the soil to form a composite material that can withstand significantly higher loads than the soil alone. This enhancement in strength contributes to the overall load-bearing capacity of the SSCS. Moreover, it redistributes the applied ultimate loads more uniformly across the SSCS. By spreading the load over a larger area, it can reduce stress concentrations on individual components, thereby enhancing the safety margin against catastrophic failures or collapse.

2.6. Selected studies of flexible culverts on a natural scale

The main source of information about the behavior of the structure is research on real objects. Field studies of flexible soil-steel composite structure on a natural scale are presented in this subsection. Structures are tested both in the construction stage and under static load.

2.6.1. Full-scale test on box type

The full-scale test was conducted in the laboratory on box type of SSCS by Wysokowski [98]. The aim of the test was to conduct a displacement and stress analysis of box-type SSCS under conditions of failure load. As shown in Fig. 2.11, the structure had the following dimensions: a span of 3.55 m, longitudinal width of 13.7 m, rise of 1.42 m and 0.6 m height of cover. The shell was assembled from a corrugated profile made of commercial name, multi-plate 150 mm x 50 mm (pitch x depth), and had a thickness of 5.0 mm. The structure was reinforced with special ribs made of corrugated steel plates at the top section of the perimeter at the crown, with a width of 1.54 m.

The corrugated steel plates were joined by 20 mm in diameter bolts, having a minimum tensile strength of 830 MPa. For the backfill material, a well-graded soil with a maximum grain size of 32 mm was utilized. The backfill was placed in layers with a maximum thickness of 20–30 cm, and it was compacted to achieve a degree of compaction equal to 97% of the Standard Proctor test.

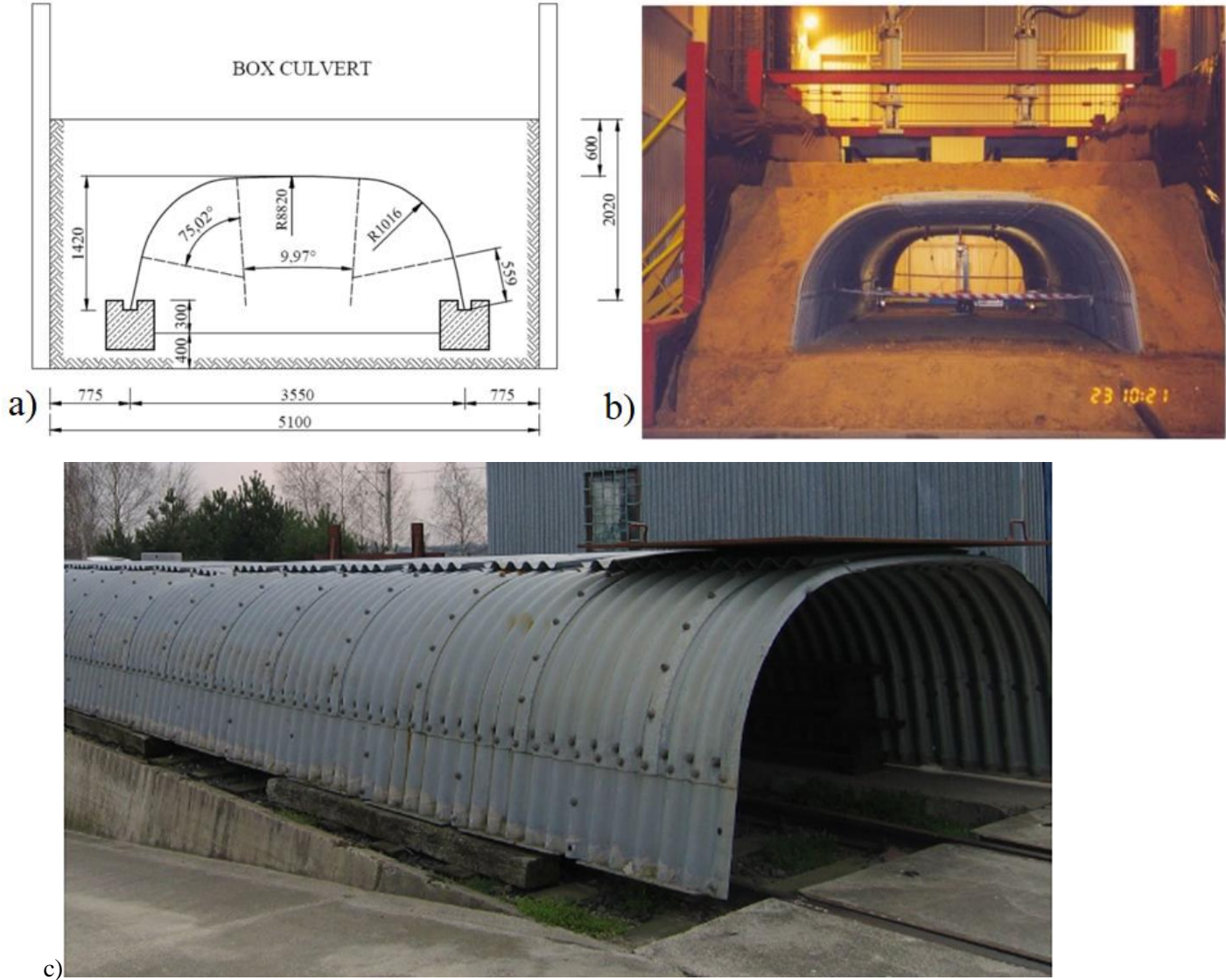


Figure 2.11: a) Cross-section of the tested structure b) after soil backfill c) general view of the tested structure [98]

Deformations and strains of the steel structure were measured at each stage of backfilling. Once the backfilling was completed, a vertical load of 1990 kN was applied to the structure to assess the response of the structure.

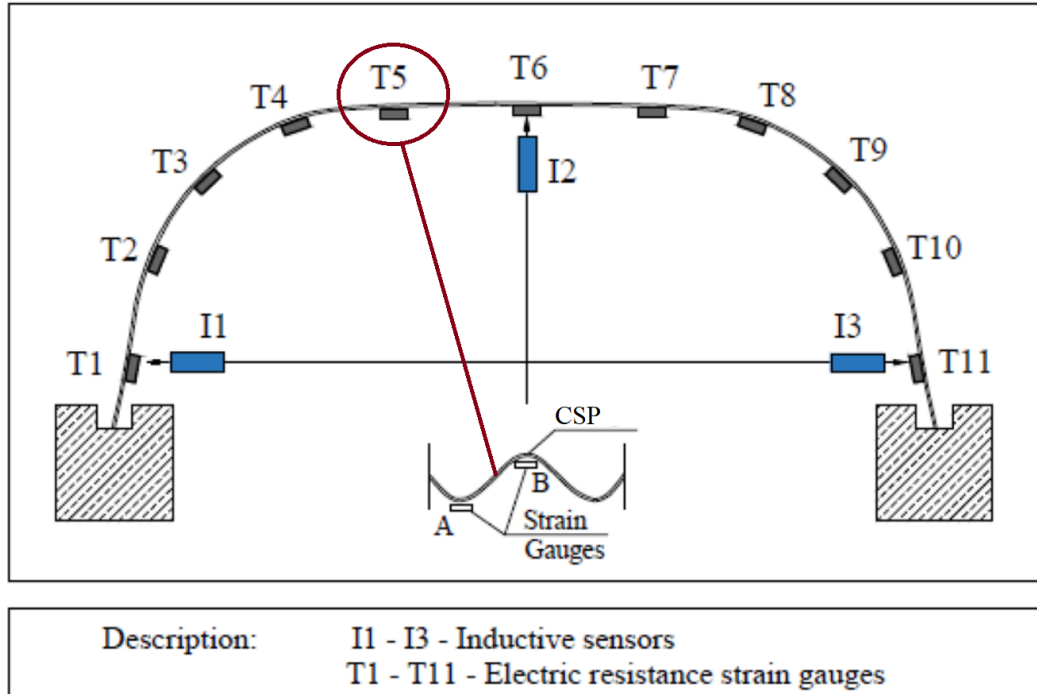


Figure 2.12: Measuring points with arrangement of displacement and strain gauges (After [98])

The displacement gauges (one vertical gauge and two horizontal ones) allowed the relative displacement of the culvert to be measured. The horizontal gauges were installed 0.37 m over the top of concrete strip foundation as shown in Fig. 2.12. Furthermore, in order to determine the stresses in the shell, twenty two strain gauges were installed on the inside surface of the culvert.

The experimental results presented indicate that, during the backfilling process, the steel shell exhibits a complex behavior, undergoing changes in its shape, including changes in displacement values and signs, which become more pronounced with an increasing number of soil layers as shown in Fig.2.13.

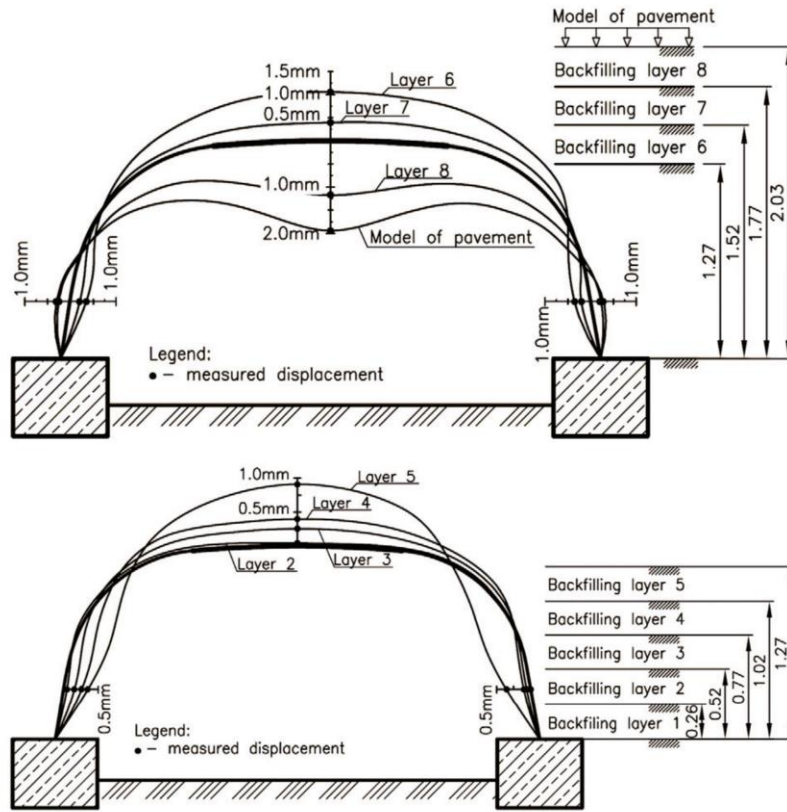


Figure 2.13: Deformation of the shell during consecutive backfilling[99]

As part of the study, an attempt was made to assess the structural integrity of the box culvert by subjecting it to a "destructive" test. Since the structure did not exhibit any damage under the limited maximum vertical load condition (with a maximum load of 2000 kN), a different approach was taken for the destruction test.

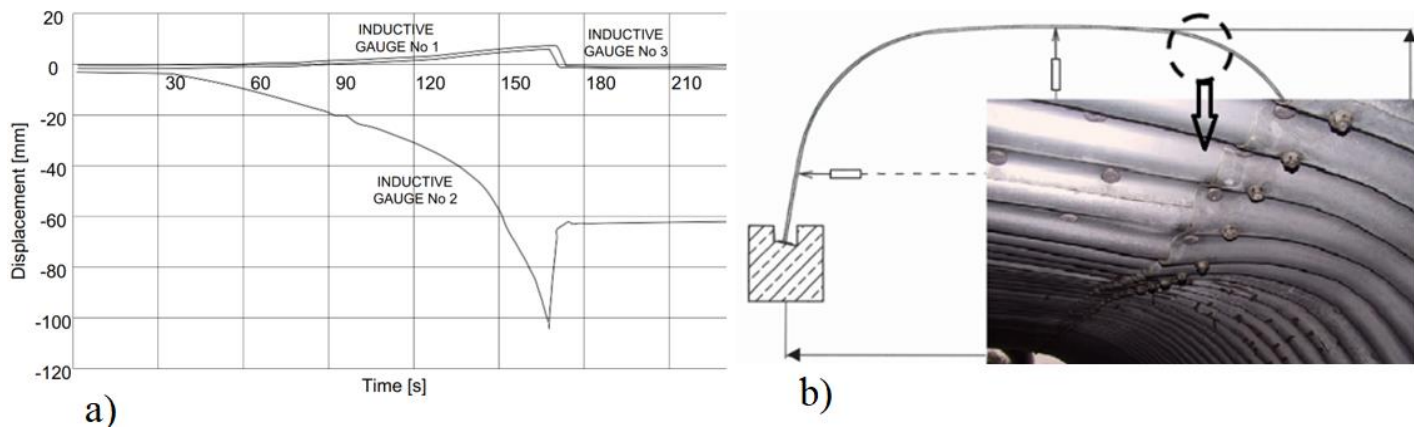


Figure 2.14: a) Displacement under destructive load for shell b) View of damage under destructive load[98].

In this test, the top layer of soil backfill was deliberately removed leaving only a 0.1-meter soil cover, then the load was applied directly to the upper surface of the steel structure. Displacement under destructive load is shown in Fig.2.14.

2.6.2. Full-scale test on pipe arch CSP structure

The culvert with a span of 2.99 m, a rise of 2.40 m and 0.3 m soil height of cover was tested at natural scale. The structure was made of commercial name Multi Plate with a profile of 150 mm x 50 mm and a wall thickness of $t = 3.75$ mm. once the backfilling is completed, the structure was tested under 2000 kN load as shown in Fig. 2.15.

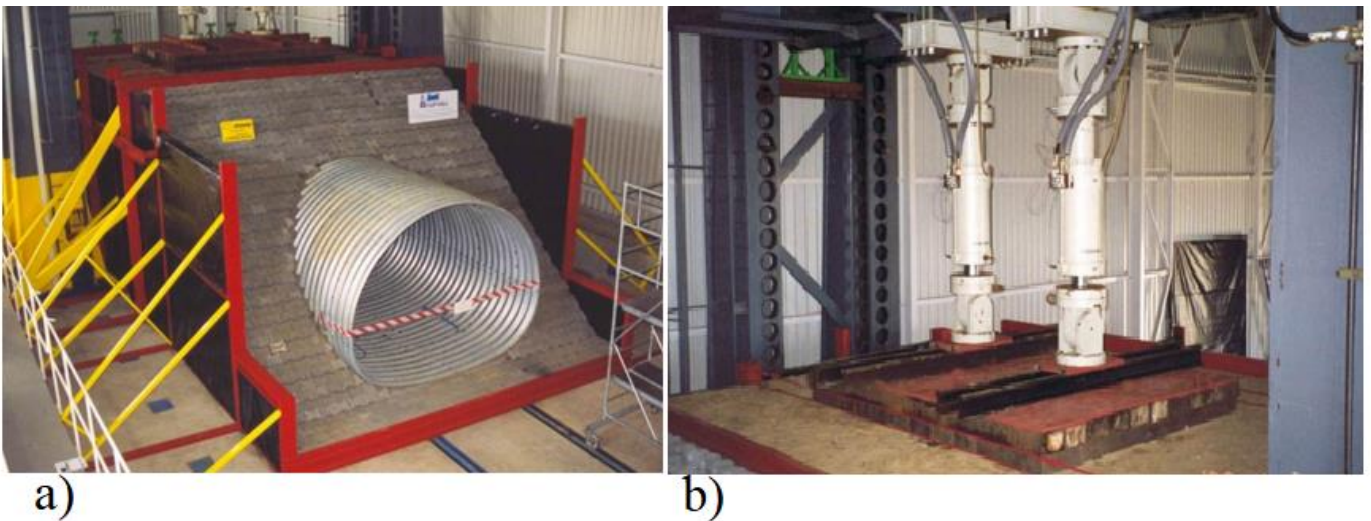


Figure 2.15: General view of the structure a) after backfilling b) the plate to transfer the load to the ground [98][99].

From the test it was observed that under ultimate load the structure did not reveal any irregularities in terms of the stability and safety of the research models. Upon analyzing the displacement and stress values, it was found that they were generally remained within permissible standard limits, except for the stress value recorded by the T12 sensor as shown in Fig.2.16.

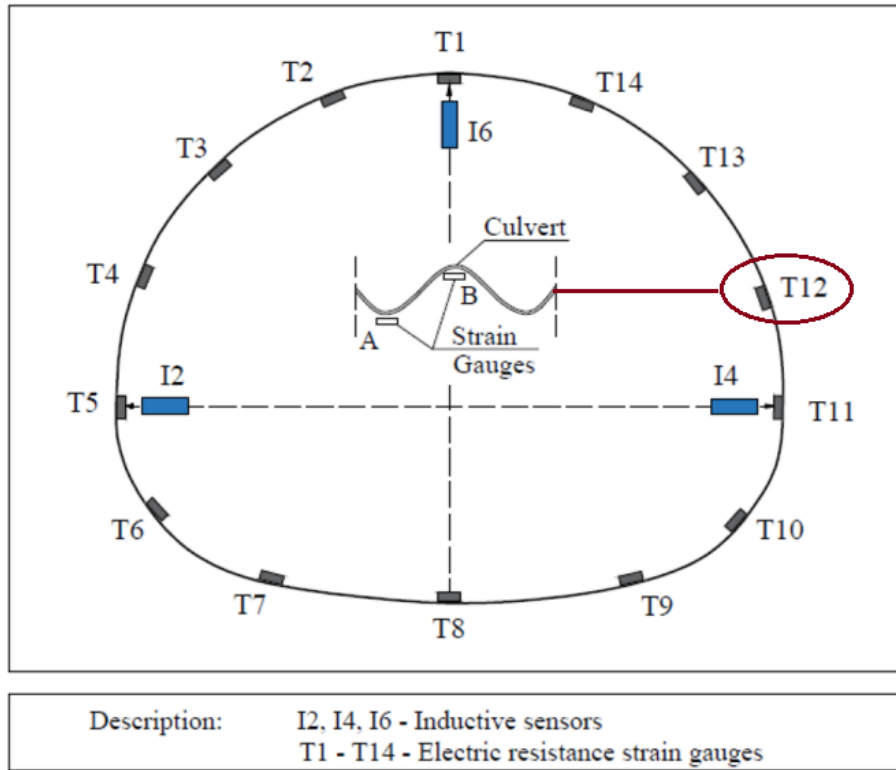


Figure 2.16: Location of strain gauges and sensors[98]

The interesting finding from this test is that, despite exceeding the allowable stresses in the structure (447.9 MPa), the shell did not lose its stability and no sign damage was observed on the surface of the steel shell. The stress distribution of the shell is as shown in Fig.2.17.

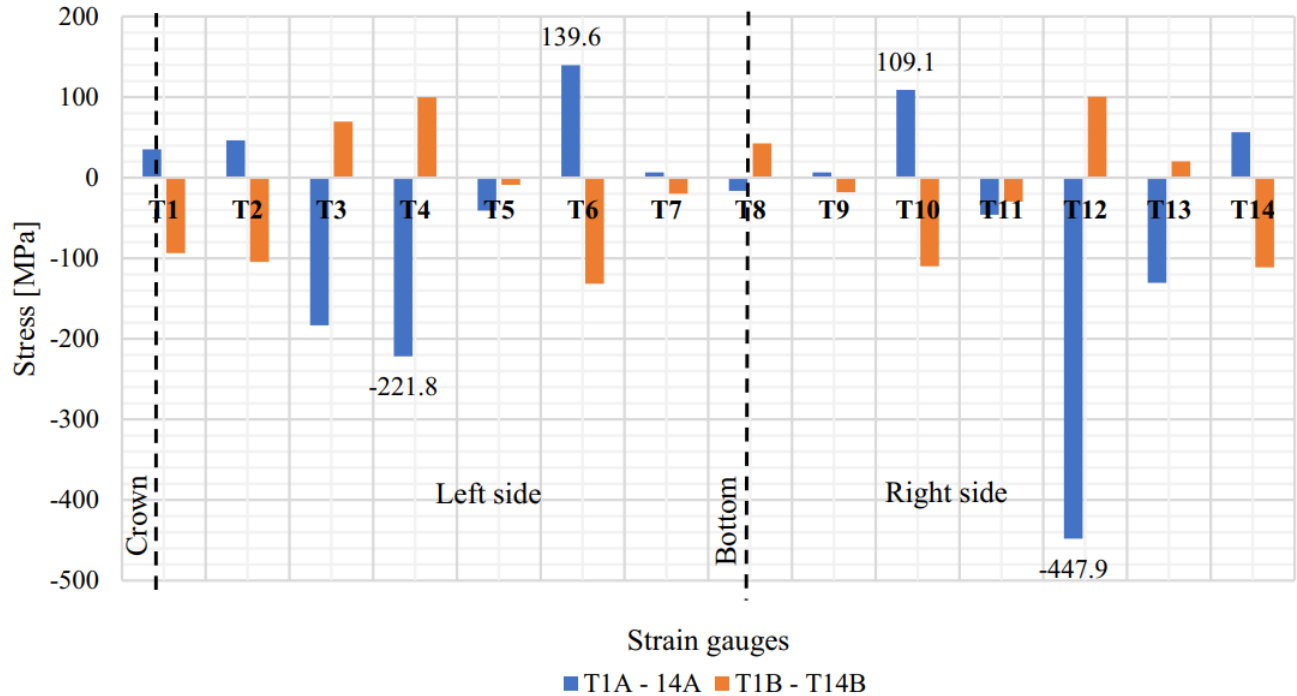


Figure 2.17: Maximum stress values in the shell[98]

The main conclusions from this test underscore that the performance and stability of the structure are directly influenced by the phenomenon of soil-steel interaction. As the steel shell undergoes lateral deformation, it leads to an increase in stresses within the soil on both sides of the shell, subsequently impacting stress distributions and displacements at the crown of the structure. Furthermore, it is important to note that the shape of the structure also plays a pivotal role in redistributing loads within the model as the applied load intensifies.

2.6.3. Full-scale laboratory test on geotextile reinforced SSCS

Wysokowski [94] conducted laboratory test on the SSCS with and without geomembrane on a natural scale. The main purpose of the test was to determine the behavior of the considered structure under the given load conditions when single layer of a geosynthetic material is placed at the center of the soil height of cover above the crown of the shell as shown in Fig.2.18. The structure had the following dimensions: a span of 3.55 m, longitudinal width of 13.7 m, and rise of 1.42 m. The shell was assembled from a corrugated profile made of commercial name, multi-plate 150 mm x 50 mm (pitch x depth), and had a thickness of 5.0 mm. The structure was reinforced with special ribs made of corrugated steel plates at the top section of the perimeter at the crown,

with a width of 1.54 m. The corrugated steel plates were joined by 20 mm in diameter bolts, having a minimum tensile strength of 830 MPa. For the backfill material, a well-graded soil with a maximum grain size of 32 mm was utilized. The backfill was placed in layers with a maximum thickness of 20–30 cm, and it was compacted to achieve a degree of compaction equal to 97% of the Standard Proctor test. To determine displacements and stresses in the steel structure, inductive gauges and strain gauges were installed on the inside surface of the culvert. During the backfilling stage, deformations and strains of the steel structure were measured.

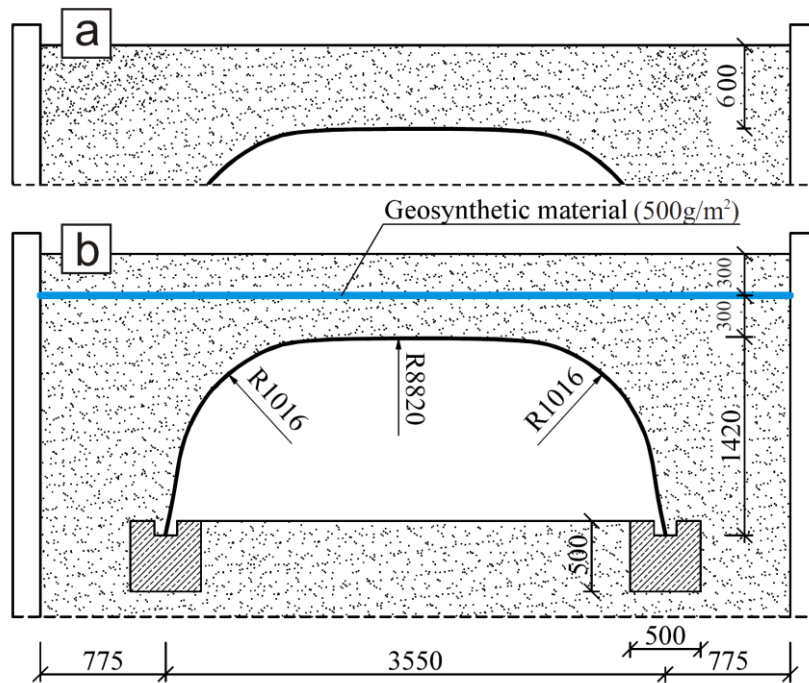


Figure 2.18: Cross-section of the tested structure after reinforcing with the geosynthetic material[94]

The load was chosen in accordance with Polish Standards[100], where the total simulated truck load was $K = 800$ kN with a safety factor $\phi = 1.5$, dynamic factor $\gamma = 1.26$ and uniformly distributed load $q = 4.0$ kN/m² and the rate of the load was 40 kN/s with the time of the maximum load $T = 600$ s. Static tests were carried out for three different load values K in accordance with Polish Standards of bridge load - PN – 85/S10030 “*Bridge structures. Loads*”

- variant A (load class A) - $K = 800$ kN,
- variant B (load class A with dynamic factor) - $K \cdot \phi (h) = 1008$ kN,
- variant C (load class A with dynamic and static factor) - $K \cdot \phi (h) \cdot \gamma = 1512$ kN.

The analysis of the results of the test confirms that the application of a single layer of geotextile in the backfill layer reduces the displacements of the tested corrugated steel structures by up to 30%. Also, a slight reduction in calculated stress values in the steel structure under maximum static loads occurs. The results for vertical displacement and stress measured at the crown section of the shell is described in Figs 2.19 -2.21.

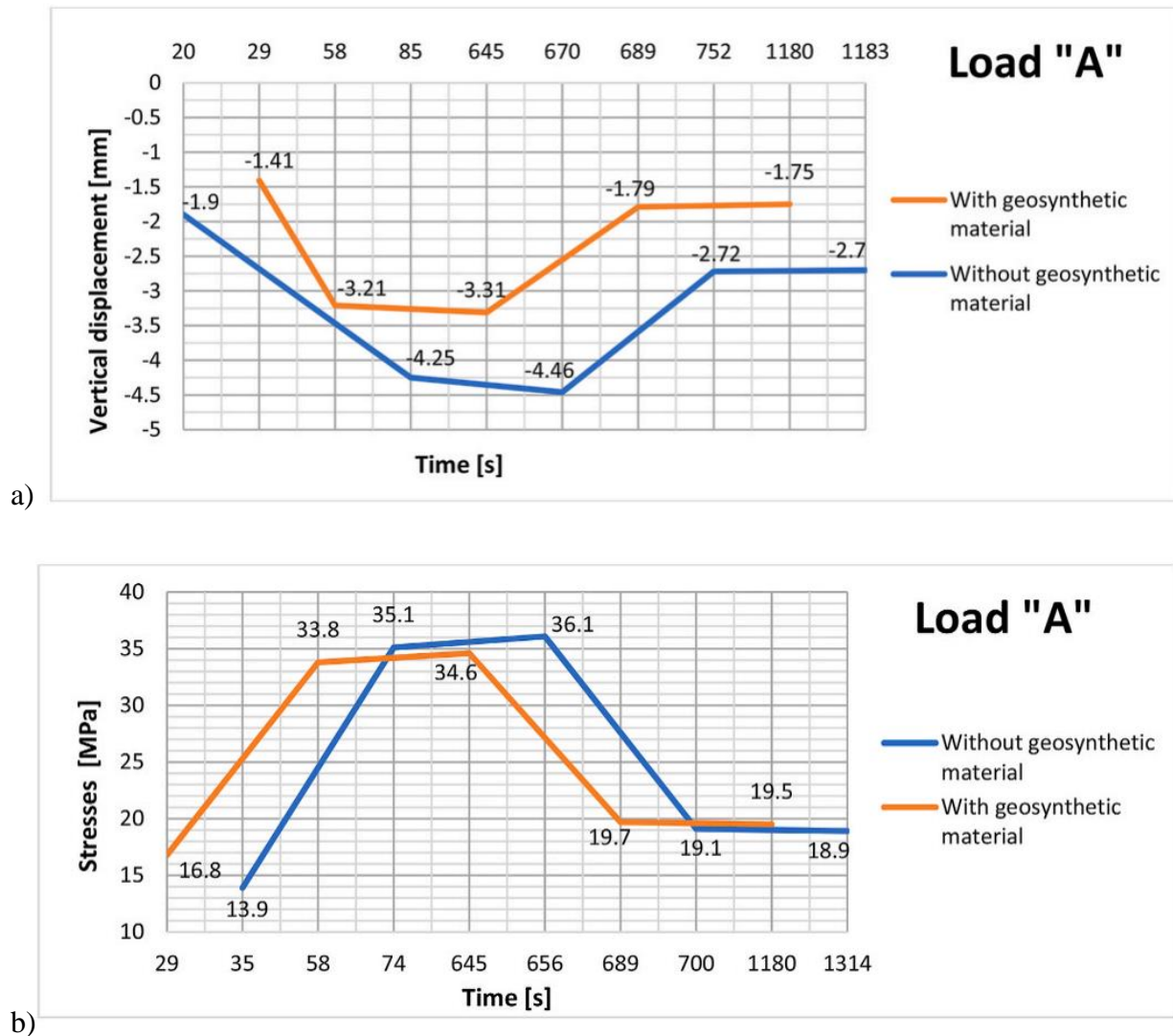
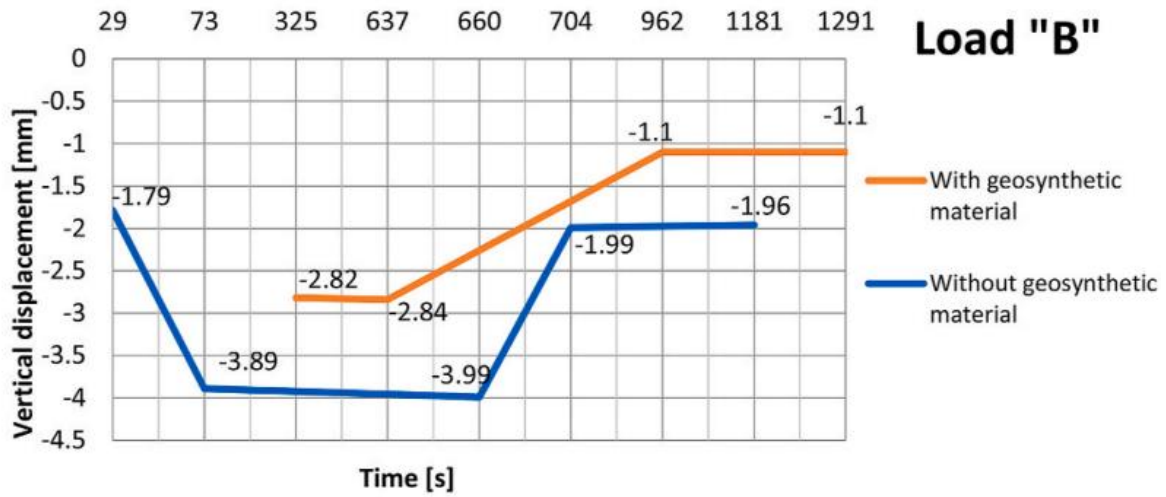
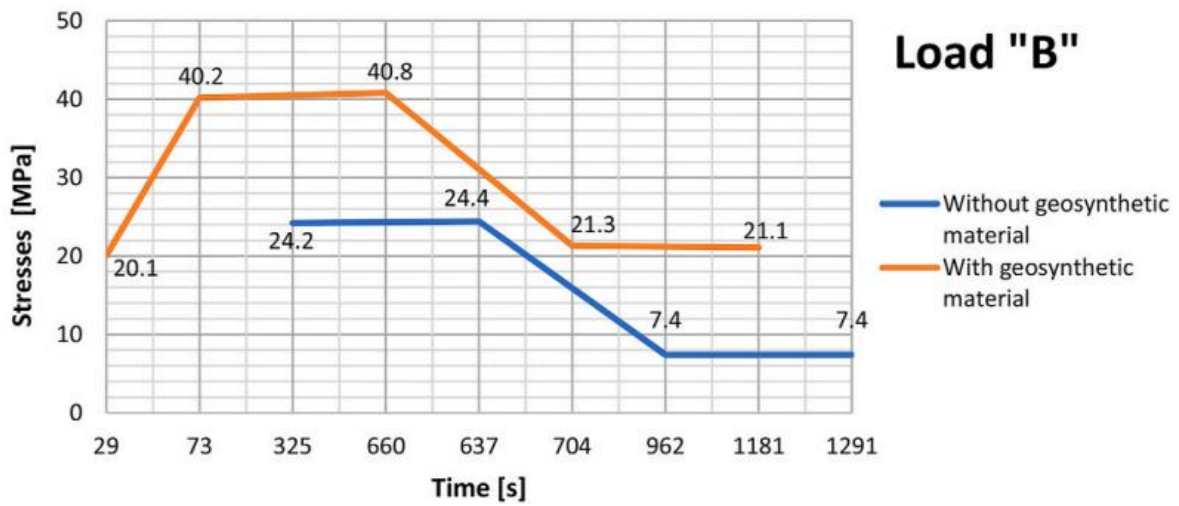


Figure 2.19: The measured results at the crown of the shell under class “A” Load a) Vertical displacement b) stress values[94]

From the conducted test, the author [94] concludes that, the quantity reduction of these parameters according to the performed full-scale laboratory tests is significant for the load-bearing capacity of buried flexible structures in engineering practice – especially in case of exploited within road and railway lines.

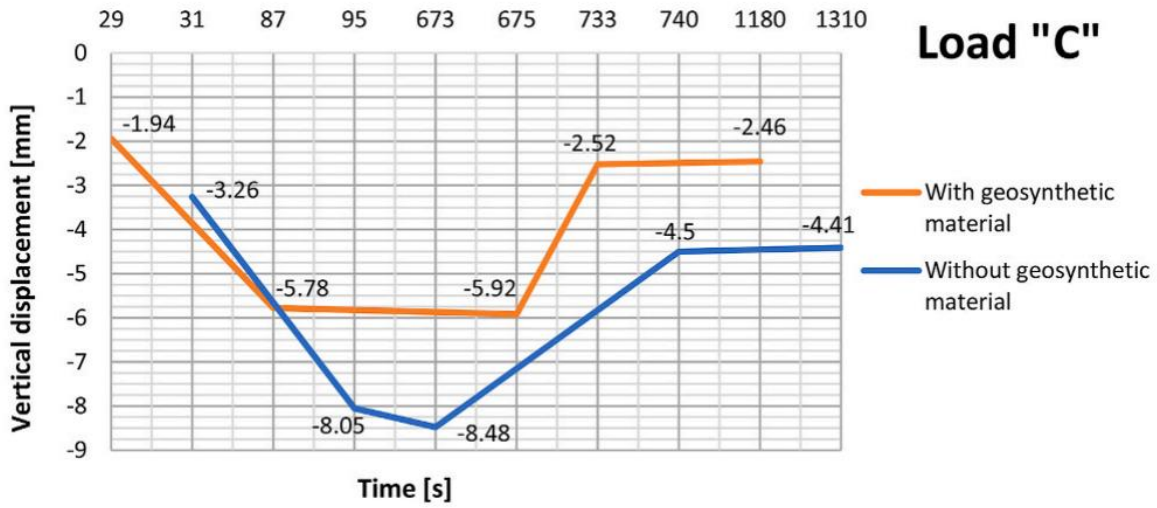


a)

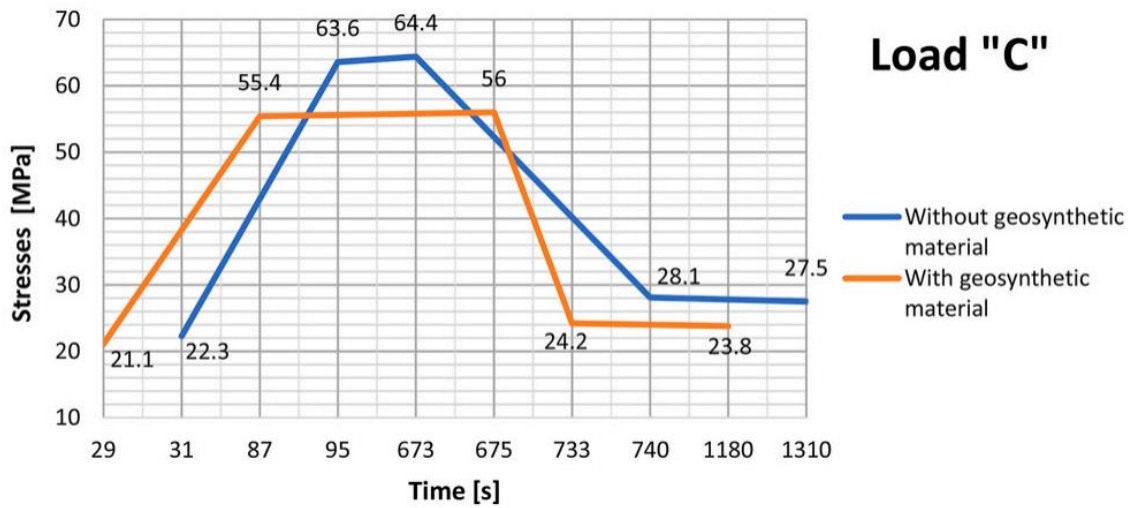


b)

Figure 2.20: The measured results at the crown of the shell under class "B" Load a) Vertical displacement b) stress values[94]



a)



b)

Figure 2.21: The measured results at the crown of the shell under class "C" Load a) Vertical displacement b) stress values[94]

2.7. Summary of the state of research

In consideration of the literature pertaining to soil-steel composite structures and the research conducted on full-scale SSCSs constructed from corrugated steel plates, the following theses are postulated:

- The mechanical behavior of the soil-steel composite structures is derived from the interaction between the soil backfill and the flexible shell. The interaction is established by an appropriate backfilling process. Thus, monitoring of shell deformation and soil compaction control must be carried out during the construction phase. Typically, maximum deflection is observed when the backfill level reaches the rise of the shell. The upward or downward deflection at the crown must be limited to 2% of the rise during construction.
- Under semi-static live load, a hysteretic effect is observed in both, real-scale test results and numerical simulations. The effect is expressed in the fact that the mechanical response of the SSCS to a moving load is affected not only by the location and value of the load, but also by the direction of its movement. This effect is said to be a result of frictional contact at the soil-steel interface as well as the non-linear behavior of the soil used for backfilling.
- Soil-steel composite bridges with a span greater than 12 m are often strengthened with stiffening elements, e.g., relieving slabs, concrete-filled steel ribs, ribs, longitudinal beams, etc. The load-bearing capacity of SSCSs has been investigated using full-scale tests by loading the structure to failure. Numerical simulations (like FEA) are also useful in this regard. They make it possible to perform parametric analyses by checking multiple cases of design assumptions (e.g., cover depth) or load configuration.
- Despite numerous research studies conducted on the impact of geomembranes on the behavior of SSCSs, the optimal positioning of the geomembrane within the soil cover above the crown of the shell remains unexplored. Moreover, there is a lack of comprehensive investigation into the effects of geomembranes on SSCSs when subjected to ultimate loads.
- Thus, the key research areas demanding deeper investigation for SSCSs encompass the evaluation of load-bearing capacity, with a particular focus on the identification of potential failure modes, especially in conditions with low soil height of cover. Additionally, there is a need to explore the influence of geotextile-reinforced backfill within the soil height of

cover above the crown of the shell on the structure's performance in ultimate limit states. Moreover, a comprehensive exploration of the failure modes in SSCS, both with and without a reinforcement rib around the crown section, as well as the failure mode of the structure reinforced with geotextile, is imperative. The effect of spacing between the shells in multi-span soil steel composite structure on the bearing capacity and failure mode needs further study. Furthermore, the effects of live load, considering aspects such as its load position, type, magnitude, and direction on multi-span SSCS with different spacing between the central shell and lateral shells remains an open avenue for research.

3. Purpose of the research

Following an in-depth review outlined in Section 2.7, a critical research gap was identified, serving as the basis for the objectives outlined in this study. This research aims to comprehensively assess the mechanical performance of SSCSs under ultimate limit state condition. Additionally, the study seeks to evaluate the reinforcing mechanism within SSCSs to enhance their load-bearing capacity. Through this investigation, valuable insights are expected to be gained, contributing significantly to understanding SSCS behavior and paving the way for potential structural improvements.

3.1. Specific objectives

The specific objectives of the conducted analyses can be outlined as follows:

- Evaluate the behavior of SSCSs under ultimate load taking into account the effects of stiffening ribs and geotextile reinforcement of backfill.
- Evaluate the influence of geotextile soil reinforcement layout on the deformation of a model SSCSs.
- Quantify and explain the influence of lateral shells on the mechanical behavior of the central shell and vice versa at various spacings within a multi-span SSCS subjected to ultimate loads at different positions.
- Quantify and explain the influence of lateral shells on the mechanical behavior of the central shell at various spacings within a multi-span SSCS when subjected to quasi-static moving loads, while also considering the direction of load movement.

3.2. Scope of the Research

- The research exclusively concentrates on soil-steel composite structures constructed using corrugated steel plates.
- The analysis covers both serviceability limit state and ultimate limit state conditions.
- The study employs numerical simulation methods to evaluate the structural behavior of composite structures.
- The investigation does not extend to other types of composite structures or materials beyond corrugated steel plates.

4. Stability of engineering structures

Stability in engineering structures refers to the ability of a structure to maintain its equilibrium under applied loads without excessive deformation or failure. A stable structure is one that can withstand the loads it is designed to bear without experiencing significant displacements, buckling, or collapse. If the structure fails to maintain its equilibrium under applied loads, it leads to excessive deformation or collapse [101].

The efficiency of design relies significantly on the ability to predict the circumstance under which failure is likely to occur. The essential variables connected with structural failure include the nature of the material, the load configuration, the rate of loading, and other conditions[102]. In the most general terms, failure refers to any action leading to an inability of the structure or machine to function in the intended manner. It follows that permanent deformation, fracture, or excessive deflection be regarded as failure modes, the last being the most easily predicted. Another way a structure may fail is through instability by undergoing large displacement from its design configuration when the applied load reaches a critical value, the buckling load [103].

The elastic design approach, also known as the permissible stress method or the allowable stress approach, is a conventional design method based on material elastic properties [102]. The design approach limits the structural use of the material up to a certain allowed stress that is less than the elastic limit as shown in Fig 4.1(a). The stresses due to service load do not exceed the specified allowable stresses, which are obtained by applying a suitable safety factor to the yield stress. The elastic design does not consider material strength beyond elastic stress. As a result, structures designed with this approach will be heavier than those designed using plastic methods.

In the plastic design approach, the ultimate load rather than the yield stress is considered as the design criterion. The term plastic has occurred due to the fact that the ultimate load is found from the strength of steel in the plastic range. The strength of ductile materials like steel beyond the yield stress is fully utilized in this method. This method will provide a rational approach for the analysis of the structure, and it provides a striking economy regarding the weight of steel since the sections designed by this approach are smaller in size than those designed by the elastic design method. Plastic analysis is the approach used to compute the structure's actual failure load, which can be considerably more than the elastic load capacity [104].

4.1. Elastic and plastic behavior of structural steel

The theory of plasticity reveals that those parts of a structure that have been stressed to the yield point cannot resist additional stresses. Instead, any additional stresses or loads will be transferred to other parts of the structure where the stresses are below yield, which is able to resist additional stresses. The theory is based on certain experimental observations on the macroscopic behavior of metals in uniform states of combined stresses. The observed results are then idealized into a mathematical formulation to describe the behavior of metals under complex stresses [105][106]. Unlike elastic solids, in which the state of strain depends only on the final state of stress, the deformation that occurs in a plastic solid is determined by the complete history of the loading. The plasticity problem is, therefore, essentially incremental in nature, the final distortion of the solid being obtained as the total of the incremental distortions following the strain path. Structural steel exhibits remarkable ductility, leading to the collapse of the structure with large deformation. The plastic design approach takes advantage of this distinctive property. The ductility of steel becomes evident when reviewing the stress-strain diagram obtained from a basic tension or compression test, as illustrated in Fig 4.1(a).

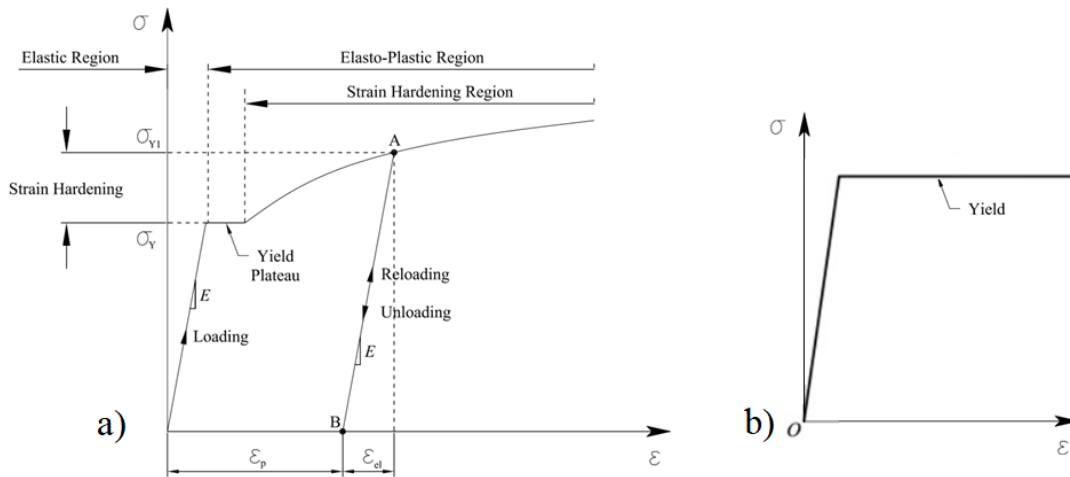


Figure 4.1: Stress-strain curve for steel structure (a) Real, (b) Ideal[107] [108]

The elastic perfectly plastic model (shown in Fig. 4.1 (b)) is a specific type of idealized material behavior used in engineering mechanics. This model assumes that a material exhibits elastic

behavior until it reaches a specific point called the yield point. Beyond this point, the material undergoes instantaneous and complete plastic deformation without any increase in stress. This means that once the yield point is reached, the material continues to deform plastically without any resistance. This model simplifies the behavior of materials like metals that exhibit yield followed by plastic deformation.

4.2. Yielding of a cross-section

Considering an arbitrary cross-section with a vertical plane of symmetry, which is also the plane of loading, the stresses can be assessed at each stage when the cross-section is subjected to an increasing load.

4.2.1. Stage 1 – Elastic stage

For many materials, the initial segment of the stress-strain curve is linear up to the proportionality limit, marked as point A in Fig. 4.2 (a). Beyond this stage, the stress-strain curve exhibits a slight curvature, but there is no clear yield point characterized by a sudden change in slope. According to international standards referenced in [109], the yield stress is determined by extrapolating the elastic slope with a 0.02% offset strain, denoted as point B in Fig. 4.2 (a).

Upon loading, the material hardens, and the stress increases with diminishing slope until the testing machine (either force or displacement controlled) is stopped. There are two possibilities. On unloading, meaning reversing the load or displacement of the cross-load of the testing machine, the unloading trajectory is straight. This is the elastic unloading where the slope of the stress-strain curve is equal to the initial slope, given by young's modulus, as shown in Fig.4.2 (c). The stress is zero at point D, but a residual plastic strain of the magnitude OD exists [109].

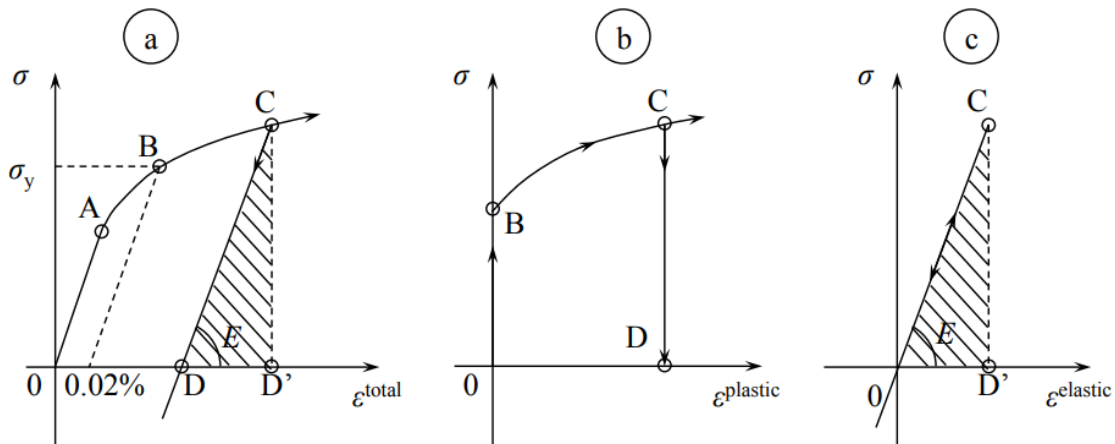


Figure 4.2: Elastic, plastic, and total stress-strain curve [109].

From loading/unloading, it can be observed that the total strain ϵ^{total} is the summation of elastic strain $\epsilon^{\text{elastic}}$ and plastic strain $\epsilon^{\text{plastic}}$ using Eq (4.1):

$$\epsilon^{\text{total}} = \epsilon^{\text{elastic}} + \epsilon^{\text{plastic}} \quad (4.1)$$

For example, if a simply supported beam is subjected to load P, and taking the arbitrary cross-section, assuming a rectangular cross-section, as the bending moment increased at certain sections of the beam, there will be a linear variation (see Fig. 4.3 (a)) of the stress until the yield stress is reached. The maximum stress is at the outer surface of the section, as shown in Fig. 4.3 (b). The bending moment at this surface is yield moment, M_y which is the bending moment corresponding to a bending stress distribution in which the stress equals the yield stress only at the outer-most fibers.

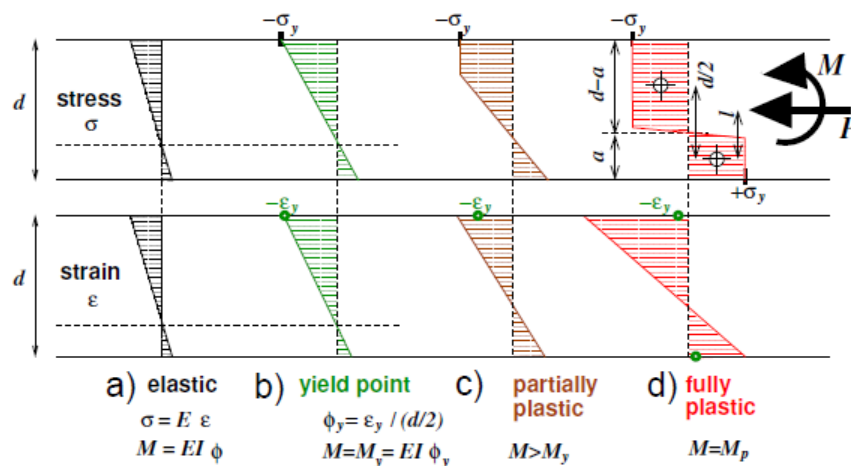


Figure 4.3: Stress distribution a) elastic b) yield c) elastoplastic d) fully plastic (Modified from [110])

4.2.2. Stage 2 – Yielding stage

At this stage the yield stress of the material is reached at the outermost part of the cross-section and all other stresses in the cross section are less than the yield stress as shown in Fig. 4.3(b). At yielding point the stress exceeds the limit value only locally and only in that point permanent strains occur, while in other points deformation is still elastic. The load which results in first yielding in any point of a structure called elastic limit bearing capacity. As shown in Fig.4.2(a), the yield stress is mapped by taking elastic slope with 0.02% strain ($\epsilon = 0.0002$) offset strain [109].

As the load increases, the inelastic action becomes more widespread, eventually resulting in general yielding. It is characteristic of most ductile materials that the load must be increased after yielding to produce further deformation. In other words, the material exhibits a strengthening termed strain hardening [103].

In finite element analysis, it is recommended to consider the von Mises yield criterion. It is a mathematical model that helps predict when a material will yield and deform plastically under different types of stress. This failure criterion is also called the maximum distortion energy theory, u_d and it states that yielding occurs when the maximum distortion energy in a material is equal to the distortion energy at yielding in a uniaxial tensile test, $u_{d,y}$.

$$u_d = u_{d,y} \quad (4.2)$$

The distortion energy is essentially the portion of strain energy in a stressed element corresponding to the effect of the deviatoric stresses. The distortion energy per unit volume can be calculated from the principal stresses using this equation.

$$u_d = \frac{1+\nu}{6E} [(\sigma_1 - \sigma_2)^2 + (\sigma_2 - \sigma_3)^2 + (\sigma_3 - \sigma_1)^2] \quad (4.3)$$

Where $\sigma_1, \sigma_2, \sigma_3$ are the principal stresses acting on the material, ν is poisson's ratio and E is young's modulus of the material. At yielding during a tensile test, the maximum principal stress equals the yield strength of the material, and the two other principal stresses are equal to zero. So, distortion energy at yielding in a tensile test can be calculated by plugging in the appropriate principal stress values.

$$u_{d,y} = \frac{1+\nu}{6E} [(\sigma_1 - \sigma_2)^2 + (\sigma_2 - \sigma_3)^2 + (\sigma_3 - \sigma_1)^2] \quad (4.4)$$

As it was described above, at yielding $\sigma_1 = \sigma_y, \sigma_2 = \sigma_3 = 0$,

$$u_{d,y} = \frac{1+\nu}{3E} \sigma_y^2 \quad (4.5)$$

$$\frac{1+\nu}{6E} [(\sigma_1 - \sigma_2)^2 + (\sigma_2 - \sigma_3)^2 + (\sigma_3 - \sigma_1)^2] = \frac{1+\nu}{3E} \sigma_y^2 \quad (4.6)$$

Then, distortion energy at yielding defines the von Mises failure criterion is given by:

$$\sigma_y = \sqrt{\frac{1}{2} [(\sigma_1 - \sigma_2)^2 + (\sigma_2 - \sigma_3)^2 + (\sigma_3 - \sigma_1)^2]} \quad (4.7)$$

σ_y is the yield strength of the material.

The yield surface is a shape that represents the conditions under which a material undergoes plastic deformation or yielding instead of returning to its original shape when a load is removed. In this case, it's described as a cylinder with a radius of σ_Y (yield strength) and an axis aligned with the line where $\sigma_1 = \sigma_2 = \sigma_3$. When considering a situation known as plane stress, where $\sigma_3 = 0$, the yield surface takes on the shape of an ellipse, with its longer axis aligned along the line where $\sigma_1 = \sigma_2$, as shown in Fig. 4.4. Stress states located inside the yield surface are within the elastic range, meaning the material will return to its original shape once the load is removed. Stress states on the yield surface are in the elasto-plastic range, meaning the material will undergo permanent deformation.

It's important to note that the size and position of the yield surface can change as plastic strains develop in the material, but stress states always remain on or within the yield surface. It is impossible for a stress state to exist outside the boundaries of the yield surface. This understanding is crucial in materials science and engineering for predicting when a material will yield or deform plastically under various stress conditions.

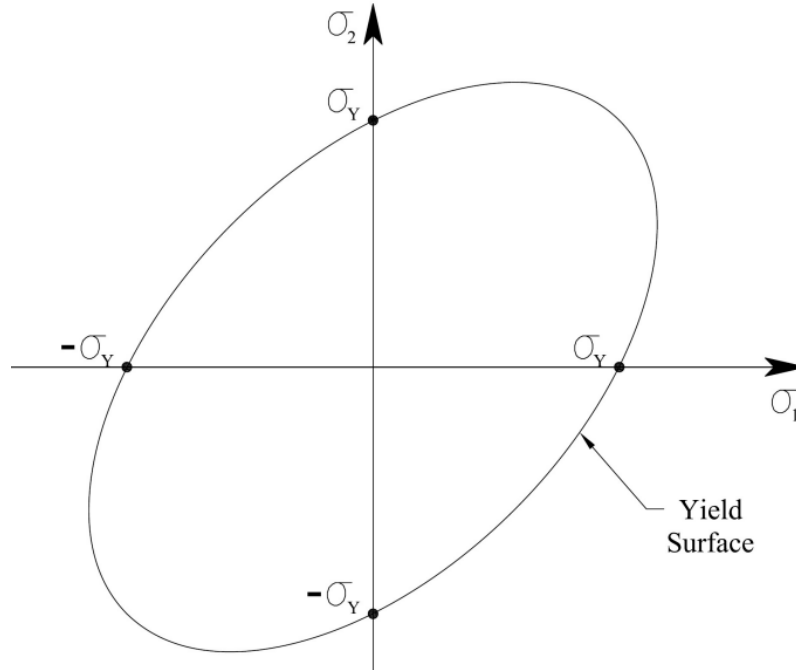


Figure 4.4: Von mises yield surface for plain stress

4.2.3. Stage 3 – Elasto-plastic stage

The elasto-plastic stage in a steel structure refers to a phase in which the material has experienced both elastic and plastic deformation under load. In this section, the load applied to the cross-section has created stress beyond the yield limit. Thus, by the concept of the stress-strain curve, the material cannot sustain stress greater than the yield stress, the section at the yield stress has progressed inwards towards the center of the beam. Due to this, there is an elastic and a plastic region over the cross-section as shown in Fig. 4.3(c). After reaching the yield point, the structure redistributes loads to regions with larger plastic capacities. This concept, known as load redistribution, plays a pivotal role in plastic analysis and design, ultimately enhancing the overall load-carrying capability.

4.2.4. Stage 4 – fully plastic stage

This section is the yielding of a system and loss of stability due to the large load that leads to a situation in which yielding occurs in all cross sections as shown in Fig. 4.3(d). Thus, the structure has lost its stability due to full plastic yielding and the value of the load, which caused it to be termed the bearing capacity of the system, and the value of the moment is termed the plastic

moment capacity (M_p) of the section. Once the plastic moment capacity is reached, the section can freely rotate and behaves like a hinge, also called a plastic hinge.

A plastic hinge refers to a localized region within a structural element, such as a beam or column, where significant plastic deformation occurs due to applied loads [110]. In essence, when a material, such as structural steel, is subjected to loads surpassing its yield strength (the point at which permanent deformation begins), it enters the plastic deformation range. Within this range, the material continues to deform plastically without an increase in stress, leading to the formation of plastic hinges. The effects of plastic hinges are defined by the moment at which the entire cross-section reaches its yield stress. This moment represents theoretically the maximum bending capacity a cross-section can withstand. When this point is reached, a plastic hinge is developed, and the structure becomes unstable.

If the load continues to increase beyond the fully plastic stage, the steel member will eventually reach a point of instability, resulting in collapse. The material's load-carrying capacity diminishes as extensive plastic deformation occurs. Thus, in structural steel design, the fully plastic stage is a theoretical concept used to determine the maximum load-carrying capacity of a member.

4.3. Influence of axial forces on plastic moment capacity

When a structural member experiences both axial forces and bending, the plastic moment capacity of that member tends to decrease [110]. In ordinary portal frames, the axial load is typically small, and its influence can often be disregarded. However, in situations where the axial forces are relatively large, as is the case with structures like the shell of a soil steel composite structure, their influence must be considered and incorporated into the analysis [108].

Plastic limit analysis of a structural member subjected to bending assumes that at a particular moment value, known as the plastic moment (M_p) of cross-section. The member forms a plastic hinge when the plastic moment is reached. Considering the fully plastic section in Fig.4.3(d) and assuming the rectangular cross-section having width b and height d , the tensile stresses (positive) have a resultant force $P_t = \sigma_y ba$ and the compressive (negative) stresses have a resultant force $P_c = \sigma_y b(d - a)$. To maintain equilibrium, the net axial force must satisfy $P_c - P_t = P$.

$$\sigma_y b(d - a) - \sigma_y ba = P \quad (4.8)$$

This can be rewritten after algebraic rearrangement.

$$\frac{a}{d} = \frac{1}{2} \left(d - \frac{P}{P_y} \right) \quad (4.9)$$

where P_y is the yield force in the selected cross-section, given by:

$$P_y = \sigma_y b d \quad (4.10)$$

The distance between the centroids of the compressive and tensile stress blocks is given by:

$$\frac{1}{2}(d - y) + \frac{1}{2}y = \frac{1}{2}d \quad (4.11)$$

The moment in the cross section is a summation of the moments of P_c and P_t around a pivot point, about which the moment of P_c is equivalent to the moment of P_t . Denoting the position of the pivotal point at a distance l from the centroid of the tensile stress block, the moment of P_t around the pivot point equals the moment of P_c around the same pivot point. In essence, P_t and P_c form a couple about the pivot point. Then the ultimate moment (M_u) can be found as:

$$M_u = P_t l + P_c \left(\frac{d}{2} - l \right) = 2P_t l \quad (4.12)$$

This can be rewritten after algebraic rearrangement.

$$M_u = 2\sigma_y \frac{b d^2}{4} * \left(1 - \frac{P}{P_y} \right) \left(1 + \frac{P}{P_y} \right) \frac{1}{2} \quad (4.13)$$

$$M_u = M_p \left(1 - \left(\frac{P}{P_y} \right)^2 \right) \quad (4.14)$$

$$\frac{M_u}{M_p} = \left(1 - \left(\frac{P}{P_y} \right)^2 \right) \quad (4.15)$$

The largest (ultimate) moment that can be applied to a beam-column is reduced by the presence of axial (compressive or tensile) load on the beam-column. If the axial load is zero, the ultimate moment equals the plastic moment. However, if the axial load is close to the tensile yield load, the beam-column cannot sustain any moment. The axial force-bending moment interaction curve which is used to determine the maximum load-carrying capacity of the element while considering both axial and bending loads is described in Fig.4.5.

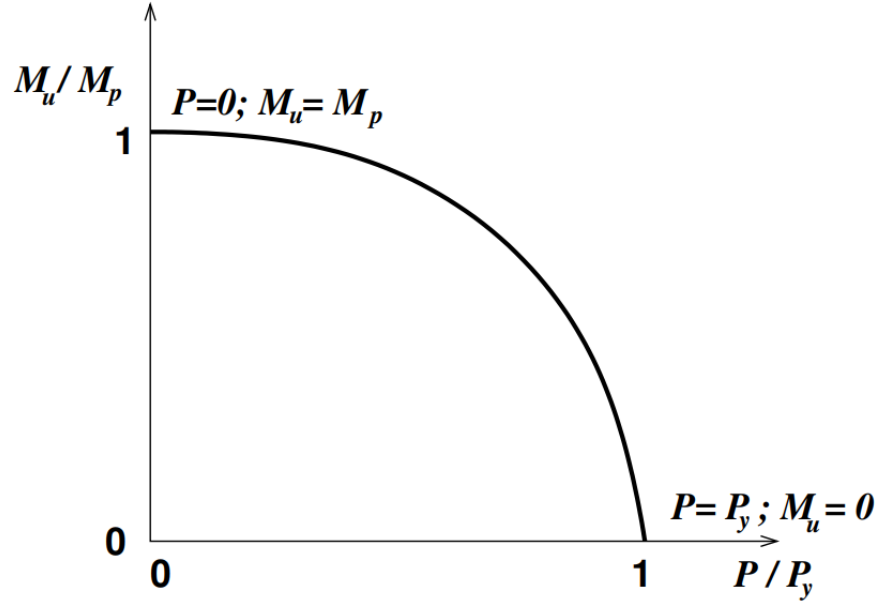


Figure 4.5: Typical axial force-bending moment interaction curve.

Several scholars [17] [64] [111] [112] have emphasized that the consideration of bending moment is essential when predicting the load-bearing capacity of soil-steel composite structures. As referenced in [64], the criterion stated within Eq.(4.14) is inherently controlled by defining shell as non-linear beam element in 2D finite element analysis. The authors checked the effect of out of plane bending on buckling behavior of steel shell and they confirmed that, out of plane bending does not control the buckling. Thus, buckling behavior of SSCS can be analyzed using 2D plane strain method. Sun Hao-Jun, *et al* [17] proposed strength design recommendations for SSCS under combined compression-bending moment through Eq.(4.15). They considered geometric nonlinearity and material nonlinearity, investigating numerous numerical examples to obtain their respective peak loads i.e.,

$$\left| \frac{N}{N_u} \right| + 0.75 \left| \frac{M}{M_f} \right| \leq 1 \quad (4.16)$$

Where, N_u represents the load-bearing capacity of the shell under uniform radial pressure, and it is calculated as $N_u = \varphi A \sigma_y$; M_f signifies the elastic moment capacity of the shell and can be determined using the formula $M_f = W_f \sigma_y$. σ_y represents yield strength of the material while W_f is elastic section modulus. According to the authors, the section shape coefficient for the corrugated section is approximately 1.3, meaning that the ratio of $M_p/M_f \approx 1.3$, where M_p represents the plastic moment capacity of the entire corrugated metal section.

Hence, the calculated value of M is approximately 1.3 times the value of M_f , given as $1/0.75M_f$, when N equals 0 in Eq. (4.15). This implies that the ultimate moment-bearing capacity of SSCS is considered to form plastic hinges in Eq.(4.15). when the structure is not subjected to axial compression.

4.3.1. Design Codes and Standards

The stability of soil steel composite structure relies on support from the surrounding backfill soil [113]. Soil steel composite structures are designed and checked against possible failure modes like soil failure above the shell, including shear, tensile or plastic yielding, global or local elastic buckling of the shell, and inelastic buckling of the shell with the formation of plastic hinges.

Current design codes and standards outline simplified methodologies for soil-steel composite structures. For instance, Canadian Highway Bridge Design Code (CSA 2019), the LRFD Bridge Design specifications by the American Association of State Highway and Transportation Officials (AASHTO 2019), and the Swedish Design Method [57]. These streamlined design approaches encompass uncomplicated equations employed to ascertain the resultant axial force and bending moment magnitudes within the steel framework.

4.3.1.1. CHBDC (CSA, 2019) and AASHTO (AASHTO, 2019)

The strength necessary to ensure the serviceability of the soil-steel composite structure, preventing buckling of the conduit wall, is governed by the interaction of combined bending moment and axial thrust. Thus, Eq.(4.16) expressed the ultimate limit state required by CHBDC (CSA, 2019) and AASHTO (AASHTO, 2019)

$$\left(\frac{N}{N_p}\right)^2 + \left|\frac{M}{M_p}\right| \leq 1.0 \quad (4.17)$$

Where, N_p plastic axial capacity N is designing compressive strength [kN/m], $N_p = \phi \sigma_y A$ and M_p plastic moment capacity of the steel cross-section, $M_p = \phi \sigma_y Z$. N is compressive force from characteristic loads [kN/m]; M is bending moment in the shell section per unit length in the longitudinal direction; σ_y is the steel yield stress; Z is the plastic section modulus of the corrugated steel cross-section; ϕ is the plastic hinge for completed steel structure; A is the cross-sectional area of the steel per unit length in the longitudinal direction.

4.3.1.2. Swedish design method

The safety before the beginning of yielding in the shell structure wall in the serviceability limit state (SLS) can be expressed in terms of maximum stress in the shell structure wall based on the equation proposed by Navier:

$$\frac{N}{A} + \frac{M}{W} < f_{yd} \quad (4.18)$$

N , M are design normal force and bending moment, respectively in the SLS, A is cross-sectional area, W is section modulus, f_{yd} is yield strength of steel. It is assumed that the plates do not deflect from the z-axes. At the ultimate limit state, a check against the development of plastic hinges in the upper part of the structure is based on Eq. (4.18). This simplified interaction equation is detailed in the Swedish design method by Pettersson and Sundquist[24]) as;

$$\frac{N}{\frac{x_y N_{RK}}{\gamma_{M1,steel}}} + k_{yy} \frac{M}{\gamma_{M1,steel}} \leq 1.0 \quad (4.19)$$

N_{RK} and $M_{y,RK}$ factored axial compressive strength and bending moment of the corrugated steel cross-section; x_y is a reduction factor for flexural buckling and given by ($x_y = \frac{N_{cr}}{N_u}$). N_{cr} is the critical buckling load per unit length, $N_u = N_p$ is the axial compressive strength per unit length. $\gamma_{M1,steel}$ material partial coefficient for steel (instability, recommended value 1.0). k_{yy} is an interaction coefficient for second order effects of the axial forces on deformed members and given by:

$$k_{yy} = \frac{C_{my}}{\left(1 - x_y \frac{N}{N_{cr,y}}\right) C_{yy}} \quad (4.20)$$

The correction coefficient C_{my} allows for moment distributions along the shell structure, and it is typically assumed to be equal to 1.0. $N_{cr,y}$ is the buckling load for soil steel composites structure under ideal elastic conditions taking in consideration the relative stiffness between the steel structure and surrounding soil.

4.4. Buckling mechanism

The buckling mechanism in shell of SSCS refers to the behaviour exhibited by the structure when subjected axial compression or bending loads, it undergoes compressive stresses that may lead to lateral deformation. As the applied load progressively increases, a critical point is reached wherein the deformation becomes unstable. At this point, the member can suddenly and

significantly deflect in a lateral direction. This phenomenon is referred to as buckling. In essence, buckling occurs when a structure fails due to instability under compressive load, rather than due to material strength. In other word, it is a mode of failure that arises from the structure's incapability to withstand the applied load without experiencing significant lateral deflection [114]. The soil-steel composite structures designed for road traffic may experience buckling due to various factors. Uneven settling of the surrounding soil can result in differential loading on the shell. Furthermore, insufficient consideration of dynamic loading from heavy vehicles passing over the culvert can contribute to buckling. Therefore, ensuring proper soil compaction and load distribution is crucial to maintaining uniform loading on soil-steel composite structures.

4.4.1. Buckling of the flexible culvert wall

Elastic buckling arises locally and can occur in the crown of the structure, in its lower part or anywhere else, depending on where the critical combination of axial forces, bending moment, material imperfections and local stresses occur. In fact, a failure of a flexible corrugated steel culvert due to buckling has never been reported, apart from the occurrence of excessive deformations in the culvert shell [115].

During model tests of flexible culverts made of corrugated sheet, covered with soil with a low modulus of deformation, it was noticed that the sheets were damaged by buckling. With an increase in the difference between the soil deformation modulus and the stiffness of the sheet itself, the failure occurred through the plasticization of the steel [116]. The following buckling condition has been proposed for the design of flexible culverts with large spans:

$$f_b = \frac{2}{A} \sqrt{\frac{eEI}{1-\nu^2}} \quad (4.21)$$

Where:

f_b – buckling critical pressure,

A – cross-sectional area of the culvert per unit length,

e – modulus of soil resistance,

E – Young's modulus for the culvert,

I – moment of inertia of the culvert cross-section per unit length,

v – Poisson's ratio for the culvert material

Theoretical analysis of the buckling phenomenon has been made by many researchers and included in the design standards. However, according to [117] they are not widely used in design. The reason for this is that failures to constructed culverts that could be attributed to buckling never occurred unless there was excessive deformation prior to failure [117]. For box-type soil steel composite structure reinforced by addition stiffening rib, the critical force due to global buckling can be estimated using the methodology presented by Pettersson [16]. According to Pettersson [16], the moment bearing capacity of the shell with stiffening rib is checked in the same way as a culvert without stiffening rib using the section parameters for the stiffened section. However, Pettersson [16] recommended to use the cross-section area for the barrel (main shell) only when calculating the ultimate normal force N_u , neglecting the effect of the stiffening rib. This recommendation is due to the fact that, the normal force is carried mainly through the barrel itself. On the other hand, stiffening rib will naturally have an effect on the critical normal force. In case the length of the stiffening rib in the crown area is less than the length of the top radius plate itself the critical normal force of the stiffened top shell could be calculated using equation 16 and could be increased by calculating the factor γ using the diagram shown in Fig. 4.6. However, for this particular thesis, since the length of the stiffening rib at the crown section is equal to the length of the top radius, the critical force increment factor, γ will be unit.

$$N_{cr} = \frac{\pi^2 E I_2}{\gamma L^2} \quad (4.22)$$

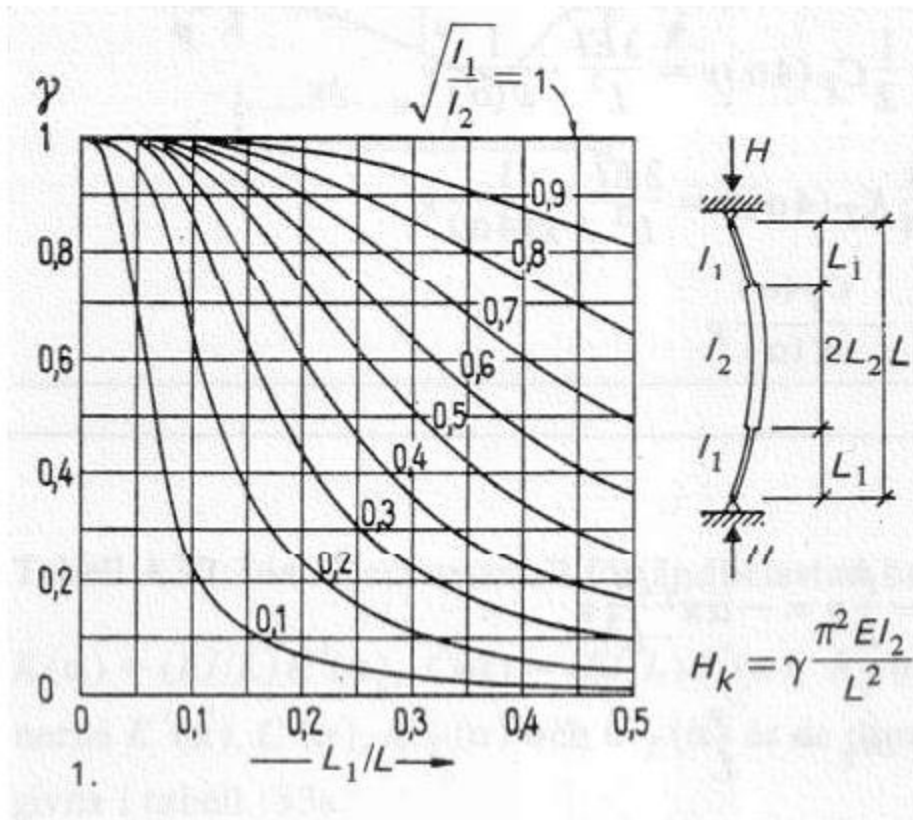


Figure 4.6: Adjustment of the critical normal force depending on the stiffness and length of the reinforced section of a reinforced member (Source: Pettersson [16])

4.4.2. Buckling according to Swedish design method

From the second-order theory, for a circular pipe ($R = R_t$) which is embedded in soil that extends for a long distance outside the pipe, the buckling force, under simplified ideal conditions, can be calculated from the expression:

$$N_{cr,el} = 1.2 \sqrt{\frac{E_{soil}(EI)_{steel}}{R}} \quad (4.23)$$

Where;

E_{soil} – the design tangent modulus for the soil, kN/m^2

$(EI)_{steel}$ – the stiffness of the pipe per unit length, kNm

$N_{cr,el}$ – buckling load for a buried pipe under ideal elastic conditions, kN/m

The risk of local buckling risks must be considered and checked for the selected corrugated profile.

This can be done using the following relationship:

$$M_{ucr} = \left(1.429 - 0.156 \cdot \ln \left(\left(\frac{m_t}{t} \right) \left(\frac{f_{yk}}{227} \right)^{1/2} \right) \right) M_u \quad (4.24)$$

where m_t and t are the corrugated profile's tangent length and thickness respectively; f_{yk} yield stress of the steel. A condition is that $M_{u,cr} \leq M_u$. The ratio of M_{ucr} / M_u is plotted as a function of sheet metal thickness for the profiles Eq (4.23) is illustrated in Fig.4.7 where the ratio.

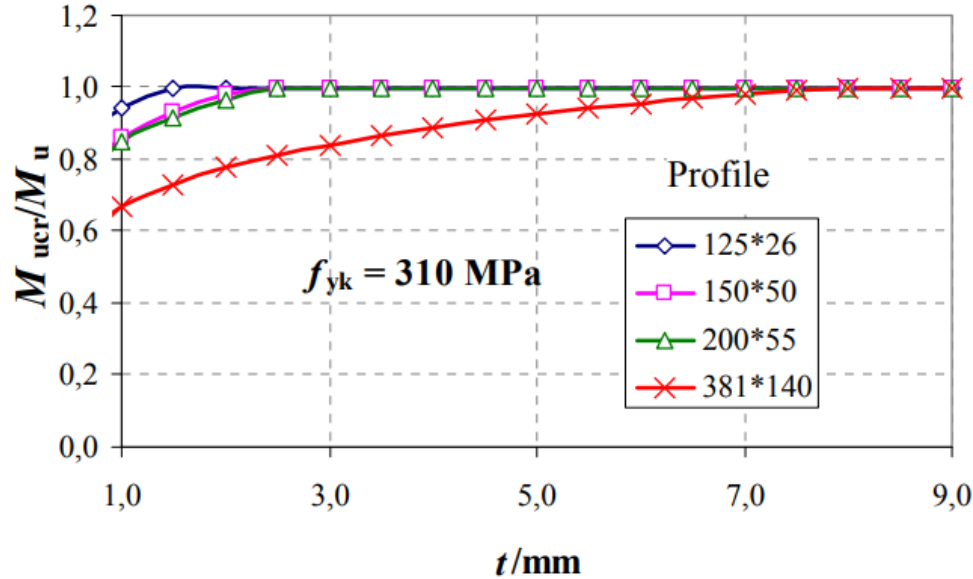


Figure 4.7: The ratio $M_{u,cr} / M_u$ as a function of corrugated steel sheet thickness for the selected profiles [57].

If cross corrugation is used the following reduction factor can be used by modifying Eq.4.24 as:

$$M_{u,cr} = 0.6M_u \quad (4.25)$$

However, this reduction is applicable for $t \geq 5.0$ mm. For thinner metal, the specific factor needs to be determined.

The equations and theoretical analysis presented in this chapter are used to identify potential failure mechanisms in soil-steel composite structures in the following chapters. A comprehensive understanding of the structural behavior under various loading conditions provides a foundation for predicting how these structures might fail. This groundwork allows for a more in-depth examination of the failure modes in SSCS.

5. Soil-steel composite structures under ultimate load: effects of stiffening ribs and geotextile

Soil-steel composite structures (SSCSs) offer versatile and sustainable technology for various civil engineering applications. Ongoing research in this field continues to refine design practices, improve structural performance, and contribute to the development of cost-effective and environmentally friendly infrastructure solutions [118] [119] [120] [121] [122] [123]. Several methods are available to improve the bearing capacity of SSCSs, and a commonly used approach is the use of additional ribs [15][33] [96] [93]. Sanaeiha et al. [15] conducted a field test on a large-span SSCS stiffened by concrete rings during backfilling. The authors compared the test results with well-known design methods and provided detailed recommendations based on their findings. Reinforcing the soil cover above the crown of the shell using geotextiles or geogrids emerges as a cost-effective solution [96]. According to Wysokowski [94], placing a geomembrane in the backfill 0.3 m above the crown of the shell increases the load bearing capacity of the structure by approximately 30%. A comprehensive full-scale test has been conducted by Vaslestad *et al.* [96]. The authors analyzed the influence of geogrid on the mechanical behavior of box type SSCS. As described above, there is still a need for further research on the failure mode of soil-steel composite structures under ultimate loads. Furthermore, a comprehensive exploration of the failure modes in SSCS, both with and without a stiffening rib, as well as the failure mode of the structure reinforced with geotextile, is imperative. Therefore, the study in this chapter investigates the behavior of SSCSs, emphasizing the role of stiffening ribs and geotextile reinforcement through comprehensive numerical modelling. For the analysis, experimentally validated computational model was developed using the finite element method (FEM) and implemented in the ZSoil FEA numerical program.

5.1. Experimental detail

Wysokowski [98] conducted a full-scale experiment conducted at the Research Institute of Roads and Bridges in Żmigród, Poland shown in Fig.5.1. The structure had a span of 3.55 m, longitudinal width and rise of 13.7 m and 0.6 m, respectively. The shell was assembled using corrugated profiles with a commercial designation, specifically the multi-plate 150 mm x 50 mm (pitch x depth), and it had a thickness of 5.0 mm. To enhance its strength and stability, the structure was reinforced with the ribs made from CSP located at the top section of the perimeter, specifically

at the crown, with a width of 1.54 m (See Fig.5.2). The corrugated steel plates (CSP) were joined by 20 mm (in diameter) bolts, having a minimum tensile strength of 830 MPa. For the backfill material, a well-graded soil with a maximum grain size of 32 mm was utilized. The backfill was placed in layers with a maximum thickness of 25 cm, and it was compacted to achieve a degree of compaction equal to at least 97% of the Standard Proctor test.

Once the backfilling process was completed, reaching a soil height of 0.6 m above the crown of the shell, the structure was subjected to steadily increasing load up to the value of 2000 kN. The overall view of the assembled shell, along with the structure after backfilling, is illustrated in Fig. 5.1(b). The test stand consists of two actuators with a maximum exciting force of 1000 kN and a maximum travel of 400 mm. The loads from the actuators are transmitted to the backfill through the four positions, spaced 1.0 m center to center indicated by green arrows in Fig. 5.1 (b). Further details about the load configuration can be found in [98].



Figure 5.1: Model of the soil steel composite structure in laboratory test: a) general view of the assembled corrugated steel structure, b) after backfill model prepared for ultimate loading test [98]

Initially, the structure showed no signs of failure under a load of 2000 kN. Consequently, the top layer of backfill was removed, leaving only a 0.10 m thick soil cover above the shell. The structure was then reloaded, resulting in the observed failure of the shell. The results obtained for this setup, in the form of a load-displacement curve under ultimate load, as well as the displacement taken during the backfill, are directly used to calibrate the numerical model. Detailed results from the

full-scale test are provided in section 2.6.1, covering measurements taken during backfill and under ultimate load.

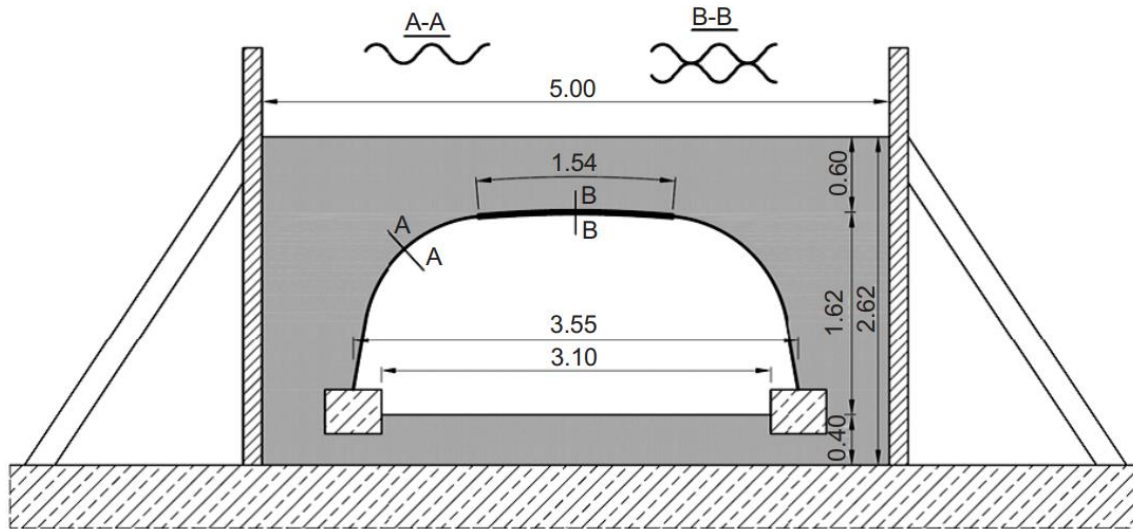


Figure 5.2: Geometry of the tested structure.

5.2. Numerical modelling

The numerical model used in the thesis reflects the structure considered in [98]. The ZSoil software [124], based on finite element method (FEM), was used for the numerical analysis of the soil-steel composite structure. It was modeled as a 2D object in plane strain. The finite element mesh and kinematic boundary conditions are shown in Fig.5.2. In terms of boundary conditions, the vertical edges of the domain were restrained against horizontal displacement and the bottom boundary was fixed in all directions. To ensure computational stability, the loading to failure is simulated in a displacement-driven manner. Selected nodes at the top boundary of the domain are restricted in the vertical direction, as (See Fig. 5.3). The connection between the shell and the foundation was assumed to be pinned with fixed displacement in both directions and free in rotation. To account for second-order effects, the large deformation mode is activated. Furthermore, a mesh size sensitivity analysis was performed to ensure that the results are not influenced by the element size. Finally, a fine mesh size of 5 cm was employed for both the shell and the surrounding backfill.

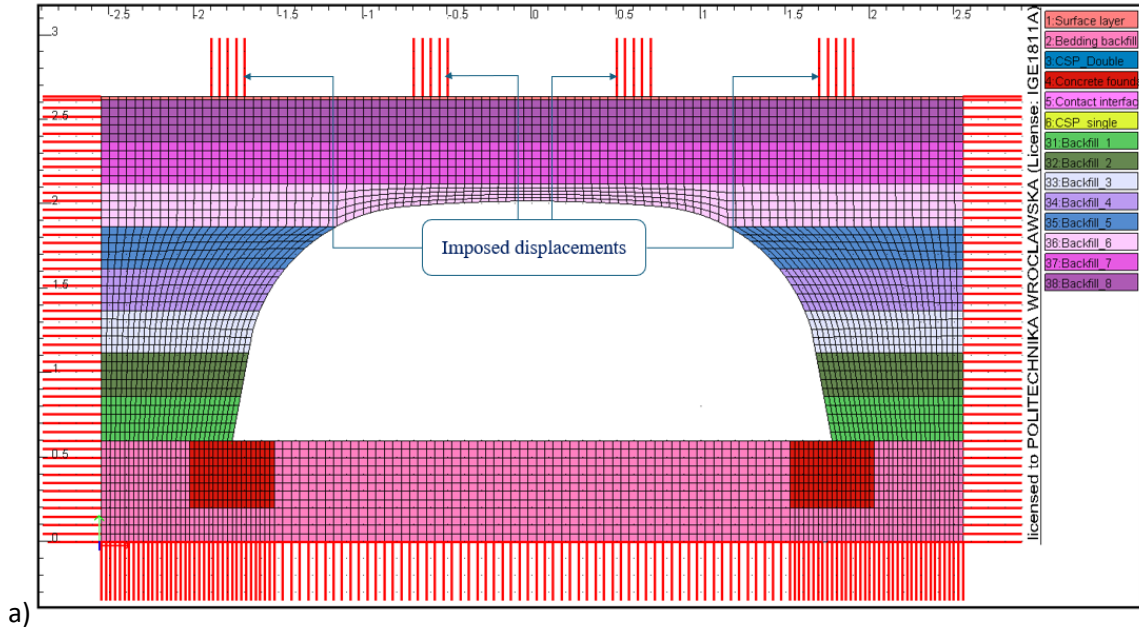


Figure 5.3: Model of considered SSCS: finite element mesh and boundary conditions adopted in the numerical model.

The shell is modelled utilizing nonlinear beam elements, employing an elastic-perfectly plastic constitutive relation. It is also assumed to be continuous in the out-of-plane Z direction, following the considerations presented in previous works [46] [125] [126]. The parameters of the CSP are taken from the manufacturer catalog [6]. Accordingly, the cross-sectional area and moment of inertia for a single CSP are $A_1 = 6.30 \text{ mm}^2/\text{mm}$ and $I_1 = 1978 \text{ mm}^4/\text{mm}$, respectively. For the section with stiffening rib, employing Steiner's theorem, the corresponding values are $A_2 = 12.6 \text{ mm}^2/\text{mm}$ and $I_2 = 13,485 \text{ mm}^4/\text{mm}$. Therefore, a perfect connection between the main shell and the stiffening cover is assumed (See Fig.5.4). In reality, the structure comprises a series of corrugated plates bolted together at specific locations. A study by [127] revealed that explicit modeling of the overlap between the shells or bolt connections has no significant impact on the structural response. Therefore, in the present study, the bolted connection between CSP is not explicitly included in the model. Similar assumptions are considered in recent studies[83] [128].

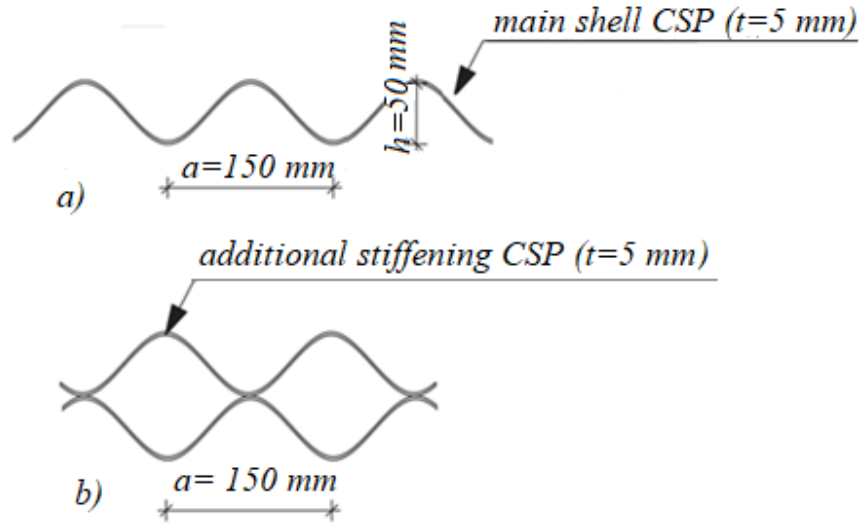


Figure 5.4: Corrugated steel plate model a) main shell b) main shell with stiffening rib.

The CSP is characterized by Young's modulus ($E=205$ GPa), Poisson's ratio ($\nu=0.3$), a unit weight ($\gamma=78.6$ kN/m³) and by strength parameters specified in European Standard EN 10025, in particular, yield stress limit of $\sigma_y=250$ MPa. The elastic-perfectly plastic constitutive model with Coulomb-Mohr yield criterion is assumed for the backfill modelled with solid 2D elements. Initially, soil parameters, including Young's modulus ($E=40$ MPa), Poisson's ratio ($\nu=0.2$), cohesion value ($c=0$ kPa) and internal friction ($\phi=39^\circ$) were assumed based on national standards for coarse sand/sand with gravel. However, initial simulations revealed a significant difference between the simulated and measured results. Recognizing the need for improvement, an extensive calibration process was undertaken to refine the soil parameters. Following this calibration, a good fit was observed between the simulation and measurements. This issue is addressed in the next section. The unassociated plastic flow rule is prescribed by adopting a dilatancy angle determined based on the ZSoil user manual [124]:

$$\psi = \max(0.1\phi, \phi - 25^\circ) \quad (5.1)$$

where ψ is the dilatancy angle and ϕ the angle of internal friction.

To properly reflect the interaction between the soil and shell at the interface, a one-sided contact condition was assumed. This follows that the soil medium may separate from the shell if the shell moves away from the backfill material, and subsequent contact renewal is allowed when the shell and backfill material come close together again. The behavior of the contact interface was described using the Coulomb condition. The plastic slip was governed by a non-associated plastic

flow rule with the dilation angle value set to $\psi = 0$. The Coulomb condition governs the value of the maximum tangential stress in contact elements:

$$|\tau_f| \leq a + \sigma \tan \delta \quad (5.2)$$

Where adhesion $a = 0$, the internal angle of friction $\delta = 0.6 \varphi \approx 22^\circ$ and φ is the internal angle of friction of the adjacent soil. Elastic deformation moduli (normal and tangential stiffness) for interface elements were determined in accordance with ZSoil Users' Manual [124] as:

$$K_n \approx K_t = \frac{E}{h} \quad (5.3)$$

Where E is the elasticity modulus of weakest adjacent material, h represents the size of finite element (representing the backfill) adjacent to the contact interface. Based on Eq. 3, the values of normal and tangential stiffness utilized in the calculation were estimated as $K_n = K_t = 1.0e^6 \text{ kN/m}^3$ for the interface between the soil and the shell., while $8.0e^4 \text{ kN/m}^3$ for the interface between the geotextile and the backfill. Similar assumption is considered in the numerical model described in [93].

The concrete foundation was modeled as linear elastic, while the geotextile was modeled as nonlinear, assuming elastic-perfectly plastic behavior with limited tensile stress, accounting for the prestressing effect. In the current model, a prestress of approximately 6% of the tensile strength of the geotextile material is considered. The tensile strength of the geotextile in the model is 3.4 MPa, with zero compressive strength and a thickness of 4.2 mm.

5.3. Numerical model validation

The full-scale test described in section 5.2, which conducted by Wysokowski [98] on box-type SSCS is used to validate the numerical model. The measurements of displacement taken on the box-type SSCS were used to adjust the parameters of the numerical model. A parametric analysis was carried out so that to fit the simulation results to the measured data. The validation process included test results from both stages: backfilling and external loading.

5.3.1. Simulation of construction stage

In the initial stage of calculations, the problem was solved considering only the deadweight load of the structure, including the backfill, shell, and foundation. Subsequently, as backfill was added

layer by layer, a compaction load was applied to each layer of backfill. During the actual backfilling process, once a new layer of backfill is placed on both sides of the shell, compaction equipment is employed to perform repeated cyclic compaction. This process gradually transforms the backfill from a loose state to a dense state. Upon completion of compaction, a residual lateral stress, known as compaction-induced stress [129], remains in the backfill. According to [130], the magnitude of this stress is significantly higher than the geostatic lateral effective stress at rest value, or even greater than the passive earth pressure of the backfill layer. To model this compaction process, different approaches are proposed by scholars. For example, the work of McGrath et al. [131] introduced three practical approaches for modelling the compaction of a backfill layer placed adjacent to a the shell of SSCS. These approaches, as depicted in Fig. 5.5, can be summarized as follows:

- First approach applying vertical surface loads to the surface of the backfill layer.
- The second approach is squeezing the most recently placed layer of backfill between vertical upward and downward forces.
- The third approach is applying horizontal normal forces or imposing prescribed displacement to the shell.

In accordance with [130], the first and second approaches offer an advantage in modelling the deformation and internal forces in the shell caused by compaction loads. However, a crucial limitation emerges in using an elastic constitutive model for the backfill in these first two approaches, when simulating the backfilling process. The issue lies in the fact that deformations produced by elastic models will be lost once the surface loads are removed. In such cases, elastic soil models can lead to a rebound effect in the structure's deformations and internal forces, making them unsuitable for accurately representing the practical backfilling process. The third approach is regarded as a post-compaction method, involving the direct application of lateral nodal forces or imposing prescribed displacement to the culvert body.

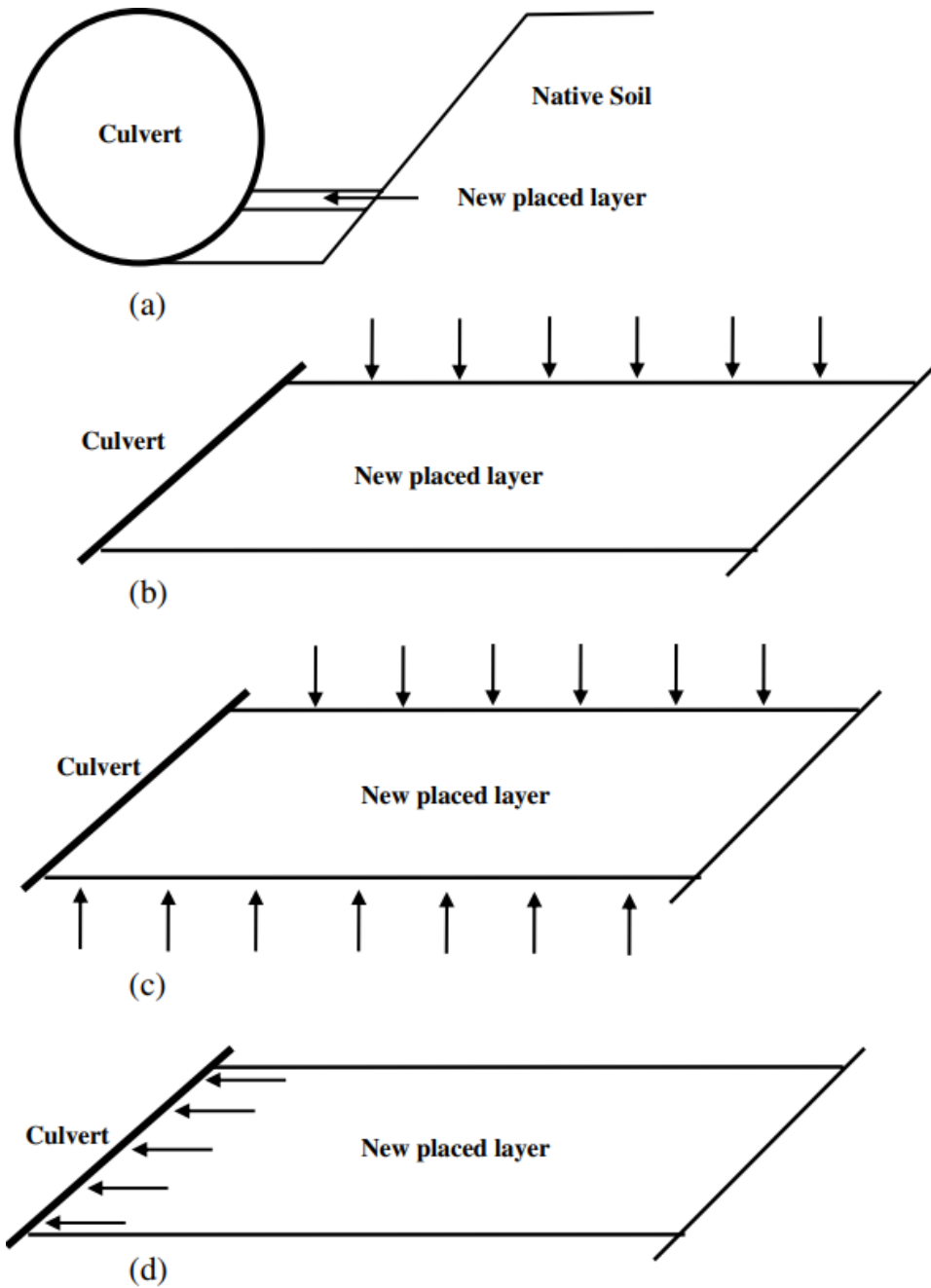


Figure 5.5: Diagram of practical procedures for compaction models of a backfill layer placed adjacent to a the shell: (a) new layer of backfill; (b) vertical surface load on new layer; (c) loads that squeeze the new layer; (d) the third approach is application of horizontal loads to shell [130].

Among the three approaches, the first approach is considered in this model. Then, the surface load of 50 kPa was applied on the surface of each layer. This process continues until the backfilling process is completed (See Fig.5.6 (a-j)). To replicate the test results [98], the modeling approach incorporates eight layers of backfill, each with a maximum thickness of 0.25 m.

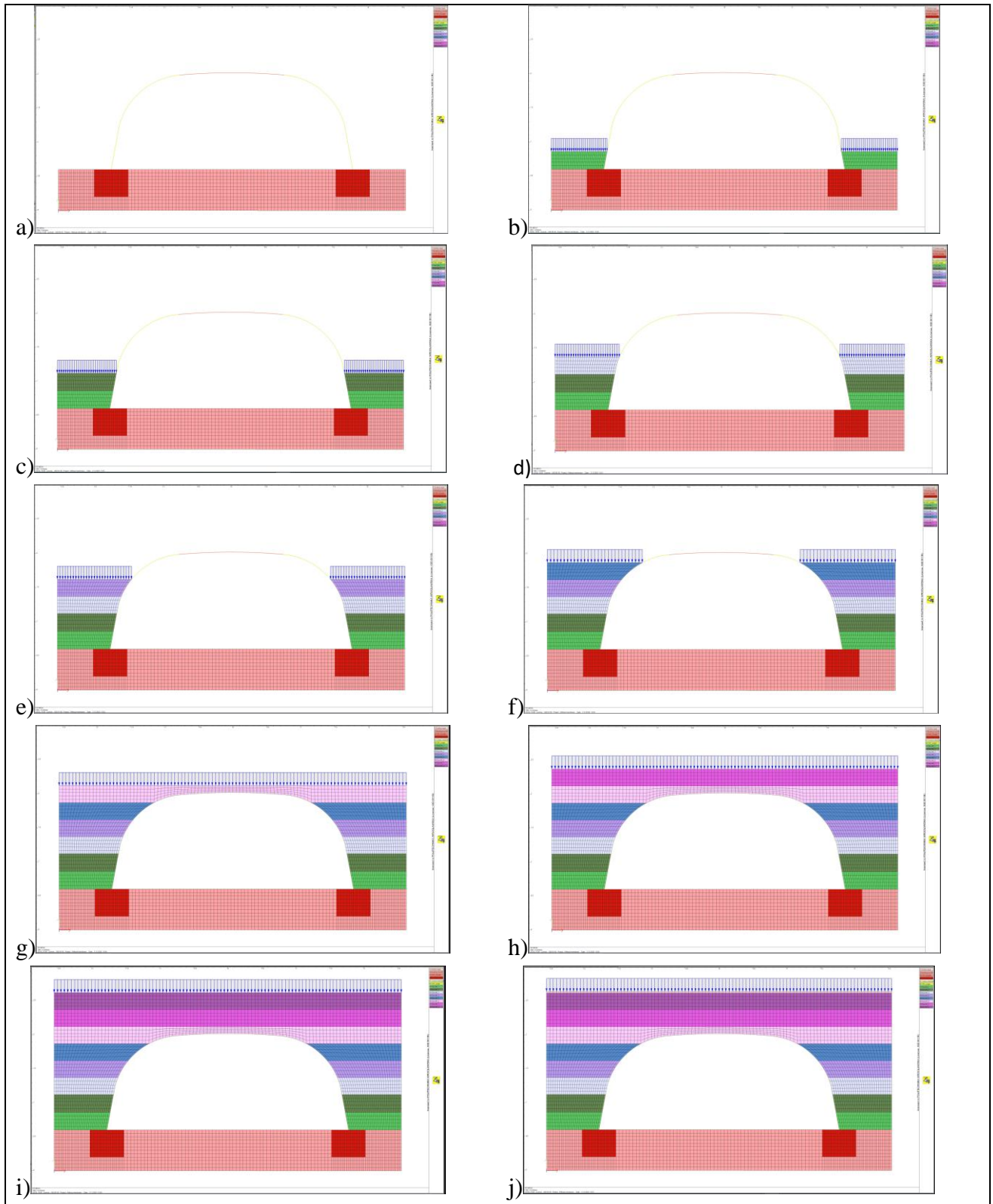


Figure 5.6: Successive backfilling and compaction process.

The simulation of backfilling and compaction follows a sequential process: initially, a layer of backfill is activated, generating geostatic backfill stresses. Subsequently, a compaction load is applied, and the model is computed. This iterative process continues until the backfill reaches its final stage. Once the backfilling is completed, the structure is subjected to external loading to failure. Similar assumptions were made in [75] [132] [133] in modeling SSCS during the construction stage and under external load. The vertical displacement results at the crown of the shell are shown in Fig. 5.7 for both measurements and numerical modeling. In the model, the crown of the shell initially exhibited upward deflection as the backfilling process progressed, and this displacement continued until the backfill reached layer five. Subsequently, as the backfilling process extended beyond layer five, the crown of the shell started moving downward. By the time the backfilling reached the final stage, which is layer eight, the maximum downward movement reached approximately -1.70 mm. In the measurement, the observed behavior showed an initial upward deflection until the backfill reached layer six. After reaching this point, the shell started moving downward slowly as subsequent backfilling layers were added. Upon the completion of the entire backfilling process, a total vertical displacement of -1.89 mm was recorded.

The FE model accurately determines displacements within the shell during the construction stage. However, it slightly underestimates the peak displacement (both upward and downward), deviating by approximately 11% from the field measurements. The maximum upward and downward vertical displacement of the shell during construction were less than 0.1% of the structure rise, which is in agreement with the requirements of CHBDC (CSA 2019) [134] code limit of 2%.

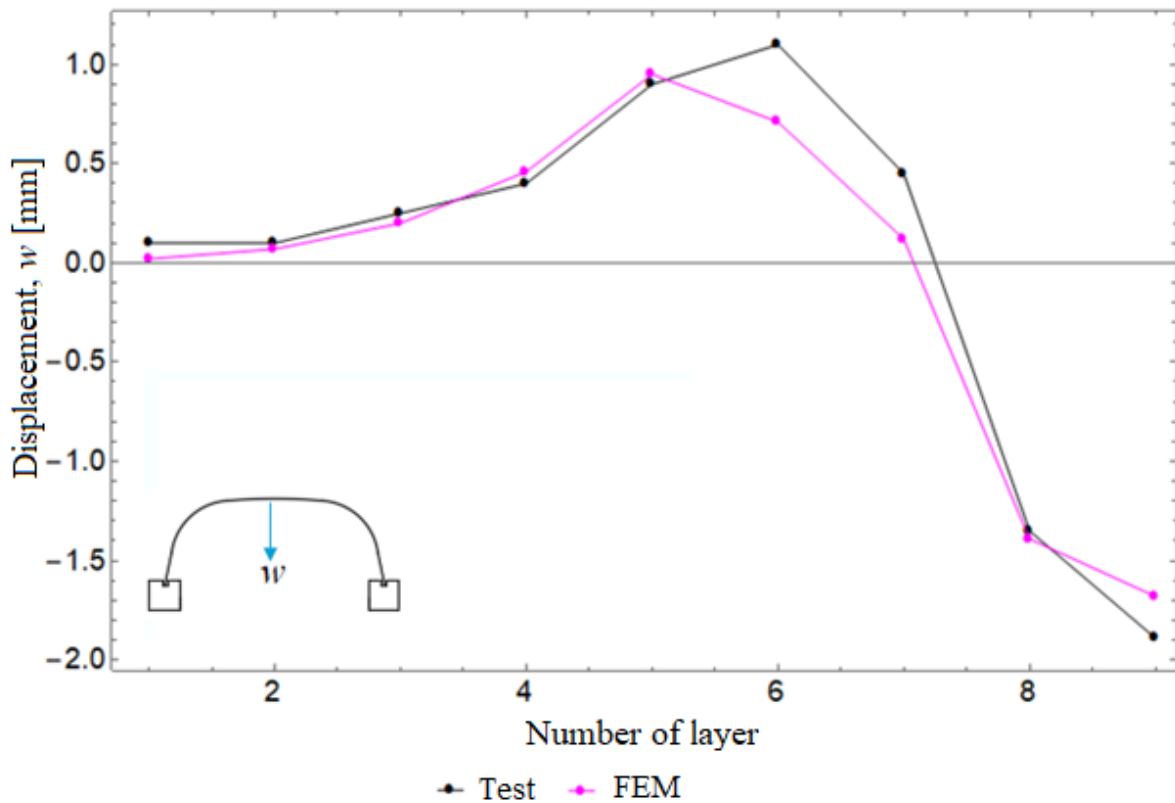


Figure 5.7: Comparison of measurements and numerical modeling results for the crown displacement during backfilling.

5.3.2. Simulation of ultimate load test

As mentioned, the reduction of the soil cover above the crown of the shell was intentionally carried out to facilitate the observation of shell failure. The loading-to-failure model was executed subsequent to decreasing the soil cover to a mere 0.1 m, as described in Fig. 5.8. After completing the backfilling phase during simulation, the nodes on the top surface were gradually moved downward, and the total loading force was calculated as the sum of nodal reactions. This allowed us to plot the curve of load versus displacement, as shown in Fig.5.9. Simultaneously, the corresponding results from measurements [98] are also plotted in the same graph.

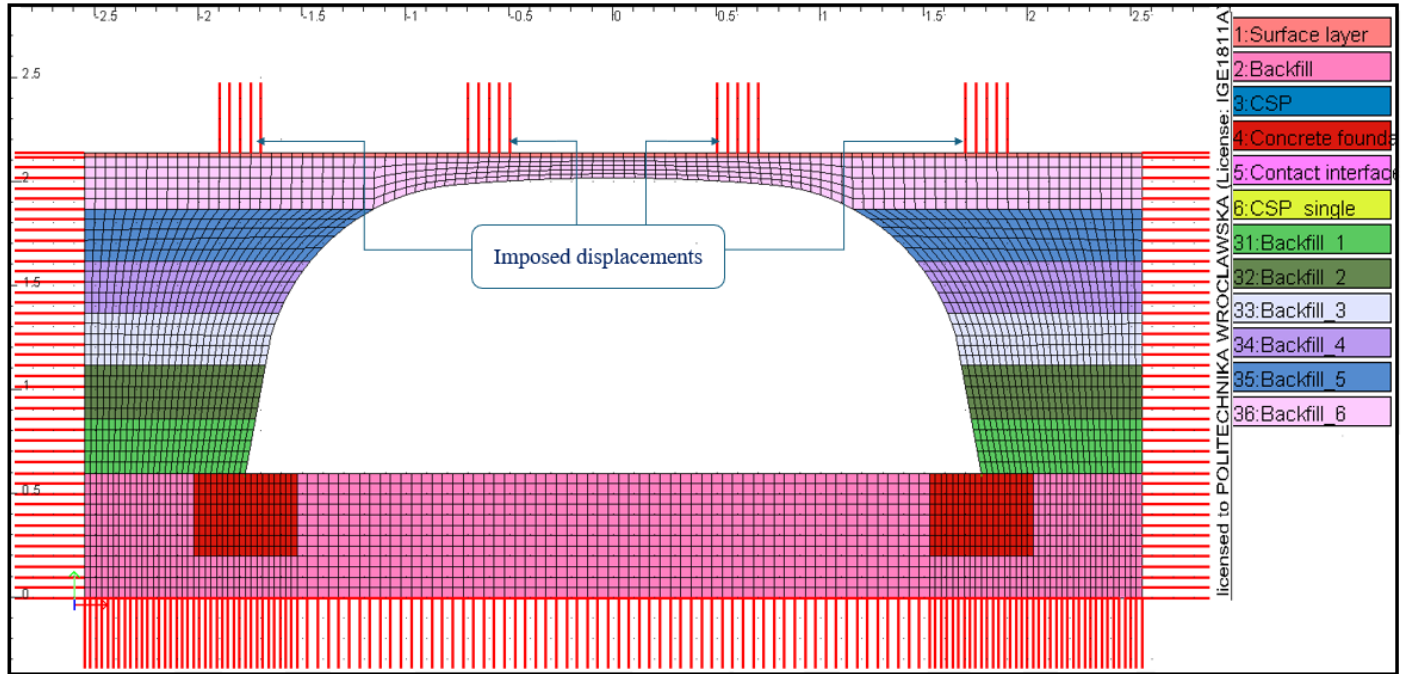


Figure 5.8: The SSCS model with reduced soil height of cover

The load-displacement behavior (See Fig.5.9) observed in both datasets exhibits notable congruence and reveals essential insights into the structural response. Up to 900 kN load, the structure demonstrates a nearly linear response marked by a relatively flat slope, signifying the initial, elastic phase of deformation. Beyond the aforementioned value, load increase rate drops apparently, what is reflected by a steeper slope of the plot. This is attributed to the transition from elastic to plastic deformation of soil. This phase culminates in peak value of load less than 1990 kN, signifying ultimate capacity of the entire, composite structure. The agreement in these pivotal load-displacement characteristics underscores the numerical model's ability to replicate the result from the measurement. Especially, the convergence of simulated and measured load bearing capacity has to be emphasized. It was achieved after robust model calibration based on the displacement results recorded during backfilling the shell. Therefore, as the validation process encompassed the entire loading history divided into two main stages—namely, the construction stage (backfilling) and operational loading—the same set of material parameters was applied. This consistency resulted in a good agreement between measurements and simulations, confirming the accuracy of the performed calibrations. In conclusion, it can be stated that the finite element model successfully described the performance of the structure and accurately determined its load-bearing capacity.

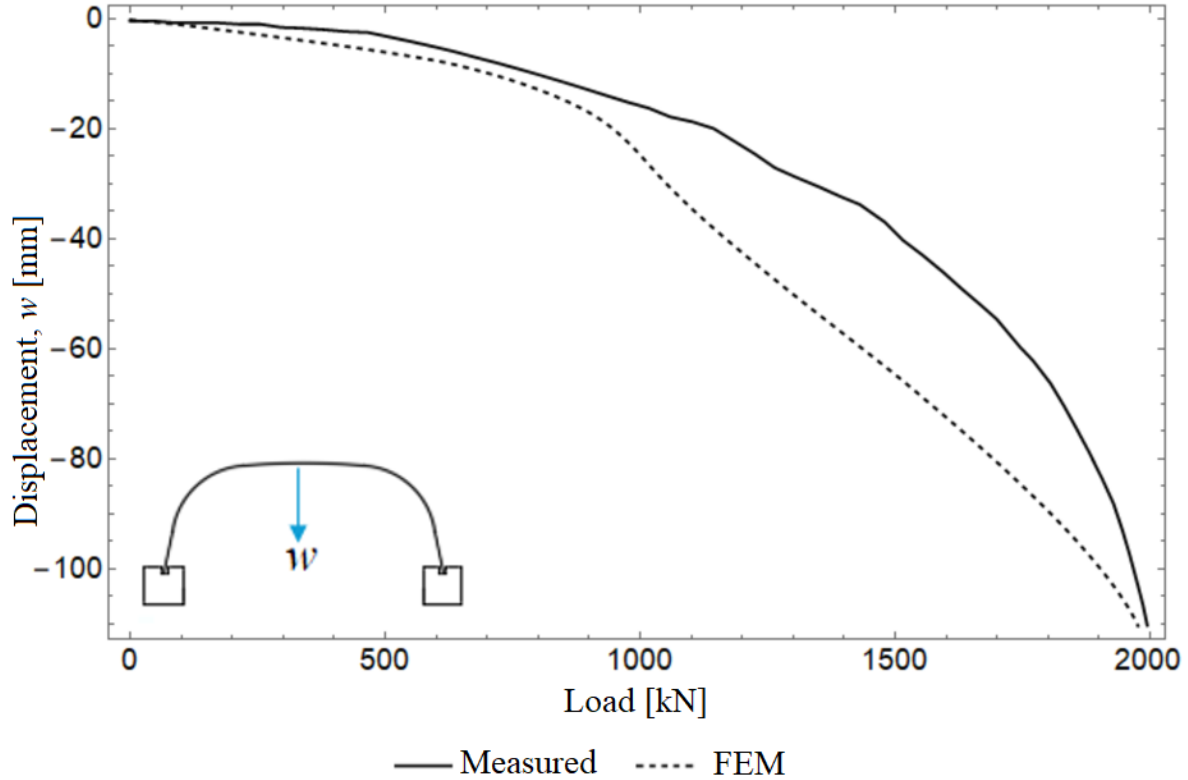


Figure 5.9: Load-displacement curve.

The material parameters used in the present analysis, including those which were calibrated, are given in Table 5.1.

Table 5.1: The summary of the material parameters used in the computations.

Name	Steel	Backfill	Concrete
Young's modulus (MPa)	205,000	60	25,000
Tensile strength (MPa)	270	-	-
Yield limit (MPa)	250	-	-
Poisson ratio	0.3	0.15	0.2
Unit weight (kN/m ³)	78.6	19	24
Cohesion (kPa)	-	12	-
Friction angle (°)	-	36	-
Dilatancy angle (°)	-	11	-

Now that the model is validated and the parameters are considered, the subsequent sections conduct an in-depth analysis on a box-type SSCS model with a span of 3.55 m under four cases of reinforcement: Model-I (with a stiffening rib), Model-II (without a stiffening rib), Model-III (with a stiffening rib and geotextile), and Model-IV (without a stiffening rib but with geotextile), as shown in Fig. 5.10 (a–d).

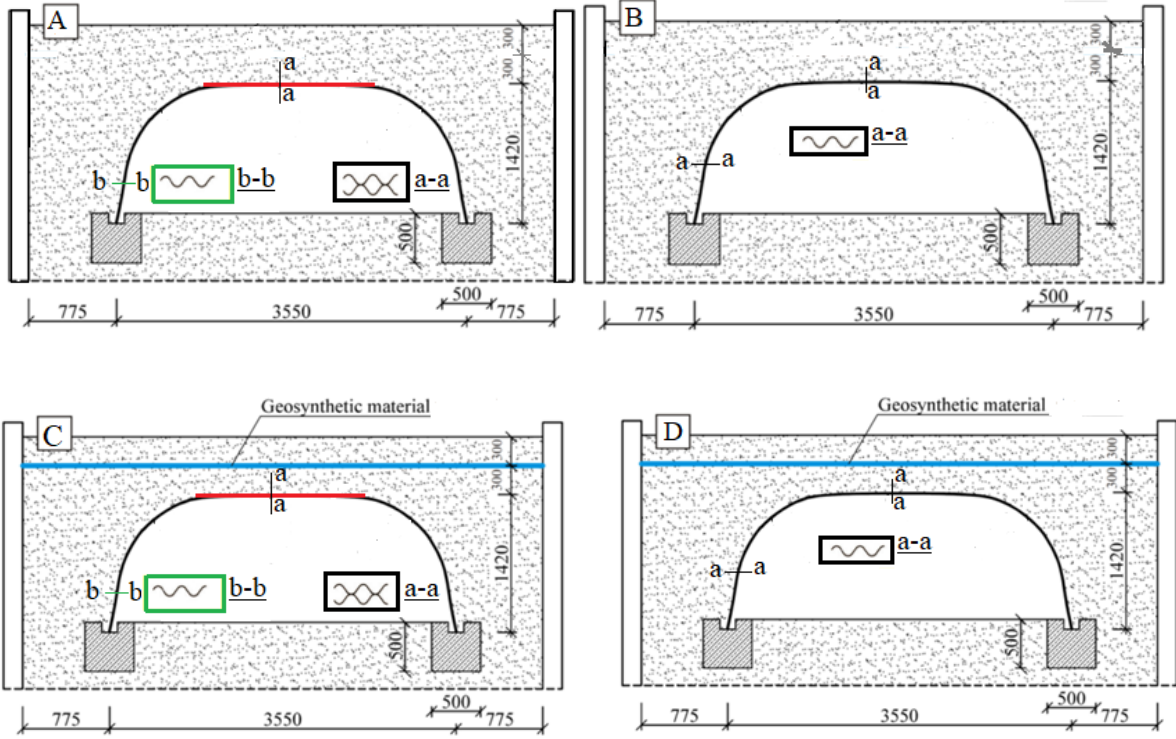


Figure 5.10: Schematic presentation of reinforcement in the models: a) Model-I, b) Model-II, c) Model-III, d) Model-IV (all dimensions are in millimeter)

In the analysis of all models, material, geometrical, and contact nonlinearity are considered. Material nonlinearity is accounted for in both the shell and the surrounding backfill. The geometrical nonlinearity model accommodates large deformations, due to the flexible nature of the structure's response to applied loads. Additionally, the interfaces are assumed between the soil and the shell, as well as between the soil and the geotextile. Various parameters are assessed, including maximum displacements, bending moments, axial forces, and stresses under ultimate loads for these four numerical models.

5.4. Effects of stiffening ribs

In this section, two models are specifically compared: Model-I (with stiffening ribs) and Model-II (without stiffening). The comparison involves the structural response, including displacement, bending moments, and axial forces for both models. While the primary focus is on the structural response of the crown section, the distribution of section forces at the shoulder is also presented and discussed.

5.4.1. Load–displacement curve.

The deflection at the crown point was extracted and compared for both models. In Fig. 5.11, a load-displacement graph is presented, illustrating the behavior of the structures. Initially, the structure exhibited practically linear deformation. Next, the plot bends and its slope increases, reflecting the transition from elastic to plastic deformation. As the applied load continues to increase, it finally leads to yielding in the entire area of the shell cross-sections. Consequently, the structure is unable to carry more load. Its limit value is identified as the overall load bearing capacity of the structure. Then, this limit value of the load, i.e., bearing capacity of the structure, was back-calculated from the reaction forces of the imposed displacement (in this case, at a controlled node).

Model-I, which incorporates the stiffening rib, demonstrates a robust bearing capacity of 2533 kN. In contrast, Model-II, which does not incorporate the stiffening rib, exhibits a considerably lower bearing capacity, amounting to 1732 kN. The presence of the stiffening rib in Model-I exerts a notable positive impact on bearing capacity when compared to Model-II. Specifically, Model-I bears 801 kN more total load, equating to a substantial 47% higher bearing capacity than Model-II. This improvement is attributed to the additional role of the ribs in optimizing load distribution within the structure. It ensures more advantageous redistribution of applied load, thereby mitigating localized stress concentrations that might otherwise lead to premature structural failure. The displacement at which the structure reaches peak load capacity provides insight into how much displacement can be expected until a failure occurs. Accordingly, at the peak load value, the crown of the shell exhibited a displacement of 115 mm and 140 mm respectively for Model-I and Model-II.

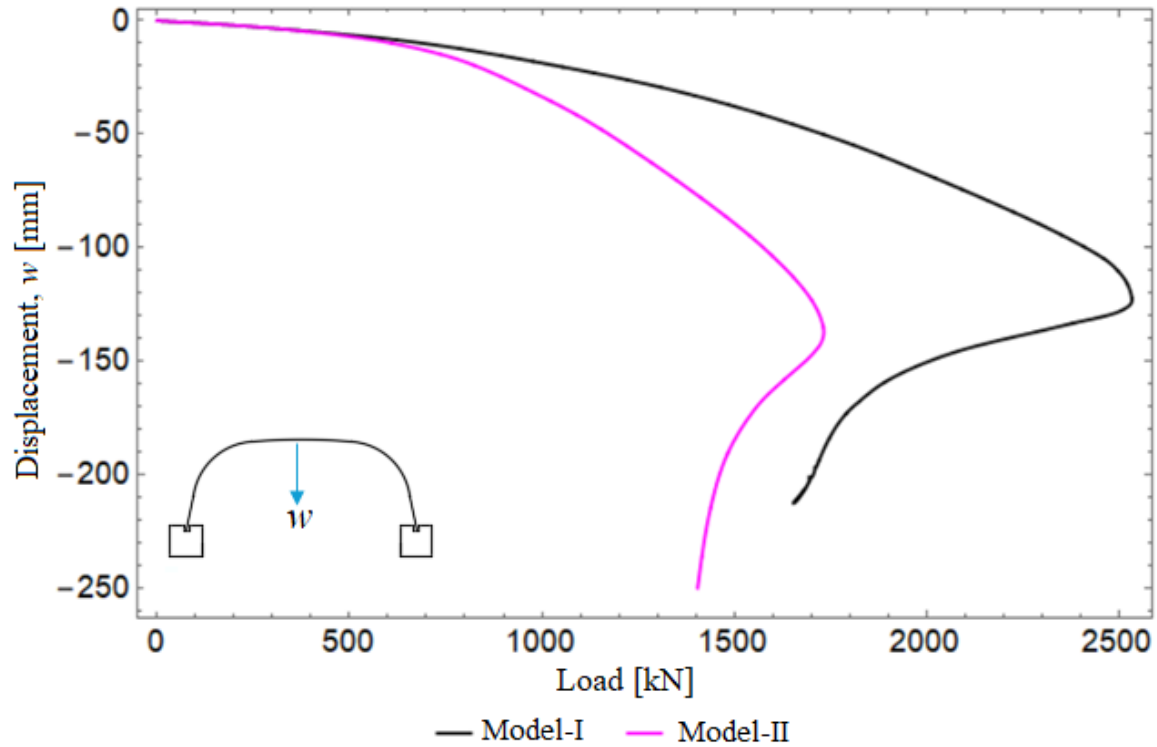


Figure 5.11: Load displacement curve for the model with and without additional rib at the crown.

The failure mode of a considered soil-steel composite structure at which the structure cannot carry more load is determined by bending failure of the shell. The same is concluded in previous study [63]. Specifically, as the load surpasses the structure load-carrying capacity, the load-displacement curve changes sign of its slope indicating distinct inflection point. Beyond it the SSCS behavior transits to post-failure mode. The structure does not break suddenly but undergoes plastic flow in a wide range of displacement. It is to be reminded here that the simulation was performed in a displacement-driven scheme. Nevertheless, such type of ductile behavior of the structure marks favorable property in terms of safety.

The failure mode of the structure is predicted under combined axial compression and bending moment, considering critical locations for this type of structure: at the shell's crown and at its shoulder (at the end of stiffening rib). Additionally, the haunch of the shell was checked.

Employing the interaction equation one can check whether the cross-section becomes fully plastic or not. According to CSA 2019 and AASHTO 2019 the following inequality remains true:

$$\left(\frac{N}{N_p}\right)^2 + \left|\frac{M}{M_p}\right| \leq 1.0 \quad (5.4)$$

rearranging the equation

$$M_u \leq M_p \left(1 - \left(\frac{N}{N_p}\right)^2\right) \quad (5.5)$$

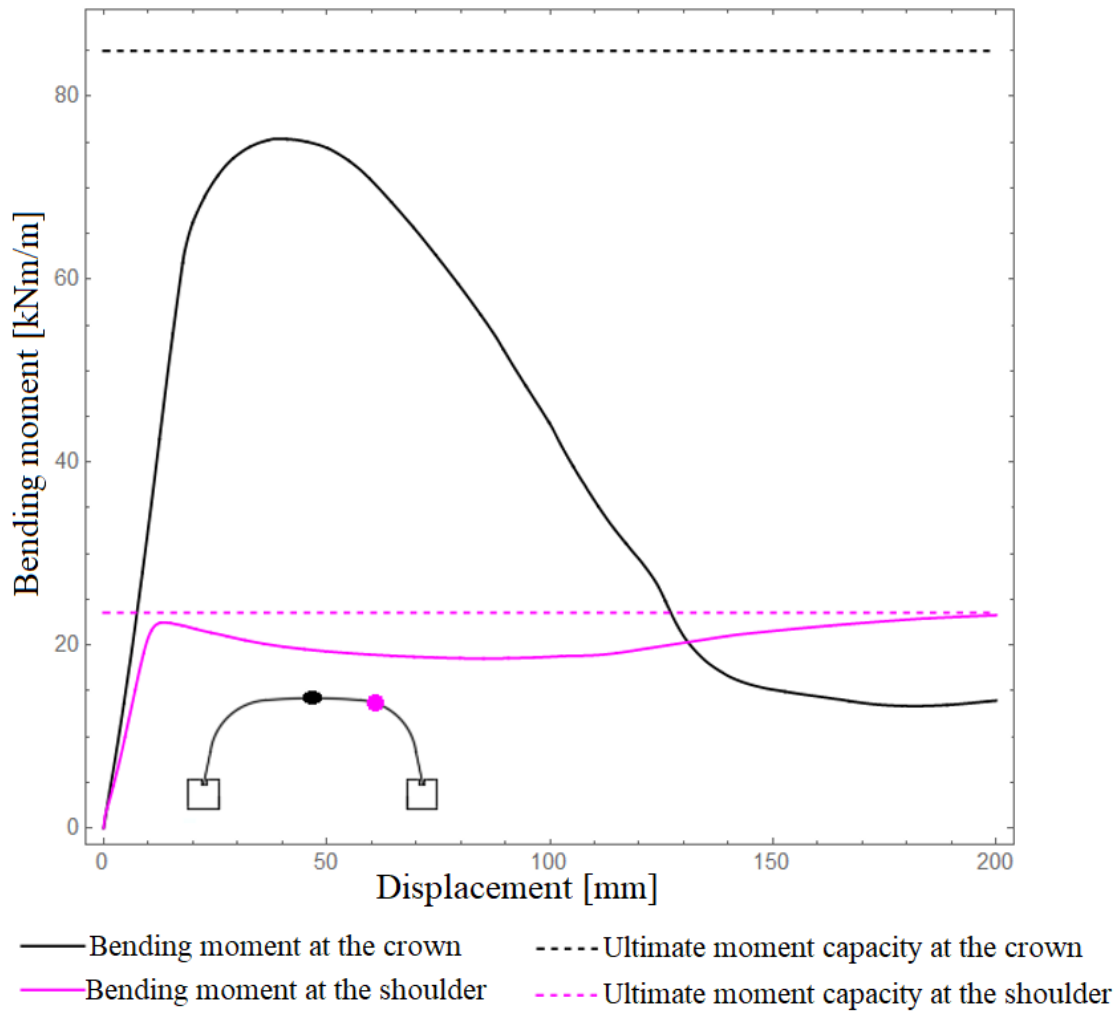
where:

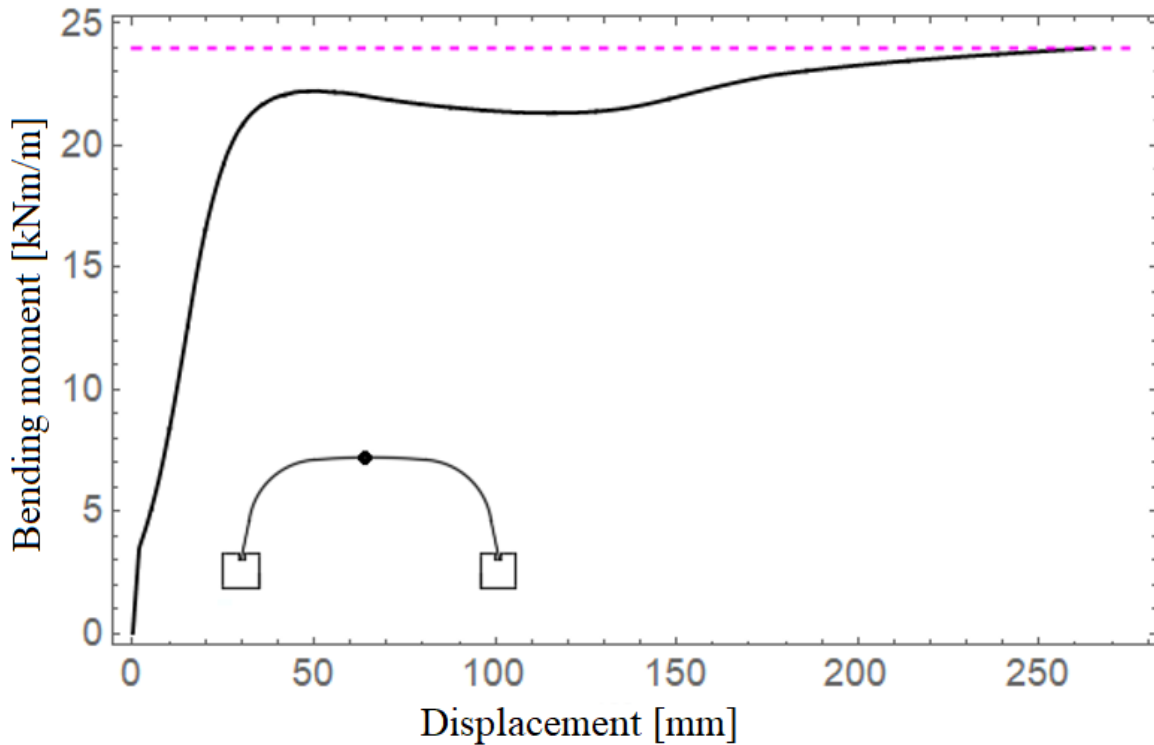
- M_p is plastic moment capacity of the shell ($M_p = \sigma_y Z$)
- σ_y is the yield strength of the steel (250 MPa)
- M_u is ultimate bending moment capacity of shell.
- N_p is maximum capacity of the shell wall against normal force ($N_p = \sigma_y A$)
- N is normal force at maximum bending moment in the calculation
- Z is plastic section modulus of the cross-section

At the crown section, the calculated values are as follows: $M_p = 88.5$ kNm/m, $N_p = 3136$ kN/m and $Z = 354$ mm³/mm. The normal force $N = 618.425$ kN/m is extracted from the numerical model at maximum bending moment and at this point the corresponding load is 1563 kN. Using Eq. (5.5), the ultimate moment capacity of the shell under ultimate load at the crown section for Model-I is determined to be $M_u = 85.06$ kNm/m. Then, the maximum bending moment induced in the shell is extracted from the numerical model, which was found to be 75.2 kNm/m at the crown of the shell. It is worth noting that this value is less than the shell's ultimate capacity. This means the calculated value employing the interaction equation (Eq. 5.4) provided is 0.89. This shows, the shell failed before reaching the unity value of the interaction equation at the crown.

To assess whether the ultimate moment capacity of the shell is reached at other sections, further checks were conducted. Given that the first yielding occurred at the shoulder of the shell (at the end of the stiffening rib), the check was performed at this particular section. At this location, the shell is not overlaid with an additional rib, necessitating the recalculation of cross-sectional and strength parameters for the single shell. Subsequently, the plastic moment capacity of the shell was calculated as $M_p = 24.18$ kNm/m and the maximum capacity of the shell wall against normal force $N_p = 1575$ kN/m. The normal force from the numerical model $N = 268.88$ kN/m, and plastic section modulus of the cross-section $Z = 96.7$ mm³/mm. Then, utilizing (Eq. 5.5), it was determined that

the ultimate moment capacity of the shell under ultimate load at the shoulder section is $M_u = 23.48$ kNm/m. At this specific location, the calculated maximum bending moment extracted from the simulation reaches the ultimate capacity as shown in Fig. 5.12 (a). Employing the interaction equation (Eq. 5.4) the calculated reached 1.0. Accordingly, the structure failed after reaching the unity value of the interaction equation at this section of the shell. Furthermore, as per Pettersson's [16] recommendations, the design evaluation of the box-type SSCS extends beyond the crown section to include the haunch area. Consequently, an examination of the haunch section of the shell was conducted, revealing full yielding during the assessment, ultimately leading to failure at this specific section. Thus, the structure with stiffening ribs (Model-I) loses its carrying capacity due to bending at the shoulder and haunch.





b) — Bending moment at the crown - - - - Ultimate moment capacity at the crown

Figure 5.12:: Bending moment vs vertical displacement curve for a) Model-I b) Model-II

For Model-II, the cross-sectional and strength parameters are as follows: plastic moment capacity of the shell $M_p = 24.18$ kNm/m, maximum capacity of the shell wall against normal force $N_p = 1575$ kN/m, normal force in the calculation $N = 129.80$ kN/m, and plastic section modulus of the cross-section $Z = 96.7$ mm³/mm. The maximum moment capacity of the shell under ultimate load at the crown of the shell is extracted from the numerical simulation and it is 24.06 kNm/m. The corresponding load to the maximum bending moment and normal force for this particular section is 1675 kN. Similarly, employing the interaction equation (Eq.5.4) the calculated value is 1.0. Unlike Model-I, in Model-II the crown section is fully plastic under peak load. Like Model-I, a check was performed on another critical section for this type of SSCS—specifically, the haunch section. The results indicated that the section underwent full plastic deformation under the ultimate load. Therefore, for Model-II, the failure mode is bending failure at the crown and haunch section of the shell as shown in Fig. 5.12 (b).

The ultimate moment capacity's variation between the two models is primarily attributed to the presence and absence of the additional stiffening rib. In Model-I, the capacity is reached at the

shoulder due to the load redistribution facilitated by the rib. However, in Model-II, it is achieved at the crown, resulting in bending failure. These findings underline the complex interplay between geometry, materials, and structural elements in shaping the behavior and failure modes of such structures under ultimate loads, like the additional rib, on the bending failure mode of the soil-steel composite structure.

The overall circumferential bending moment distribution for model-I and model-II is depicted in Fig.5.13(a) and Fig.5.13(b), respectively. These figures reveal notable distinctions in the locations of bending moment concentration and the positions of peak positive and negative bending moments between the two models. For instance, in Model-I, the peak positive bending moment concentrates around the shoulder of the shell. In contrast, for Model-II, this concentration shifts to the crown, which indicates the location of potential failure.

In Fig.5.13(a), a noteworthy observation is the asymmetrical distribution of bending moments at post failure. Initially, this distribution was nearly symmetrical until the load approached its peak. Beyond the peak load, a rapid change in both the rate and sign of displacement occurred, as illustrated in the load-displacement curve in Fig. 5.10. This abrupt shift signifies the onset of plastic flow within the structure, coinciding with the initiation of the asymmetrical bending moment distribution. The pronounced concentration of bending moments, particularly around the left-side shoulder, can be attributed to the presence of a stiffening rib. This is evident when comparing Model-II in Fig.5.13(b), where the distribution appears almost symmetrical, to the asymmetrical distribution observed in Model-I. The stiffening rib encircling the crown of the shell in Model-I plays a pivotal role in redistributing bending moments before the point of failure. Another noteworthy observation in Model-I is the first yielding occurring at the left side of the shell around the shoulder section, precisely next to the end of the stiffening rib and haunch. This localized yielding significantly influences the overall distribution of bending moments. Furthermore, in the model with the stiffener, plastic hinge development is prone at two distinct points—specifically, at both ends of the stiffening rib. In Model-I (Fig.5.13(a)), it prominently manifests on the left side. However, it is imperative to highlight that an equivalent risk of collapse exists on the right side, as demonstrated in the case of Model-III in Fig. 18(a). Moreover, the asymmetrical distribution of bending moments in the structure represents a post-failure mode. This analysis not

only enhances understanding of structural behavior but also provides valuable insights into potential failure mechanisms.

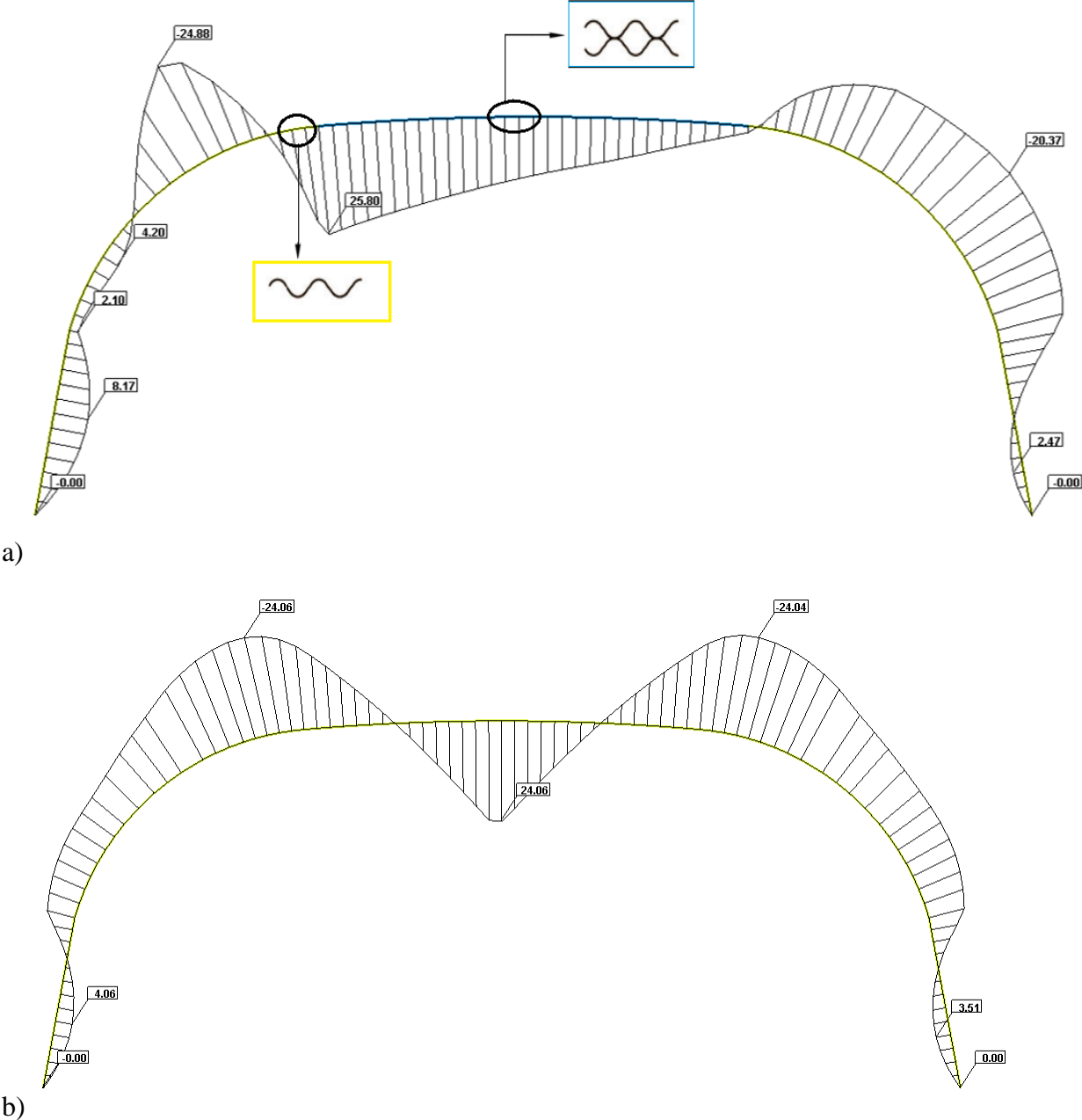


Figure 5.13: Bending moment distribution on the shell of SSCS for a) Model-I b) Model- II

5.4.2. Axial force

The axial thrust of the shell in a soil-steel composite structure under ultimate load represents the maximum compressive force experienced by the wall of the shell and is a critical parameter for assessing the structural safety and integrity of the entire system.

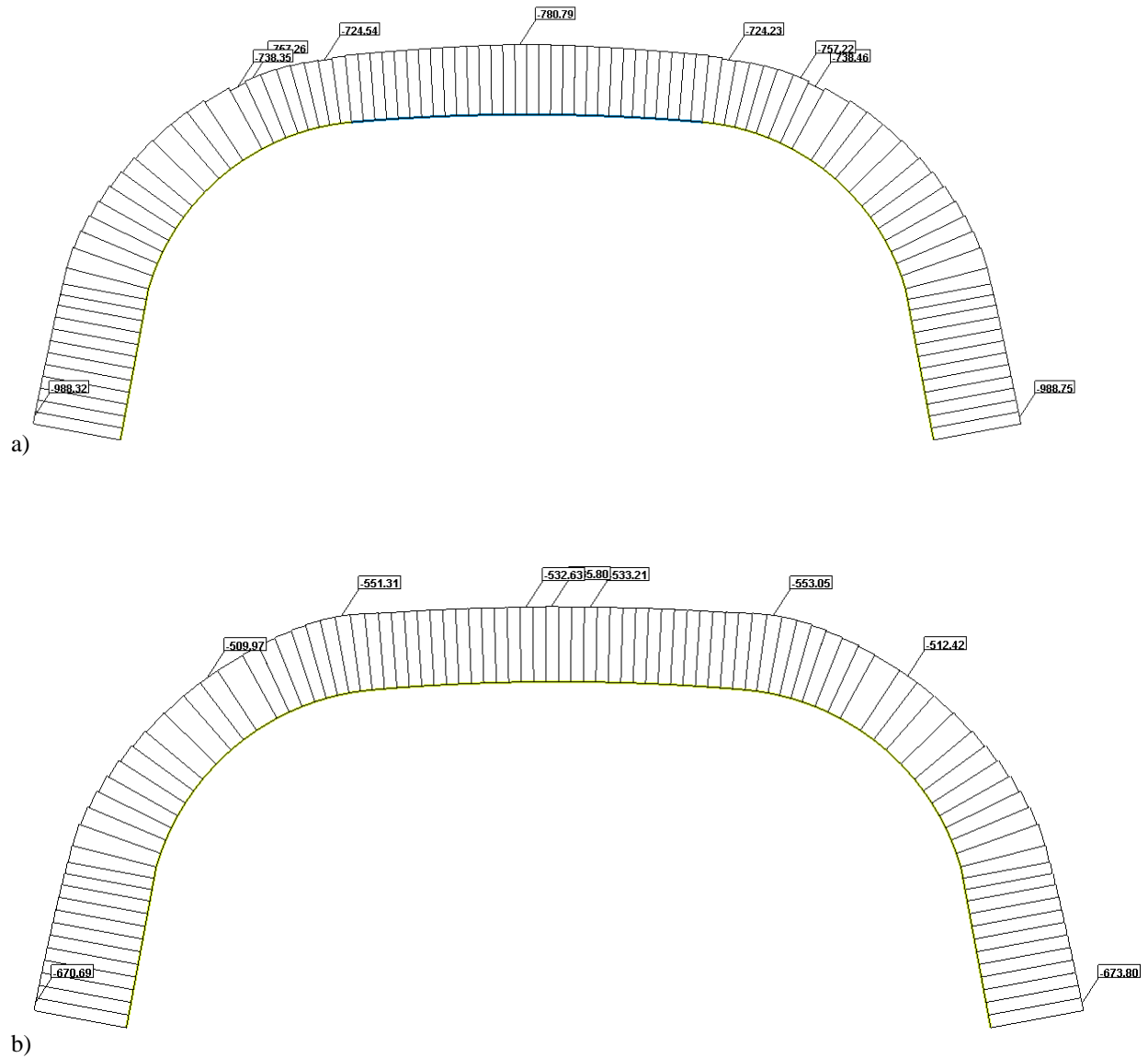


Figure 5.14: Maximum axial thrust distribution on the shell of SSCS under ultimate load; a) Model-I
b) Model -II.

In both models, the analysis reveals that the maximum axial compressive thrusts reach -989 kN/m for Model-I and -674 kN/m for Model-II, as illustrated in Fig. 5.14 (a) and Fig. 5.14 (b), respectively. In Model-I, the maximum axial thrust represents approximately 63% of the shell's

wall capacity at this specific section, which amounts to 1575 kN/m. In contrast, for Model-II, this value is around 43%. This concentration is a crucial observation, as it defines the areas of the structure subjected to the highest loading conditions. Importantly, this finding aligns with the results presented in [33].

In both models Fig. 5.14(a) and Fig.5.14(b), negative axial forces throughout the shell's circumference indicate uniform compression. This behavior aligns with the norm for such structures, as concluded by Moore and Taleb [80]. The peak values of the axial forces are observed near the footing of the shell.

From the results, it can be concluded that the shell without stiffening ribs (Model-II) does not reach the axial thrust capacity of the wall. This finding suggests that, in the context of axial thrust, additional reinforcement is not necessary for such types of shells. This conclusion highlights that Model-II, despite lacking stiffening ribs, still maintains a safety margin with respect to its axial thrust capacity. Therefore, for the specific structural conditions analyzed in this study, the use of additional reinforcement ribs, as present in Model-I, may not be required to ensure that the shell can safely resist axial thrust under ultimate load conditions. This finding was also reported by [33], who conclude that, the shell model without stiffening ribs do not exceed the allowable stresses and displacements in the shell.

5.5. Behavior of geotextile reinforced SSCS under ultimate load.

5.5.1. Load displacement curve.

The bearing capacity of Model-III, which incorporates a geotextile, was determined to be 3200 kN, representing a 26% increase when compared to Model-I, which does not utilize a geotextile. Similarly, Model-IV exhibited a bearing capacity of 2140 kN, reflecting a 23% increase in comparison to Model-II, which lacks geotextile reinforcement. Under ultimate load conditions, the vertical displacement at the crown of the shell experiences a significant reduction, as illustrated in Fig. 5.15. This decrease in displacement and the improvement in load-bearing capacity can be attributed to the redistribution of the applied load on the shell's top surface due to the presence of the geotextile. Geotextile reinforcement enhances the stiffness of the backfill, exerting a substantial influence on the failure mode and overall structural stability.

As shown in Fig. 5.15, the reinforcement's effect becomes more pronounced as the load increases. Consequently, a notable reduction in displacement is observed when the structure is subjected to the ultimate load. For instance, when the reinforced structure undergoes a service load (e.g., 800 kN, following the Polish Standards of bridge load [100]), the reduction in displacement is significantly less compared to when the structure is exposed to loading conditions leading to failure. This observation underscores the effectiveness of geotextile reinforcement in enhancing structural performance under critical loading conditions, providing improved stability, and minimizing displacement during ultimate load scenarios. A similar finding was observed in the full-scale test conducted by [94]. When the geotextile-reinforced structure is subjected to service load, the reduction in maximum vertical displacement at the crown was less than 20 %. This further supports the effectiveness of geotextile reinforcement in reducing vertical displacement and improving the structural performance during service load conditions.

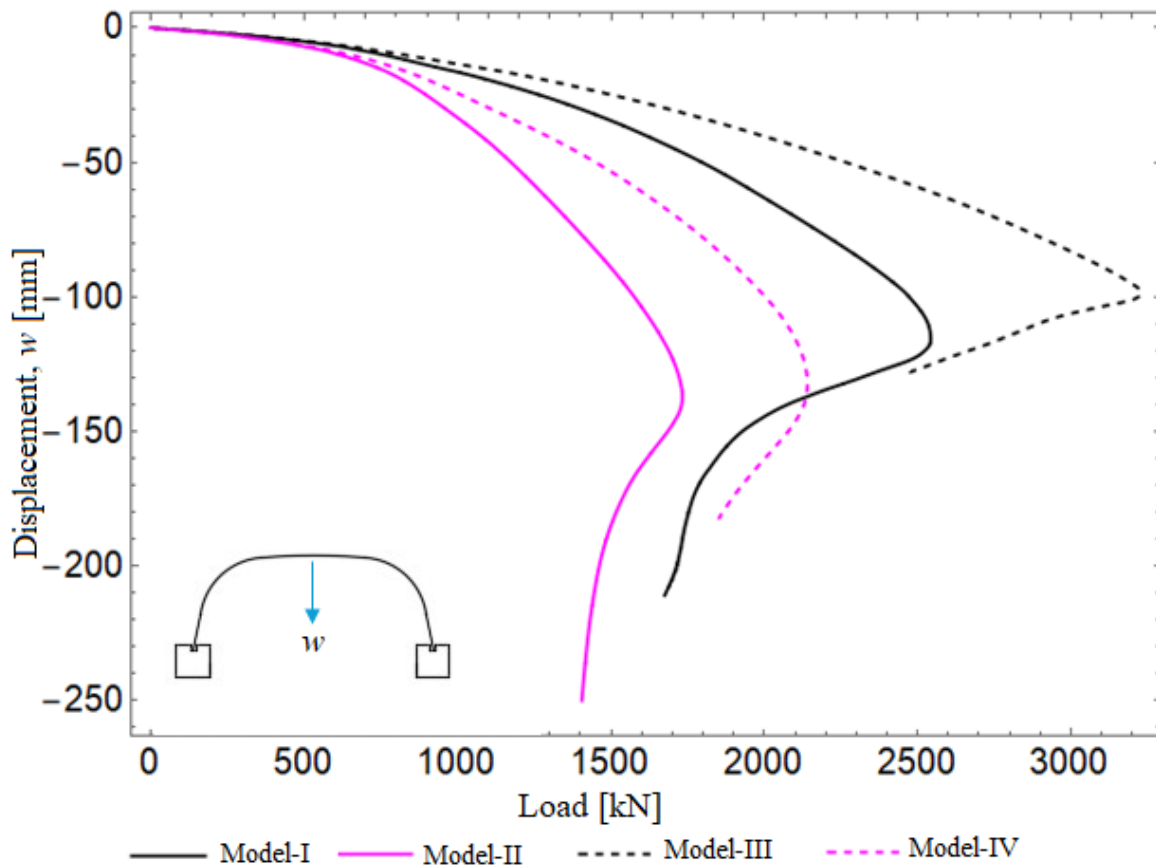


Figure 5.15: Load-Displacement curve at crown.

At the peak load value, the crown of the shell exhibited a displacement of 98.43 mm and 131.95 mm respectively for Model-III and Model-IV. Similar to the Model-I and Model-II, an interesting feature is that post-failure behavior is stable. Under peak load, the vertical displacement at the crown exceeds the permissible standard for all models except Model-III. According to the Polish standard, the maximum deflection percentage (vertical displacement to structure span ratio) should be less than 3%. Model-III complies with this requirement, with a deflection percentage of 2.8%.

5.5.2. Bending moment

The maximum bending moment in the shell at the crown is illustrated in Fig. 5.16. It can be observed that the bending moment increases when the structure is reinforced with the geotextile.

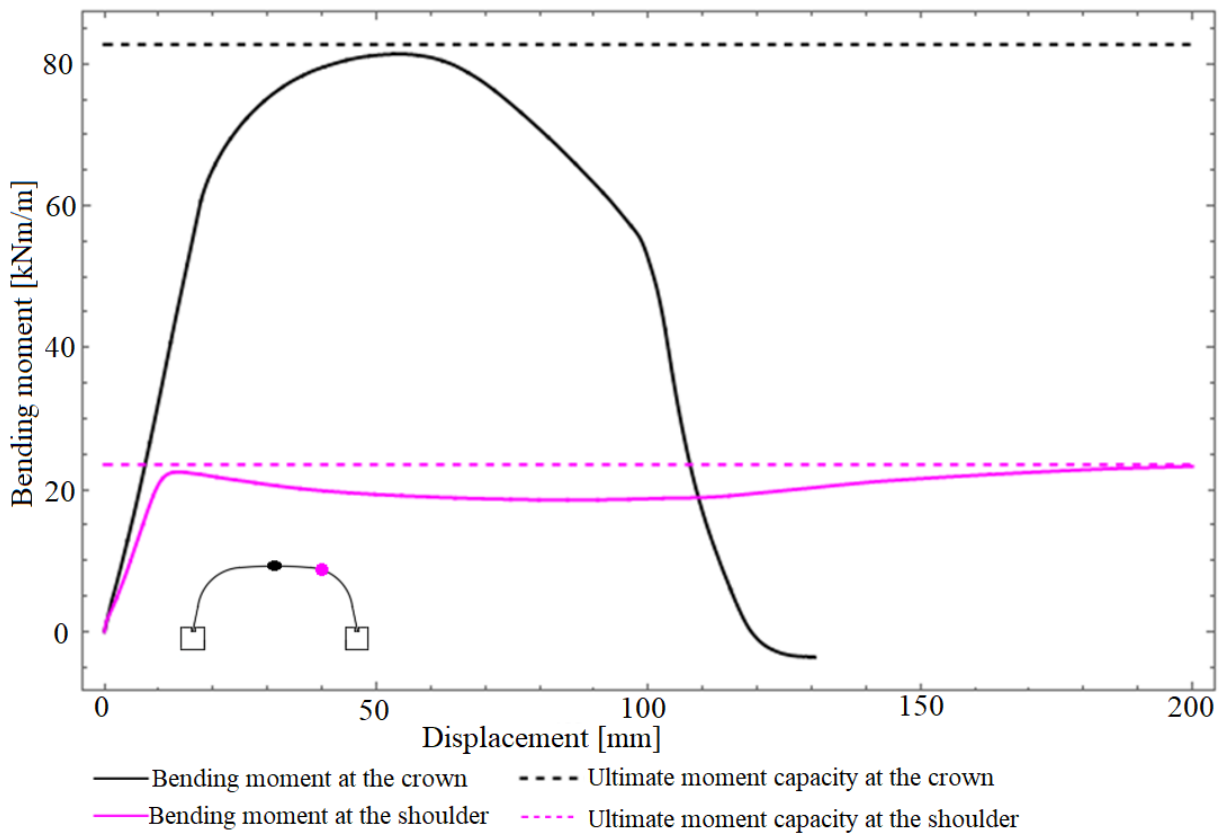


Figure 5.16: Bending moment displacement curve at the crown and shoulder for Model -III

Utilizing Eq. (5.4), previously applied to Model-I and Model-II in Section 5.3, the ultimate plastic moment capacity (M_u) for Model-III at the crown section is estimated. The geometric and strength parameters for this model are identical to those of Model-I, except the inclusion of geotextile. The axial compressive thrust at maximum bending moment for this model is extracted

from the numerical model as, N (855.6 kN/m). Accordingly, using Eq. (5.5), the estimated M_u for the shell in this particular model is calculated as 81.9 kNm/m. Once the ultimate capacity is estimated, the maximum bending moment at the crown of the shell was extracted from the numerical simulation, which amounts to 81.4 kNm/m, as shown in Fig.5.15. The load corresponding to this maximum bending moment is calculated as 2382 kN. When compared to Model-I, the maximum bending moment induced in the shell is improved by 8%. This finding aligns with the results of a numerical analysis conducted by [93] on soil-steel structures subjected to service load, where the bending moment capacity of the shell is similarly improved through the reinforcement of a single layer of membrane. Despite the increase in bending moment capacity, similar to Model-I at the crown section, the ultimate capacity of the shell due to combined bending and axial forces is not reached under ultimate load. It was confirmed by employing the interaction equation given on Eq. (5.4) and the calculated value is 0.99. From this interaction value it can be seen that, the shell is close to reaching the full yielding at the crown section.

To find if the shell capacity due to combine axial compression and bending moment is reached at other sections of the shell, further check has been carried out. Accordingly, the maximum moment capacity of the structure is reached around the shoulder of the shell. At this specific location, the calculated interaction value based on Eq. (5.4) is 1.00. Unlike Model-I, the haunch section of the shell does not undergo full plastic deformation under the ultimate load. Thus, the structure with ribs and geotextile reinforced (Model III) loses its carrying capacity due to bending at the shoulder. The distribution of bending moment is shown in Fig. 17 (a) for Model-III.

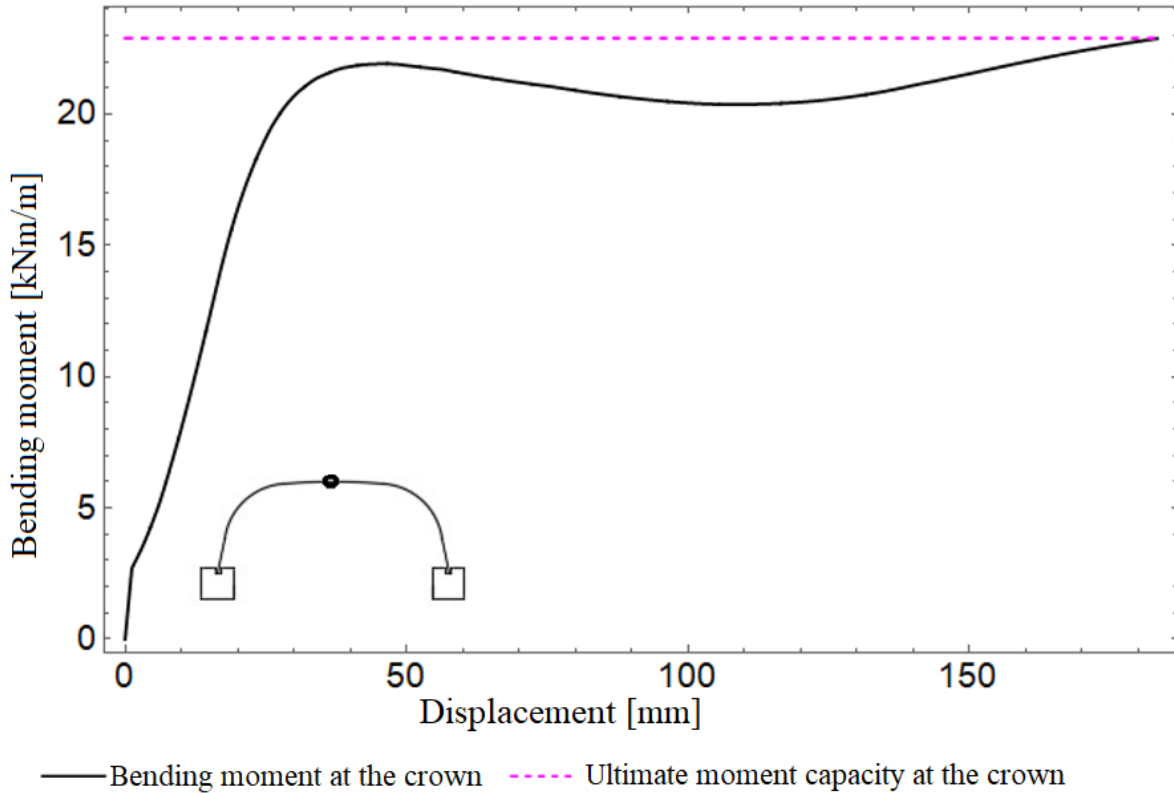


Figure 5.17: Bending moment displacement curve at the crown of the shell for Model -IV

For the Model-IV, The ultimate plastic moment capacity of the selected profile is 21.8 kNm/m, calculated using Eq. (5.5). Similar to Model-II, the shell in Model-IV failed after reaching fully plastic under peak load as shown in Fig. 5.17. And as shown in Fig. 5.18 (b) the maximum positive and negative bending moment induced in the shell is observed at the crown and shoulder section of the shell respectively. Comparing this value with the ultimate capacity of the shell, it can be concluded that the shell in Model-IV failed after the cross-section at crown and haunch reached fully plastic section. Thus, potential failure modes for this structure are a local bending moment, and the development of plastic hinges.

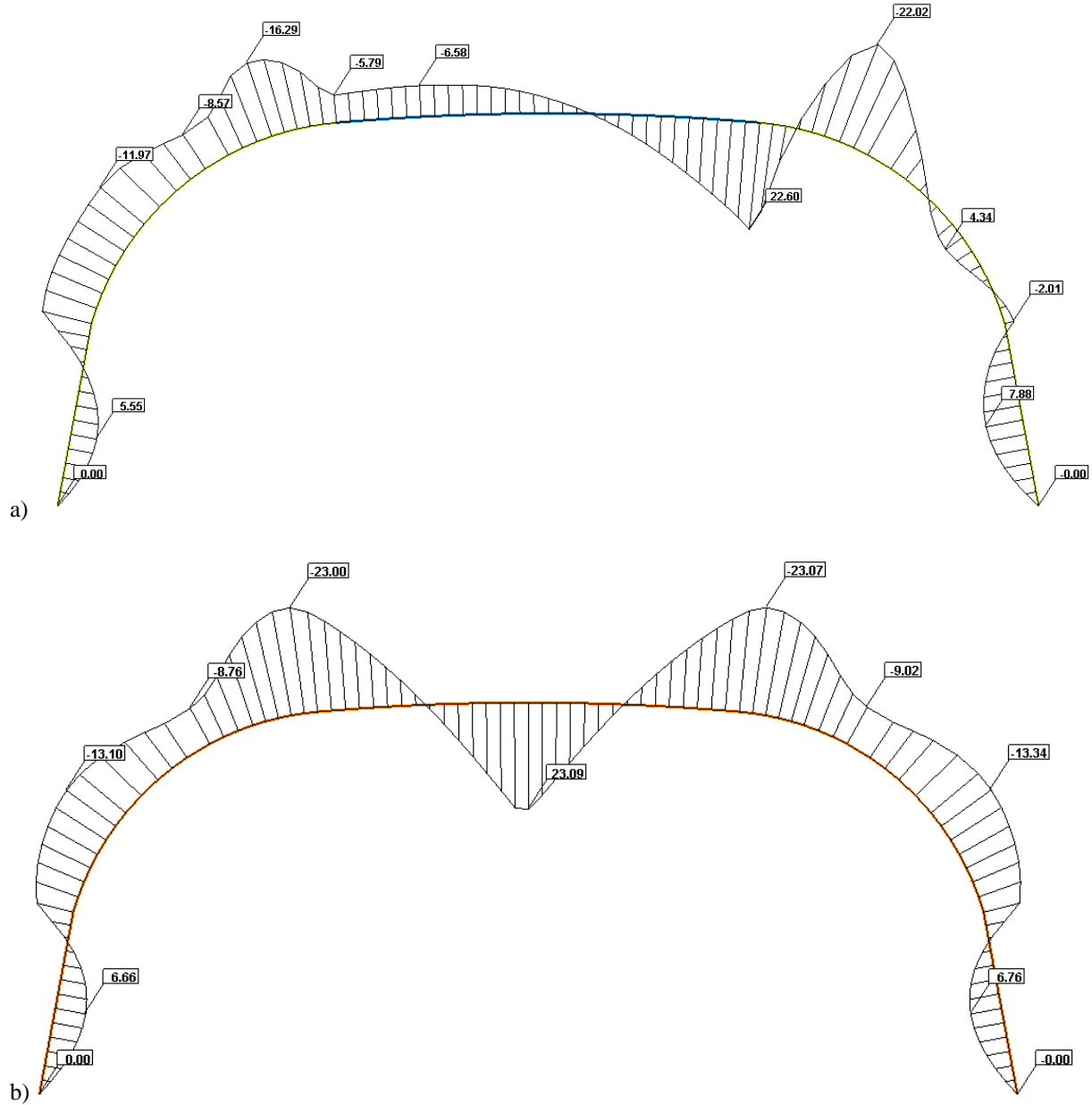


Figure 5.18: Bending moment distribution on the shell of geotextile reinforced SSCS under ultimate load for a) Model-III b) Model-IV.

The presence of geotextile enhances the bending capacity of the shell, particularly in the lower section near the foundation. For instance, in Model-II, the maximum bending moment at this section is approximately 4.06 kNm/m (as shown in Fig. 5.13(b)), whereas in Model-IV, it increased to 6.66 kNm/m (as depicted in Fig. 5.18(b)). This represents an increment of around 64%.

5.5.3. Axial force

The maximum calculated axial thrusts for Model-III and Model-IV are presented in Fig. 5.19(a) and Fig. 5.19(b), respectively. In Model-III, the maximum calculated axial thrust (compressive) reaches 1225 kN/m, while in Model-IV, it amounts to 839 kN/m. These values are observed in the shell near the foundation. When comparing Model-I (a model without geotextile) with Model-III, there is a 16% increase, and when comparing Model-II (another model without geotextile) with Model-IV, there is a 24% increase.

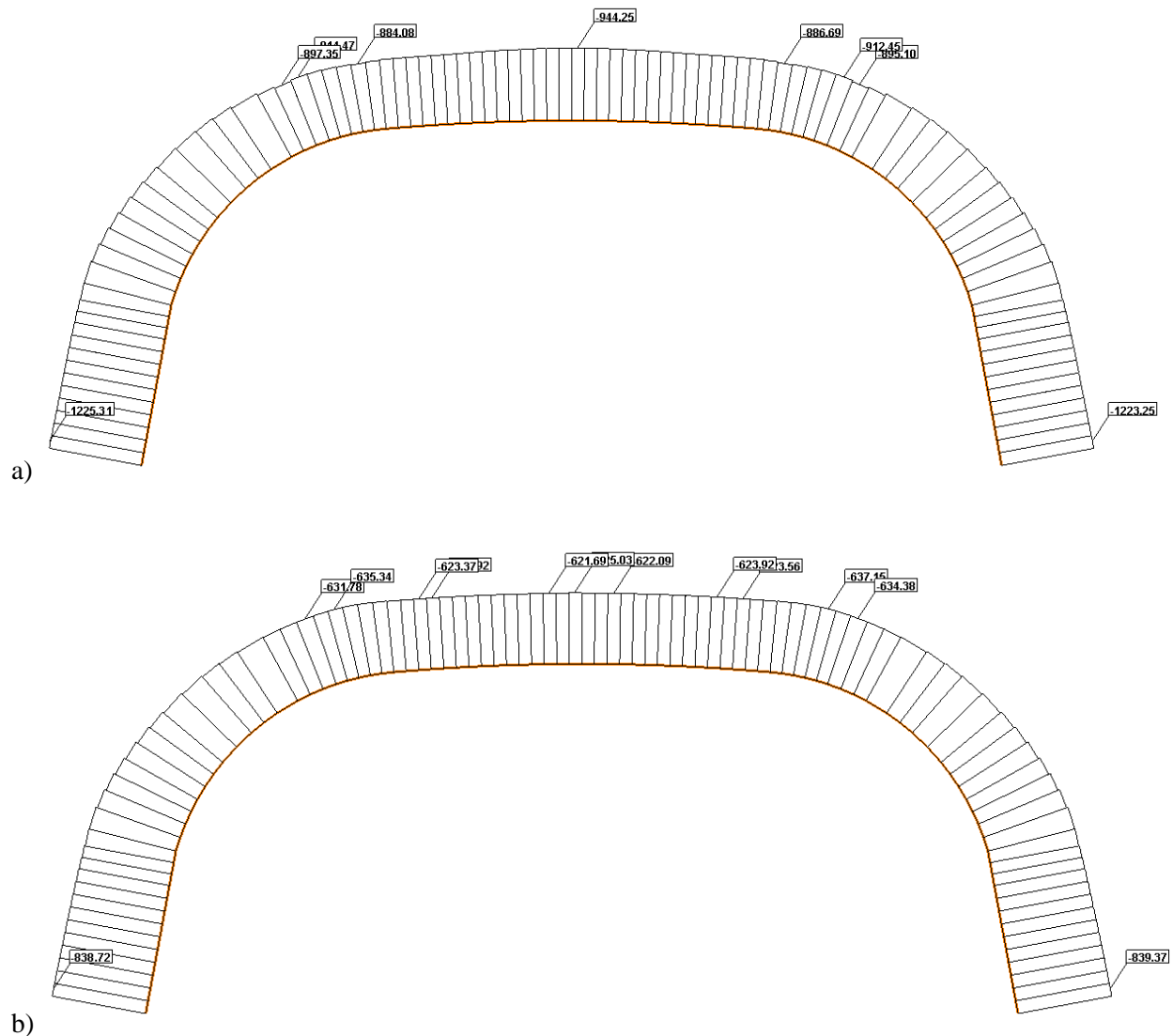


Figure 5.19: Maximum axial thrust distribution on the shell of geotextile reinforced SSCS under ultimate load; a) Model-III b) Model-IV.

Furthermore, it's worth noting that the maximum thrust value for Model-III, 1225 kN/m, accounts for 78% of the theoretical crushing load, which is calculated to be 1575 kN/m. In the case

of Model-IV, this value represents 53% of the theoretical crushing load. The theoretical load signifies the thrust required to induce compressive yield across the entire cross-section.

Additionally, the introduction of geotextile contributes to structural stability. It acts as a stabilizing agent, mitigating deformations that could compromise the integrity of the composite structure. This aligns with prior research [94], which emphasizes the stabilizing role of geotextile in analogous applications.

In both models, with and without geotextile reinforcement, two critical zones were observed based on the bending moment distribution that induce maximum compressive and tensile stresses. The identified critical zones are the crown, shoulder, and haunch sections of the shell. On the research conducted by [135], on large span structure, similar finding was observed both in field test and numerical simulation. Furthermore, the critical force due to global buckling were estimated using the methodology presented by Pettersson [16]. However, the induced normal force in the shell has kept much less than the critical value for the entire course of simulation. That fact indicates that the global buckling of the shell is not likely to occur.

5.6. Summary

In this chapter, numerical analysis was employed to examine the failure modes of box-type soil-steel composite structures under ultimate load conditions. The numerical analysis was based on 2D nonlinear finite element analysis validated with full-scale test of soil steel composite structure during both backfilling and under ultimate load. Due to the flexible nature of the structure with anticipated substantial deflection, the numerical model incorporated a large deformation mode at all simulation stages. The material and contact nonlinearity were included in the numerical simulation. The numerical models presented in this study highlight the substantial impact of stiffening ribs and geotextile reinforcement of the backfill on the bearing capacity of soil-steel composite structures. The results reveal that reinforcements substantially enhance the load-bearing capacity, with geotextile placement in the upper part of the backfill effectively reducing shell deflection due to bending. However, it is important to note that the findings of the study are limited to the assumptions and methods described in the thesis. The main conclusions drawn from the numerical simulations conducted are as follows:

- The FE model accurately predicts displacements in the shell during construction but slightly underestimates peak displacements (both upward and downward) by around

- 11% compared to field measurements. The maximum upward and downward vertical deflection of the shell during construction were less than 0.1% of the structure rise, which is in agreement with the requirements of CHBDC (CSA 2019) code limit of 2%.
- The addition of a stiffening rib at the crown section enhances the structure's load-bearing capacity by 47%, while the utilization of a single layer of geotextile reinforcement contributes to an approximate 26% increase in load-bearing capacity.
 - The structures with stiffening ribs reach their load carrying capacity due to creation of a plastic hinge at the shell's shoulder and haunch. On the other hand, in the structures without stiffening ribs the crown and haunch sections of the shell becomes fully plastic under peak load.
 - For both structures, reinforced and unreinforced by geotextile, under peak load the maximum axial thrust is not reached the maximum capacity of the shell due to compression. Maximum axial thrust is shown in geotextile reinforced structure, reaching 78% of the shell maximum capacity due to compression.
 - The bending moment in structures reinforced by geotextile is increased by 8%, and the bending capacity of the shell is not reached at the haunch section, in contrast to unreinforced structures.
 - Asymmetry in bending moment distribution is evident in Model-I and Model-III, contrasting with the nearly symmetrical distribution in Model-II and Model-IV. This asymmetry results from the influence of the stiffening rib on redistributing bending moments before failure. Additionally, plastic hinge development is prone at both ends of the stiffening rib, with Model-I exhibiting it on the left side. Notably, an equivalent risk of collapse exists on the right side, as demonstrated in Model-III.
 - The potential impact of local buckling may not be comprehensively addressed due to adopting the two-dimensional model. Nevertheless, an assessment of critical forces associated with global buckling was conducted, and the induced normal force in the shell consistently remained well below the critical value throughout the entire simulation. This observation suggests that the occurrence of global buckling in the shell is highly unlikely.

As the analysis performed showed a significant improvement in load capacity due to the application of geotextiles, the following chapter explores their usage in more detail. Specifically,

an analysis was conducted on the impact of positioning geotextile layers at different locations within the soil cover above the shell crown. This analysis focused on evaluating the mechanical behavior of SSCSs during the construction stage and under external loads. Additionally, the study examined the effects of employing a double layer of geotextile reinforcement.

6. Influence of geotextile soil reinforcement layout on the deformation of a model SSCSs

Geotextiles have garnered significant attention in recent scientific research due to their capacity to alleviate pressure on soil masses and buried structures. In the previous chapter, a thorough analysis of Soil-Steel Composite Structures (SSCSs) was conducted under ultimate load conditions. This analysis included an exploration of the impact of placing a single layer of geotextile at the central position of the soil cover above the shell crown on the behavior of the SSCSs. However, existing literature lacks detailed documentation regarding the optimal placement of geotextiles over the crown of SSCSs. Notably, studies such as those by Wysokowski [94], Jeyapalan, and Lytton [97], Dai, *et al* [136], Vaslestad *et al* [96] and Maleska *et al.* [93] have examined the influence of a single layer of geotextile, primarily focusing on reducing displacements and stresses in the shell.

This chapter aims to bridge aforementioned gap by analyzing the effects of positioning geotextile layers at various locations within the soil cover above the shell crown on the mechanical behavior of SSCSs under different static loads. Furthermore, the study delves into the effects of utilizing a double layer of geotextile reinforcement. Subsequent discussions in this chapter will present numerical simulations showcasing the results of deformation and stresses in the SSCS shell when the backfill is reinforced by geotextile at different locations in the soil cover over the crown. A comparative analysis will be provided to contrast results obtained with and without geotextile reinforcement. Importantly, the structure considered in this analysis shares a similar geometry with that studied in Chapter 5, ensuring continuity and validation of the input parameters using the ZSoil FEA numerical program. The geometry of the structure is shown in Fig. 6.1.

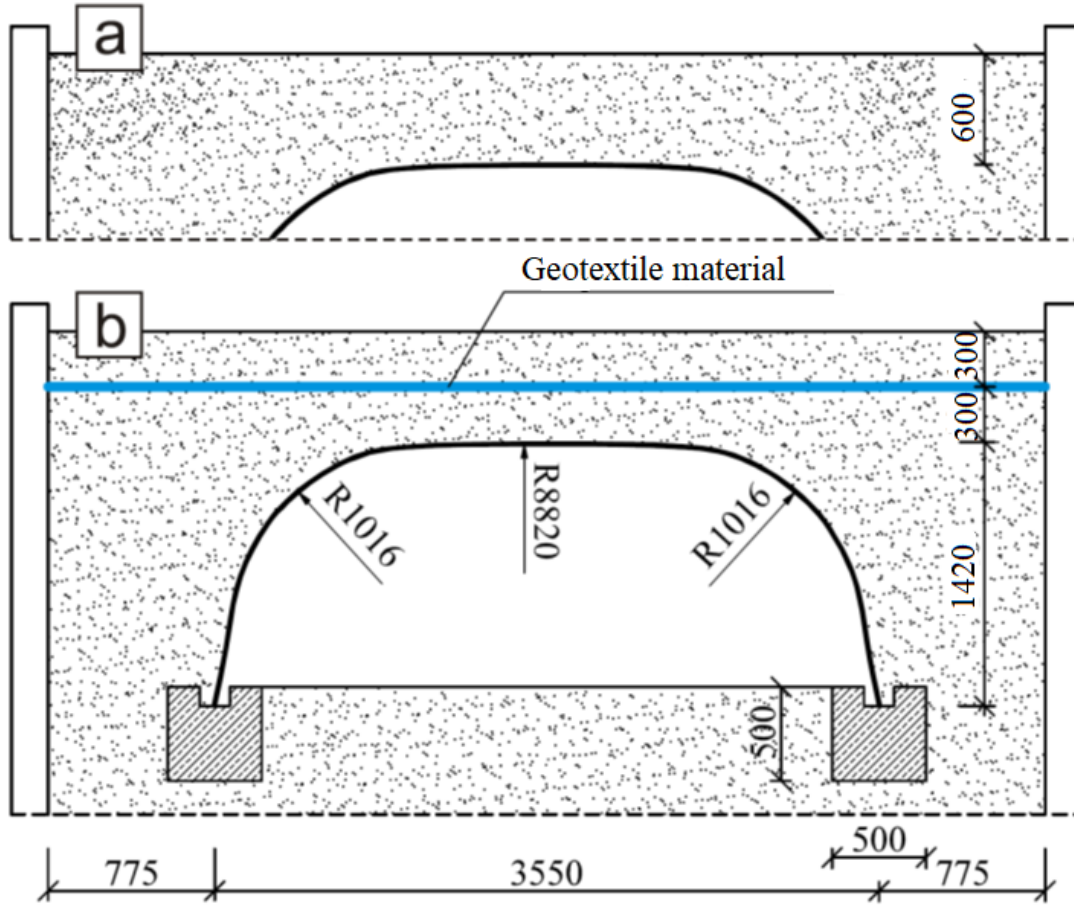
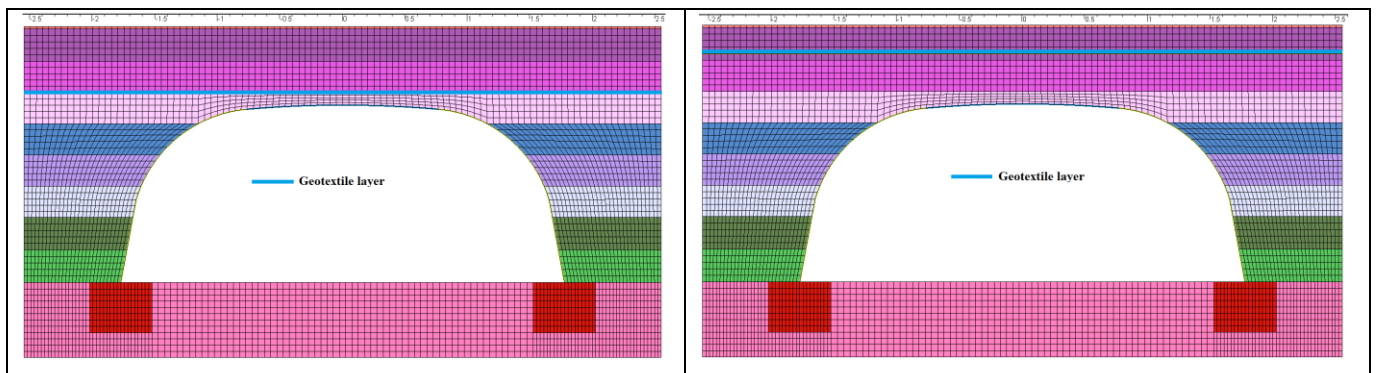


Figure 6.1: Model of SSCS a) without reinforcement, b) with geotextile at the centre of the soil cover

6.1. Numerical Modelling

For the analysis, six models were prepared by placing geotextile at different positions. The finite element mesh and location of the single layer of geotextile is shown in Figs. 6.2 (a–e). Additionally, another model is prepared by placing two layers of geotextile at different positions, as illustrated in Fig. 6.2 (f).



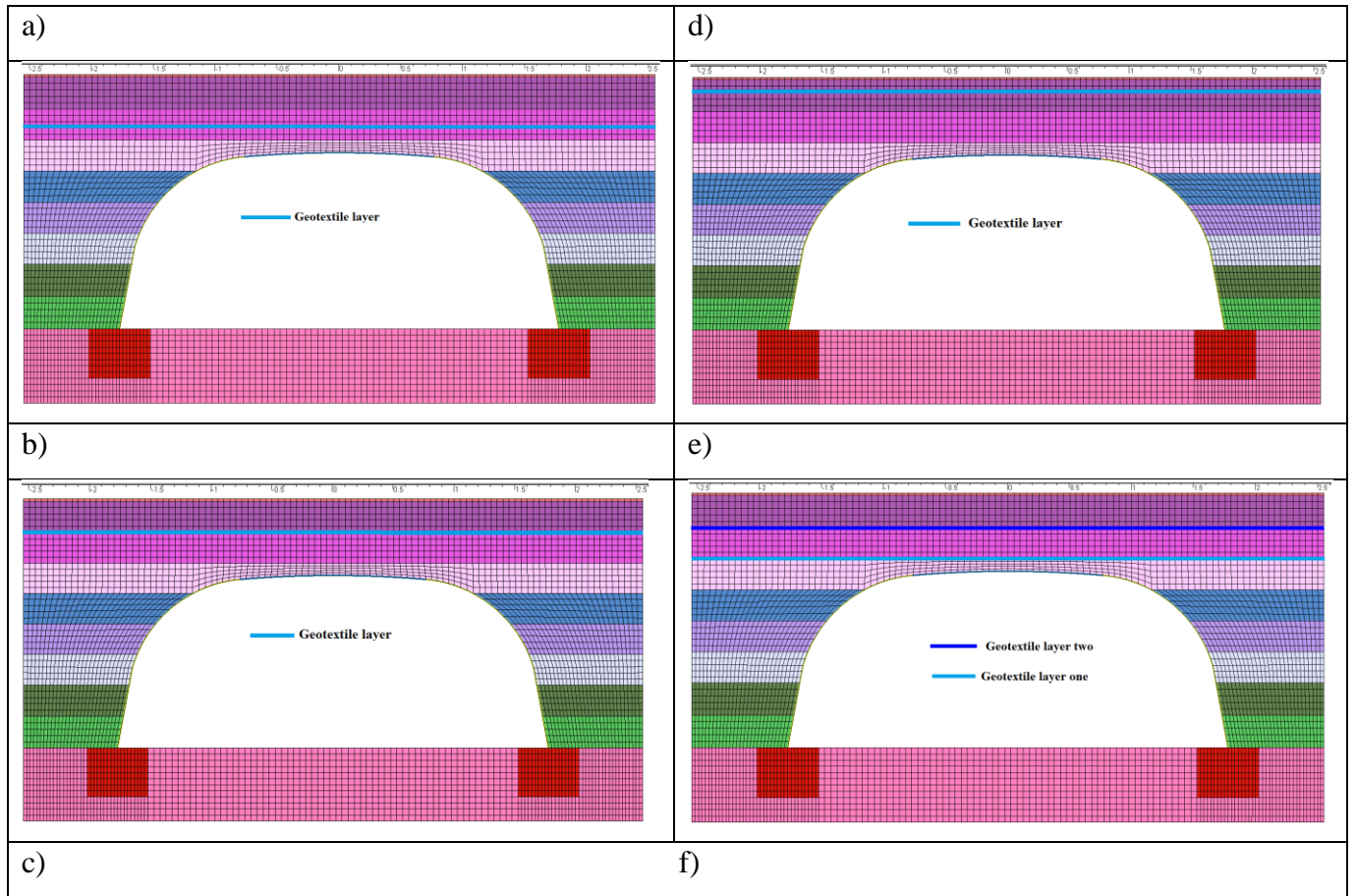


Figure 6.2: Position of geotextile: a) Model I, b) Model II, c) Model III, d) Model IV, e) Model V, f) Model VI

The summary of the models and their respective locations is presented in Table 6.1.

Table 6.1: The position of geotextile in the soil above the crown of the shell.

Model	The position of the geotextile
Reference	Without geotextile
Model-I	0.1 m above the crown of the shell
Model-II	0.2 m above the crown of the shell
Model-III	0.3 m above the crown of the shell
Model-IV	0.4 m above the crown of the shell
Model-V	0.5 m above the crown of the shell
Model-VI	0.1 m and 0.3 m above the crown of the shell

The 2D analyses were performed step by step, starting with placing the shell on $0.50 \text{ m} \times 0.50 \text{ m}$ concrete footing with backfilling. After placing each backfill layer, a compaction load, which was related to the actual soil compaction process, was simulated as a surface load. This compaction load is symmetrical with respect to the vertical axis of the structure. The compaction load at a fifth layer of the model is shown in Fig. 6.3. Once the final layer of fill has been placed over the top of the structure, loads are applied to simulate the behavior of the structure under different static loads, including the ultimate load. According to [125], the effect of shell prestressing can be reproduced by taking into account staged backfilling. This will help to reproduce the real behavior of the structure under different loading conditions.

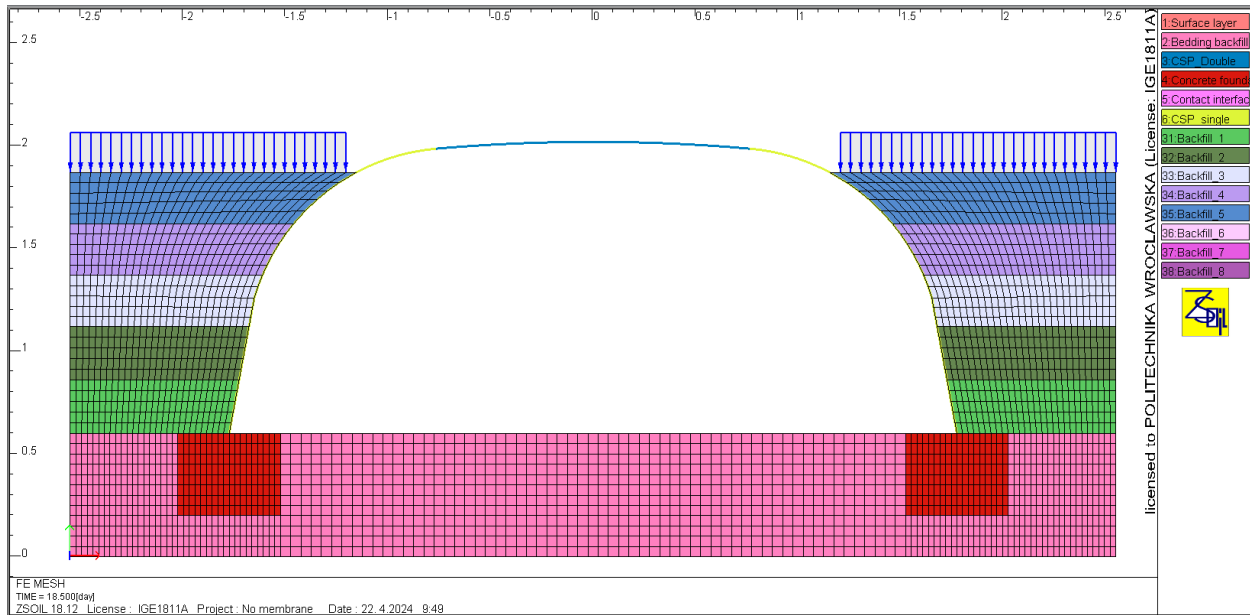


Figure 6.3: Backfill and compaction load in the fifth layer of the model.

6.2. Effect of geotextile at construction stages

The presented numerical model demonstrates that the behavior of the shell structures during the backfilling process is complex. As the number of layers increases, the displacement values and signs change. This finding is consistent with the results of Korusiewicz and Kunecki [99], who conducted a full-scale test to investigate the mechanical behavior of the SSCS during backfilling. Furthermore, in the numerical model, when the single layer of geotextile was placed at the center of the depth of soil cover, the vertical displacement during backfill was reduced by 22 % (see Fig. 6.4). The maximum reduction in vertical displacement occurred when the geotextile was

placed at a shallower depth (closer to the zone of influence of the load), specifically at 0.5 m above the crown of the shell, where the reduction reached 37%.

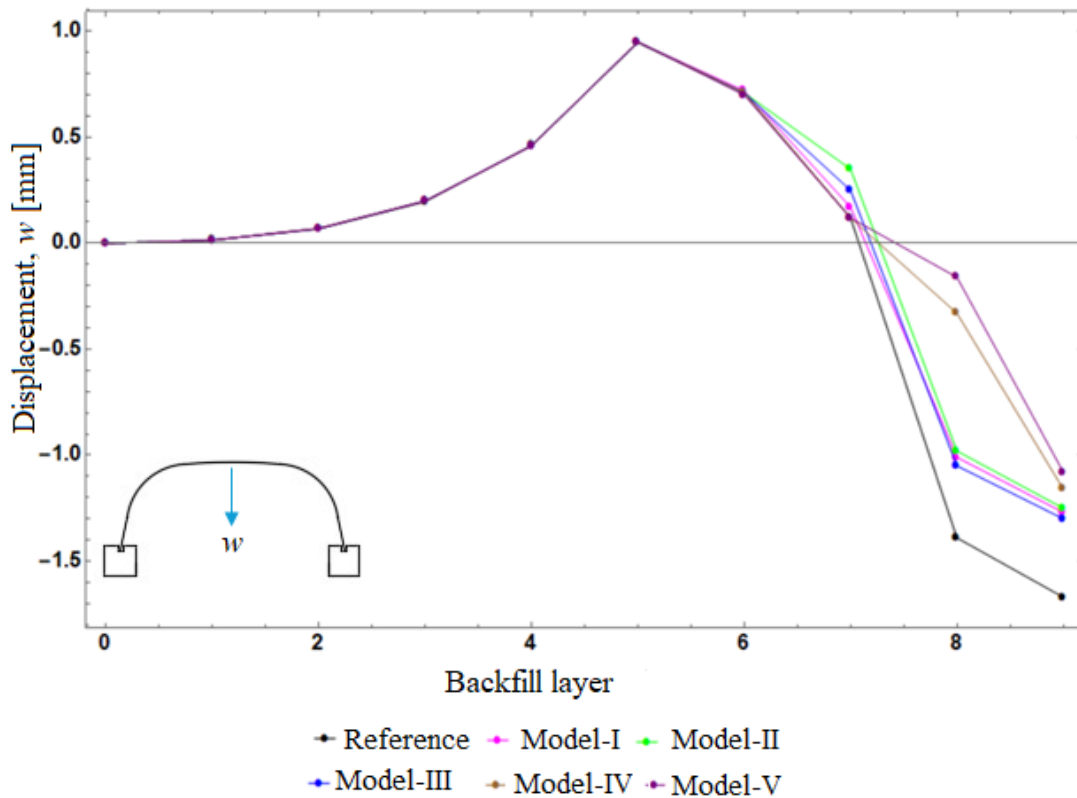


Figure 6.4: Vertical displacement at the crown of the shell during backfilling by placing geotextile at different position above the crown of the shell.

Following the investigation into the impact of a single layer of geotextile on the deformation behavior of the shell during the backfilling and compaction process, the study proceeds to examine the effects of positioning two layers of geotextile at varying locations. In Model-VI (shown in Fig 6.2(f)), one layer of geotextile is strategically positioned 0.1 m above the crown of the shell, while the second layer is situated at the center of soil cover, 0.3 m above the crown of the shell. This configuration aims to evaluate the influence of double reinforcement on the shell's deformation behavior, which is subsequently analyzed and visualized in Fig. 6.5.

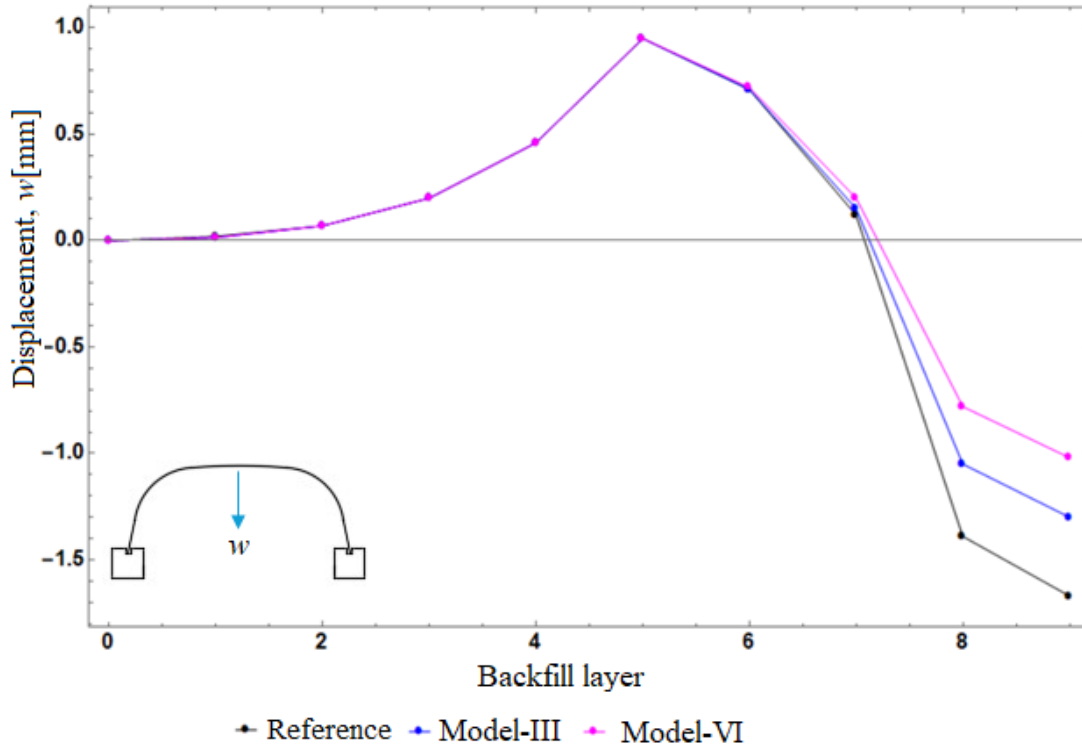
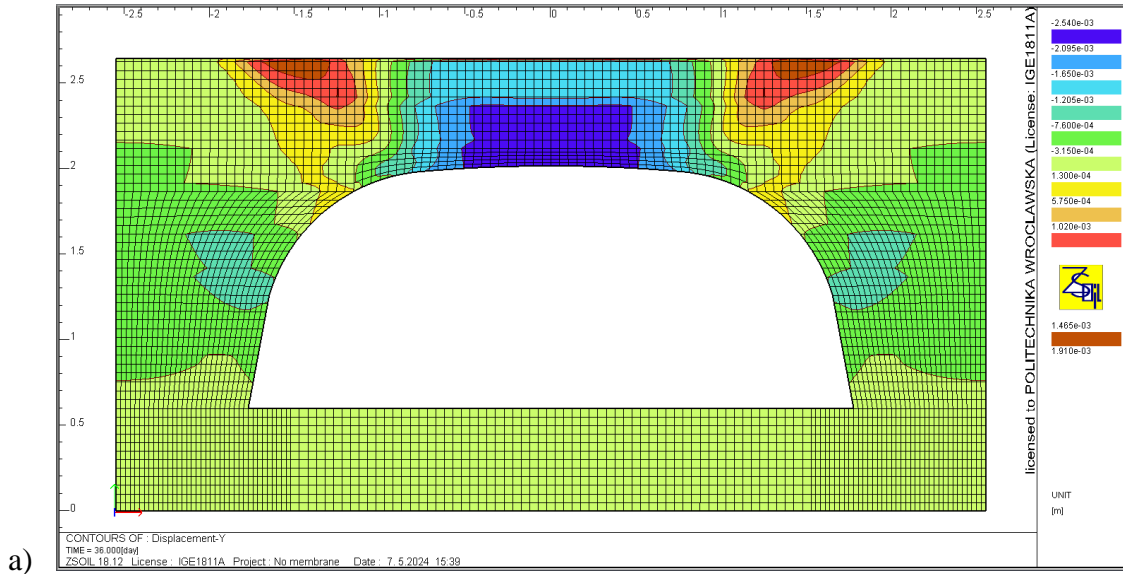


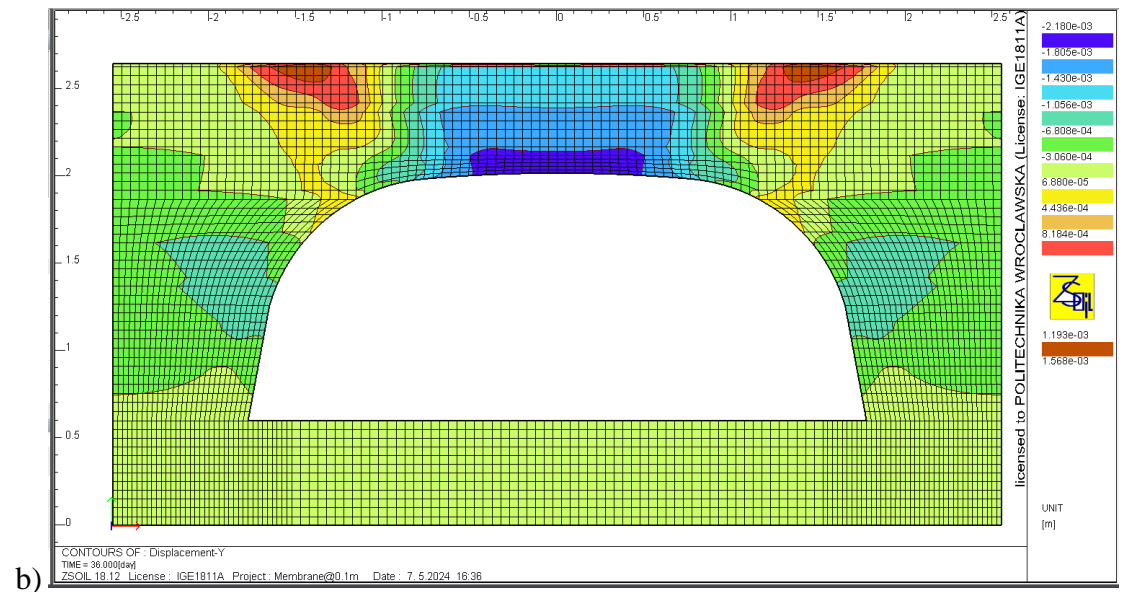
Figure 6.5: Effect of double membrane on the vertical displacement of the shell at the crown during backfilling.

By doubling the geotextile layer, a significant improvement in the structural performance is achieved. As shown in Figure 8, there is a notable 40% reduction in vertical displacement compared to the unreinforced structure. Additionally, when compared to the single-layer reinforcement scenario, a substantial 22% reduction in vertical displacement is still observed. These findings emphasize the effectiveness of employing a dual-layer geotextile reinforcement strategy for enhancing structural stability.

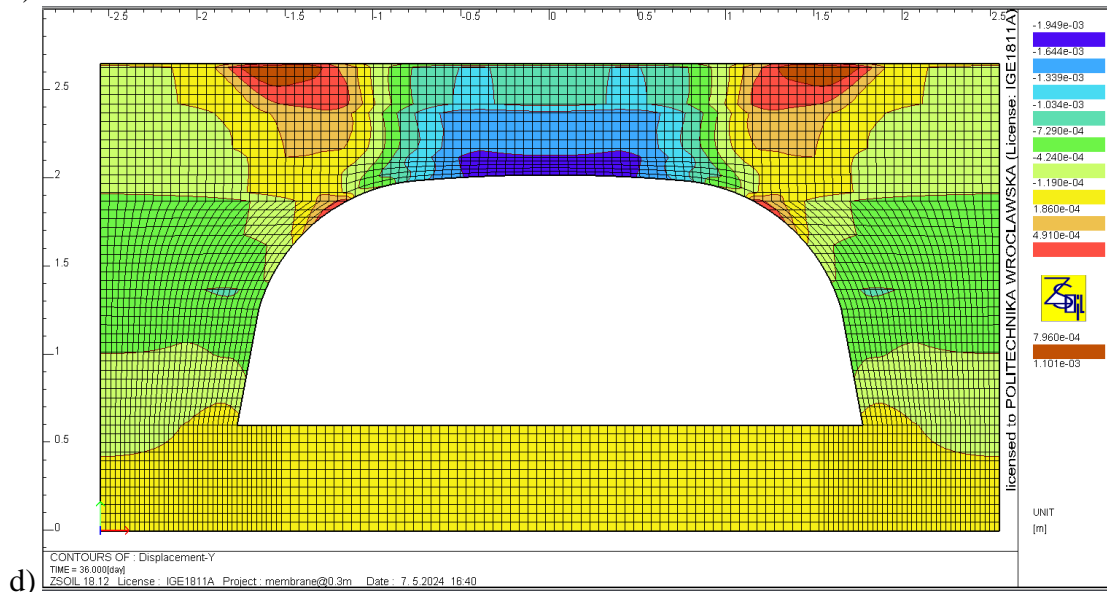
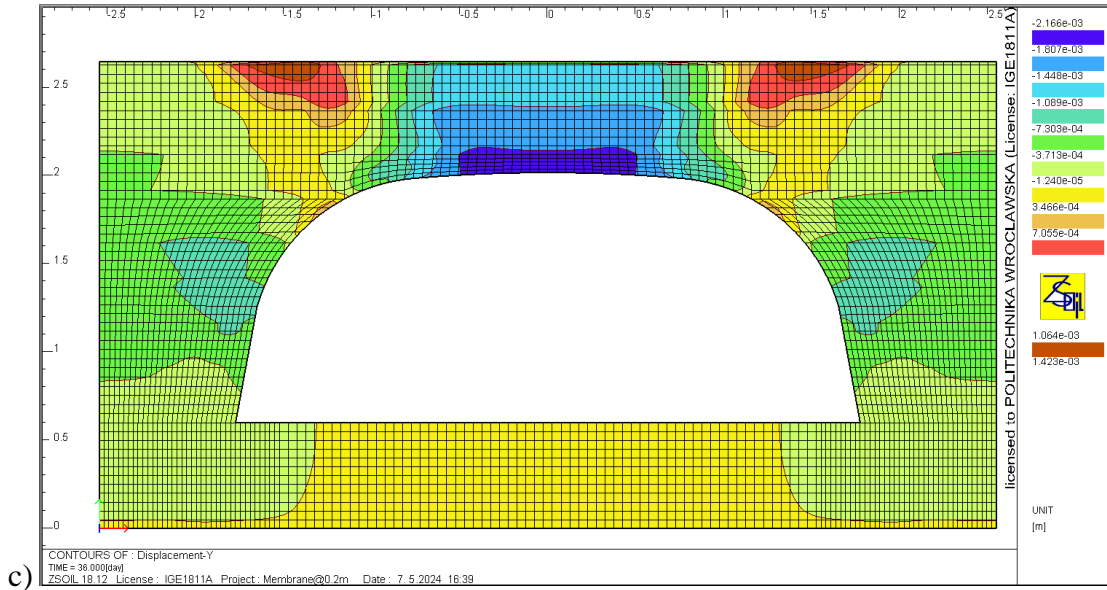
Figure 6.6 shows the vertical deformation of the backfill at the end of backfilling and compaction. The highest vertical soil deformation occurs near the top of the shell, corresponding to the peak deformation observed during backfilling at that location. Importantly, the effectiveness of geotextile reinforcement layer on the vertical deformation of the backfill is evident. The extent of deformation in the unreinforced scenario is greater compared to the reinforced case. The most significant reduction in vertical soil deformation occurs when reinforcement is placed at shallow depths, as demonstrated by Model-IV and V.

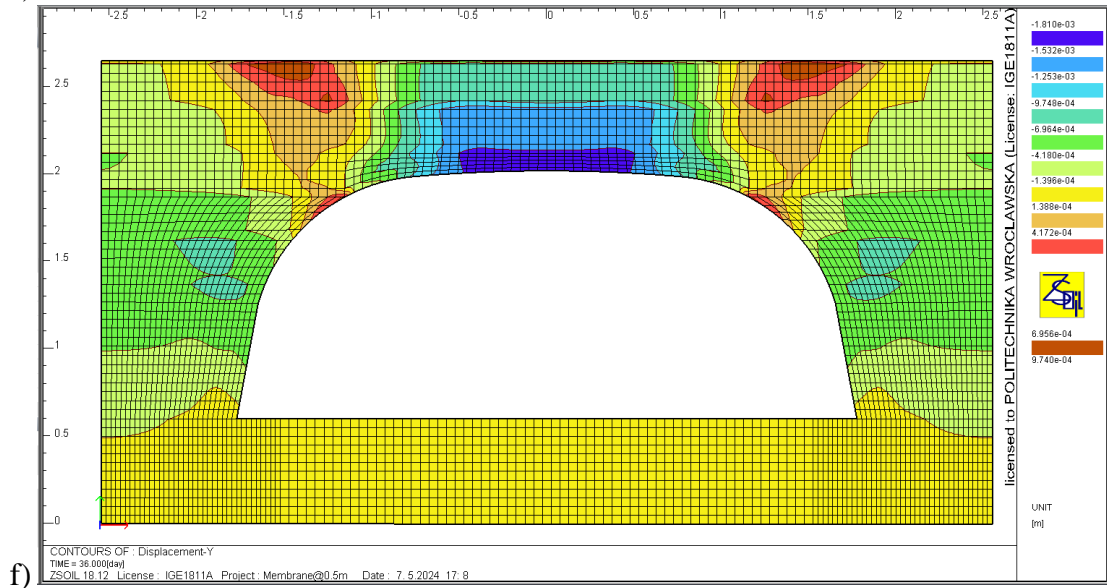
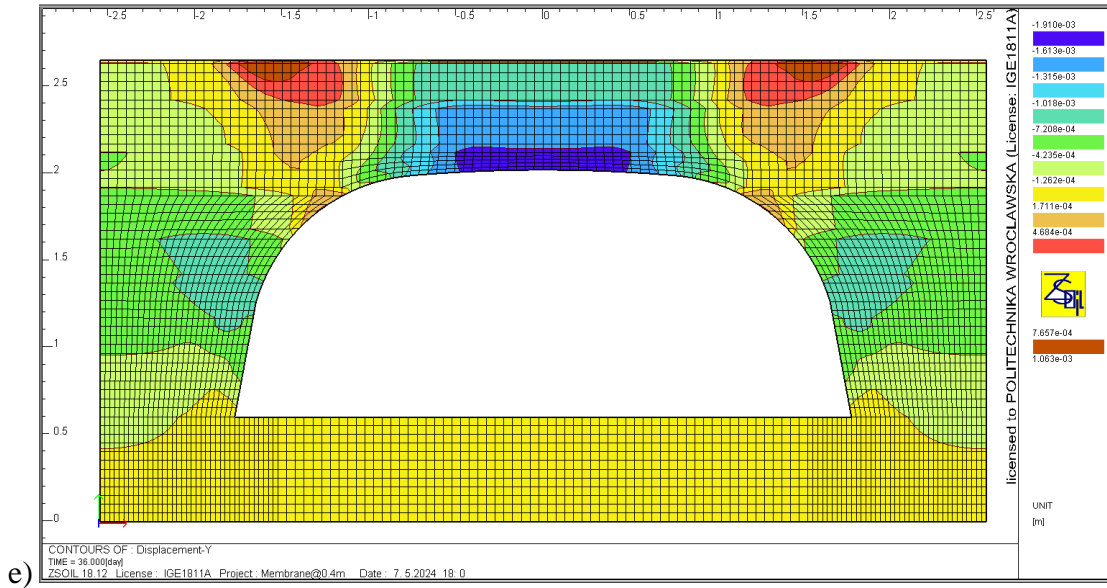


a)



b)





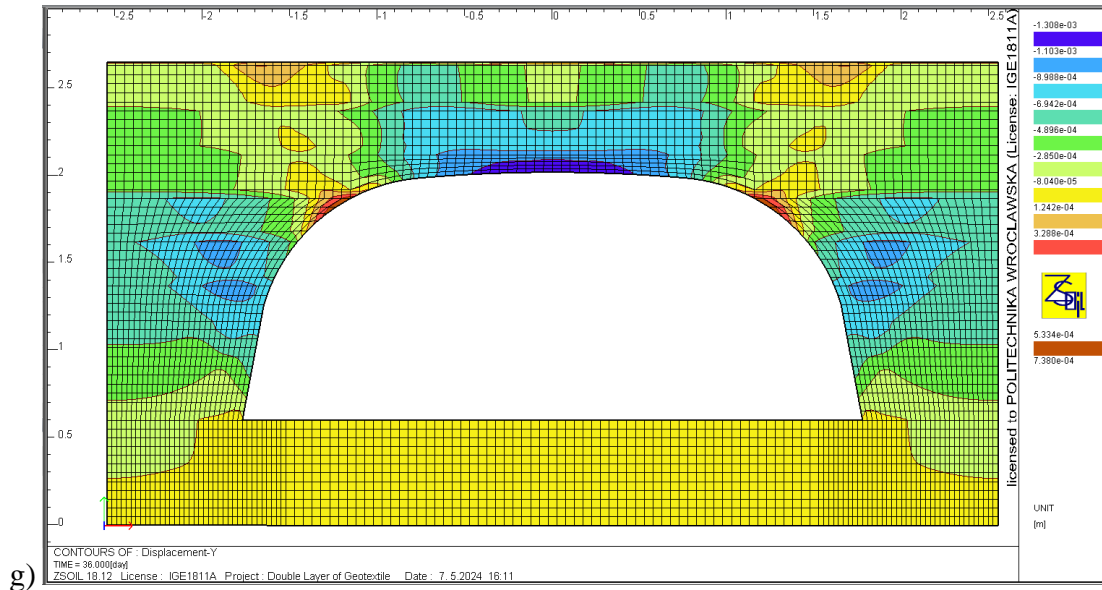


Figure 6.6: Distribution of vertical deformation of the soil: a) Reference, b) Model I, c) Model II, d) Model III, e) Model IV, f) Model V g) Model VI.

Furthermore, the use of two layers of geotextile as reinforcement demonstrates a significant reduction in vertical deformation in the soil around the crown of the shell. Comparative analysis with the unreinforced scenario, employing double reinforcement, reveals a noteworthy reduction of approximately 49% in peak vertical deformation near the top of the shell (See Figs. 6.6 (a) and (g)). This finding underscores the effectiveness of double geotextile reinforcement in mitigating soil deformation in SSCSs. This observation aligns with a study conducted by HaiYing *et al.* [136] on the behavior of shallowly buried SSCSs reinforced by a single layer of geotextile. Their study also noted a reduction in vertical deformation in the backfill when reinforced by geotextile compared to the unreinforced condition. These findings collectively highlight the positive influence of geotextile reinforcement on minimizing soil deformations in SSCS structures, thus emphasizing the practical significance of geotextiles in civil engineering applications.

6.3. Effect of geotextile subjected to external load.

The structure previously analyzed during the construction stage in section 6.2 was subjected to a static load of 1512 kN. Following the application of this load, the vertical displacement at the crown of the shell was extracted for all considered models to evaluate the structural behavior and deformation characteristics. Upon analysis and comparison of the results, it was observed that the

incorporation of a single-layer geotextile at various positions within the soil cover significantly influenced the vertical displacement of the crown of the shell structure. Notably, Fig. 6.7 illustrates the substantial reductions in maximum vertical displacement, ranging from 17% to 21%, when a single-layer geotextile placed at different positions.

The most notable reduction in vertical displacement occurred when the geotextile was positioned near the top of the soil cover, as seen in Model-V, or in close proximity to the load application point, approximately 0.5 m above the crown of the shell. The placement of geotextile near the load application point is crucial as it effectively redistributes stresses and mitigates overstressing effects on the shell structure. By introducing reinforcement at these positions, the structure demonstrates improved performance and enhanced load-carrying capacity.

Conversely, when the geotextile was placed at a closer distance to the shell, such as at 0.1 m (Model-I), a notable but slightly lesser reduction of 17% in displacement was observed. This observation highlights the sensitivity of reinforcement effectiveness to its placement within the soil cover.

Placing the geotextile further away from the shell and closer to the loading surface, as seen in Model-V, aligns with finding was obtained by [95]. In their work, it was reported that the reinforcement is more effective when placed at shallower depths. The effectiveness of reinforcement at shallower depths, as noted by previous studies, is attributed to the geotextile's capacity to strengthen the backfill soil and facilitate a more uniform distribution of loads. This redistribution of loads throughout the soil depth is crucial in maintaining structural integrity and minimizing localized deformations, ultimately enhancing the overall stability and performance of SSCSs under external loading conditions.

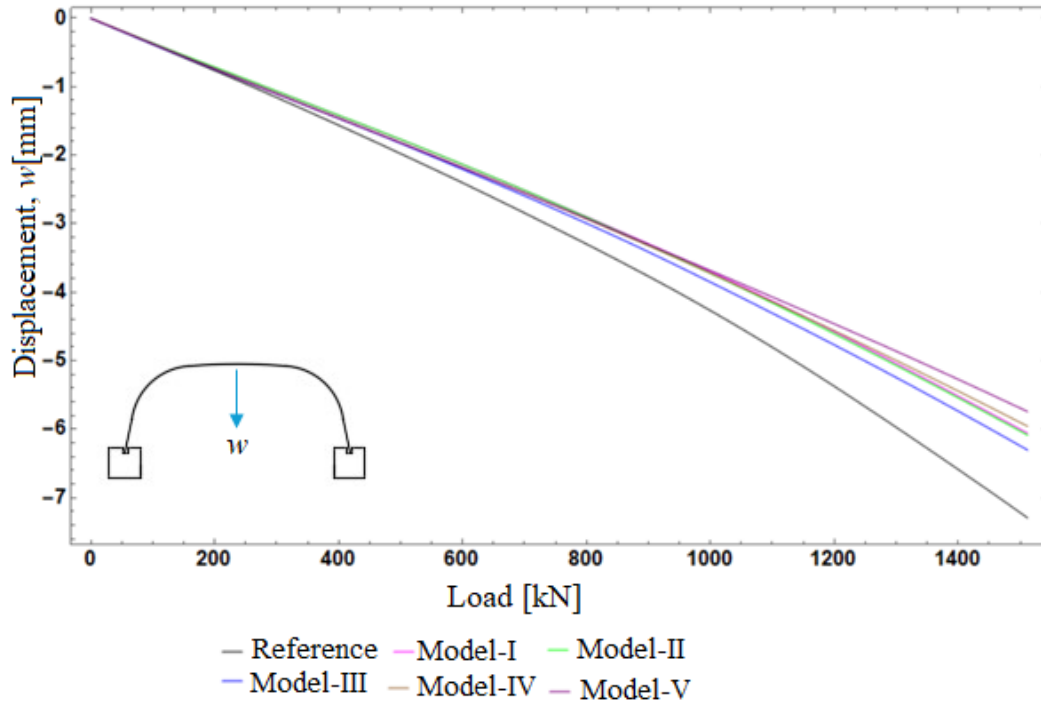


Figure 6.7: Vertical displacement at the crown of the shell by placing geotextile at different positions

In the case of stress values in shell at the crown of the structure, notable differences were observed between the reinforced and unreinforced structure. The maximum stress was reduced by 32 % when reinforcement was employed. Similar to the displacement, this maximum reduction was observed when the reinforcement was placed near the top surface, specifically at position 5, as illustrated in Fig. 6.8. According to [94], when the backfill soil above the shell is reinforced with a single layer of geotextile, the stress in the shell of the soil steel structure can be significantly reduced, with potential reductions of up to 40%.

The stress at the crown of the central shell, presented here as a numerical simulation result, was calculated based on Eq. (6.1):

$$\sigma_x = \frac{(N-N_0)}{A} + \frac{(M-M_0)}{I} \cdot \frac{h}{2} \quad (6.1)$$

Where N , M stands for the axial force and the bending moment, respectively, and N_0 and M_0 are the values of the axial force and moment for the calculated structure at the start of the calculation, I and A are moment of inertia and the cross section area respectively, while h is the thickness of the steel shell.

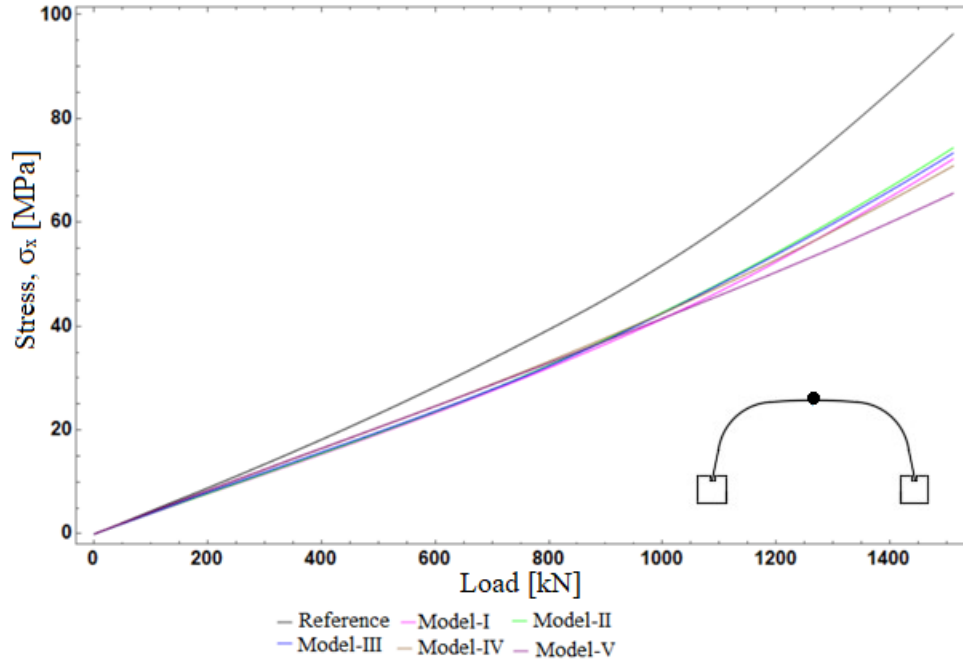


Figure 6.8: Stresses at the crown of the shell by placing geotextile at different positions

The conducted tests showed that a significant reduction in maximum stresses and displacements is observed with the application of a single-layer geotextile. Furthermore, analyses of the effect of the position of the geotextile layer clearly showed that the reinforcement is more effective when it is placed at a shallower depth (closer to the zone of influence of the load).

6.4. Effect of double layer of geotextile subjected to external load.

The model investigates the effect of reinforcing the structure with a double layer of geotextile. To investigate the influence of a double layer of geotextile, membranes were strategically placed at specific positions above the crown of the shell. In particular, membranes were placed at the center, precisely 0.3 m above the crown of the shell, and also at a position, 0.1 m above the crown, as depicted in Fig. 6.2(f), Model-VI. For comparison purposes, a single layer of geotextile reinforcement was also considered, positioned at the center, approximately 0.3 m above the crown of the shell (Model-III).

The comparative analysis revealed notable insights into the effectiveness of double geotextile reinforcement. When compared with single membrane reinforcement (Model-III), the vertical displacement at the crown of the shell demonstrated a reduction of 11% with the use of double

reinforcement, as illustrated in Fig. 6.9. This reduction indicates a significant improvement in structural stability and load-bearing capacity.

Furthermore, the study showcased that the reduction of vertical displacements at the crown can reach up to approximately 32% with the application of a double layer of membrane (Model-VI). This substantial reduction highlights the enhanced performance achieved through the strategic placement of double geotextile reinforcement, reinforcing the structure's ability to withstand external loads and minimize deformations.

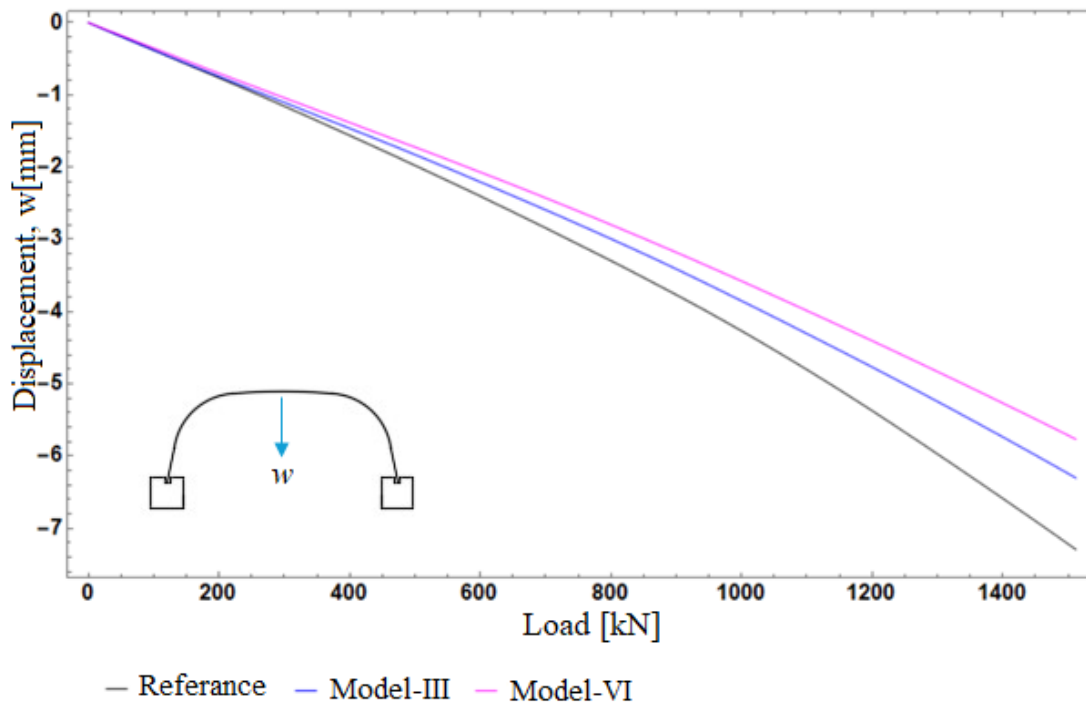
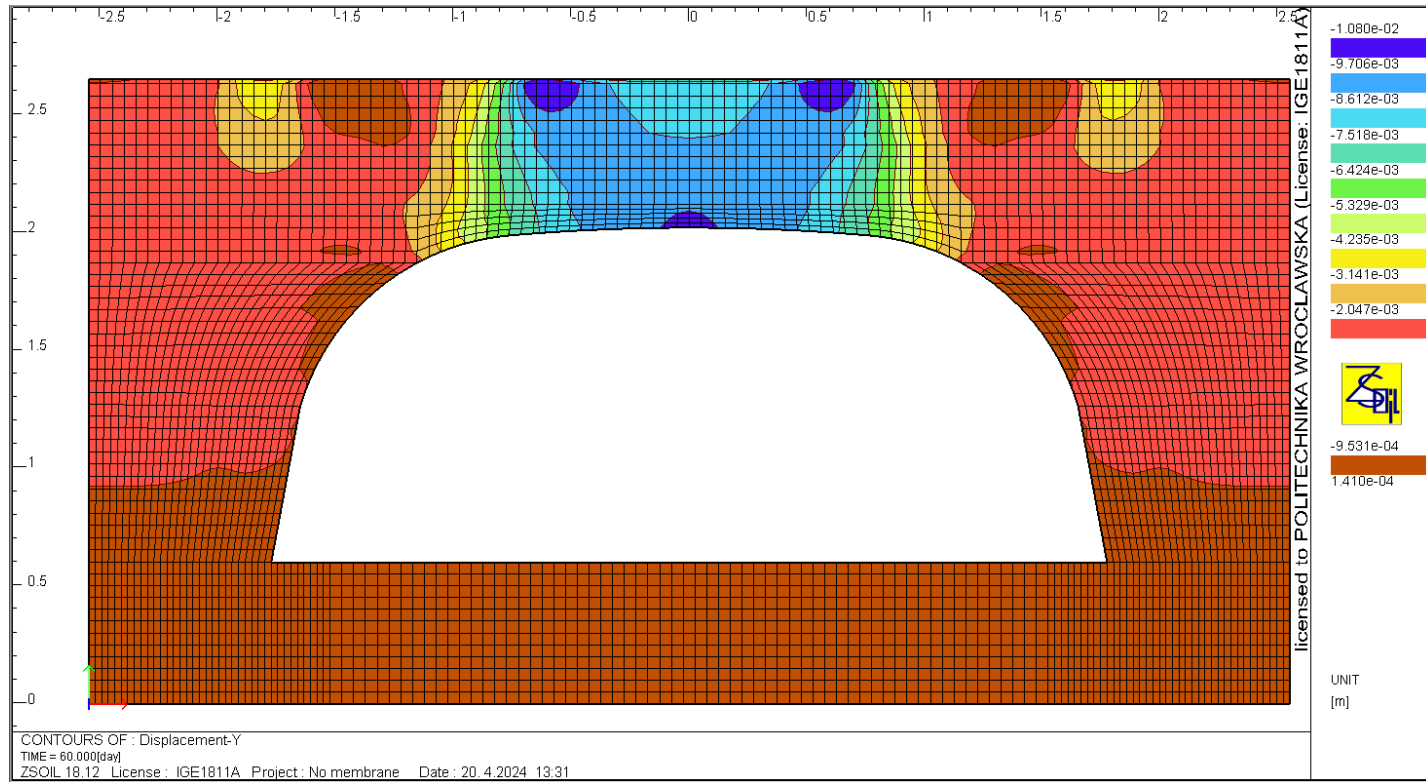


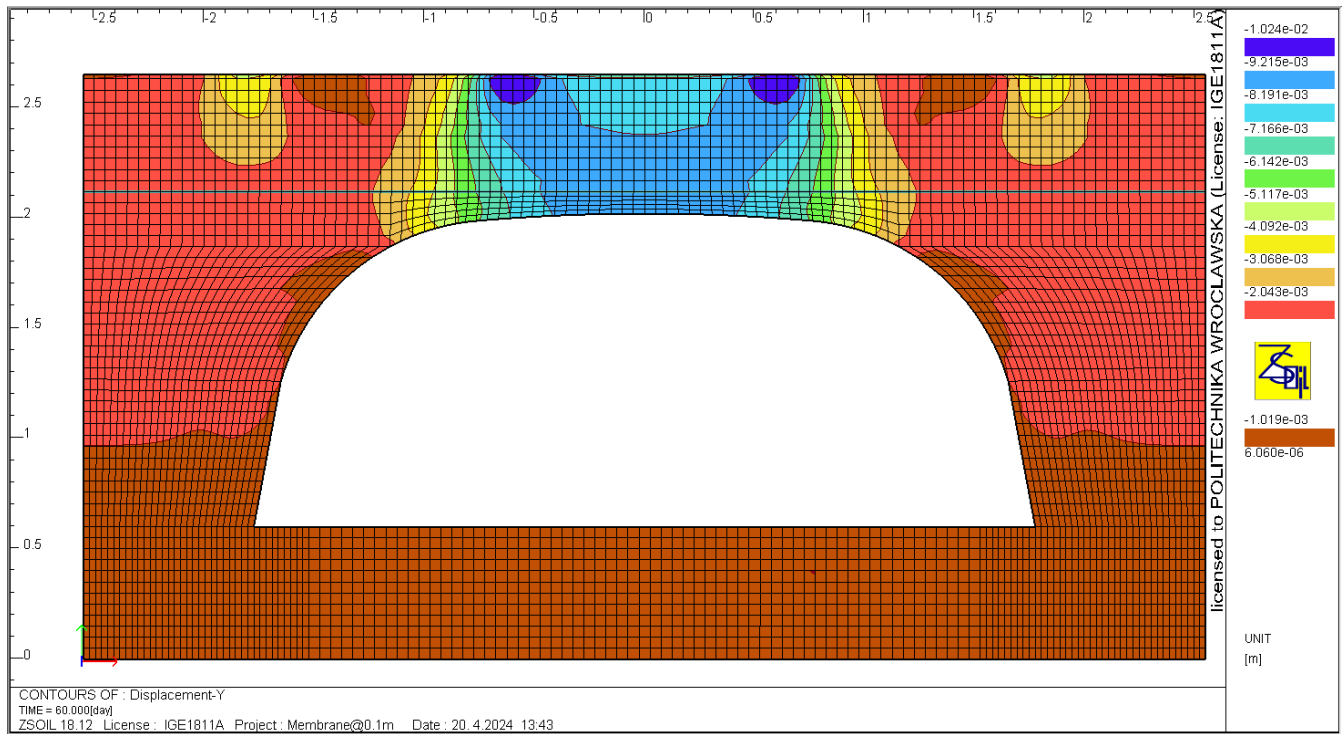
Figure 6.9: The influence of single and double layers geotextile on vertical displacement of the shell at crown

Fig. 6.10 shows the distribution of the vertical deformation of the backfill surrounding the shell under applied load. It is evident that the unreinforced structure, as showed in Fig. 6.10 (a), exhibits the highest deformation, whereas the scenario with a double layer of geotextile reinforcement, illustrated in Fig. 6.10 (g), demonstrates the least deformation. This underscores the notable effectiveness of the geotextile reinforcement layer in mitigating vertical deformation within the backfill. Notably, when evaluating the impact of a single layer of geotextile, the greatest reduction in vertical soil deformation occurs when the reinforcement is positioned at shallower depths, as clearly evidenced in Fig. 6.10 (f). Furthermore, the deformation of the backfill around the crown of the shell is significantly reduced with the use of geotextile. Overall, the analysis reveals a

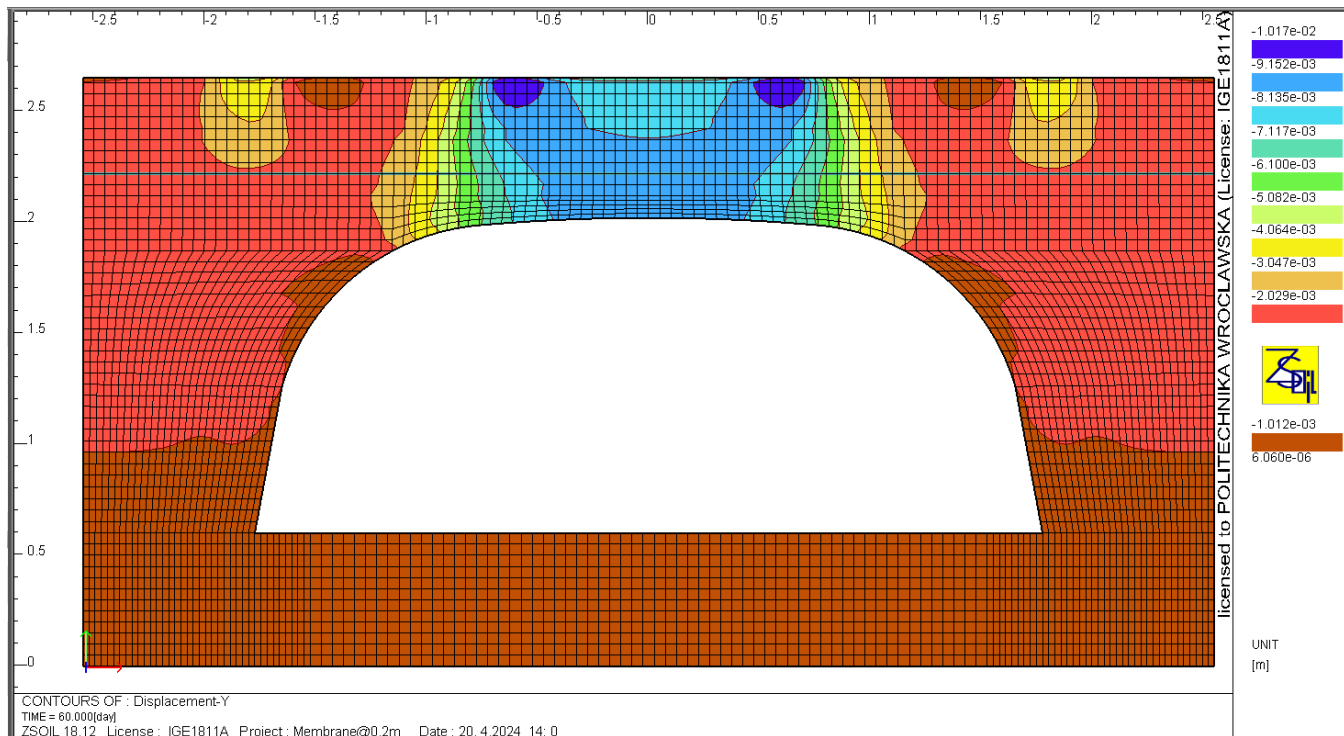
significant reduction in deformation around the shell when the backfill is reinforced with geotextile.



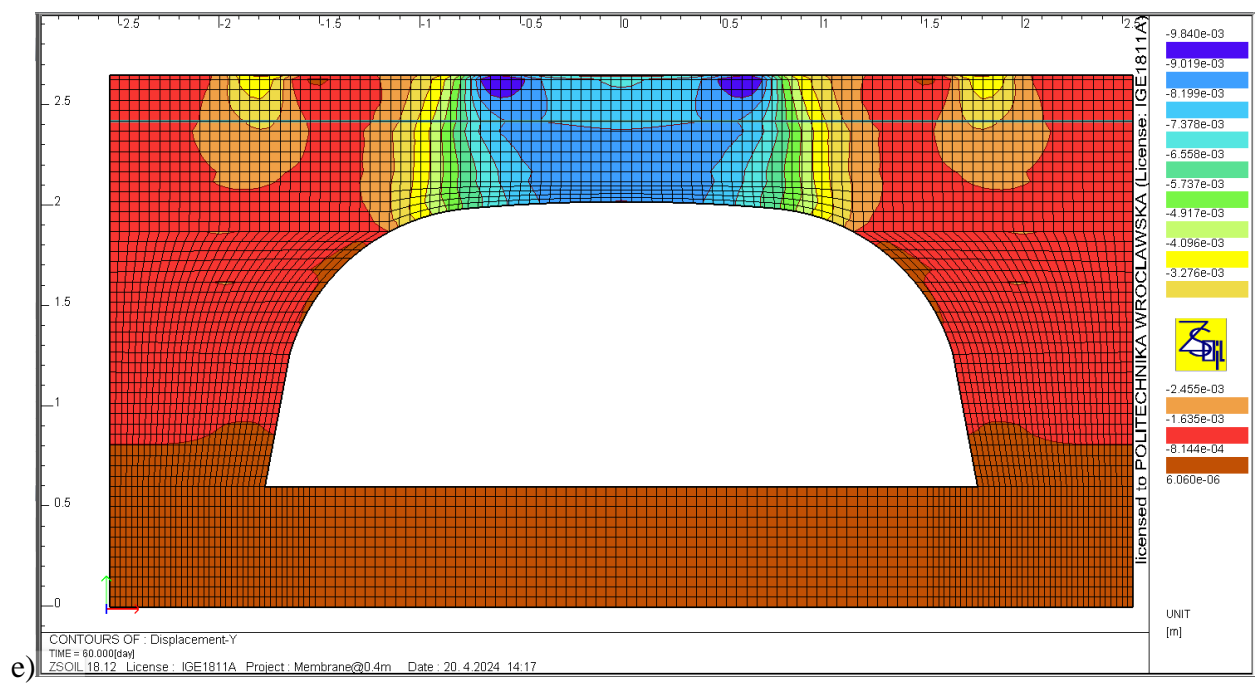
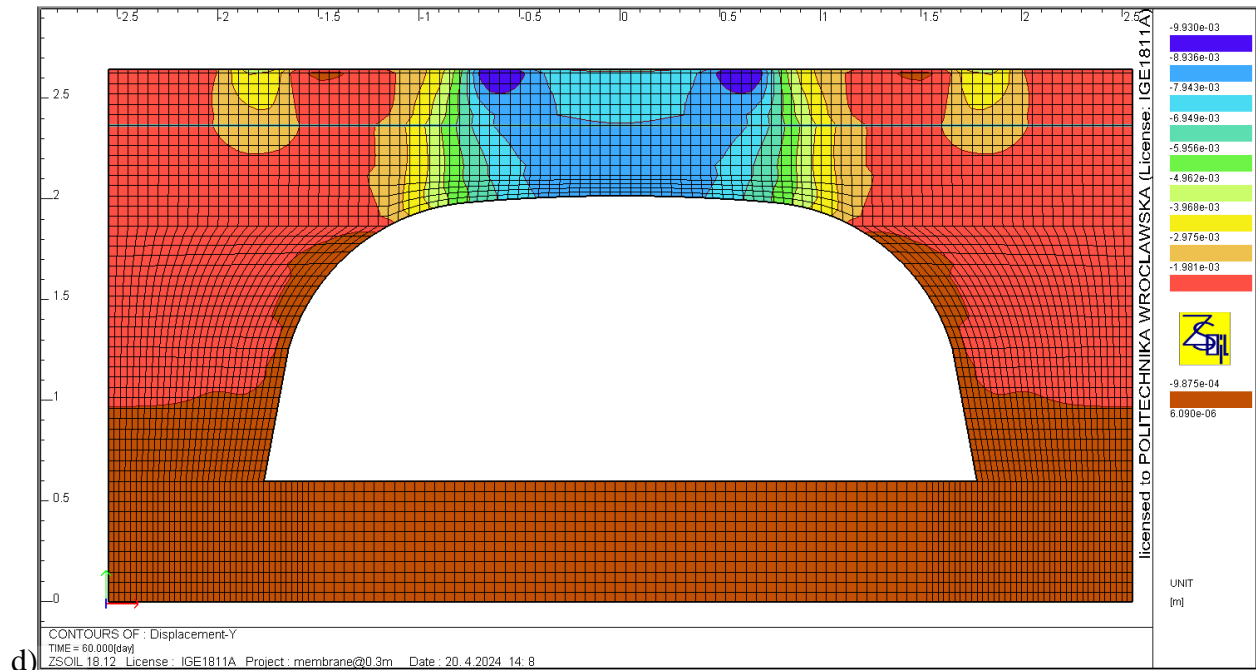
a)



b)



c)



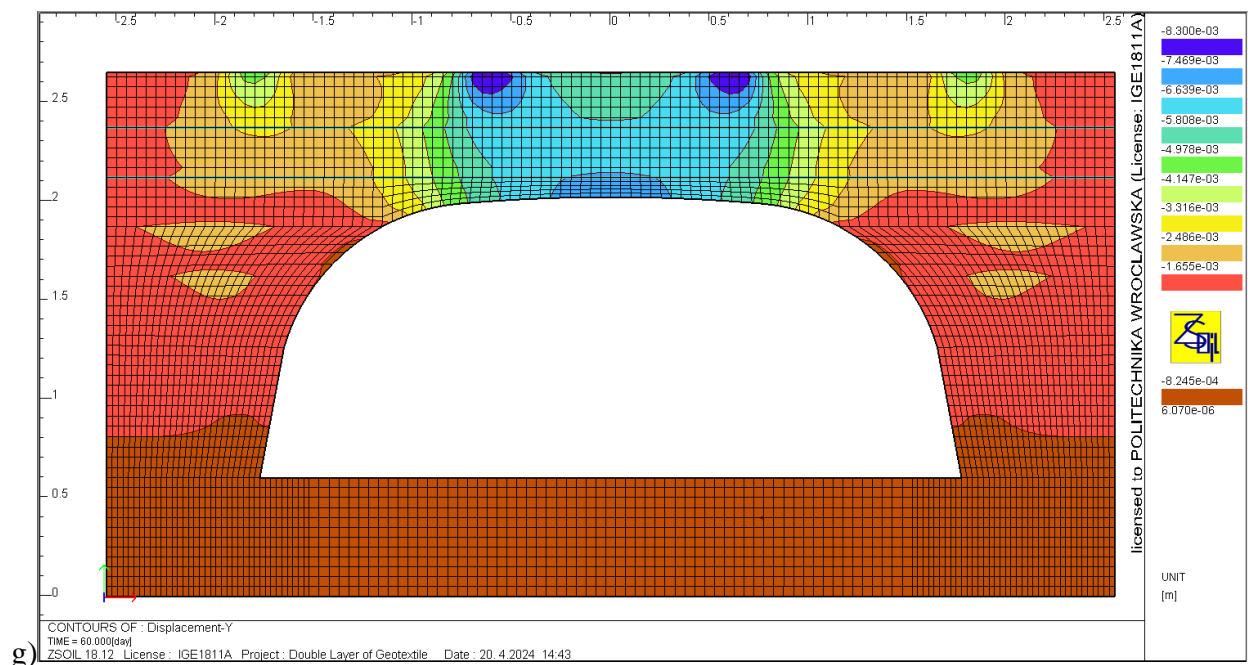
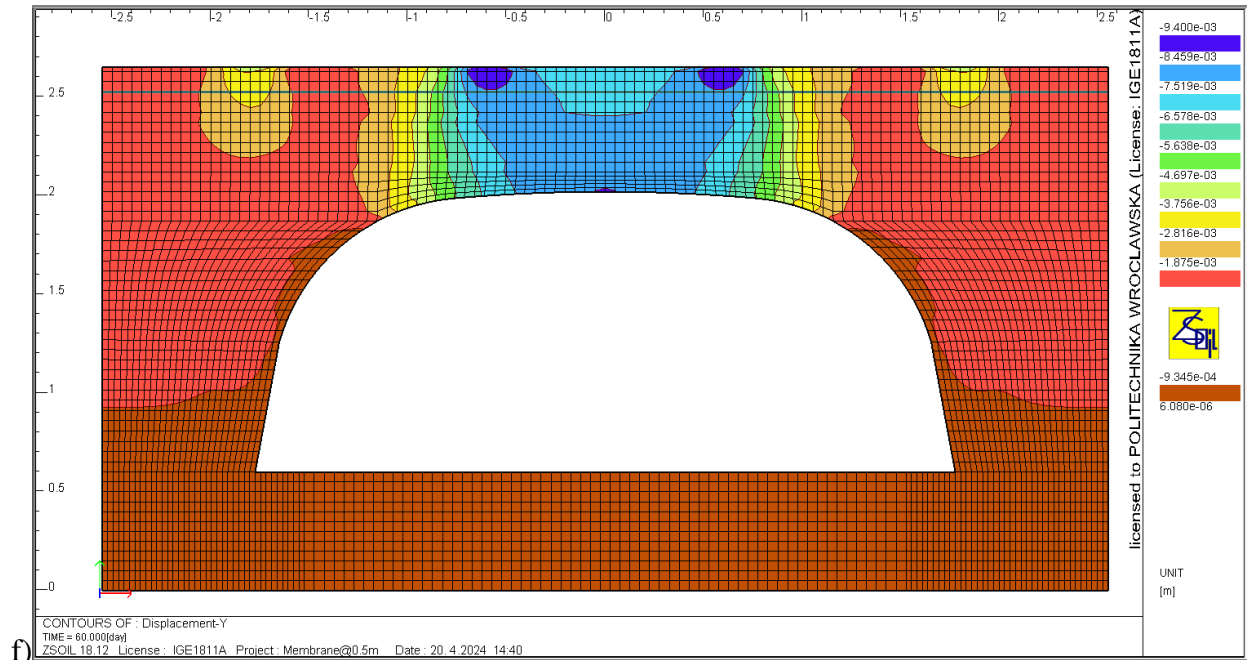


Figure 6.10: Distribution of vertical deformation of the soil: a) unreinforced, b) reinforced (Model I), c) reinforced (Model II), d) reinforced (Model III), e) reinforced (Model IV), f) reinforced (Model V) g) double reinforced (Model VI).

6.5. Summary

In conclusion, the findings from the conducted tests underscore the remarkable potential of geotextile applications in enhancing the structural stability of various systems. The implementation of a single-layer geotextile has demonstrated a noteworthy reduction in both maximum stresses and displacements, highlighting its efficacy in mitigating the detrimental effects of external forces. Moreover, the utilization of a double layer of membrane has proven to be particularly advantageous, showcasing an impressive fifty percent reduction in vertical displacements within the crown.

The significance of geotextile placement has also been highlighted through rigorous analyses. These investigations have clearly indicated that the positioning of the geotextile layer profoundly influences its reinforcing capabilities. Specifically, when situated at a shallower depth, closer to the load's zone of influence, the geotextile's ability to bolster the structural integrity becomes more pronounced.

Among the main conclusions of the analyses, the following should be briefly highlighted:

- When the single layer of geotextile is placed at the center of the depth of soil cover, the vertical displacement during backfill is reduced by up to 37 %.
- A significant reduction in maximum stress and displacement values is observed using single-layer geotextile. This reduction in vertical displacement at the crown can reach to fifty percent using a double layer of membrane.
- Geotextile is more effective when it is placed at a position of shallower depth that is nearby the loading surface.
- The effect of the reinforcement generally becomes more significant as the load increases.
- As it was presented in the previous chapter, the structure's load-bearing capacity is significantly improved using a single layer reinforcement. For economic reasons, it should be placed at the appropriate position.

These insights collectively emphasize the importance of thoughtful geotextile implementation in engineering and construction practices. By tailoring the placement and configuration of geotextile materials, designers and engineers can harness their potential to optimize structural performance and resilience. Continuing to explore innovative solutions for enhancing

infrastructural sustainability, these findings offer a valuable roadmap for harnessing the benefits of geotextiles. This can lead to the creation of safer, more resilient systems capable of withstanding a wide range of environmental pressures and loading conditions.

In the next chapter, the behavior of multi-span SSCSs were analyzed during construction stage and under ultimate load.

7. Behavior of multi-span SSCS under ultimate load: effect of shell spacing

In previous chapters, extensive analysis was conducted on the behavior of single-span soil-steel composite structures (SSCSs) under various loading conditions. Furthermore, there has been a notable surge in the adoption of multi-span SSCSs within the construction industry [85]. Numerous scholars have investigated this area, including a study that conducted numerical simulations on the performance of multi-span SSCSs during construction and operational stages under vehicle loads [85][87][88]. Findings highlighted an initial rapid increase in stress and deformation with load cycles, followed by stabilization.

Another notable research effort delved into the numerical analysis of a two-span SSCS under railway loads, demonstrating the impact of interactions between adjacent shells on internal forces [88]. Three different structural models with varying spacings between adjacent shells: 0.72 meters, 1.3 meters, and a model without an adjacent shell (single shell) were developed. Increasing the spacing between shells from 0.72 meters to 1.3 meters led to significantly lower values of internal forces, indicating a more efficient distribution of loads, and reduced cross-sectional forces on the structure.

Despite these advancements, research on the behavior of multi-span SSCSs under ultimate loads with variable lateral shell spacing remains limited. Therefore, the focus of the numerical simulations presented in this chapter is to study the behavior of multi-span soil-steel composite structures under ultimate load conditions. Specifically, the aim is to analyze the effects of spacing and loading positions on the deformation and internal forces of these structures.

This analysis considered three loading positions and five spacing between the shells. It examines the influence of lateral shells on the central shell and vice versa, comparing these effects with those observed in single-span structures. Subsequently, the exploration of the behavior of multi-span SSCSs under various loading conditions aims to understand how shell spacing affects their behavior and load-carrying capacity across different loading positions.

7.1. Spacing and load configuration

An investigation was conducted on a soil-steel composite structure with a span of 3.55 m, rise of 1.42 m and, with a soil depth of cover measuring 0.6 m. In the current model, to minimize the boundary effect, the two external lateral boundaries are located at length greater than the span of the structure. The span, rise and soil cover are shown in Fig. 7.1. The details of assumptions and parameters for shell and backfill used in this model are the same as the one described in Chapter 5.

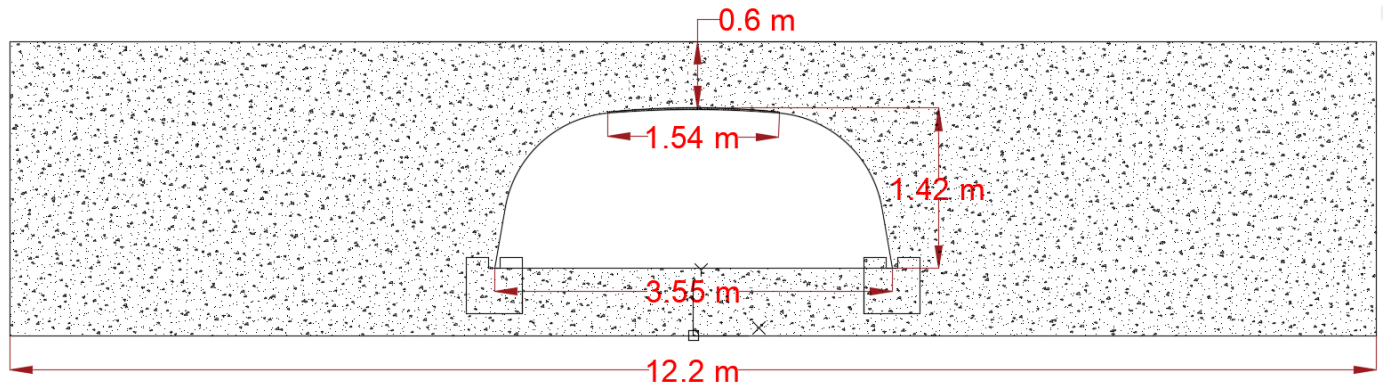


Figure 7.1: Geometry of box-type SSCS considered as the reference model in the study.

The finite element mesh, along with the load position for the reference model (single shell), is illustrated in Fig. 7.2. The corresponding models for multi-span SSCSs, depicting the shell with span D and spacing S , are shown in Figs. 7.3.

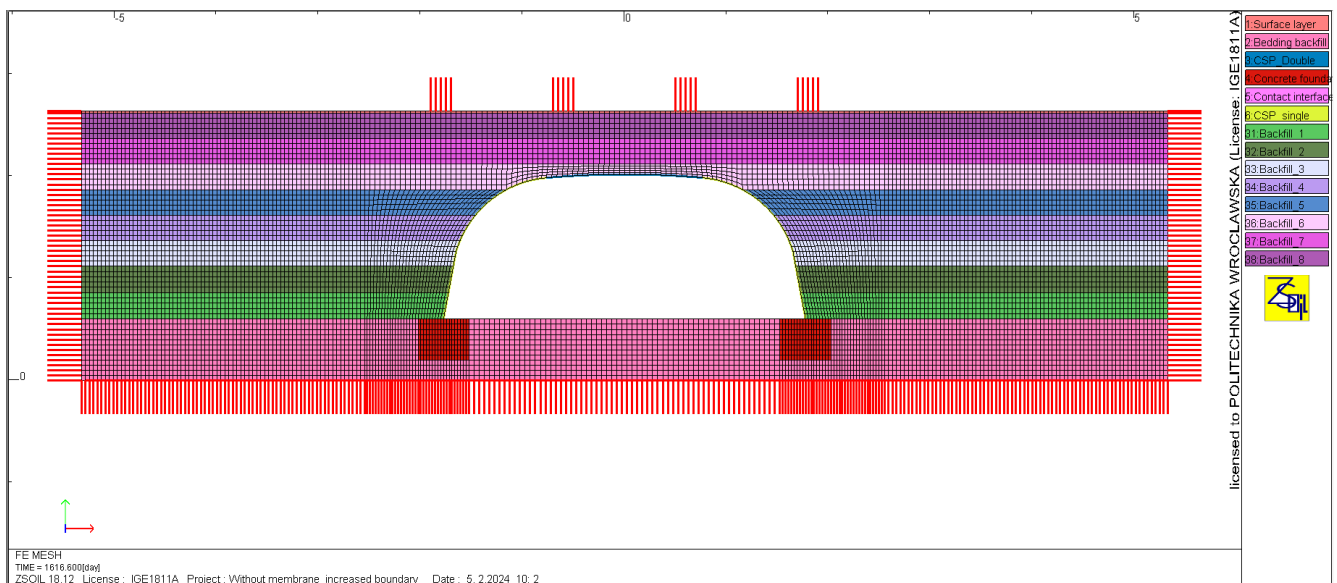


Figure 7.2: Finite element mesh and boundary condition for a reference model (single span)

The analysis commences with an examination of the behavior of the single-span SSCS under ultimate load, serving as the reference model. Subsequently, five models of the multi-span SSCS were developed by adjusting the spacing between the central and lateral shells while maintaining consistent geometric characteristics for both. The lateral shells were positioned at intervals corresponding to spacings of 0.15 m, 0.355 m, 0.8875 m, 1.775 m, and 3.55 m, representing spacing to span ratios (S/D) of 0.04, 0.1, 0.25, 0.5, and 1.0, respectively.

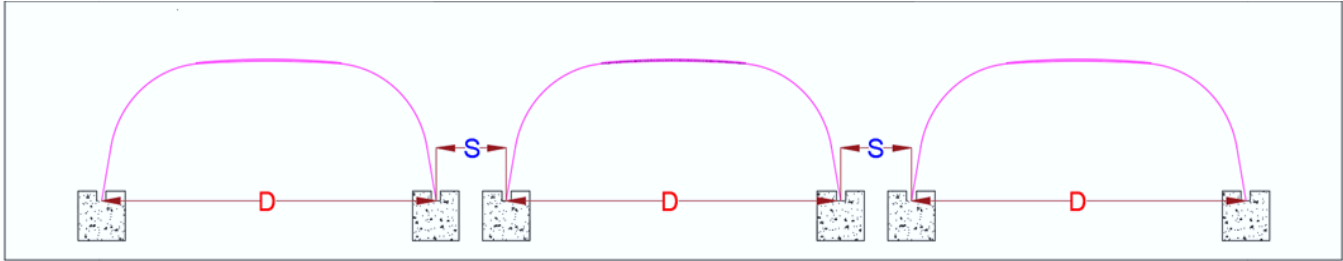


Figure 7.3: Geometry of three span box-type SSCS with span (D) and spacing (S)

In the first loading position (hereafter Model-C), failure-inducing loading was exclusively applied in terms of imposed displacement solely over the central shell (See Fig. 7.4), and this loading position is constant as S/D varies. This specific configuration allows for a focused assessment of the central shell's response under the failure load. Additionally, this loading scenario enables an examination of the influence of both lateral shells on the behavior of the central shell.

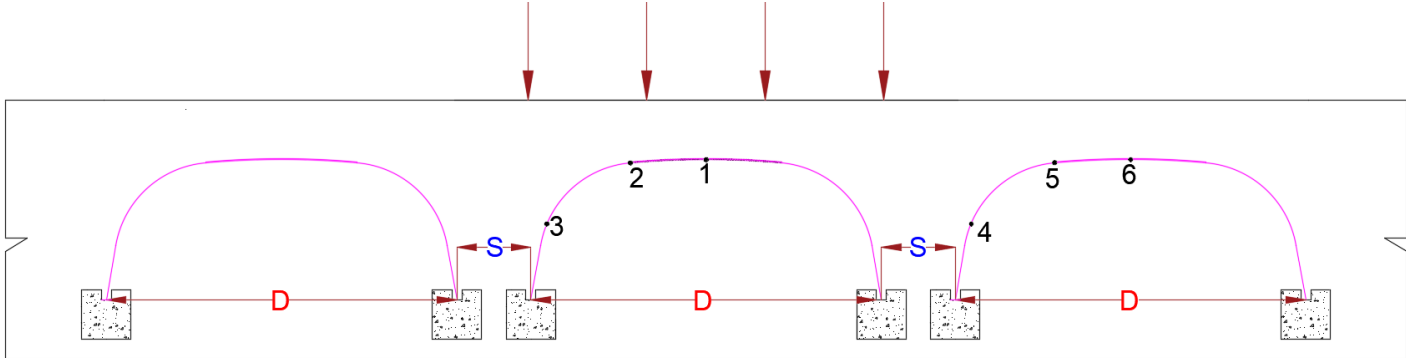


Figure 7.4: Loading position and location of characteristic points for Model-C.

As shown in Fig.7.4, six characteristic points located at the crown of the shells (1 and 6), shoulder of the shells (2 and 5) and haunch of the shells (3 and 4) are chosen for the consideration; in these points the maximum bending moment, normal force and deformations are analyzed and

presented. The finite element mesh, along with the load position, for the multi-span SSCS is illustrated in Figs 7.5 to 7.9 for Model-C.

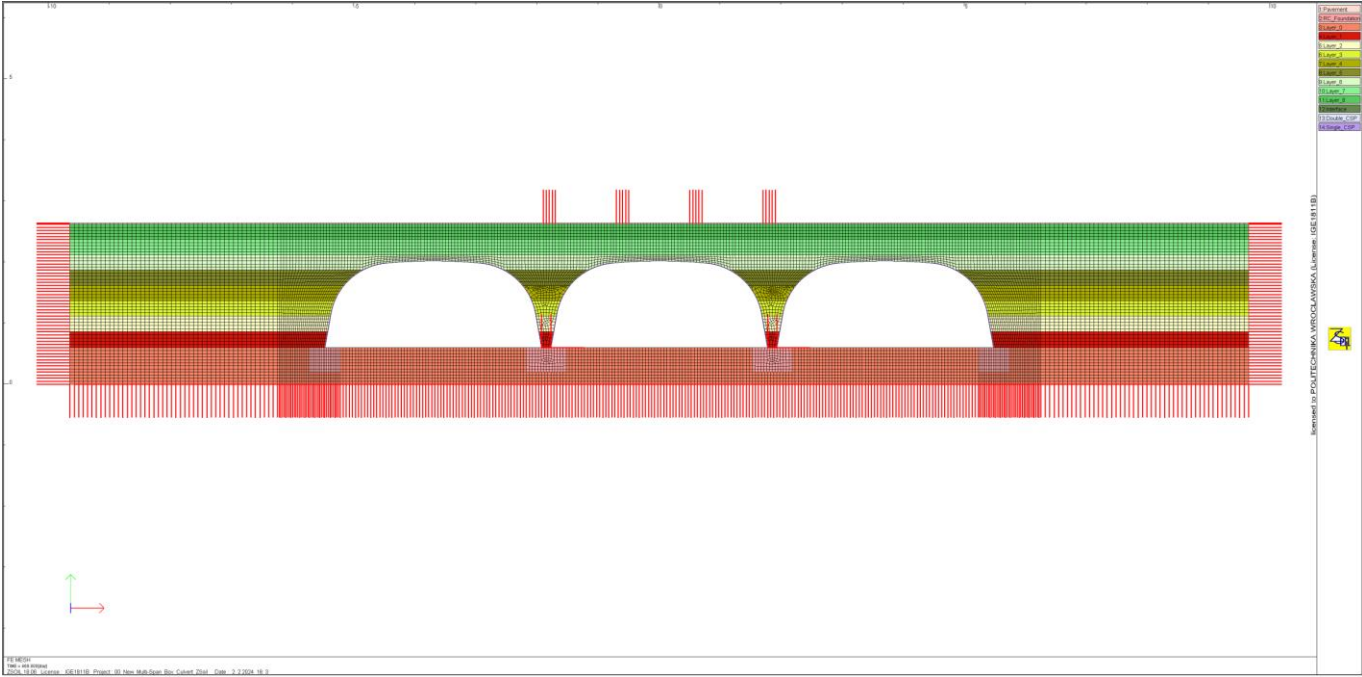


Figure 7.5: Finite element model for Model-C (S/D=0.04)

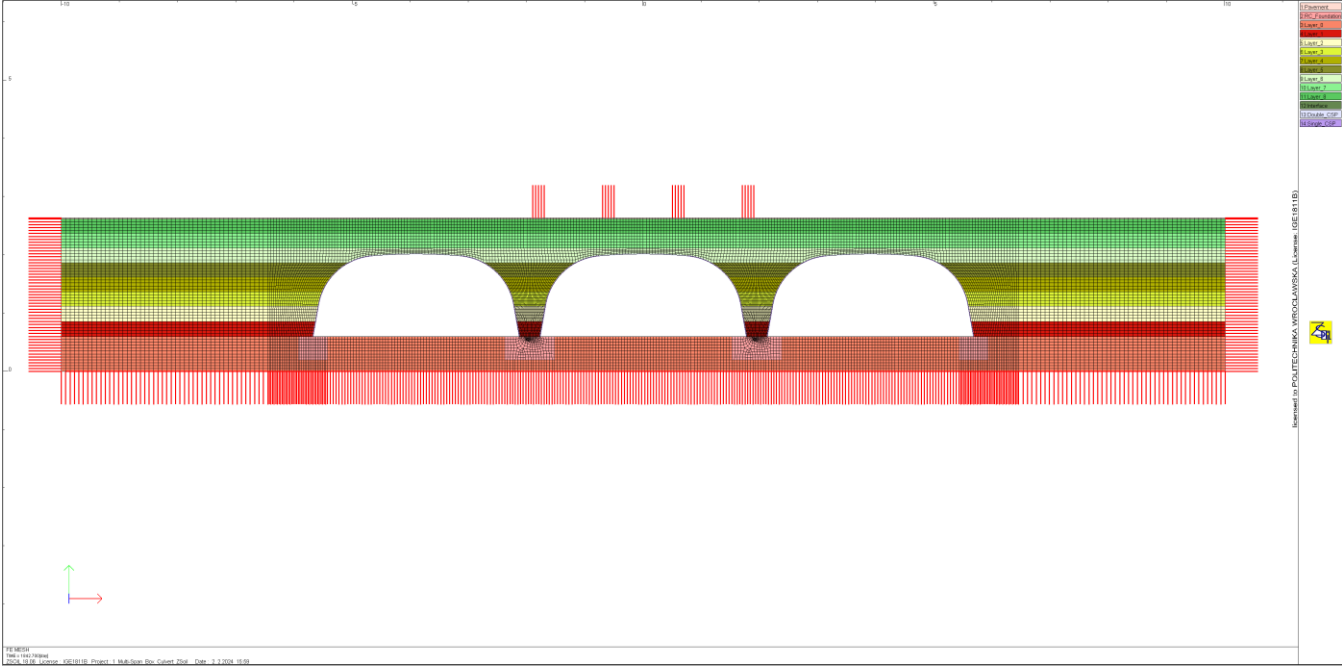


Figure 7.6: Finite element model for Model-C (S/D=0.1)

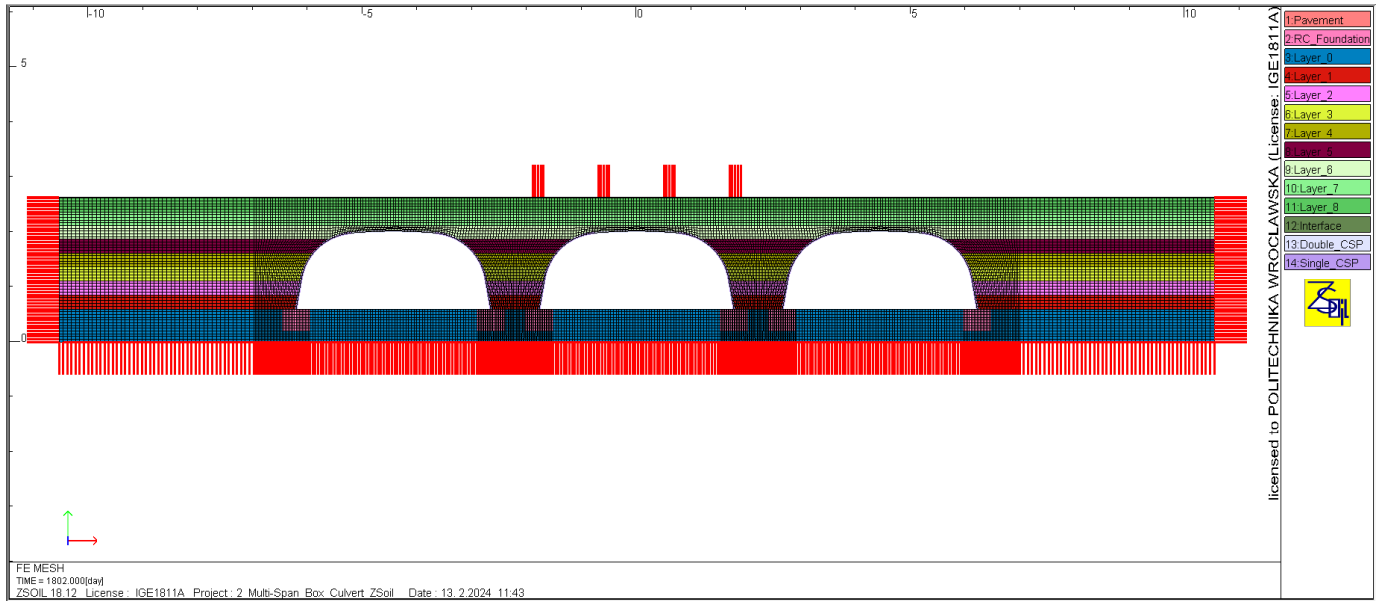


Figure 7.7: Finite element model for Model-C (S/D=0.25)

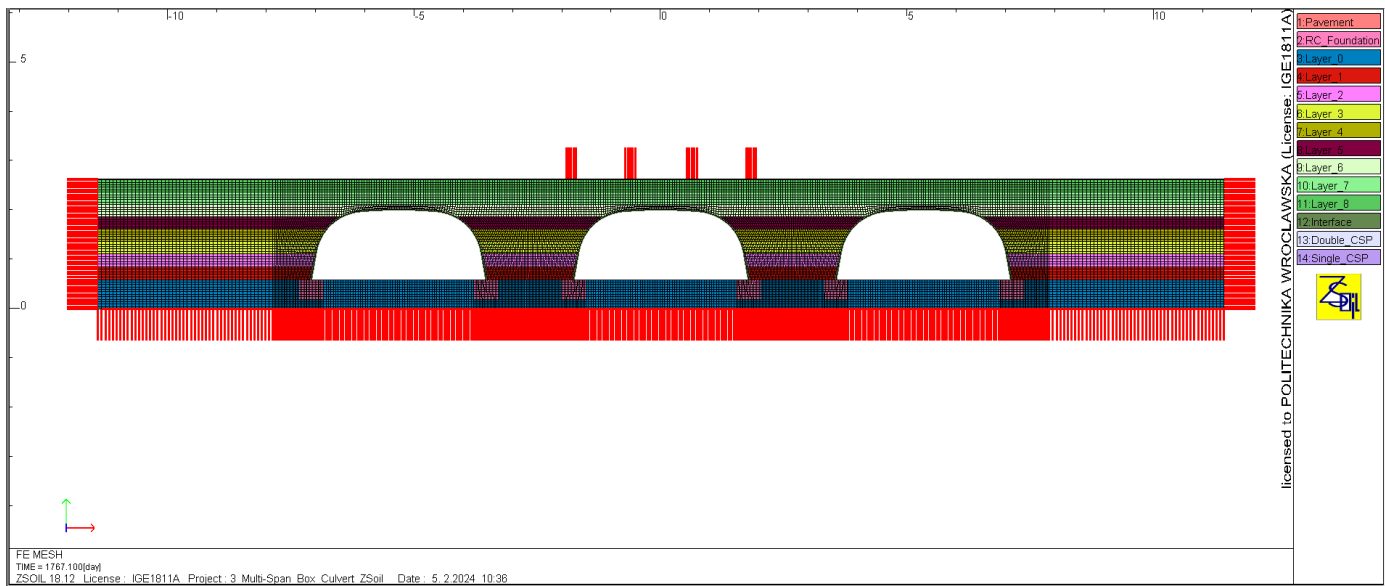


Figure 7.8: Finite element model for Model-C (S/D=0.5)

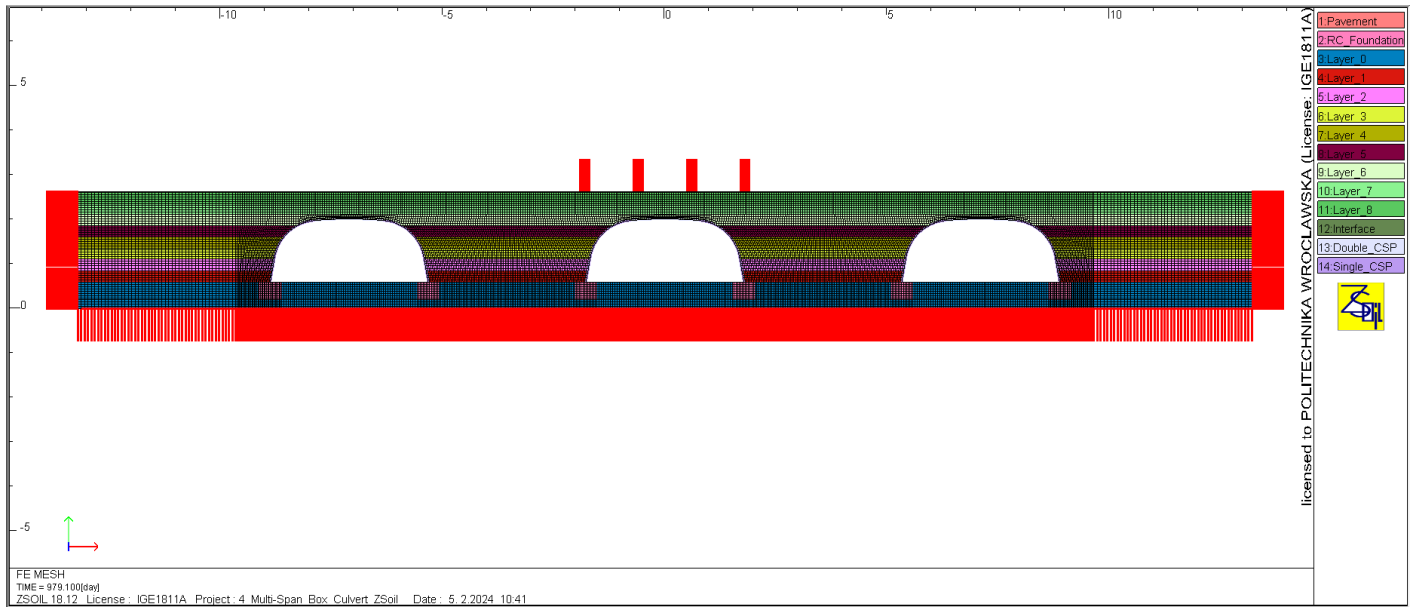


Figure 7.9: Finite element model for Model-C ($S/D=1.0$)

In the second loading position, referred to as Model-R, only one lateral shell on the right side was subjected to loading until failure, while the central and other lateral shells remained unloaded (See Fig. 7.10). This configuration allows for an examination of the effect of asymmetric loading on the load-bearing capacity and the failure mechanism of the multi-span SSCS, which is then compared with the behavior observed in the single-span SSCS.

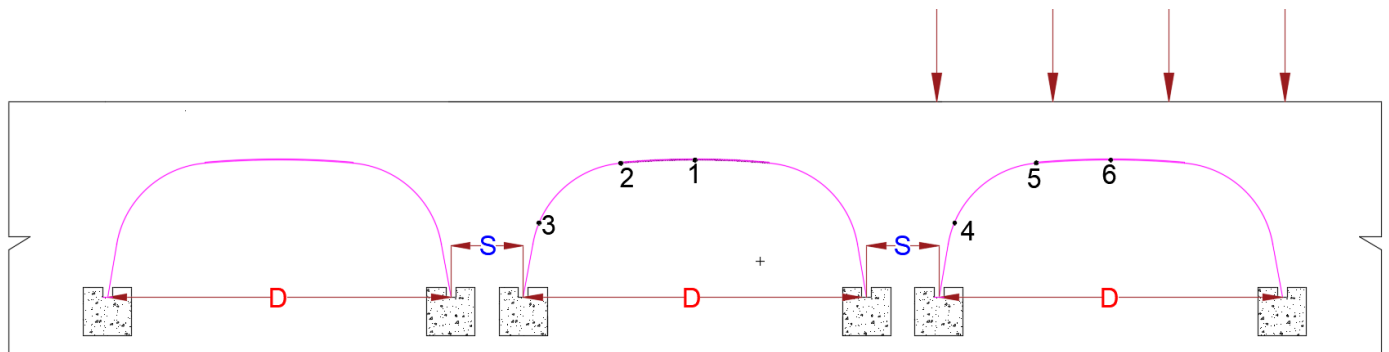


Figure 7.10: Loading position Model-R and location of characteristic points.

This loading configuration provides valuable insights into how the lateral shell responds when loaded to failure, as well as its impact on the behavior of the unloaded central and left-side lateral shells under different spacing conditions. Similar to Model-C, the finite element models used for multi-span SSCSs are shown in Figs 7.11, 7.10, 7.11, 7.12, and 7.15 for spacing-to-span (S/D) ratios of 0.04, 0.1, 0.25, 0.5, and 1.0, respectively.

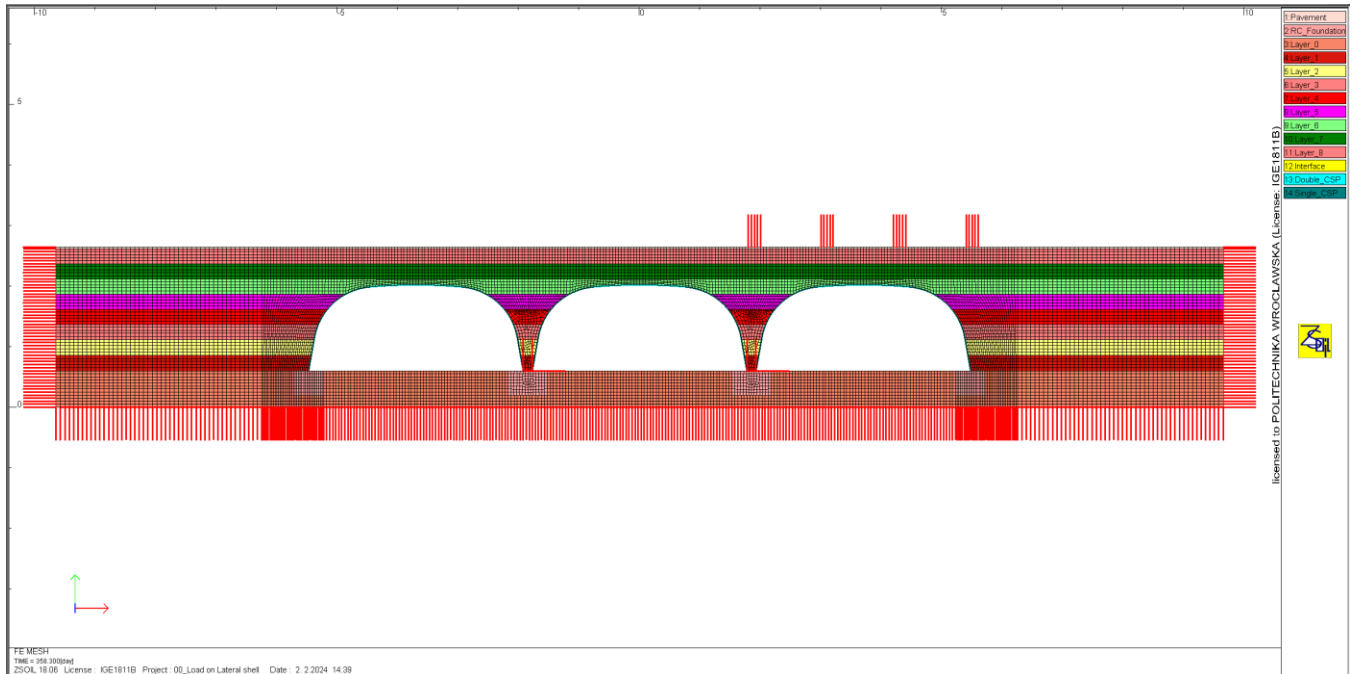


Figure 7.11: Finite element model for Model-R ($S/D=0.04$)

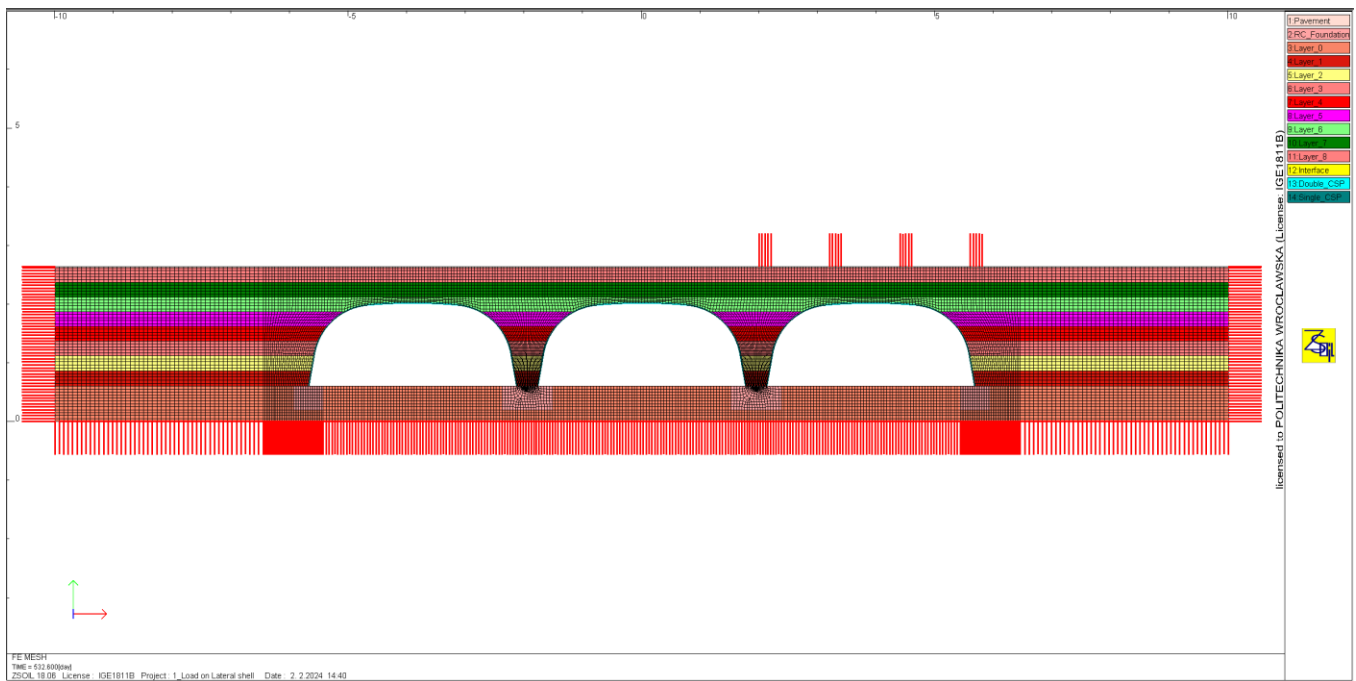


Figure 7.12: Finite element model for Model-R ($S/D=0.10$)

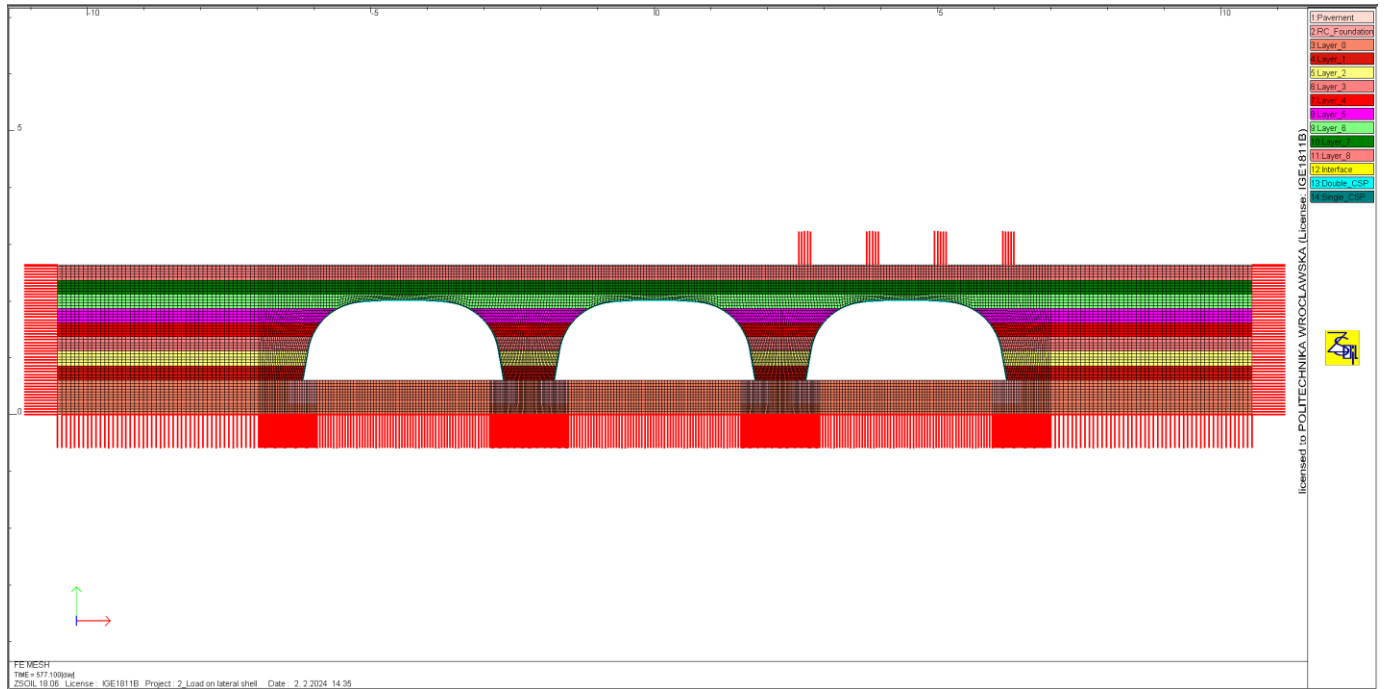


Figure 7.13: Finite element model for Model-R ($S/D=0.25$)

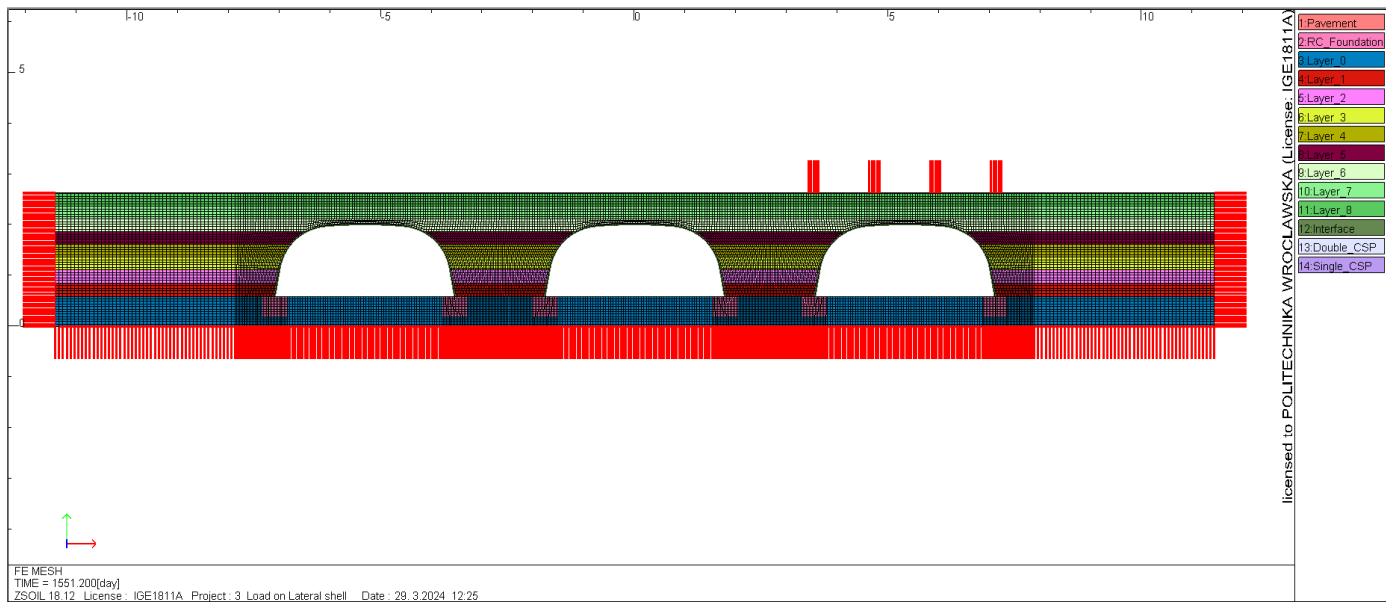


Figure 7.14: Finite element model for Model-R ($S/D=0.50$)

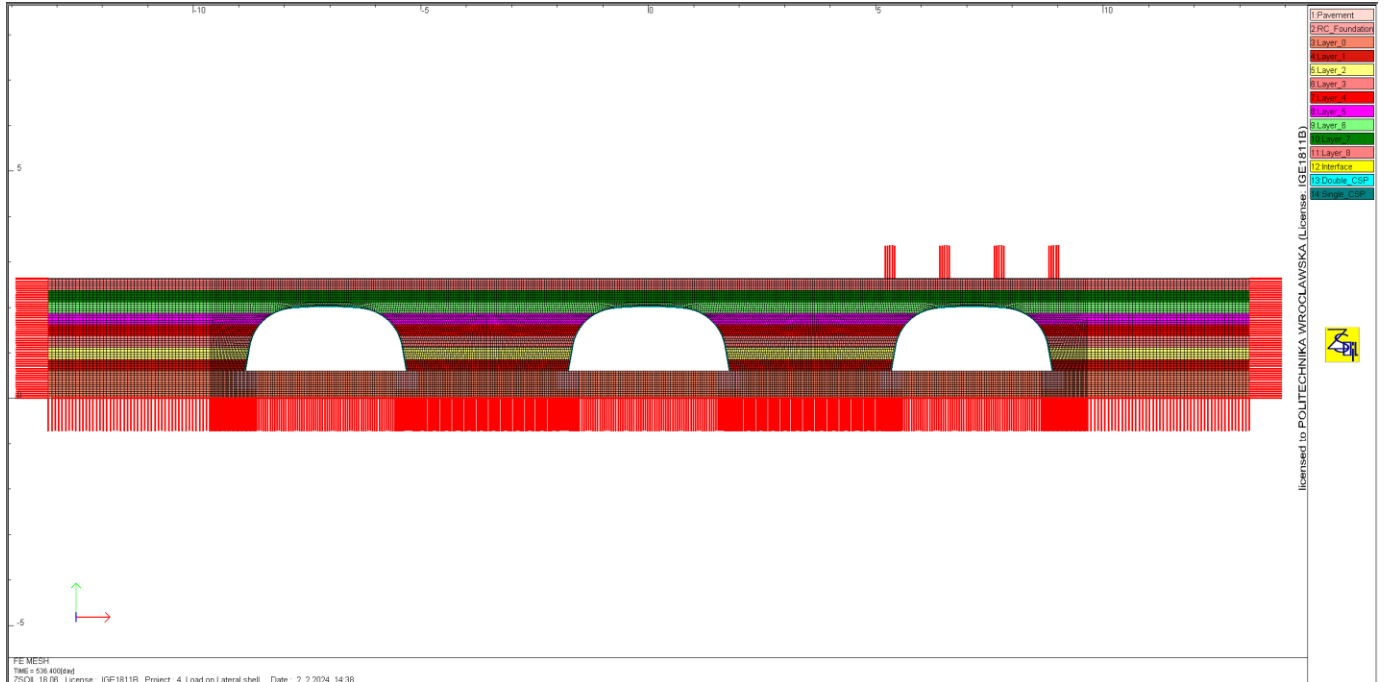


Figure 7.15: Finite element model for Model-R ($S/D=1.0$)

In the third loading position, denoted as Model-LR, symmetrical failure-inducing loading was applied to both the left and right lateral shells, while the central shell remained unloaded (See Fig. 7.16). This configuration aimed to explore the combined effect of the loaded lateral shells on the central shell's behavior, as well as the failure mechanism of both the central and lateral shells.

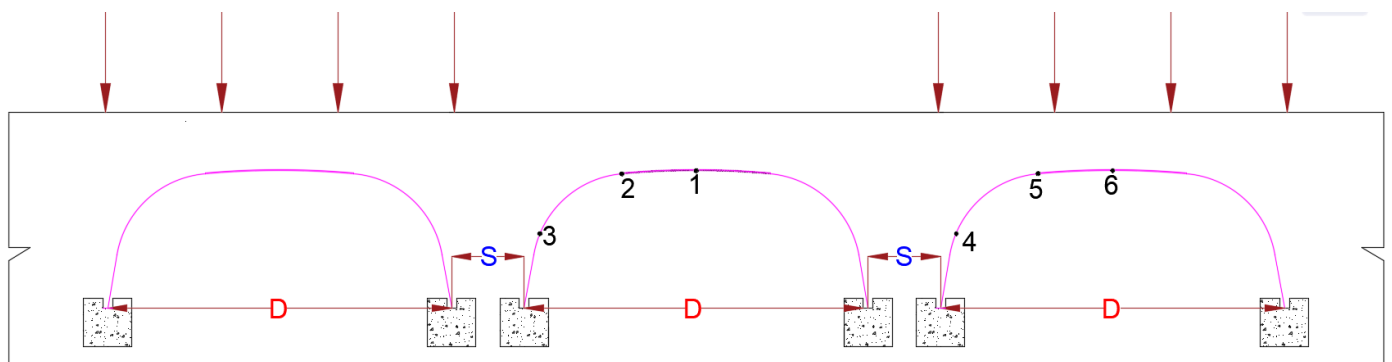


Figure 7.16: Loading position and location of characteristic points for Model-LR.

Additionally, this scenario provides valuable insights into the response of the central shell when both lateral shells are loaded to failure. Similar to Model-C and Model-LR, the finite element (FE) models and the configuration of the shell spacing used for multi-span SSCSs are depicted in

Figs. 7.17, 7.18, 7.19, 7.20, and 7.21 for the spacing to diameter (S/D) ratios of 0.04, 0.1, 0.25, 0.5, and 1.0.

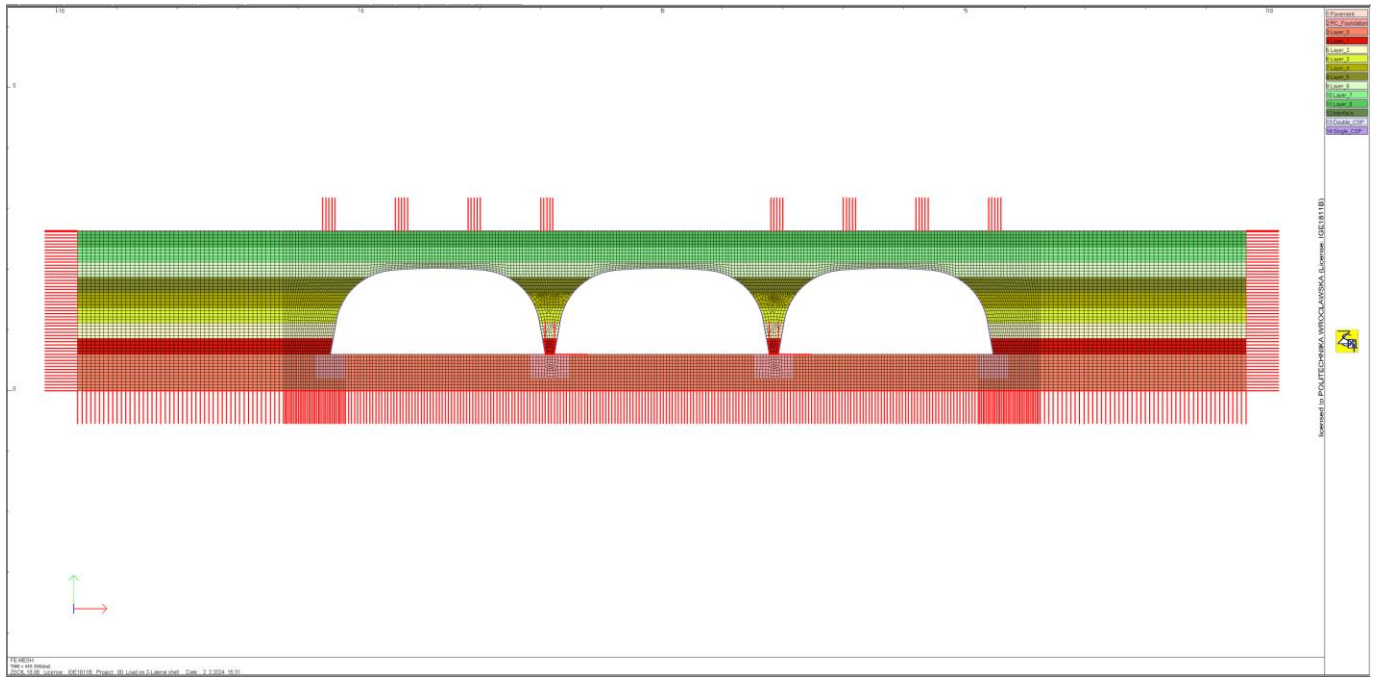


Figure 7.17: Finite element model for Model-LR ($S/D=0.04$)

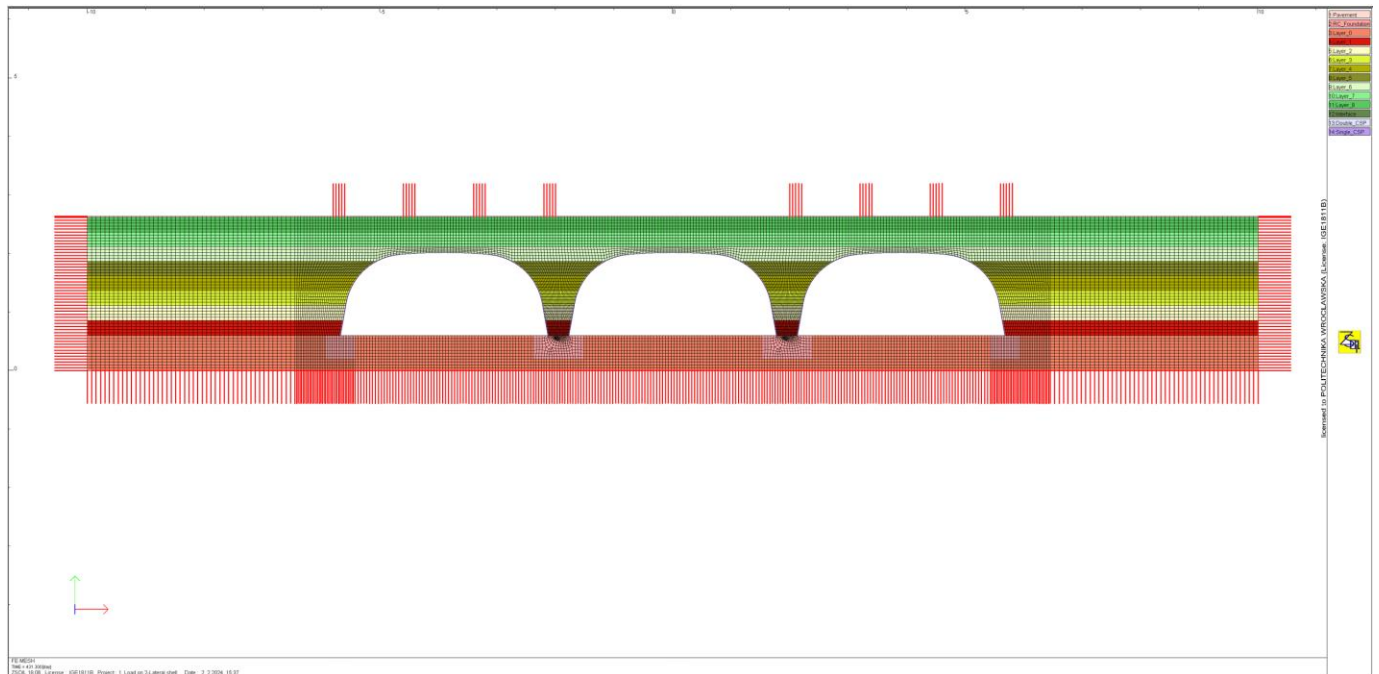


Figure 7.18: Finite element model for Model-LR ($S/D=0.10$)

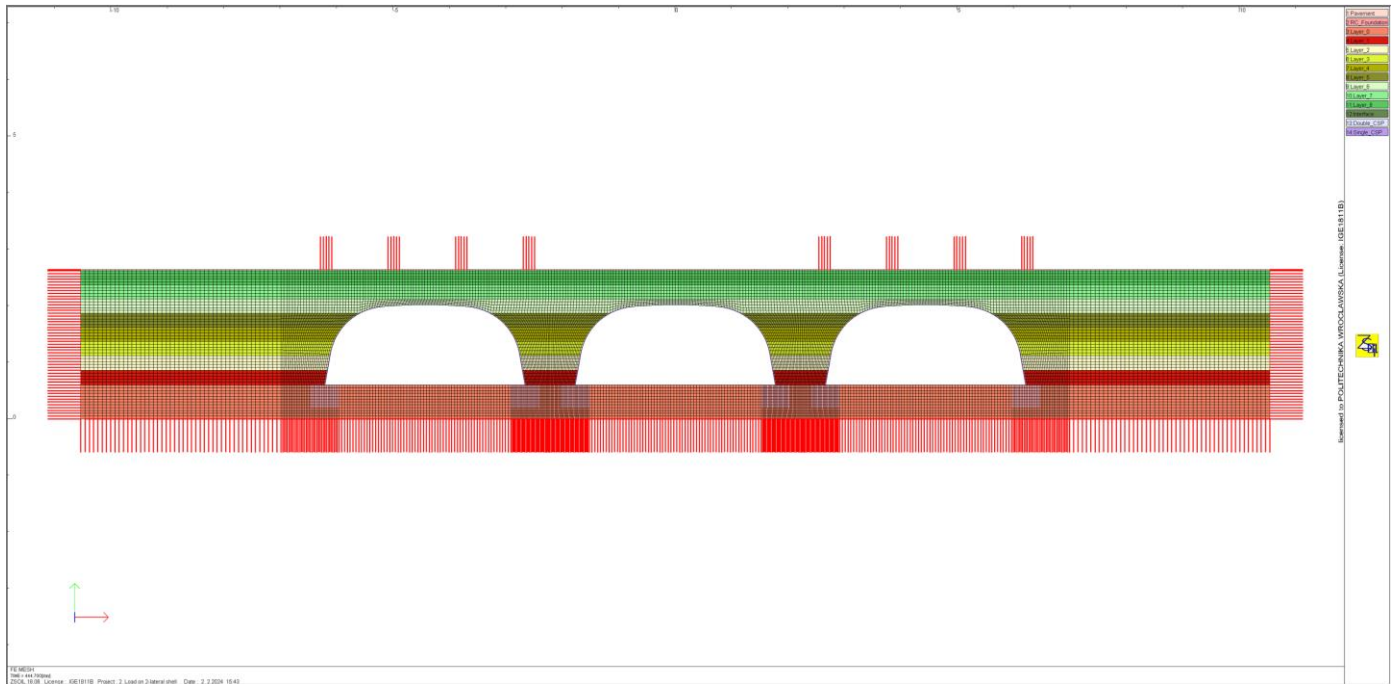


Figure 7.19: Finite element model for Model-LR ($S/D=0.25$)

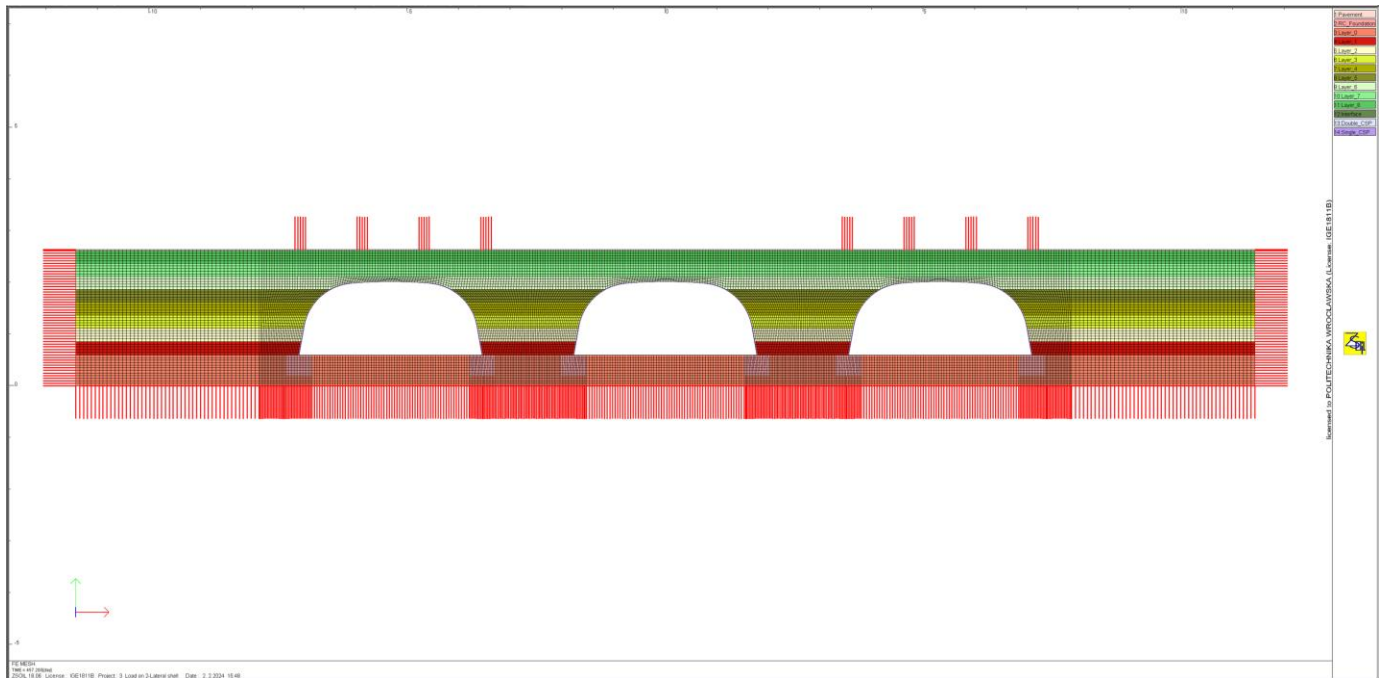


Figure 7.20: Finite element model for Model-LR ($S/D=0.50$)

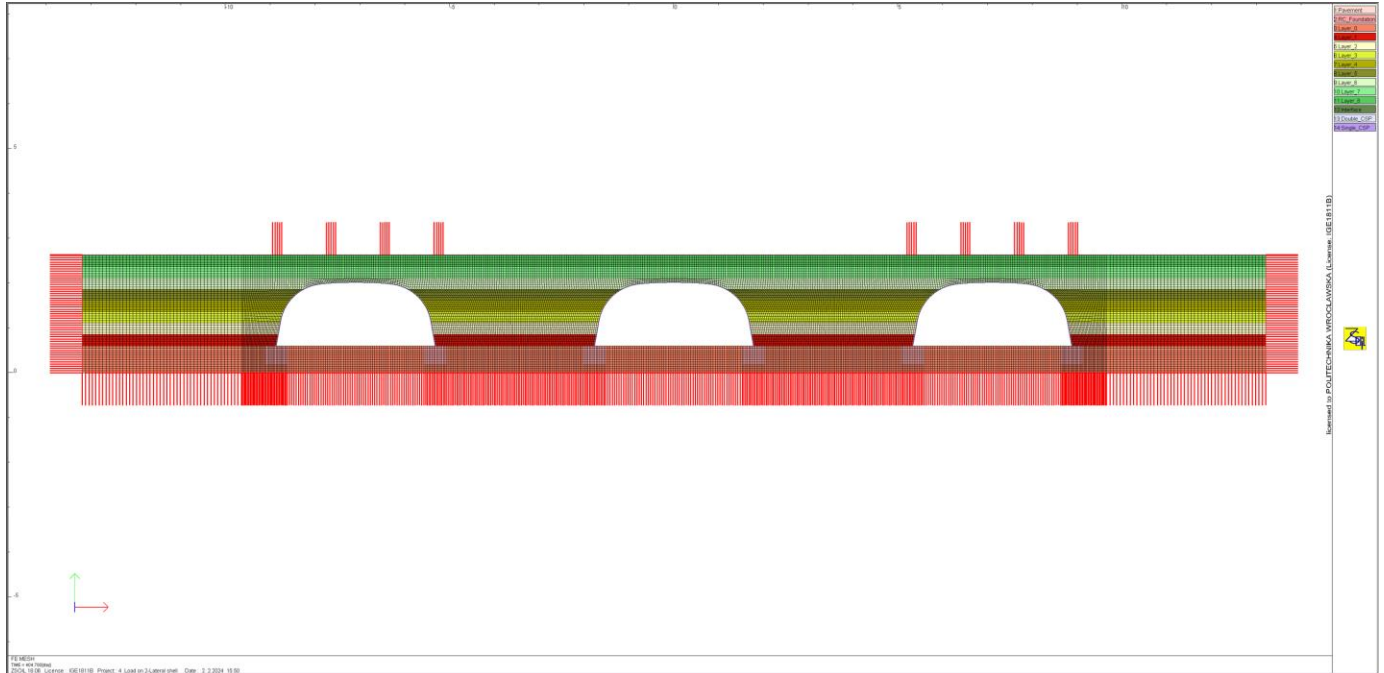


Figure 7.21: Finite element model for Model-LR ($S/D=1.0$)

For all three loading positions, detailed information regarding deformation, bending moment, and axial force distributions across all three shells was presented, providing a comprehensive understanding of the structural response under these loading conditions. Moreover, after the shells failed under the failure load, the failure mechanisms were investigated, and critical locations on the shells were identified.

7.2. Analysis and behavior of a SSCS during backfilling

7.2.1. Single span SSCS (reference model)

The investigation into the deformation during the construction stage is conducted on a single-span structure. In first two stages of backfilling, the vertical displacement at the crown as well as the horizontal displacement in both sides of the shell is relatively small, indicating that the horizontal force generated by the compaction is very limited at these stages. Consequently, theoretically, the vertical displacement at the crown during the initial stages of backfilling would remain relatively unchanged [137]. From stage three to stage five, the horizontal compression force on the shell increases to a certain extent, which further squeezes the two sides of the structure to deform inward and cause the corresponding upward deformation at the crown. At the stage six, the backfill covers the crown of the shell and deformation begins to change reversely. As the cover

height increases, the crown exhibits a downward movement under the increased backfill load, and compaction and correspondingly, the haunch section (side of the shell) starts moving outward. Upon completion of the backfilling stage, notable observations are recorded: a maximum vertical deformation of approximately -1.80 mm is identified at the crown of the shell, while the haunch (side of the shell) registers a lateral deformation of -0.44 mm. The structural deformation at the end of backfilling stage is plotted in Fig. 22 and the results at the end of each stage can be illustrated in Fig. 7.23.

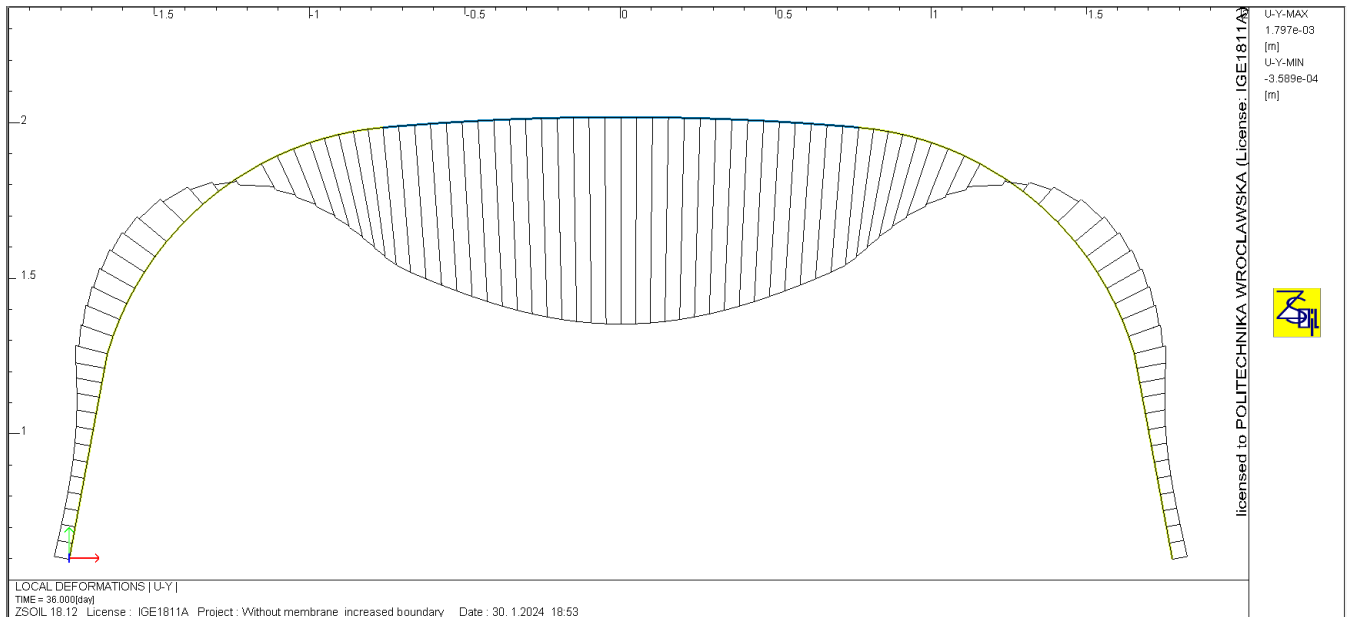


Figure 7.22: The vertical deformation distribution of the shell (Reference model)

7.2.2. Multi- span SSCS (reference model)

The vertical deformation at the crown of both central and lateral shells were calculated at different spacing between the central and lateral shell. In Fig. 7.23, a consistent rise is observed at the crown of the central shell during the constriction stage, until backfilling approaches the crown level. In all models, the maximum upward deformation of the crown of the shells is observed when the backfill reaches stage five. When backfill reaches stage, the thickness of the backfill layer is almost 90 % of the rise of the shell (which is 1.42 m), indicating that the shell is not yet fully covered by backfill. This phenomenon is attributed to the substantial lateral stresses exerted on the shell by the backfill and compaction, coupled with the absence of vertical stresses from the soil cover above the crown. This unique condition leads to an increased susceptibility of the shell to

upward deformation, emphasizing the complex interaction between backfill placement and the structural response of the shell during this phase of construction.

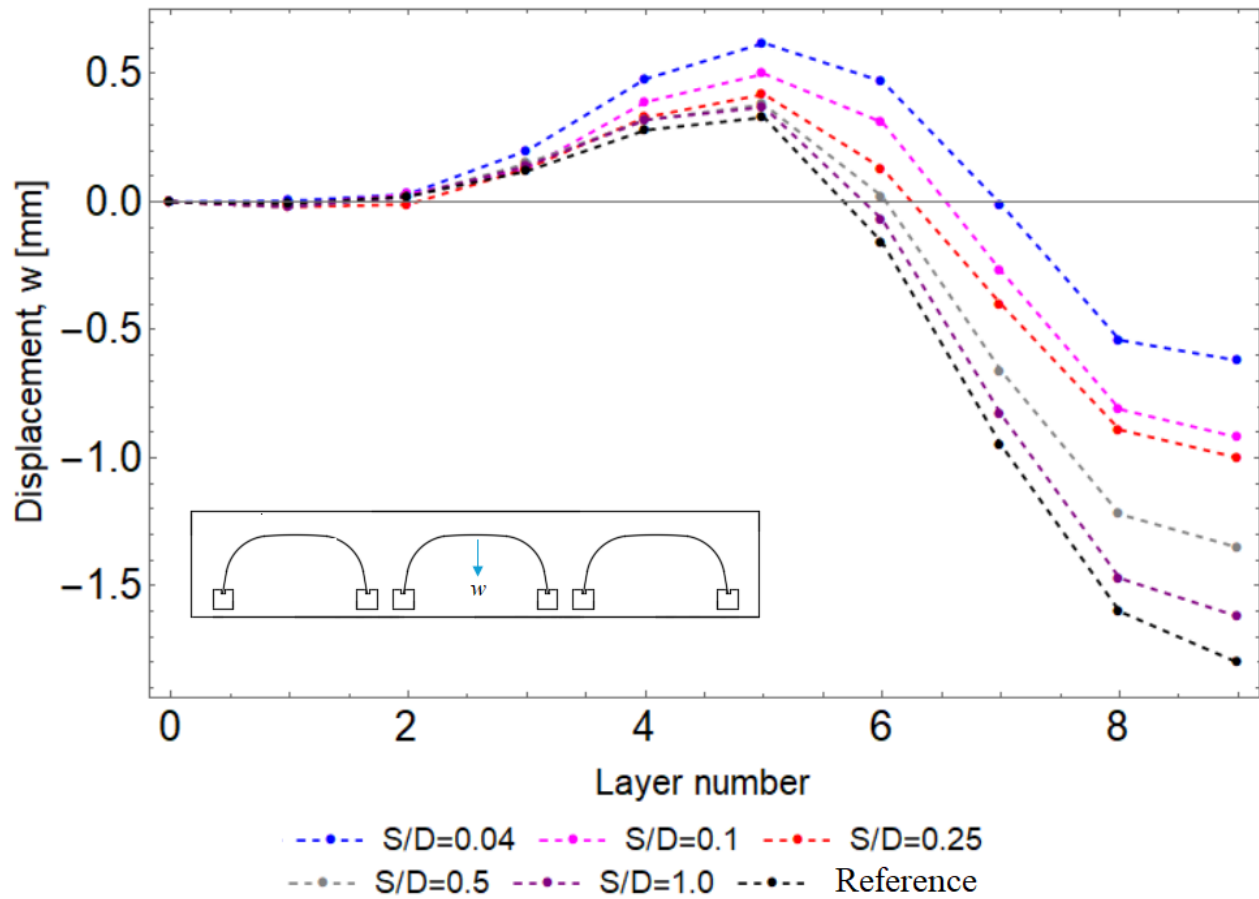


Figure 7.23: Deformation of the crown of the central shell during construction stage at different shell spacing for Model-C

Comparing all models, the maximum upward deflection is notably observed in Model-C ($S/D=0.04$), amounting to 0.62 mm. This increase is attributed to the combined lateral stresses induced by closely placed lateral shells, in addition to the backfill. It is noteworthy that this upward deformation decreases as the ratio of S/D increases, as the lateral stresses exerted by the lateral shells on the central shell decreases with the higher S/D ratio. This observation underscores the influence of lateral shell arrangement on the overall deformations during the construction phase.

The trend of the deformation behavior of the lateral shells under backfilling load is identical with that of the central shell (See Fig.7.24). Comparing the vertical deflections between the central and lateral shells, it is evident that the vertical deflections are greater in the lateral shells as shown

in Table 7.1. Nevertheless, the vertical deformation at the crown of both central and lateral shells significantly decreased as spacing between central and lateral shell decreases.

This phenomenon is consistent with the absence of lateral supports from one side in the lateral shells unlike central shell. The increased flexibility resulting from the lack of lateral support contributes to larger vertical deflections in the lateral shells as compared to the central shell, which is similar to the deformation results of Bao et.al [85].

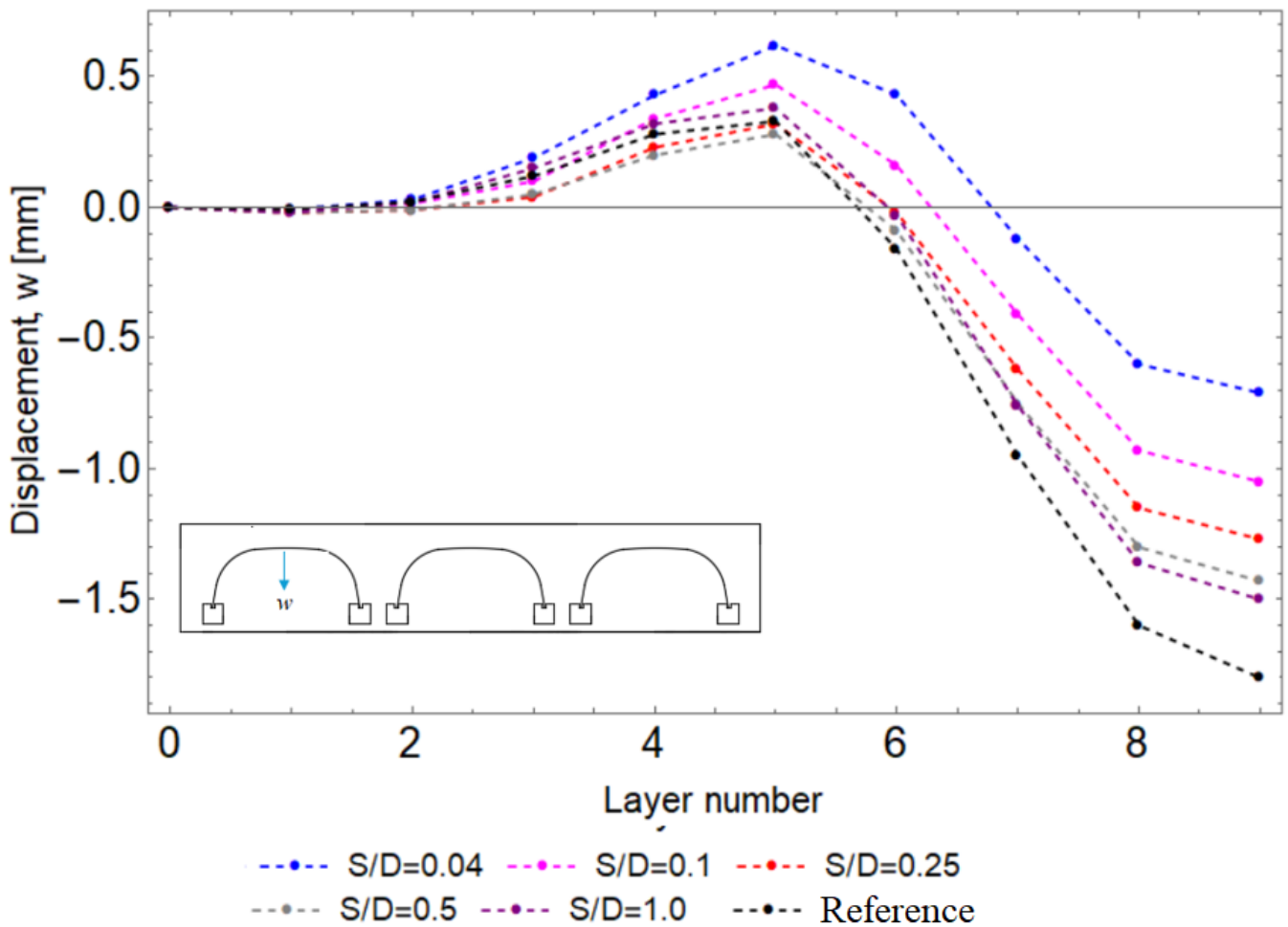


Figure 7.24: Deformation of the crown of the lateral shell during construction stage

The summary of the maximum vertical displacement of the crown of the shells after backfilling and compaction is summarized on Table 7.1 for both central and lateral shells. As described above, observing the behavior of such a structure, it becomes evident that once backfilling covers the crown, the shell initiates a downward deflection. However, rate of this downward deflection is low

when lateral shells are closely positioned to the central shell due to the rigid support provided by the lateral shells from both sides.

Table 7.1: Summary of maximum vertical displacement in the shells after backfilling

Model	Maximum downward vertical deflection of the crown (mm)		
	Latera (Left shell)	Central shell	Latera (Right shell)
S/D=0.04	-0.71	-0.62	-0.71
S/D=0.1	-1.05	-0.92	-1.05
S/D=0.25	-1.27	-1.00	-1.27
S/D=0.5	-1.40	-1.18	-1.40
S/D=1.0	-1.50	-1.35	-1.50
Reference*	-1.80		

**Single span shell without lateral shells*

Thus, as the backfilling layer covers the crown, it prompts a downward deflection, reaching its maximum upon completion of the backfilling process for all models. In comparison to the reference model, the downward deflection at the crowns of both the central and lateral shells were significantly decreased. This is attributed to the influence of the interaction between the shells in multi-span configuration. For instance, when comparing the peak deformation at the crown of the central shell with the reference model at the end of backfilling, the maximum downward deflection at the crown of central shell is reduced by 65.5%, 49.0%, 44.4%, 25.0%, and 10.0% for S/D=0.04, S/D=0.10, S/D=0.25, S/D=0.50, and S/D=1.0, respectively. The distribution of vertical deformations of both central and lateral shells after the final layer of backfill has been placed over the top of the structure are presented in Figs 7.25 to 7.29. As shown in Figs. 27 to 29, the shape of the distribution of the vertical deformation in lateral shells are almost identical with central shell once the ration of S/D is greater than or equal to 0.25.

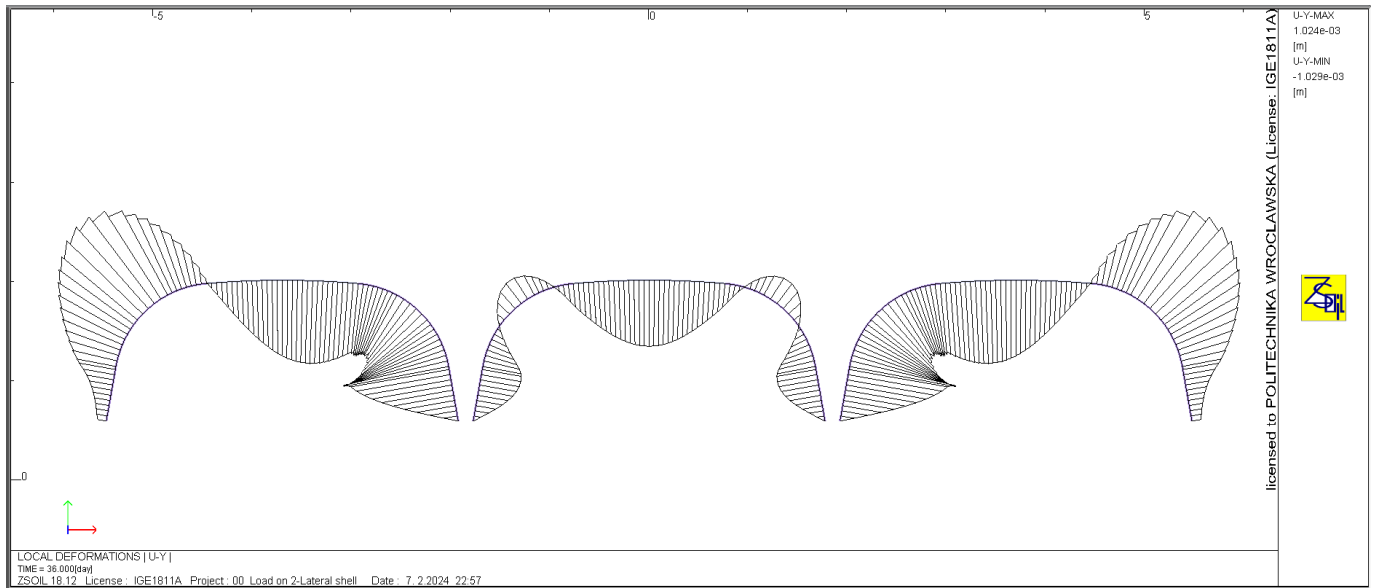


Figure 7.25: The vertical deformation distribution of the shell for $S/D=0.04$

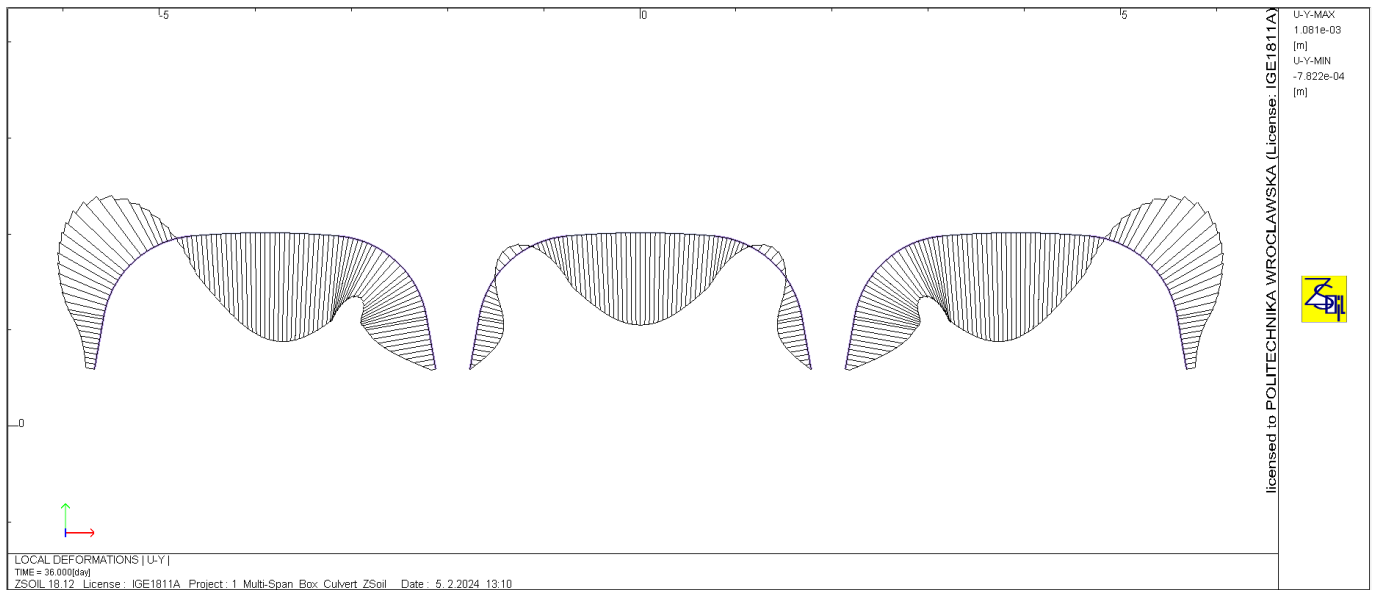


Figure 7.26: The vertical deformation distribution of the shell for $S/D=0.10$

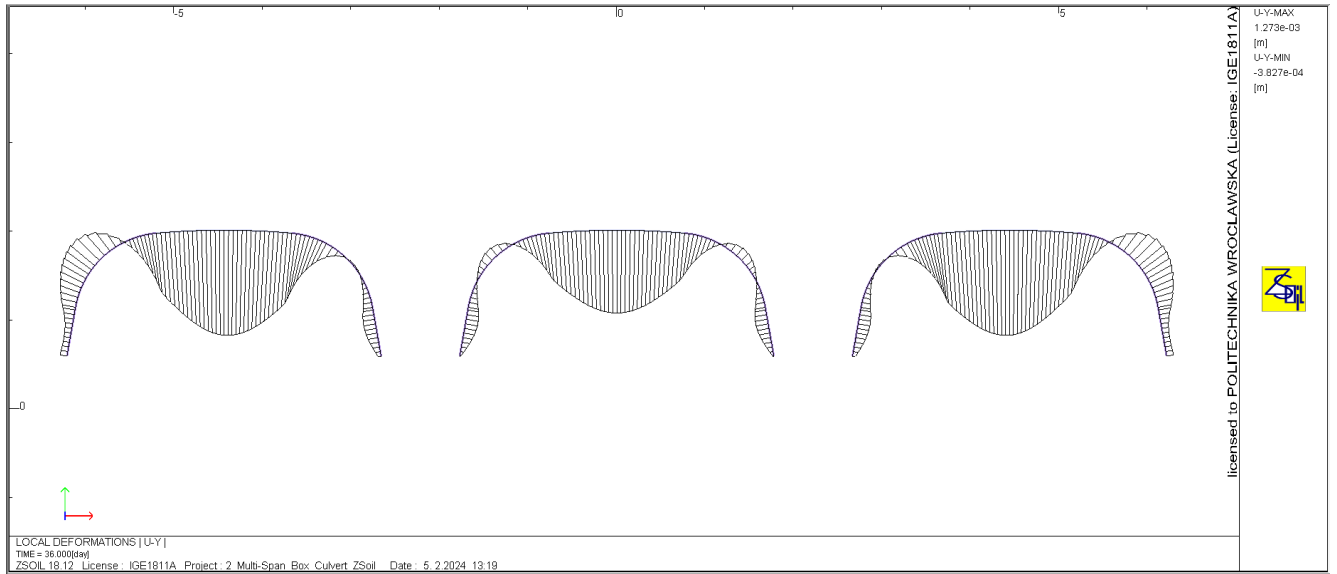


Figure 7.27: The vertical deformation distribution of the shell for $S/D=0.25$

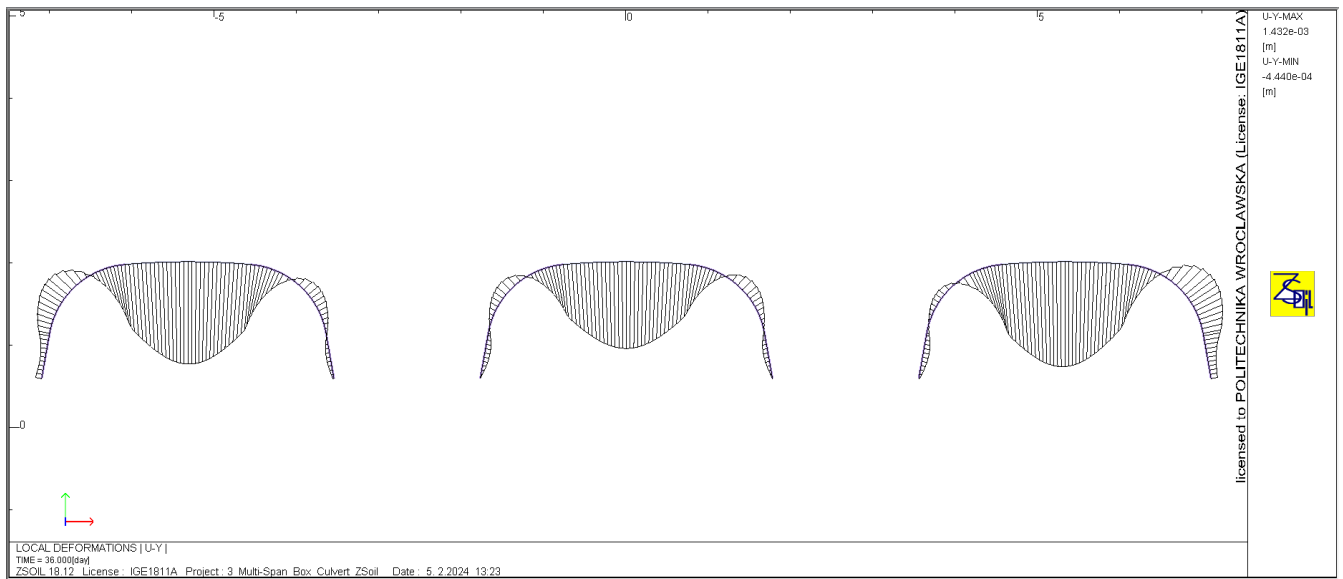


Figure 7.28: The vertical deformation distribution of the shell for $S/D=0.50$

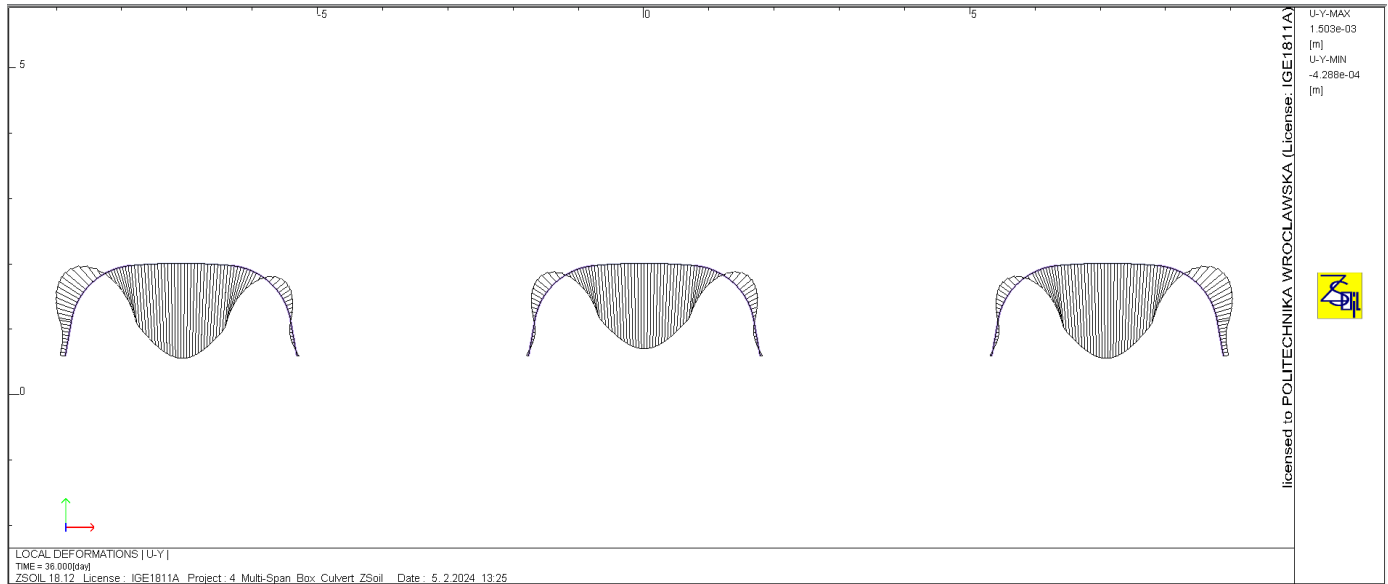


Figure 7.29: The vertical deformation distribution of the shell for $S/D=1.0$

Generally, during backfilling and compaction process, as the ratio of S/D increases, the vertical deformation at the crown of both central and lateral shell increases while the deformation around the haunch of the lateral shell decreases.

7.3. Analysis and behavior of multi-span SSCS under ultimate load (Model-C)

To investigate the influence of spacing on the load-bearing capacity of the shells, numerical models were established with S/D ratios of 0.04, 0.1, 0.25, 0.5, and 1.0. Loading was applied in terms of imposing displacement on the top of the central shell, and the results were compared with those of the reference model, which represents a single span. Furthermore, load-displacement curves, bending moments and axial forces are presented for selected locations of the shell. These critical points of the shell were chosen based on recommendations by Duncan et al [138]. According to the authors, box-type SSCSs have nearly flat crowns and large widths compared to their heights, leading to distinct behavior from conventional SSCSs. Thus, different design methods are warranted to take into account the critical locations, i.e., crown and haunch sections. Accordingly, in the following sections, the deformation, bending moment, and axial forces at these critical points are presented.

7.3.1. Load displacement curve

As shown in Figs 7.30 to 7.33, the load-displacement curves of the shells under ultimate load are presented for both crown and haunch sections. As shown in these figures, the initial linear elastic regime of the load-displacement curve is characterized by a gradual increase in load with a corresponding linear increase in displacement for all models. The slope of this segment, characterized by the initial stiffness, reflects the structural stability and material properties of the soil-steel interaction. As the loading continues beyond the elastic limit, the curve exhibits nonlinear behavior, indicating the onset of plastic deformation within the shell. The presence of yielding and localized deformations along the curve signifies the redistribution of stresses within the shell, which may lead to potential failure mechanisms. Upon reaching the peak load, a distinct change in the slope of the curve is observed, indicating the initiation of failure within the shell. This critical point marks the maximum load-bearing capacity of the shell before failure occurs. The shape of the curve beyond this point provides valuable insights into the progressive collapse mechanism, as evidenced by a rapid decrease in load carrying capacity accompanied by extensive deformations.

The deflection of the shell experiences a gradual change with an increasing S/D ratio. At S/D=0.04, the crown deformation rate of central shell is high compared with other models, resulting a peak load of 823 kN at a displacement of 67.4 mm, as illustrated in Fig. 7.30. The constrained spacing limits the lateral support provided by the backfill, exposing the central shell to increased vulnerability under load. Increasing the S/D from 0.04 to 0.10 improves the load-bearing capacity of the central shell by 8.5%, recording a vertical displacement of 71.2 mm at its peak load of 895 kN for S/D=0.1. For S/D=0.25, a displacement of 73.4 mm aligns with a peak load of 997 kN, while at S/D=0.5, a displacement of 75.10 mm coincides with its peak load of 1046 kN. Notably, at S/D=1.0, the vertical displacement reaches 80.4 mm at a peak load of 1198 kN.

The results indicate a notable reduction in the load-bearing capacity of the multi-span SSCS compared to the reference model (i.e., single-span), which has a capacity of 1206 kN. The load-bearing capacity experiences reductions of 32%, 26%, 17%, and 13% for S/D ratios of 0.04, 0.1, 0.25, and 0.5, respectively. It is noteworthy that the load-bearing capacity of the structure when S/D=1.0 is almost equal to that of the reference model, with a difference of less than 0.7%. Thus, when S/D=1.0, the three shells start to behave independently. Moreover, as described in Fig. 7.30,

when the load is less than the peak load, for example, when the load is approximately less than 600 kN, the load-displacement curve for $S/D=0.50$ and $S/D=1.0$ is the same as the reference model. This suggests that when the SSCS is subjected loads less than the peak load, for example truck load, the lateral shell has no influence on the central shell, as S/D is greater than or equal to 0.5. The author [121] also observes similar findings, noting that when $S/D > 0.5$, the lateral shell has no influence on the behaviors of the central shell when the shell is subjected to quasi-static load (the detail is described in chapter 8).

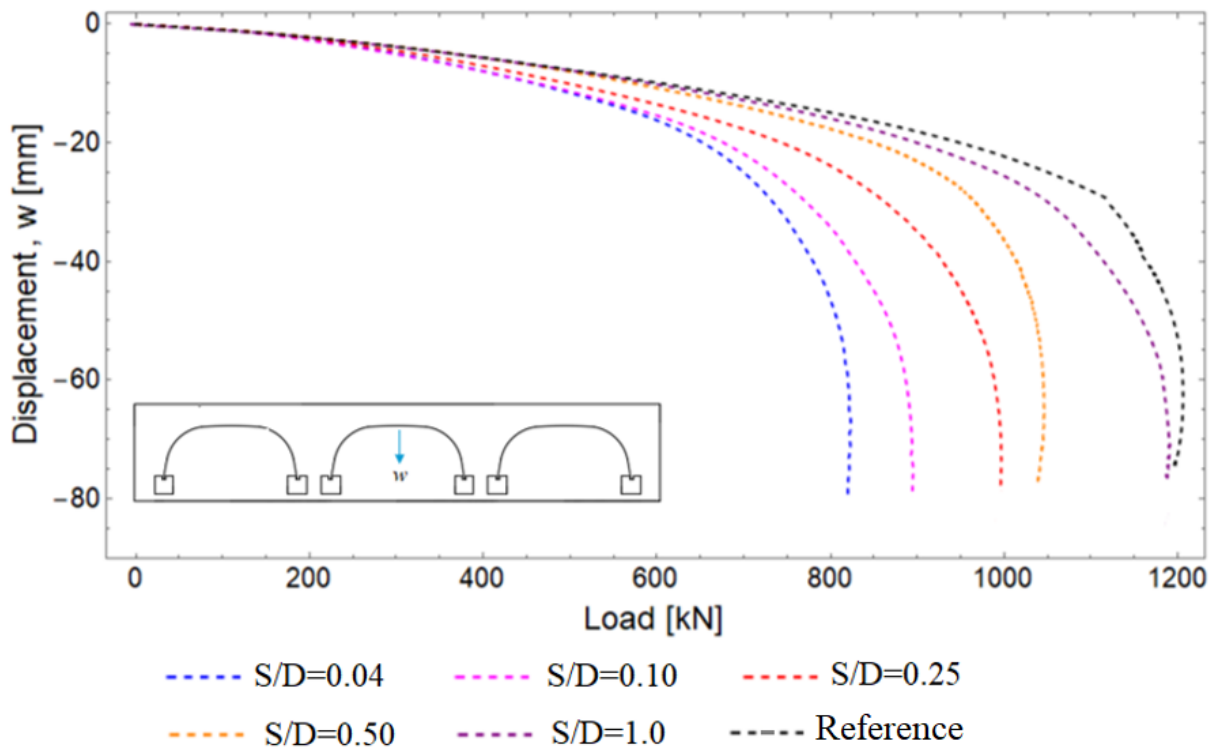


Figure 7.30: Load displacement curve at the crown of central shell

According to [139], which investigates the behavior of two adjacent shells at different S/D ratios through numerical modelling, the decrease in bearing capacity of the shell as S/D decreases is attributed to the close proximity of the shells. This closeness significantly affects their interaction because the stiffness of their mutual support may be lower than the soil support provided to the outer sides.

The results obtained from the study clearly demonstrate that an increase in the ratio of spacing to span (S/D) and the provision of adequate backfill between the shells in a SSCS result in a substantial enhancement of the shell's bearing capacity. This enhancement is evident from

Fig. 7.30, where it can be observed that the initial stiffness of the shell increases as the S/D ratio increases. For example, when $S/D=0.04$, the shell exhibits a lower initial stiffness but maintains linearity until reaching approximately 600 kN, whereas for $S/D=1.0$, the shell demonstrates a higher initial stiffness until reaching approximately 1000 kN. The lower initial stiffness observed for $S/D=0.04$ is believed to be attributable to the insufficient backfill between the shells, which limits the support provided to the shells.

This finding aligns with the core concept that, in SSCS, the load-bearing capacity of the composite structure is markedly influenced by the presence and characteristics of the backfill. The observed rise in bearing capacity with a higher S/D ratio underscores the critical importance of optimizing backfill conditions in SSCS configurations. This correlation underscores the pivotal role of backfill in reinforcing the structural stability and load-bearing capabilities of the composite structure. The findings from the work of [139] who investigate the behavior of two adjacent shells at different spacings conclude that at lower S/D ratios, the load-bearing capacity of the shell will decrease, and vice versa.

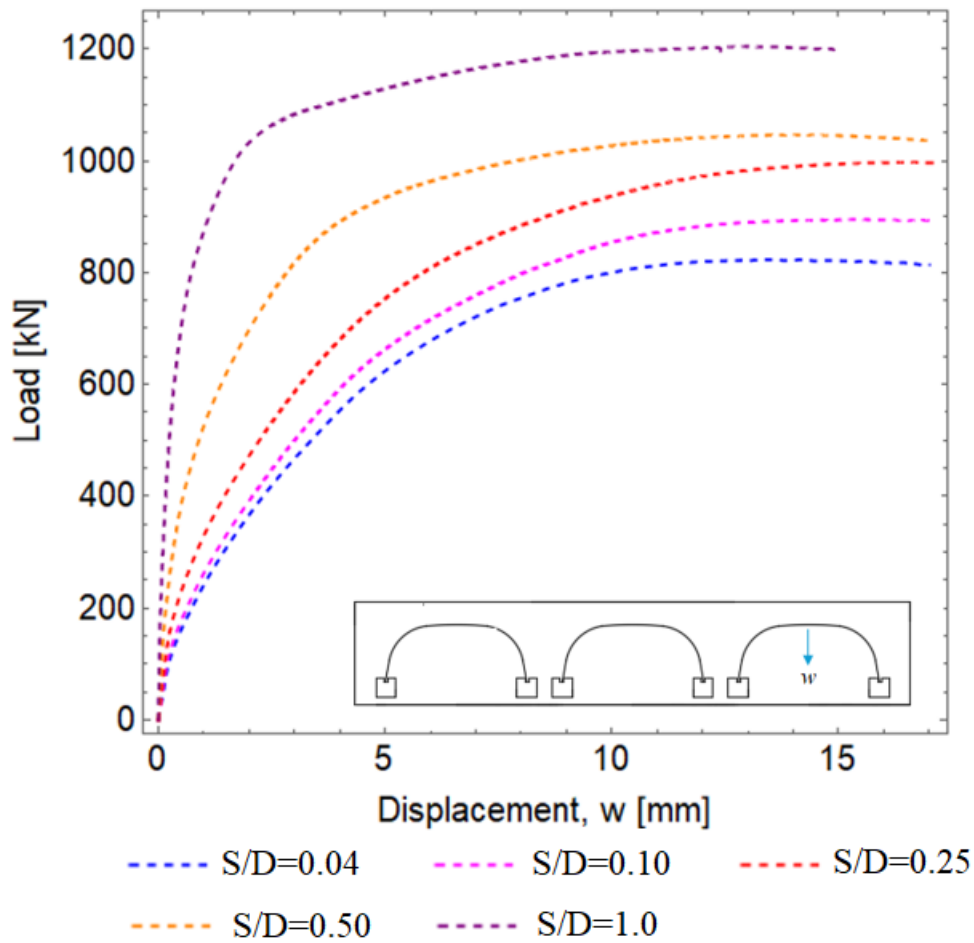


Figure 7.31: Load displacement curve at the crown of lateral shell

Under the ultimate load condition, as shown in Figure 7.30, the crown of the central shell experiences a downward deflection, while the crowns of both lateral shells display an upward deflection (refer to Fig. 7.31). This contrasting behavior arises from the load application at the top of the central shell. In such scenarios, the haunches of the central shell deflect outward, exerting lateral stress on the neighboring lateral shells. The combination of lateral stress from the central shell and the backfill pressure contributes to an upward deflection in the lateral shells.

The maximum upward deflections at peak load are measured as 16.77 mm, 15.25 mm, 14.23 mm, 13.47 mm, and 12.8 mm for $S/D=0.04$, $S/D=0.10$, $S/D=0.25$, $S/D=0.50$, and $S/D=1.0$, respectively. This observed trend indicates that the vertical deflection of the lateral shell crown diminishes with an increase in the S/D ratio. This phenomenon is attributed to the decreasing interaction between the central shell and the lateral shell as the S/D ratio rises. Consequently, the

lateral pressure exerted by the central shell on the lateral shell decreases, thereby influencing the overall deformation.

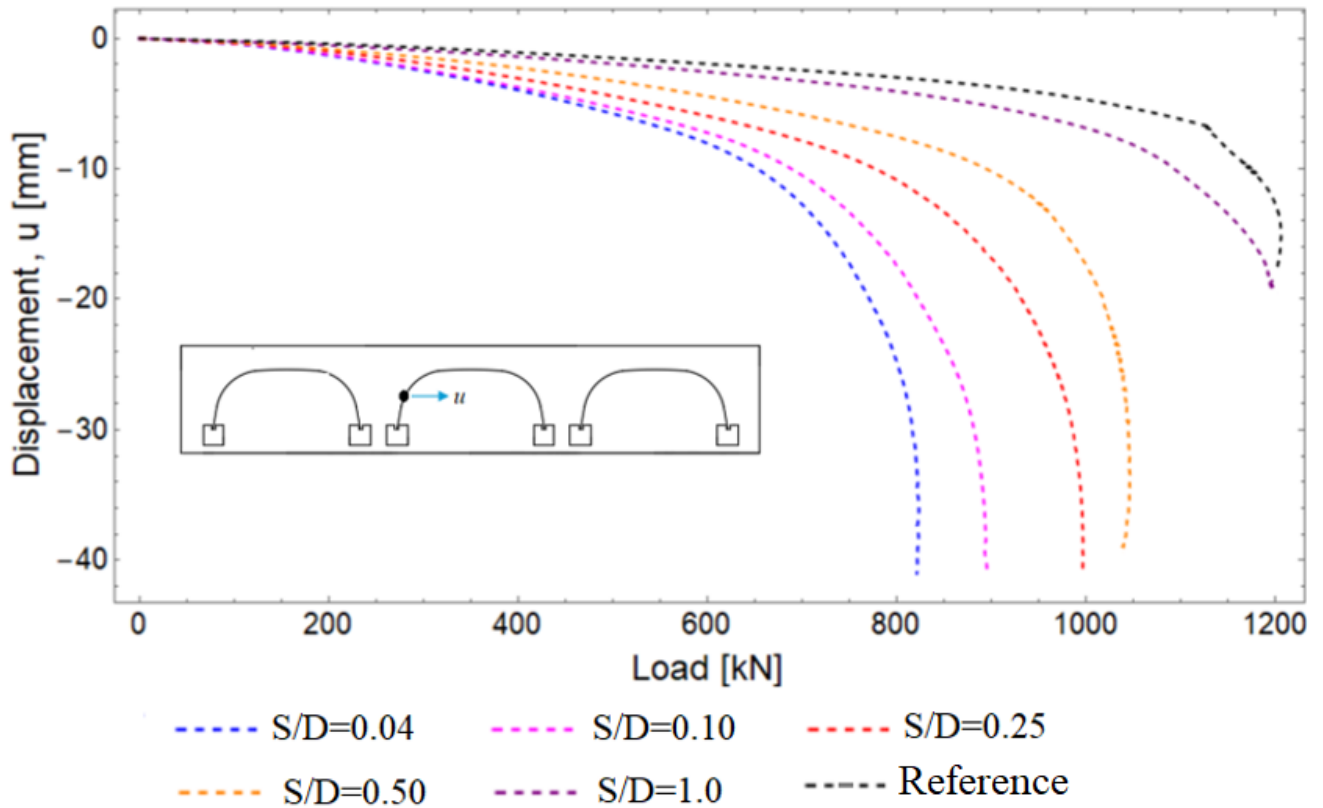


Figure 7.32: Load displacement curve at the haunch of central shell

Figs 7.32 and 7.32 illustrate the load–lateral displacement curves at the haunch section of the central and lateral shells, respectively. At the haunch section of both loaded central shell and lateral shell, outward deflection is observed, with the magnitude decreasing as the S/D ratio increases. For instance, at peak load, the lateral displacement at the haunch of the central shell is approximately 40 mm for S/D=0.04, S/D=0.10, and S/D=0.25, whereas it reduces to around 33 mm and 20 mm for S/D=0.5 and S/D=1.0, respectively. In comparison, the reference displacement is measured at 17 mm. Moreover, the lateral displacement under peak load at the haunch of the lateral shell indicates values of 37 mm, 37 mm, 34 mm, 25 mm, and 20 mm for S/D=0.04, S/D=0.10, and S/D=0.25, S/D=0.5 and S/D=1.0, respectively.

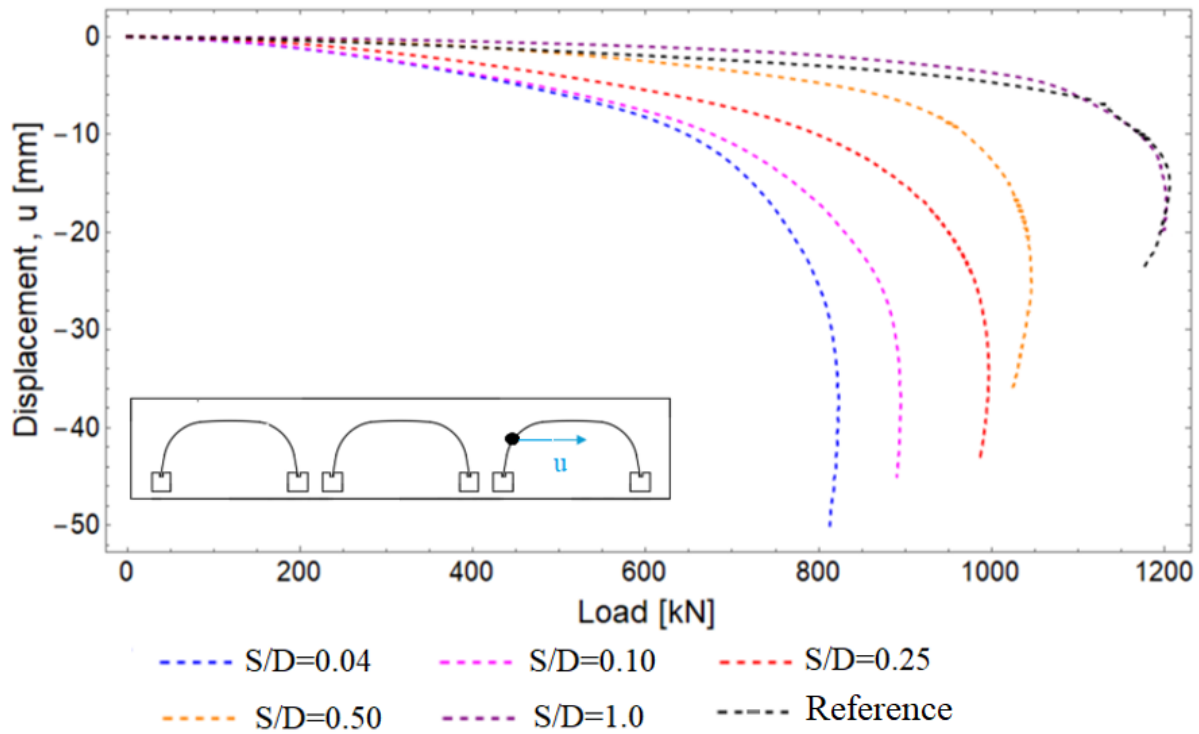


Figure 7.33: Load displacement curve at the haunch of lateral shell

7.3.2. Bending moment

The bending moment distribution for reference model is extracted at failure and shown in Fig. 7.35. In the reference model, at the failure load the maximum bending moment of 42.56 kNm/m is observed at the crown section, corresponding to the stiffened section of the shell. However, in other sections of the shell, the maximum negative bending moment of -24.18 kNm/m is observed around the haunch section. This maximum negative bending moment corresponds to the main shell without stiffening. And also, the bending moment around the shoulder is 24.5 kNm/m, this particular location is at the end of the stiffening rib or at the end of the top radius. The distribution of the bending moment is almost symmetrical.

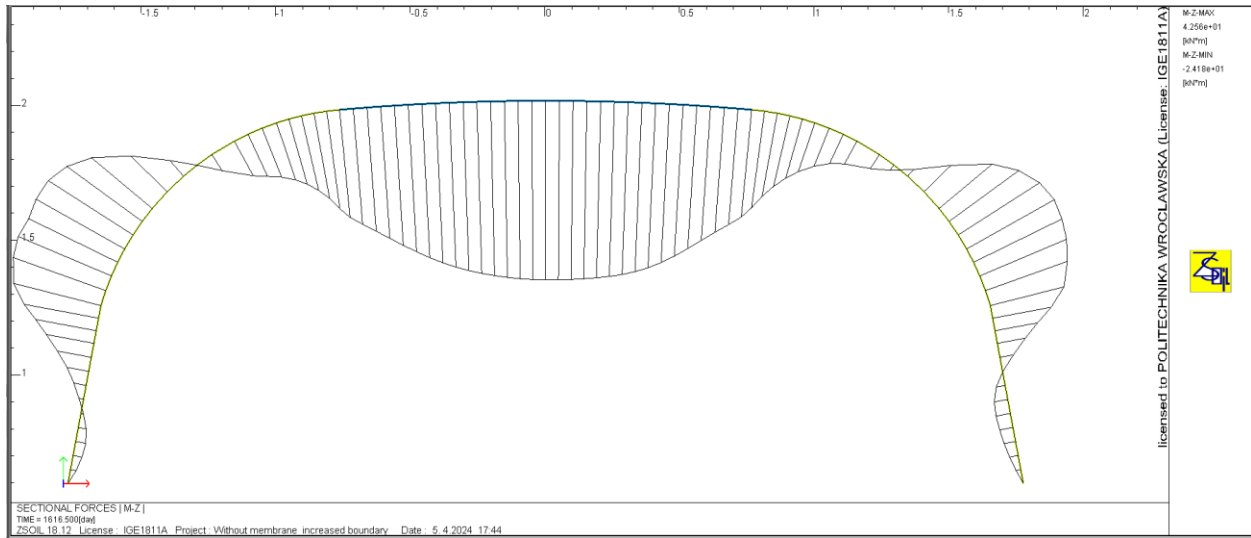


Figure 7.34: Bending moment distribution at failure load for reference model

The bending moment distributions for both lateral and central shells are illustrated in Fig. 7.35 to Fig. 7.39 for various S/D ratios. It is evident that the bending moment of the central shell at the crown exceeds the value at the haunch and shoulder due to the presence of the stiffening rib at the crown section. The distribution of bending moment is for both central and lateral shells for all considered models as shown on Fig.34 to Fig.39.

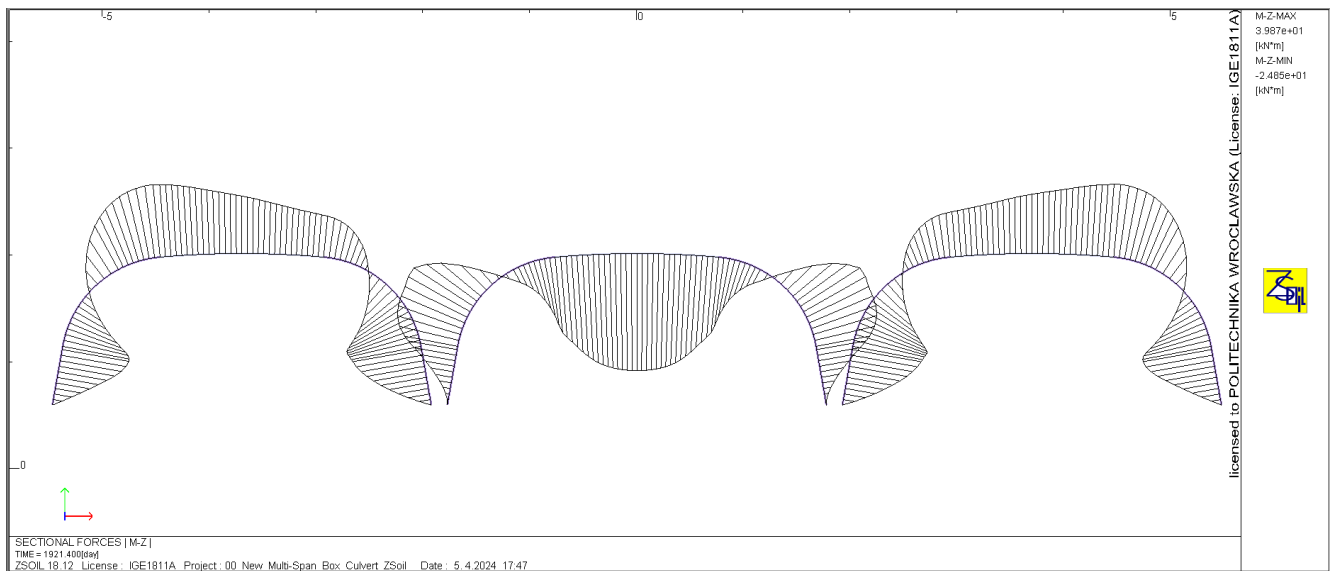


Figure 7.35: Bending moment distribution at failure load for S/D=0.04

For the lateral shells, the maximum bending moment value is identified at the bottom section of the haunch for S/D=0.04, S/D=0.10, and S/D=0.25, as depicted in Figure 7.35, Figure 7.36, and

Fig. 7.37, respectively. These locations correspond to the initiation points of plastic hinge formation. As described in Fig. 7.36, the maximum bending moment at the crown is 39.69 kNm/m for the central shell and -20.35 kNm/m for the lateral shell. The negative bending moment at the crown of the lateral shell corresponds to the upward deflection of the lateral shell when the central shell is loaded to failure.

Meanwhile, the maximum bending moment around the haunch is -24.28 kNm/m for the central shell and 25 kNm/m for the lateral shell. The occurrence of maximum bending moment in the lateral shell at the haunch section can be attributed to the following phenomenon: as loading increases on the central shell, the crown section deflects downward while the haunch section deflects outward. This outward deflection induces lateral stress on the lateral shell, causing it to deflect inward. Another critical bending moment is observed at the shoulder section, measuring 24.54 kNm/m for the central shell and -24.76 kNm/m for the lateral shell.

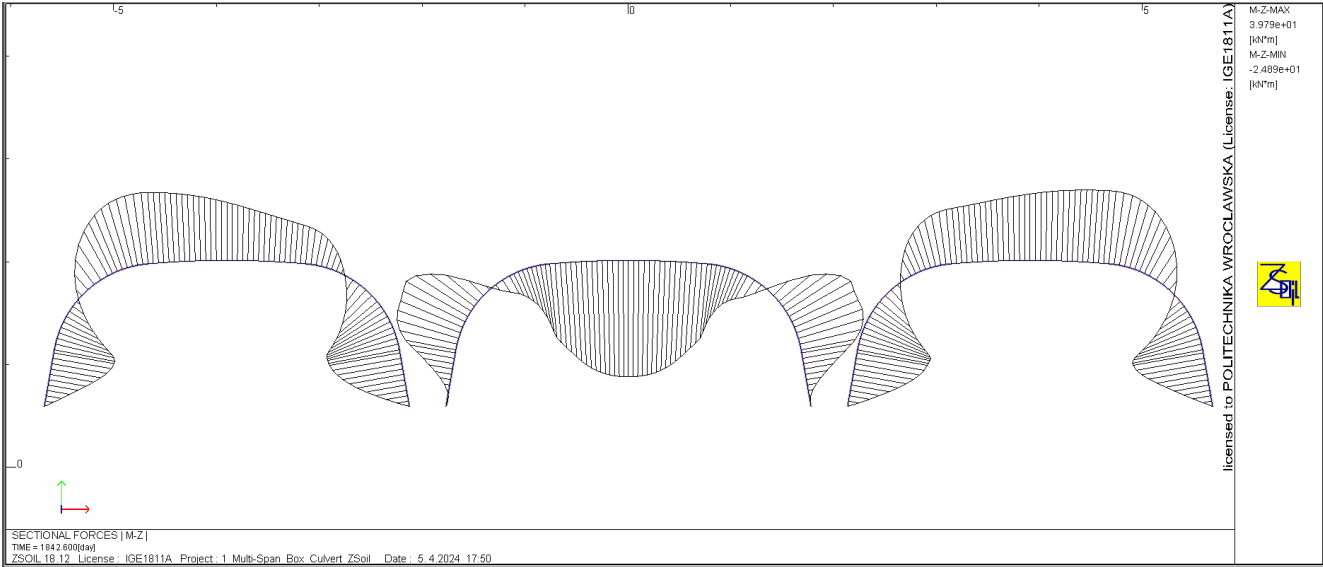


Figure 7.36.: Bending moment distribution at failure load for S/D=0.10

The bending moment distribution under failure load for Model-01 (S/D=0.1) is depicted in Fig. 7.36. Similar to S/D=0.04, the maximum bending moment of 39.79 kNm/m is observed at the crown for the central shell, while it is 25.07 kNm/m around the haunch for the lateral shell. Notably, the bending moment at the crown is less than that at the haunch for the lateral shells. Additionally, the haunch of the central shell exhibits a bending moment of -24.34 kNm/m. At the

shoulder section, the bending moment is 24.50 kNm/m for the central shell and -24.66 kNm/m for the lateral shell.

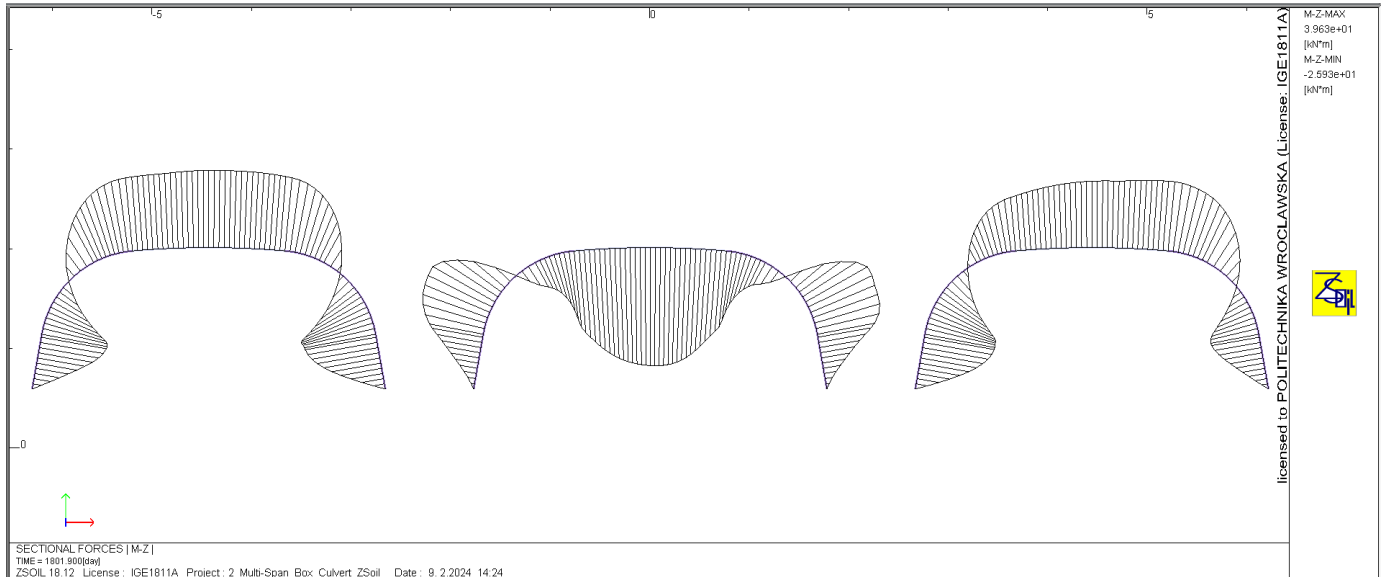


Figure 7.37: Bending moment distribution at failure load for $S/D=0.25$

When the ratio of $S/D=0.25$, the maximum bending moment is recorded as 39.63 kNm/m and -25.93 kNm/m at the crown of the central and lateral shells, respectively at the failure. Meanwhile, at the haunch section, the bending moments are -24.02 kNm/m for the central shell and 25.10 kNm/m for the lateral shell.

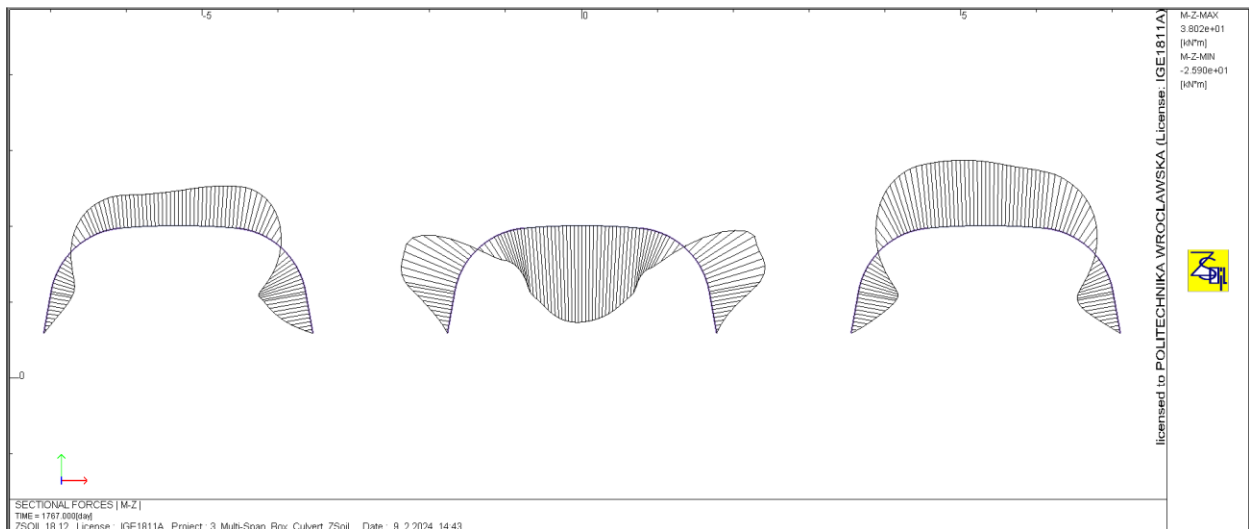


Figure 7.38: Bending moment distribution at failure load for $S/D=0.50$

At the shoulder section, the bending moments are 24.5 kNm/m for the central shell and -24.74 kNm/m for the lateral shell. This observation suggests that the critical points of the shell remain consistent with those observed in models with S/D ratios of 0.04 and 0.1. When S/D=1, the haunch of the lateral shell is no longer critical (See Fig. 7.39), as the values of bending moment at these locations are comparatively small compared to the corresponding values when S/D<0.5. Specifically, the value of bending moment at the haunch section has decreased by more than 50% compared to the values when S/D<0.5. This suggests that the central shell no longer influences their behavior. Consequently, at this ratio of S/D=1.0, the shells begin to react independently.

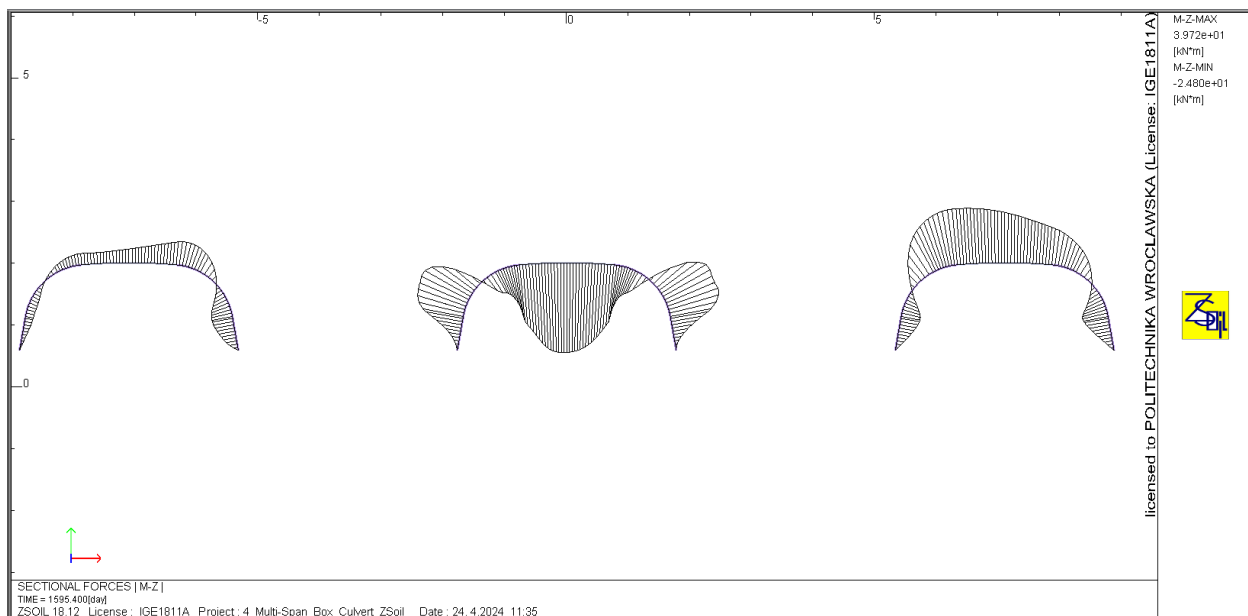


Figure 7.39: Bending moment distribution at failure load for (S/D=1.0)

Generally, as the S/D ratio increases, the bending moment at the crown of the central shell increases due to the reduction in lateral support from lateral shell decreases. While the bending moment at the crown and haunch section of the lateral shell decreases as S/D increases. This is due to the position of the load on central shell and as S/D increases the interaction between the shells decreases.

7.3.3. Axial force

The influence of spacing between adjacent shells on the maximum axial force at peak load is detailed in Table 7.3. As the ratio of S/D decreases, the axial force at both the crown and haunch of the loaded central shell also decreases. For example, in comparison to a reference model, the

axial force around the crown of the central shell experiences reductions of approximately 42%, 35%, 28%, 25%, and 5% for $S/D=0.04$, $S/D=0.10$, $S/D=0.25$, $S/D=0.50$, and $S/D=1.0$, respectively. These findings highlight how changes in shell spacing significantly affect load distribution within shell structures, with larger S/D ratios correlating with higher axial forces.

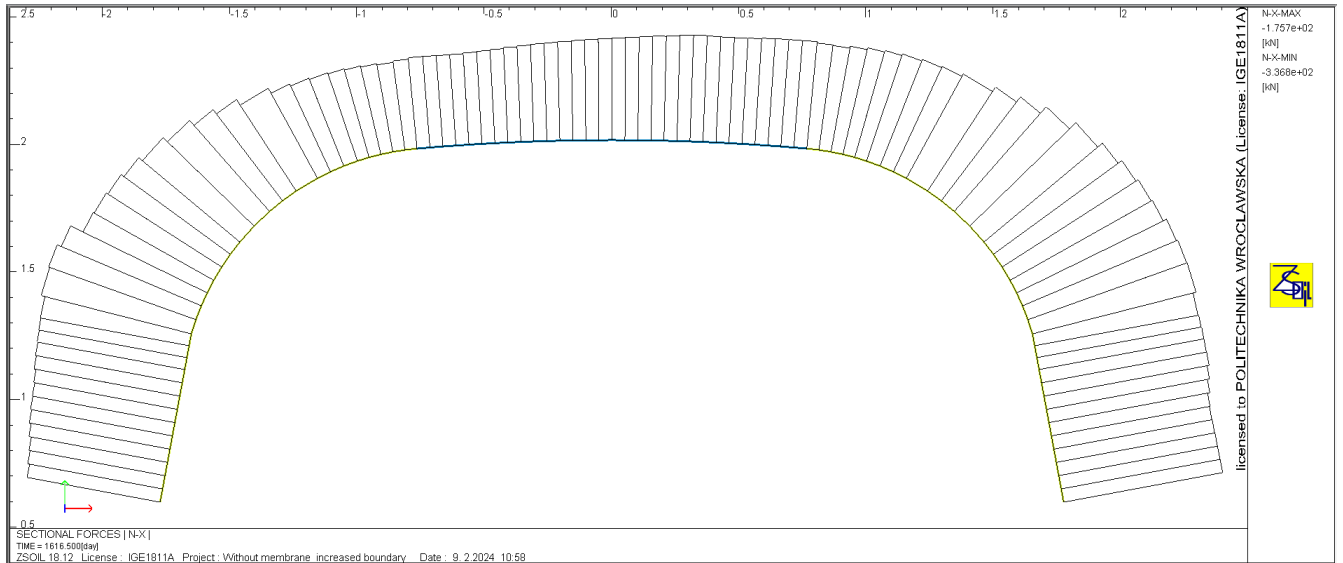


Figure 7.40: Axial force at failure load for reference model

The distribution of normal force for single span shell is shown in Fig.7.40, while the relationships between the maximum axial force and S/D ratios for both the central and lateral shells models are shown in Figs. 7.41 to 7.45

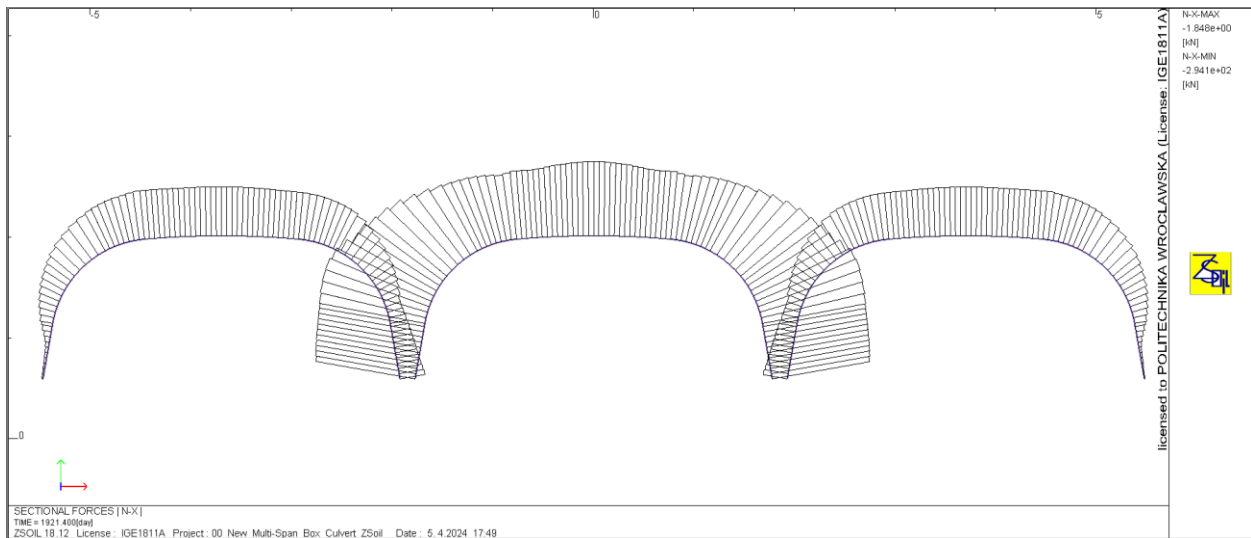


Figure 7.41: Axial force at failure load for model S/D=0.04

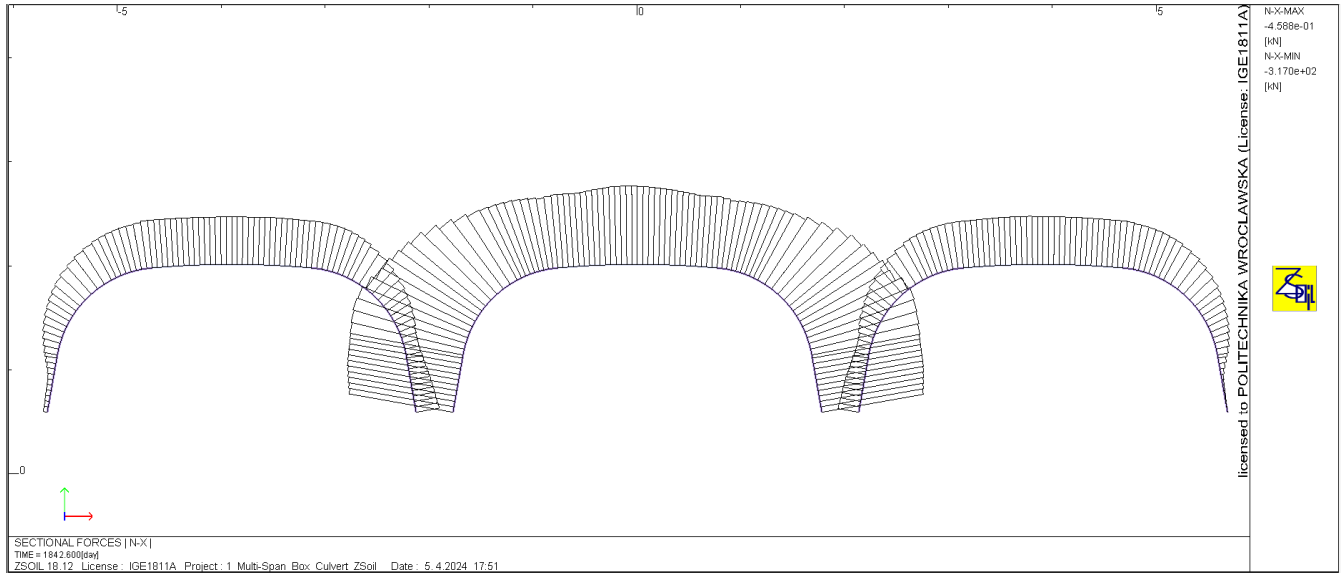


Figure 7.42: Axial force at failure load for model S/D=0.10

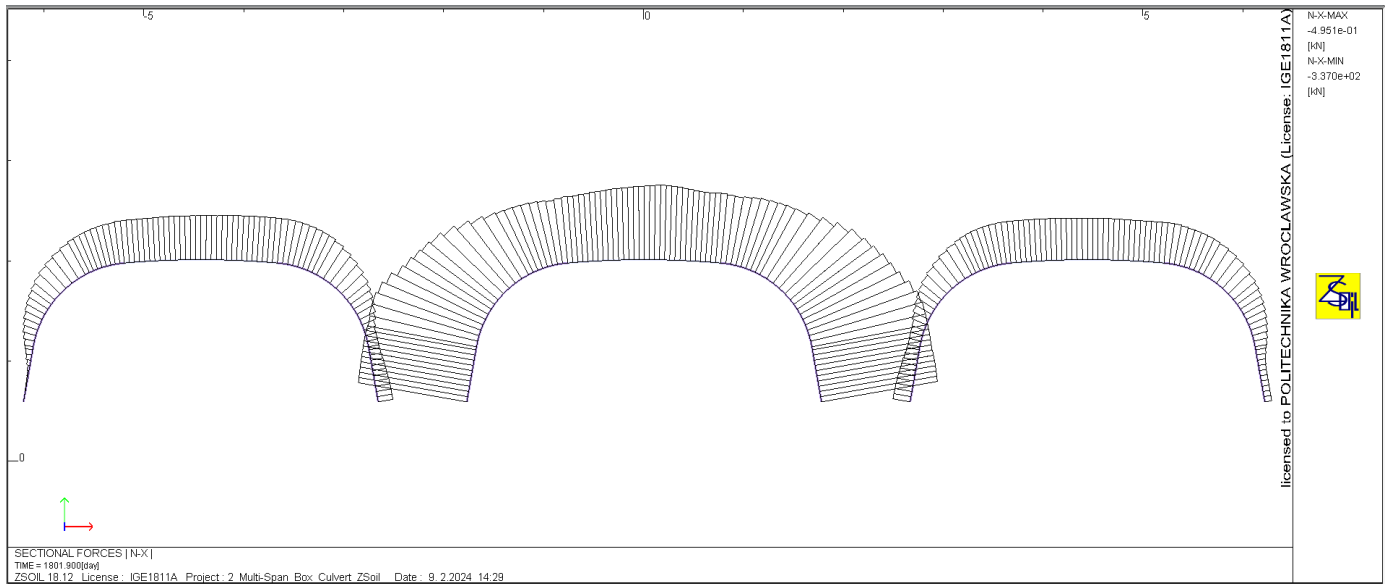


Figure 7.43: Axial force at failure load for model S/D=0.25

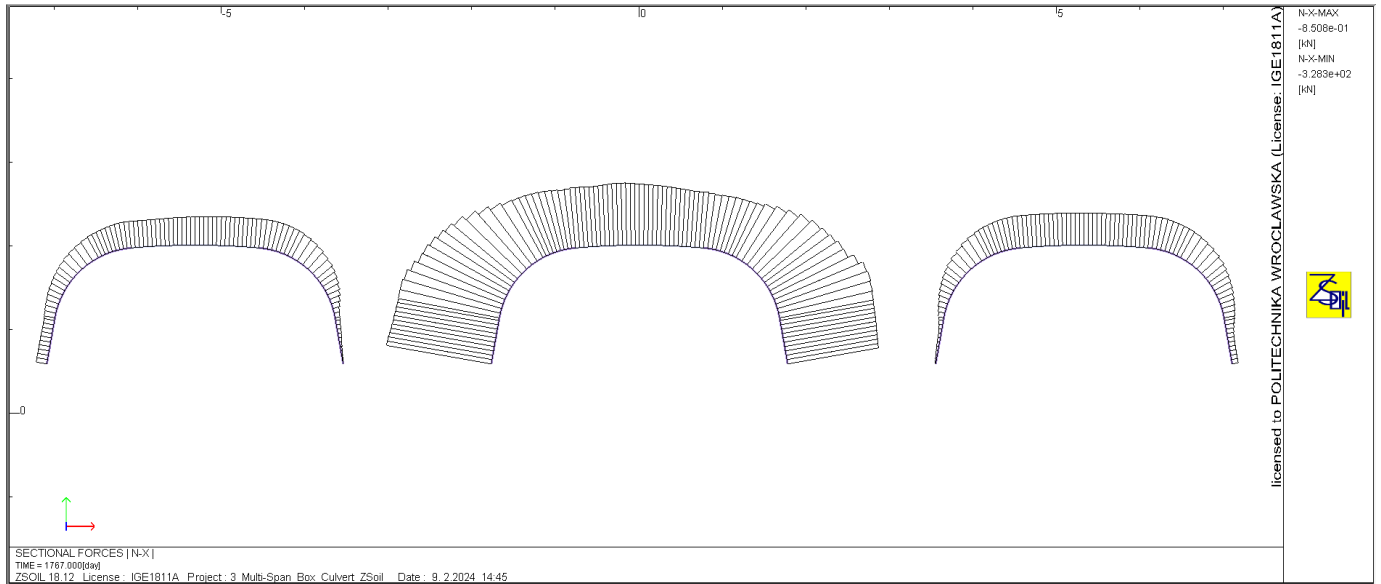


Figure 7.44: Axial force at failure load for model $S/D=0.50$

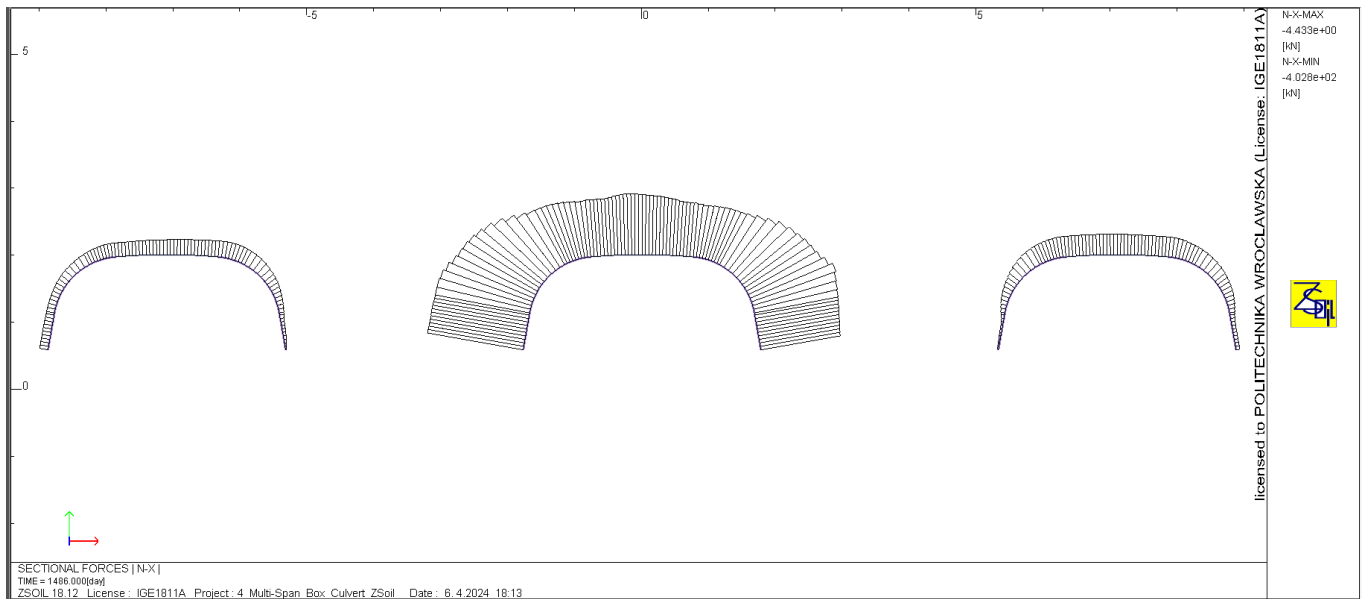


Figure 7.45: Axial force at failure load for model $S/D=1.0$

A comparison of the ultimate loads, maximum axial force, maximum bending moment at the crown, and haunch for central shell as well as lateral shells are presented in Table 7.2 for different S/D ratios under Model-c loading position. A comparison between single-shell and three-span shell configurations reveals that the maximum bending moment and axial forces at the crown under ultimate load decreases as the S/D ratio decreases. For instance, at the minimum S/D ratio of 0.04, the maximum bending moment at the crown of the central shell decreases by 19%, and the axial

force decreases by 42%. However, when S/D ratio increased to 1.0, the maximum bending moment at the crown of the central shell decreases only by 8% compared to the reference model, while the axial force decreases by 5%. Examining the comparison at the haunch of the central shell, the bending moment decreases as the S/D ratio increases. For instance, at an S/D ratio of 0.04, the maximum bending moment at the haunch of the central shell increases by 6% compared to the reference model. However, when S/D is 1.0, there is no significant difference in the bending moment at the haunches of the shell.

For the peak load, a comprehensive comparison between the single shell and multi-span shell at different S/D ratios is summarized in Table 7.3.

Table 7.2: Comparison of bending moment and axial force of central and lateral shells for different S/D ratios under Model-C at peak load

Model	Load kN	Bending Moment (kNm/m)				Axial force (kN/m)			
		Central shell		Lateral shell		Central shell		Lateral shell	
		Crown	Haunch	Crown	Haunch	Crown	Haunch	Crown	Haunch
S/D=0.04	823	53.87	-24.06	-16.24	23.22	-216.84	-358.09	-129.61	-52.47
S/D=0.10	895	53.55	-23.80	-18.33	23.66	-240.83	-361.23	-127.33	-47.76
S/D=0.25	997	57.17	-23.68	-19.65	23.89	-267.20	-400.22	-118.48	-36.70
S/D=0.50	1046	57.18	-23.53	-12.76	17.27	-280.91	-434.08	-90.08	-22.67
S/D=1.00	1198	60.71	-22.98	-11.28	12.58	-353.48	-481.23	-75.37	-20.76
Reference Model*	1206	66.32	-22.72	–	–	-372.85	-488.37	–	–

* Reference model is a model with no lateral shells

The bending moment and axial force in the unloaded lateral shells are markedly lower than the magnitudes observed in the loaded shell. As per reference [139], this indicates that the design of the shell walls is primarily governed by the loading applied above the shell.

7.3.4. Failure mode of the SSCs under Model-C loading position

For all models, the failure of the shell wall was not observed at the crown sections. This phenomenon can be attributed to the presence of stiffening ribs around the crown which covers the top radius of the shell (detailed in Chapter five). However, the loading-to-failure results indicate that in all considered models, the failure of the shell wall likely begins with yielding at the shoulder of the central shell. For example, in S/D=0.04, yielding which causes the first plastic

hinge initiated around the shoulder of the central shell at a corresponding load of approximately 655 kN. With this initial yielding around the shoulder, the deformation increases, and the load is transferred to another section of the central shell, leading to yielding in a section relatively close to the shoulder, i.e., the haunch of the central shell at a load of approximately 740 kN. As the load increases again, deformation around the haunch of central shell, i.e., horizontal deflection, increases, and the load is transferred to the lateral shells, resulting another yielding which forms a plastic hinge around the shoulder of the lateral shells at a load of approximately 822 kN. Next more plastic hinges are formed around the haunch of the lateral shell after the load reaches the peak. This suggests that the first two locations at which plastic hinge formed are on the loaded central shell. Once the central shell yields at these two points and experiences excessive lateral deformation around the haunch, it induces lateral stresses on the lateral shell, resulting in yielding in the lateral shell as well. This indicates that the failure mode of both the central and lateral shells is a localized bending failure at the shoulder and haunch. Moreover, in this loading condition, even though loading to failure is applied only to the central shell, the lateral shell also experiences failure.

For $S/D=0.1$, similar to $S/D=0.04$, the first yielding of the shell which causes the formation of plastic hinge around the shoulder of the central shell is observed when the load reaches around 680 kN. Compared when $S/D=0.1$, the load has increased by 4% to induce yielding at this location. The second plastic hinge occurs around the haunch of the central shell when the load reaches 782 kN, representing a 6% increase compared to Model-00. More plastic hinges are formed around the shoulder and the haunch of the lateral shell, when the load approximately reaches 894 kN. This load is almost equal to the peak load observed in this model, indicating a 10% increase compared to $S/D=0.1$. The sample graph illustrating the bending moment deflection curve for the selected element of the fully yielded shell cross-section is presented in Fig. 7.46 for the central shell and Fig.7.47 for the lateral shell, respectively. In both graphs, the ultimate capacity of the cross-section of the shell due to combined bending and axial force is reached at both the shoulder and haunch

under ultimate load. The crown of the shell is far from yielding due to stiffening rib.

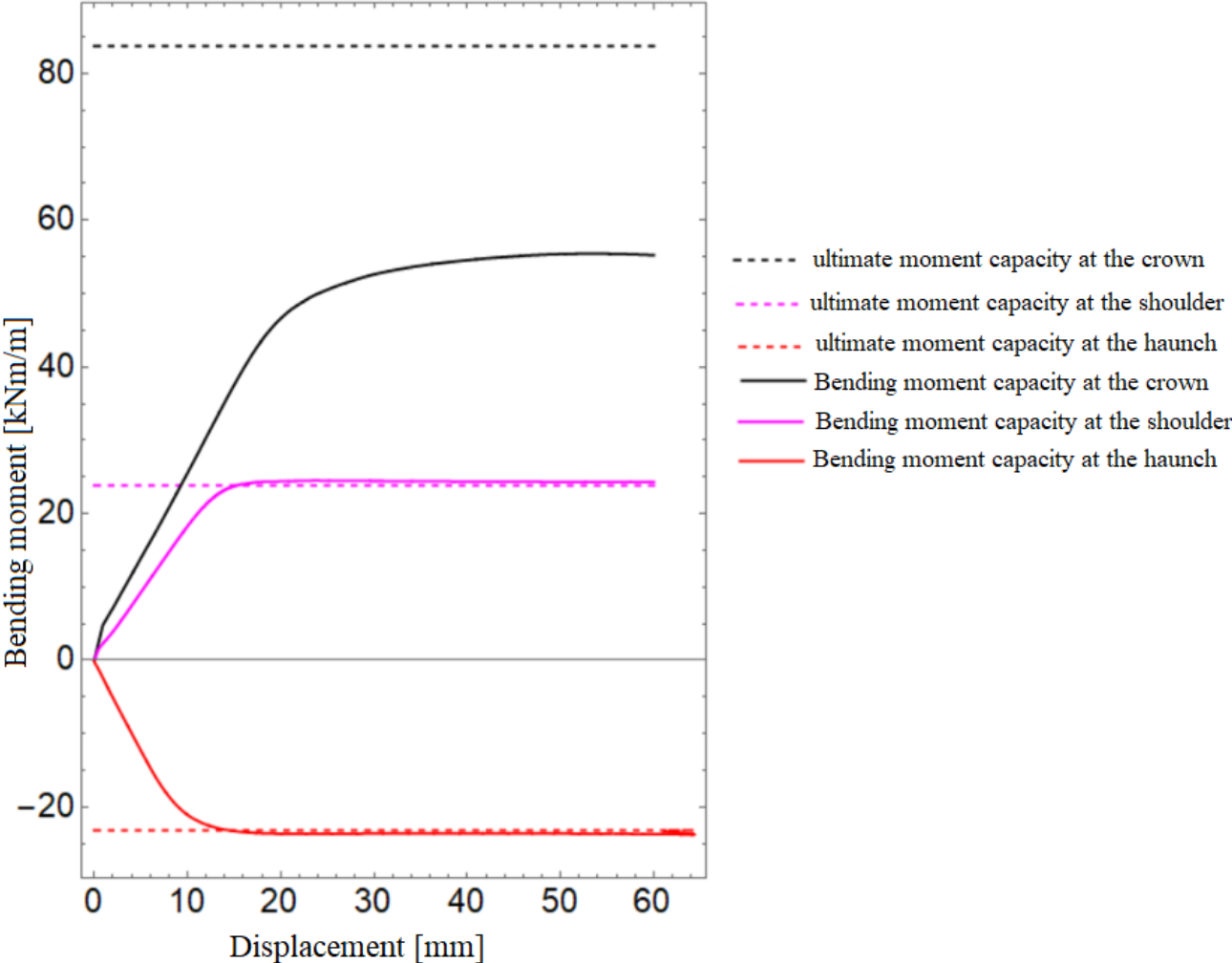


Figure 7.46: Bending moment–vertical displacement curve for central shell ($S/D=0.10$)

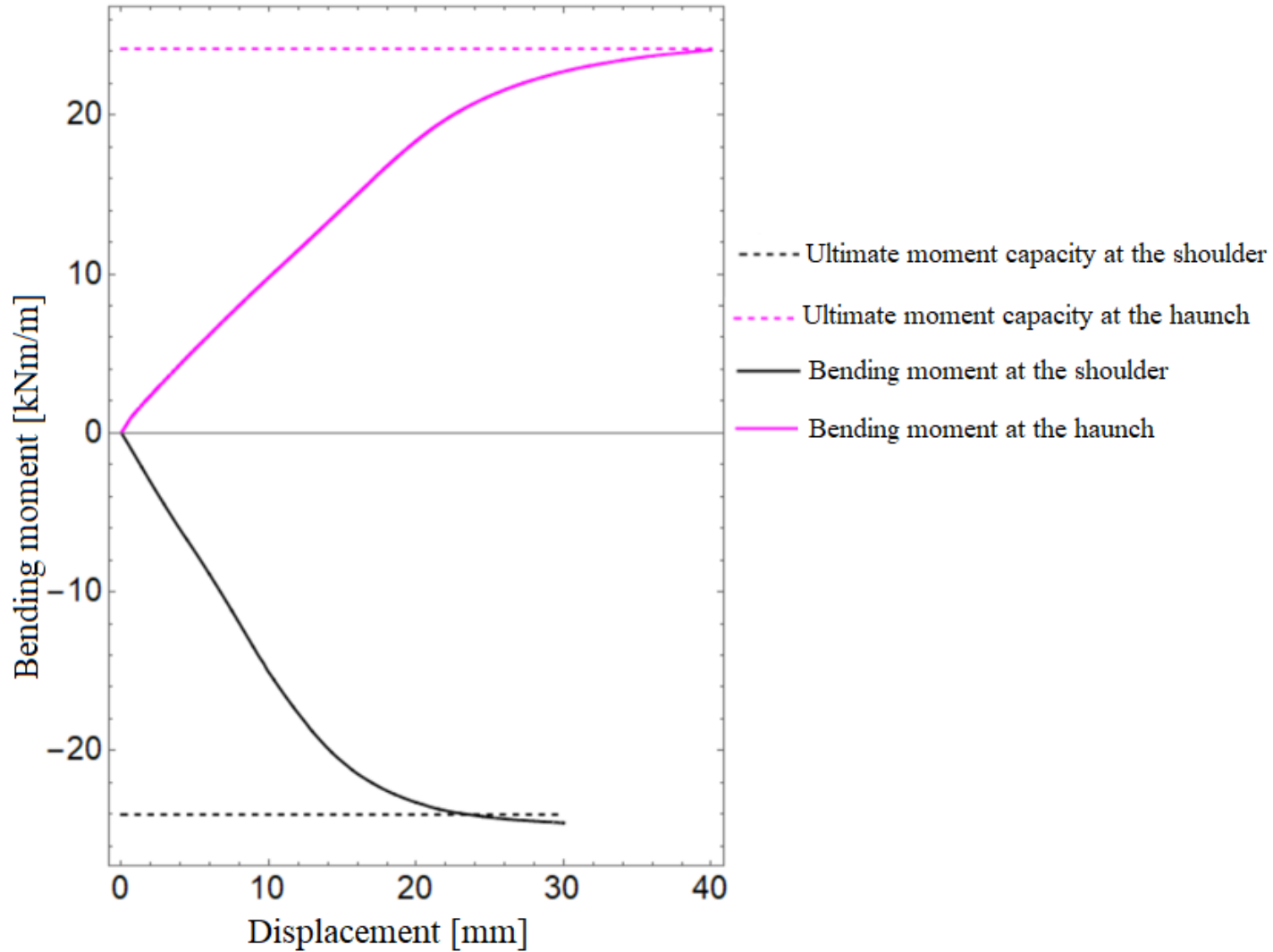


Figure 7.47: Bending moment–vertical displacement curve for Lateral shell ($S/D=0.10$)

For Model $S/D=0.25$, the first yielding is observed at the shoulder of the central shell when the load reaches around 758 kN. Compared to Model $S/D=0.04$, the load that causes the first yielding is increased by 16%. The second yielding is located around the haunch of the central shell when the load reaches 996 kN. Compared to Model $S/D=0.04$, the load that causes the second yielding is increased by 35%. The third and fourth locations of yielding are at the haunch and shoulder of the lateral shell after the load surpasses the ultimate limit.

For Model $S/D=0.50$, the first yielding is observed at the shoulder of the central shell when the load is approximately 864 kN. Compared to Model $S/D=0.04$, the load that causes the first yielding is increased by 32%. The second yielding occurs around the haunch of the central shell when the load reaches 1007 kN. Compared to Model $S/D=0.04$, the load that causes the second yielding is

increased by 36%. The third yielding is observed around the shoulder of the lateral shell. This yielding was observed after the ultimate load, during the post-failure of the central shell. However, unlike the previous three models, yielding was not observed around the haunch of the lateral shell. Thus, when $S/D=0.50$ the only failure observed in the lateral shell around the shoulder.

For Model $S/D=1.0$, similar to previous models, the failure was initiated at the shoulder of the central shell when the load is approximately 921 kN. Compared to Model $S/D=0.04$, the load that causes the first yielding is increased by 41%. The second yielding is located around the haunch of the central shell when the load reaches 1105 kN. Compared to Model $S/D=0.04$, the load that causes the second yielding is increased by 49%. The third location of the fully yielded cross-section of the shell is around the shoulder of lateral shell, once the load reaches peak. However, yielding does not occur in the other section of the lateral shell; thus, the failure of the shell in this particular model is attributed to the bending failure of both central and lateral shells. Compared with the single reference model, the load which causes the first yielding at the shoulder of the central shell is almost equal to the load which causes the yielding at the shoulder of the single span shell. Thus, the presence of the lateral shell has no influence on the failure of the central shell.

From all considered models, it can be seen that yielding initiates at the shoulder of the central shell in loading scenario Model-C, (when the load is applied to the central shell). Similar findings are observed in [63], where laboratory tests were conducted on the behavior of a horizontal-ellipse culvert during service and ultimate load. The study concluded that the failure of the culvert is attributed to yielding at the shoulder section of the shell.

The analysis of failure modes for both the central and lateral shells in the multi-span SSCS, considering interaction effects, is summarized in Table 7.3. It is observed that the shells experienced failure prior to the interaction equation reaching unity at their respective crowns. This suggests that the crowns of the shells did not undergo full yielding under peak loading conditions. As illustrated in Chapter Five, this phenomenon can be attributed to the presence of additional reinforcement ribs at the crown section of the shell.

Table 7.3: Summary of critical location and failure mode for all models under loading position –Model-C

Model	<i>Interaction value due to combined bending moment and axial force based on Eq. (5.4)</i>					
	Loaded central shell			Lateral shell		
	Crown	Shoulder	Haunch	Crown	Shoulder	Haunch
S/D=0.04	<1	1.0	1.0	<1	1.0	1.0
S/D=0.10	<1	1.0	1.0	<1	1.0	1.0
S/D=0.25	<1	1.0	1.0	<1	1.0	1.0
S/D=0.5	<1	1.0	1.0	<1	1.0	<1
S/D=1.0	<1	1.0	1.0	<1	1.0	<1

Furthermore, from all the considered models of different spacing to span ration, the wall crushing (yielding of the shell section due to axial forces only) has not been observed since the capacity of the shell against compression is much greater than the maximum axial force observed in the calculation.

7.4. Analysis and Behavior of multi-span SSCS under ultimate load (Model-R)

In this loading position, the loading to failure is imposed to the lateral shell on the right side of central shell, thus the central shell and other lateral shell was not subjected to loading. The influence of the loaded lateral shell on the performance of central shell was examined by varying the ratio of spacing to span. Moreover, the failure mode of lateral shell and central shell is also investigated.

7.4.1. Load displacement curve

The upward deflection behavior of the crown of central shell across various S/D ratios reveals consistent trends in structural response under asymmetric loading conditions. In Model S/D=0.04

and Model $S/D=0.10$, similar upward deflection patterns are observed at peak loads of 856 kN and 896 kN respectively, with the central shell exhibiting comparable deflection magnitudes. This trend continues in Model $S/D=0.25$ and Model $S/D=0.50$, where peak loads of 998 kN and 1054 kN result in nearly identical upward deflection values of around 17 mm at the crown of the central shell. Finally, in Model $S/D=1.0$, the upward deflection at the peak load of 1174 kN is recorded at 16 mm.

The observed deflection patterns highlight the load transfer mechanism within the structure. The findings suggest that when $S/D < 0.5$, the upward deflection of the central shell increases as shown in Fig.7.48. This aligned with the influence of lateral pressure from loaded lateral shell. As the lateral shell undergoes loading and yielding, plastic hinges form at critical locations, leading to increased deformation at the crown and haunches of the lateral shells. This deformation, in turn, exerts lateral stress on the adjacent central shell, resulting in upward deformation, particularly at its crown section.

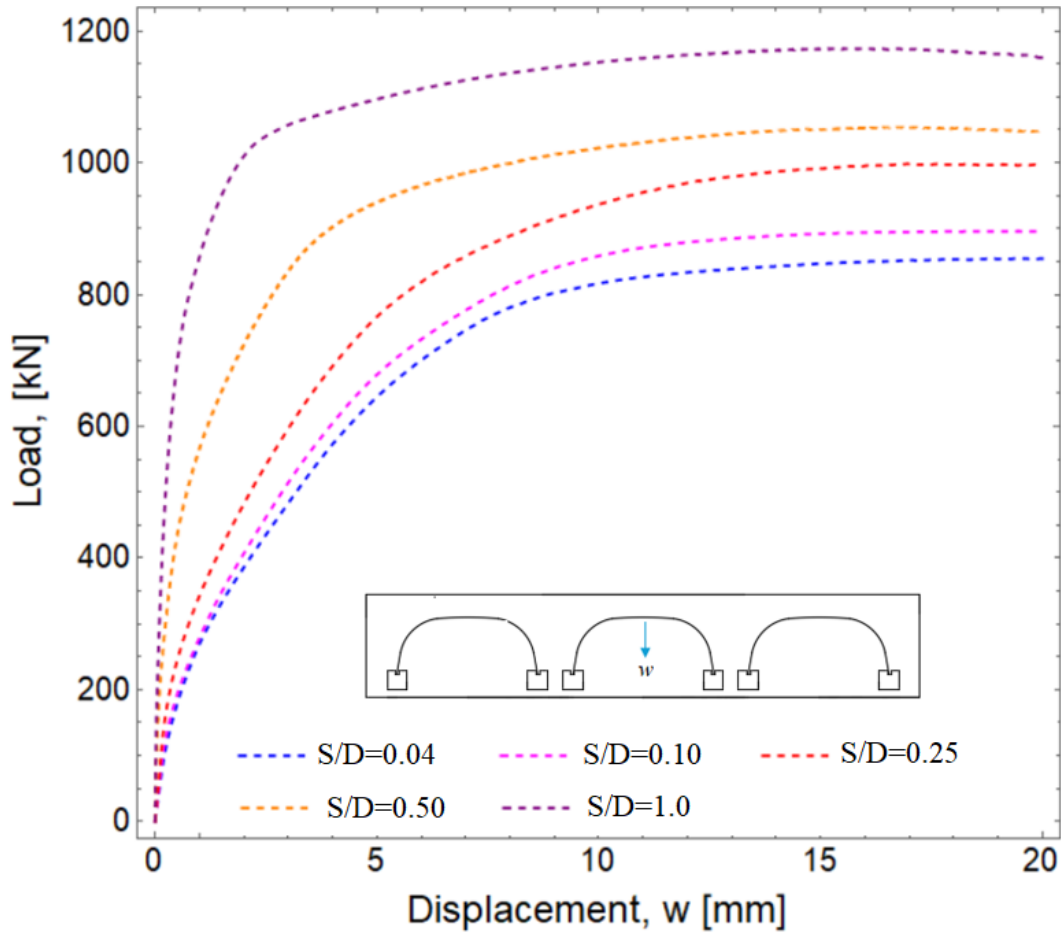


Figure 7.48: Load displacement curve at the crown of central shell.

The effect of the S/D ratio is evident, with increasing ratios leading to decreased upward deflection of the central shell. This trend underscores the influence of structural proportions on load transfer behavior, where higher S/D ratios indicate greater stiffness and resistance to deformation in the central shell.

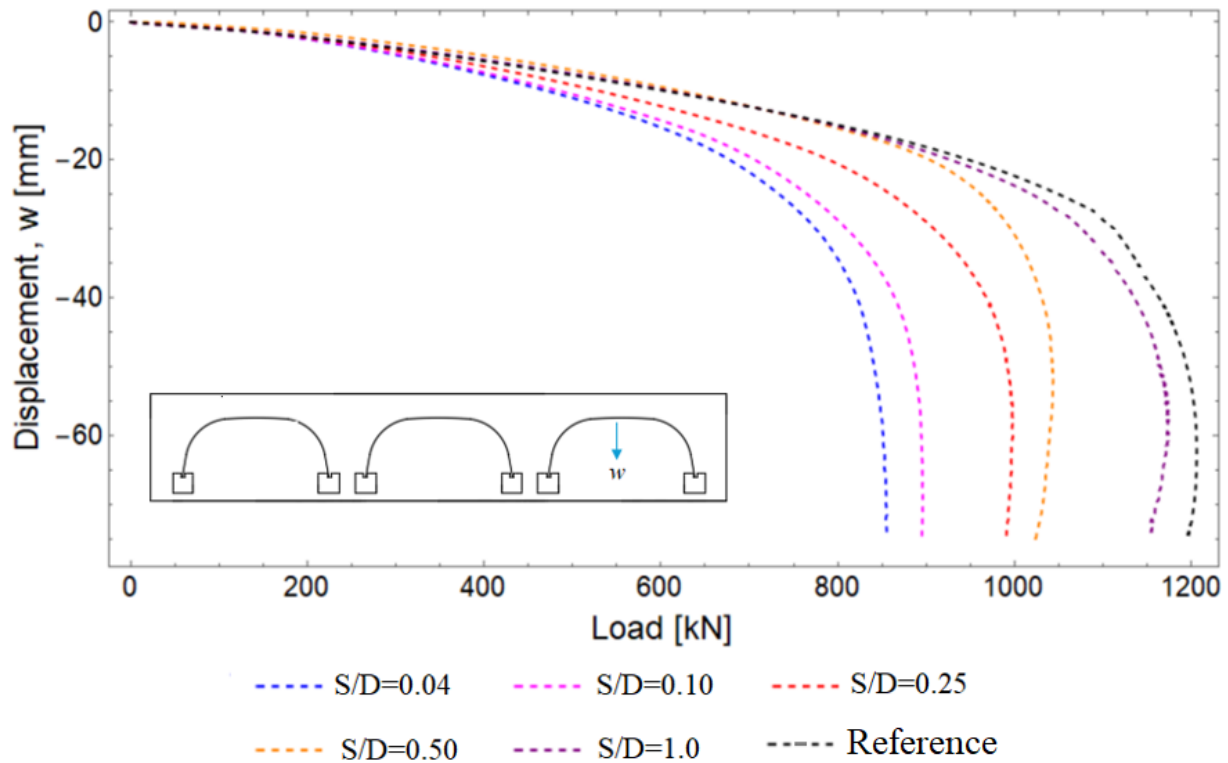


Figure 7.49: Load displacement curve at the crown of the loaded lateral shell.

The load-displacement curve of the loaded lateral shell is depicted in Fig. 7.49. At the peak load, the displacement at the crown of the loaded lateral shell measures 71 mm, 69 mm, 65 mm, 63 mm, and 60 mm respectively for Model S/D=0.04, Model S/D=0.10, Model S/D=0.25, Model S/D=0.50, and Model S/D=1.0. Comparing these displacements with the reference model, which recorded a displacement of 62 mm at the peak load, reveals an increase of 18%, 16%, and 8% for Model S/D=0.04, Model S/D=0.10 and Model S/D=0.25 respectively. However, no significant difference is observed in S/D=0.50, and Model S/D=1.0. This suggests that, in terms of vertical displacement at the peak load, the presence of lateral shells has no significant influence on the central shell when $S/D > 0.5$. Moreover, when S/D is greater than or equal to 0.5, the load-displacement curve almost approaches that of the reference model without lateral shells, as depicted in Fig. 7.49, until the load reaches approximately 900 kN.

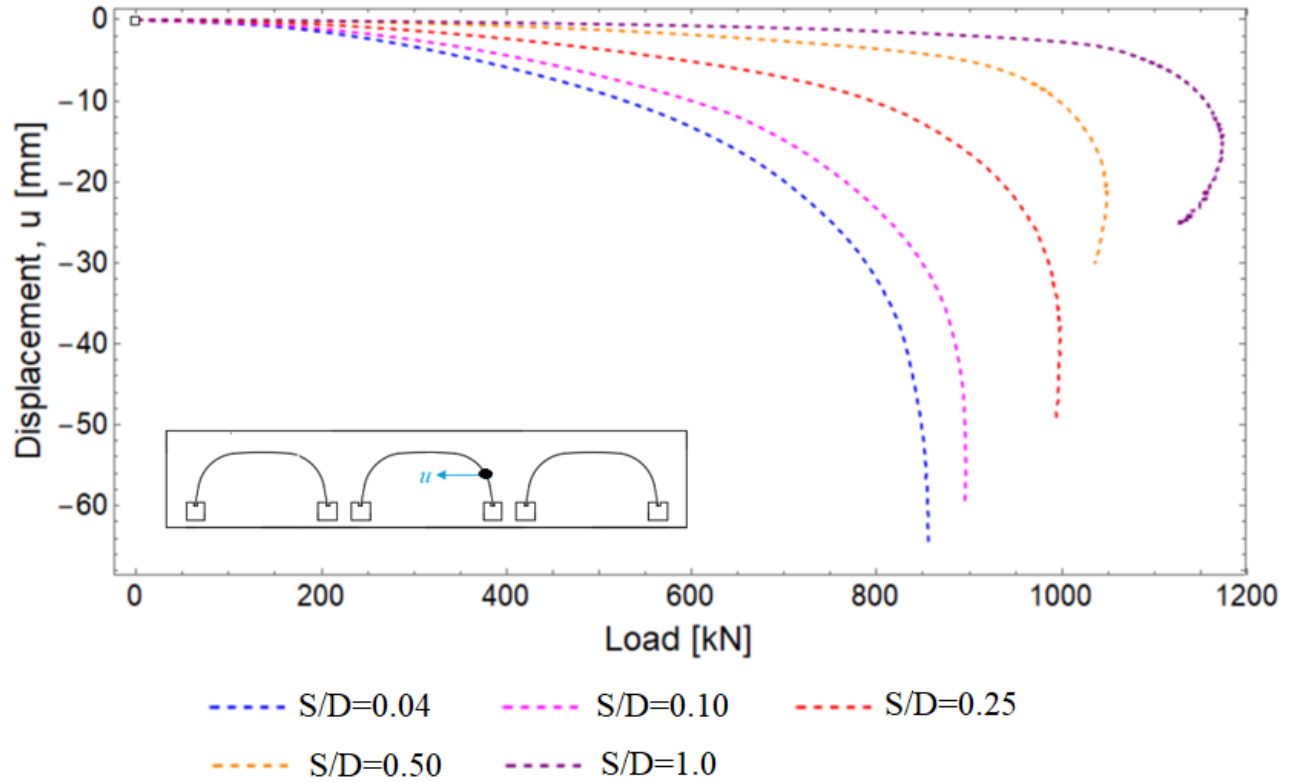


Figure 7.50: Load displacement curve at the haunch of central shell

The lateral displacements along the horizontal axis at the haunch of the central shell are shown in Fig 7.50. The lateral displacement at the haunch of the central shell at peak load is 61 mm, 54 mm, 38 mm, 22 mm, and 16 mm for Model S/D=0.04, Model S/D=0.10, Model S/D=0.25, Model S/D=0.50, and Model S/D=1.0 respectively. This shows that the lateral displacement of the shell decreases as S/D increases. Moreover, the lateral displacement when S/D=1.0 is almost less than 5 mm until the load approximately 1000 kN and the displacement increases with high rate once the load approaches to the peak load.

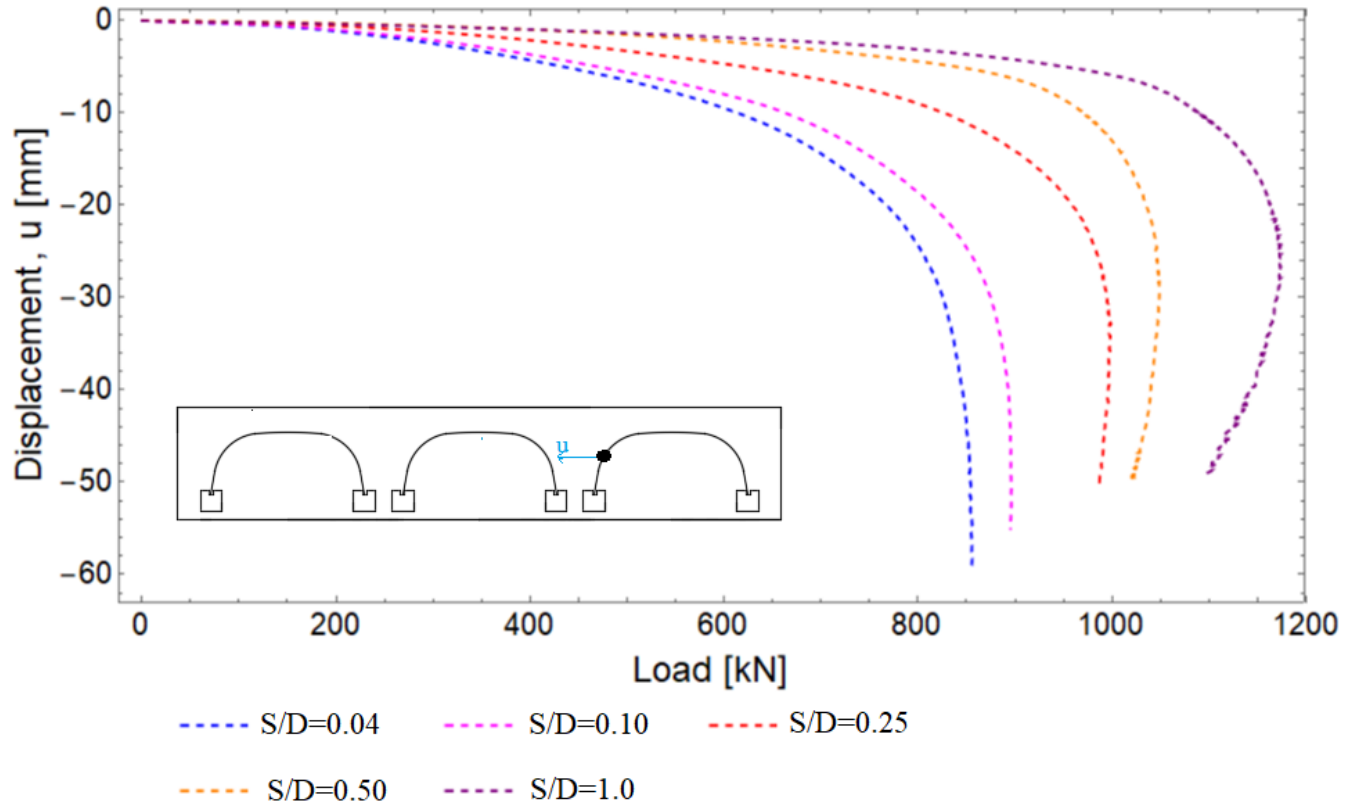


Figure 7.51: Load displacement curve at the haunch of the loaded lateral shell.

The lateral displacements at the haunch of the loaded lateral shell are shown in Fig 7.51. The lateral displacement at the haunch of the lateral shell at peak load is 55 mm, 50 mm, 33 mm, 29 mm and 27 mm for Model S/D=0.04, Model S/D=0.10, Model S/D=0.25, Model S/D=0.50, and Model S/D=1.0 respectively.

7.4.2. Bending moment

The analysis of the results offers profound insights into the behavior of both loaded lateral and unloaded central shells as influenced by varying S/D (spacing-to-diameter) ratios. A consistent trend emerges where the bending moment at the crown of the loaded lateral shell decreases proportionally with decreasing S/D ratios, while the bending moment at the haunches conversely increases. For instance, S/D=0.04, a notable 19% reduction in bending moment is observed compared to the reference model, indicating a clear relationship between S/D ratio and bending behavior. In contrast, the unloaded central shell exhibits an inverse pattern, with bending moments escalating at both the crown and haunches as the S/D ratio decreases. This phenomenon is

explicated by the interactive behavior between shells, elucidating a load transfer dynamic from the loaded lateral shell to the unloaded central shell.

The bending moment distributions are illustrated in Figure 7.52 to Figure 7.56 for various S/D ratios.

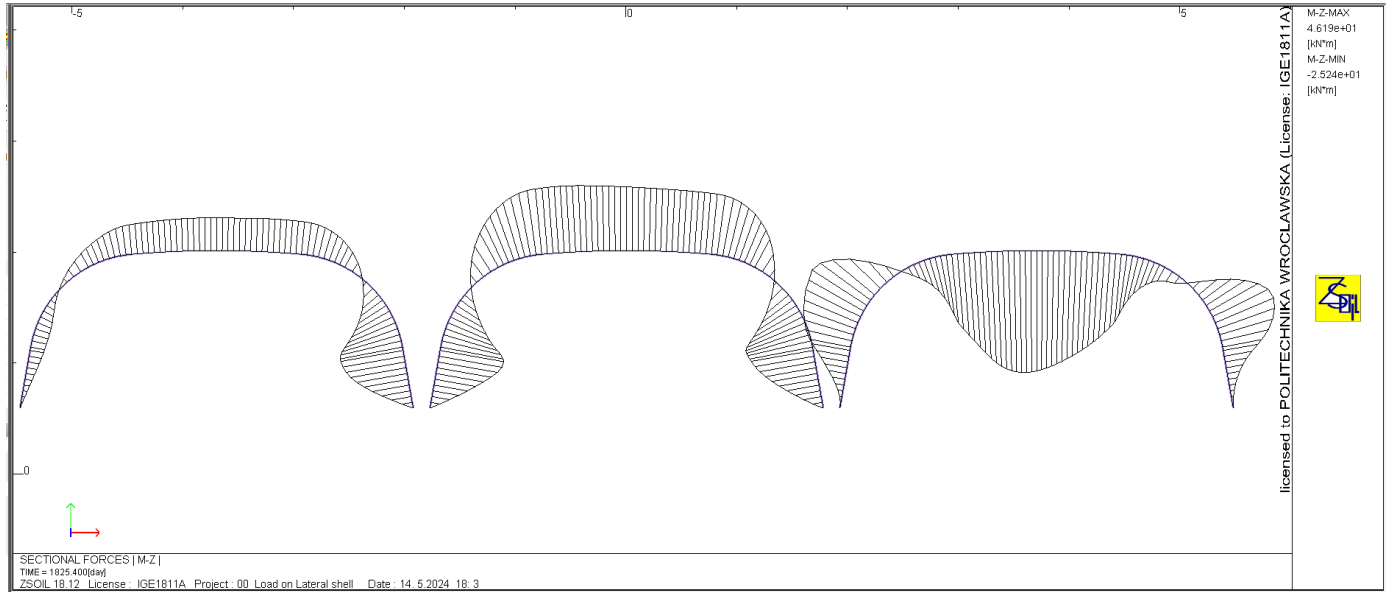


Figure 7.52: Bending moment distribution at failure load for ($S/D=0.04$)

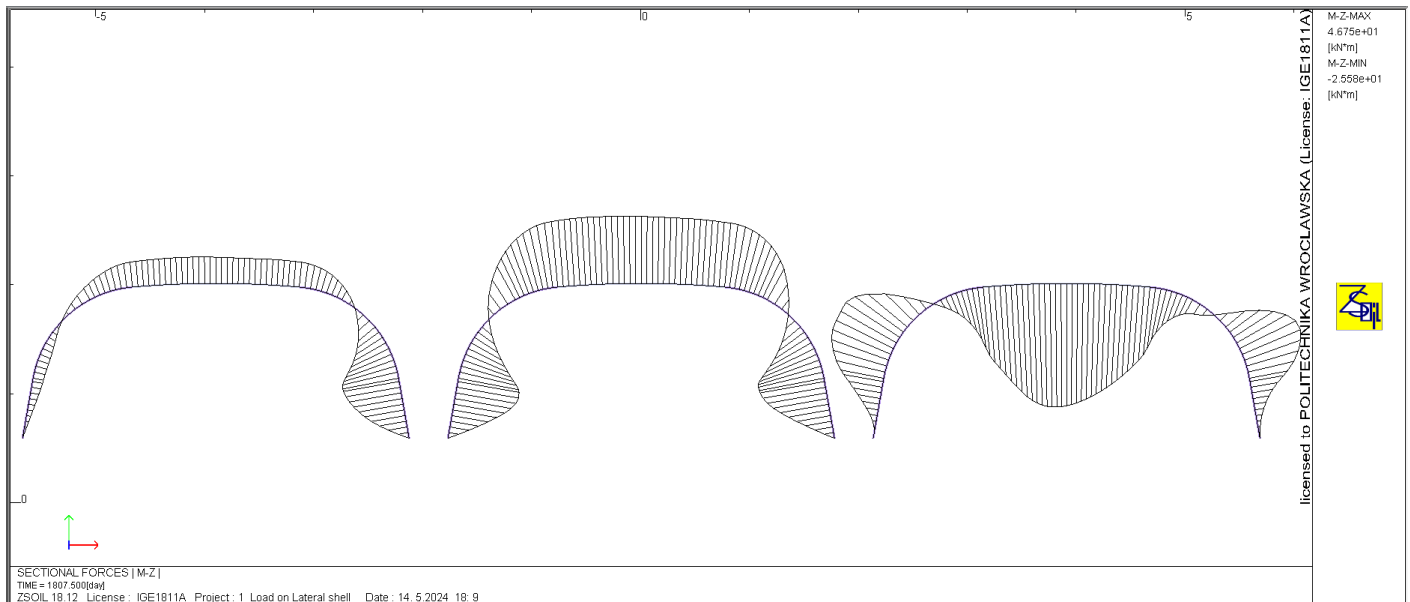


Figure 7.53: Bending moment distribution at failure load for ($S/D=0.1$)

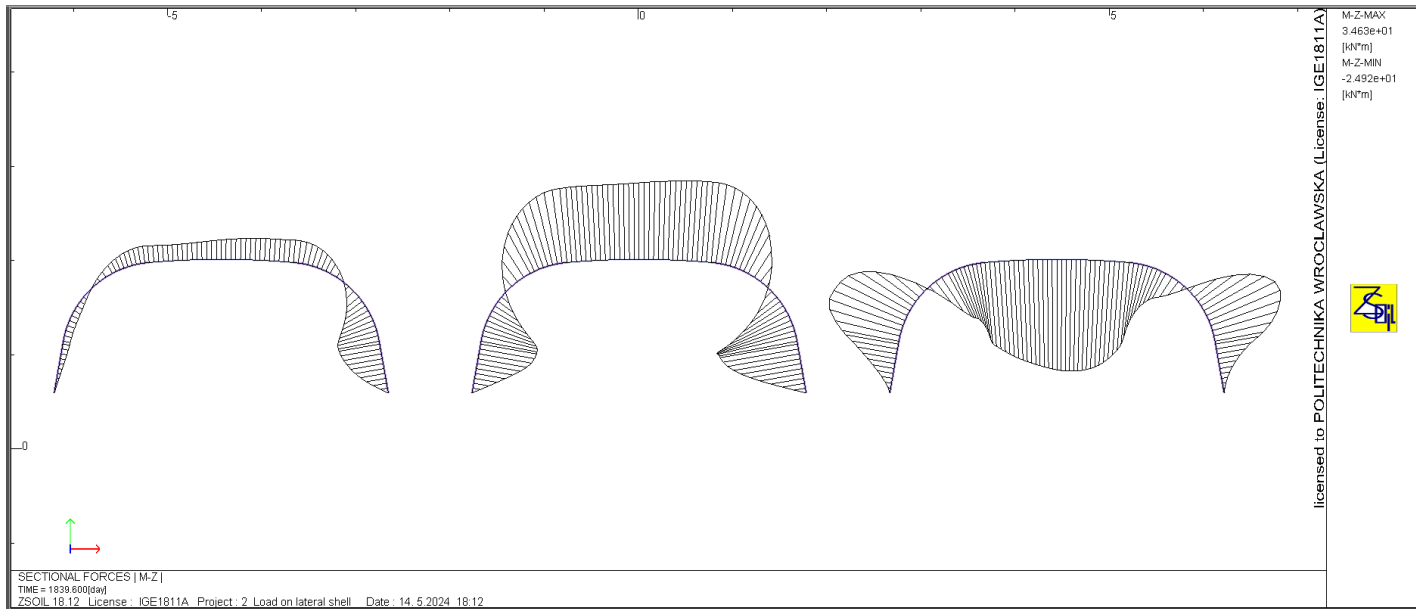


Figure 7.54: Bending moment distribution at failure load for ($S/D=0.25$)

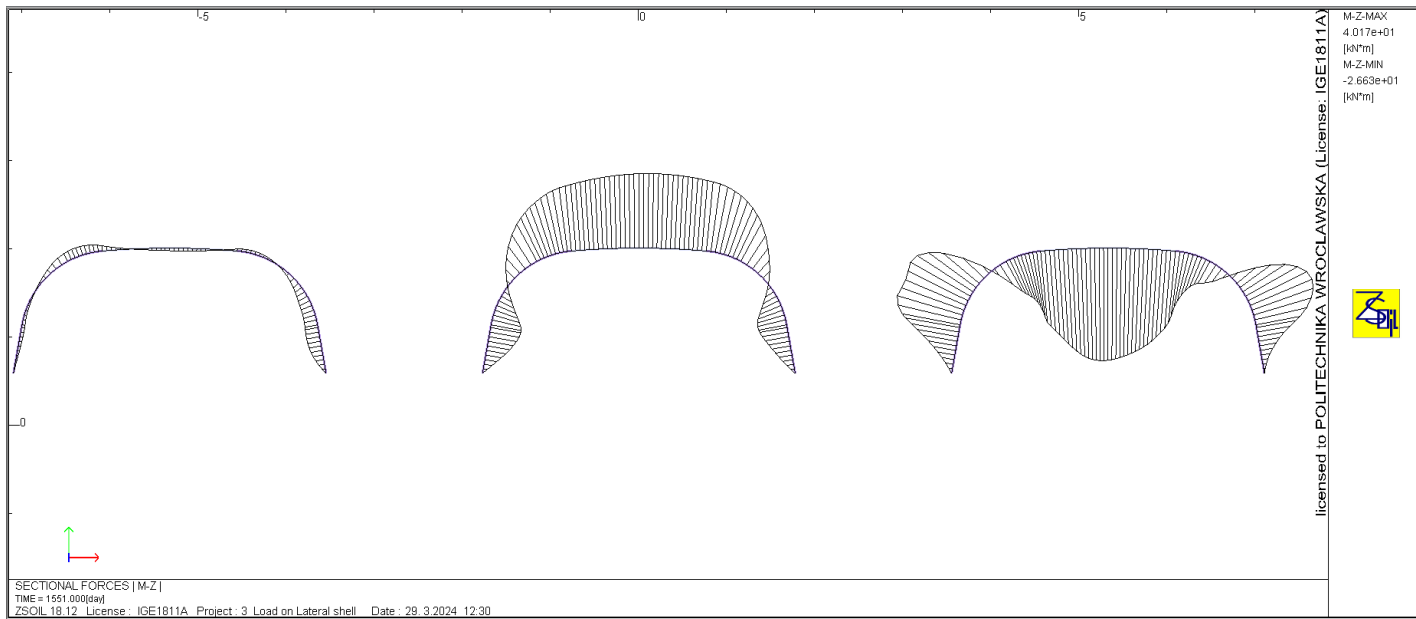


Figure 7.55: Bending moment distribution at failure load for ($S/D=0.5$)

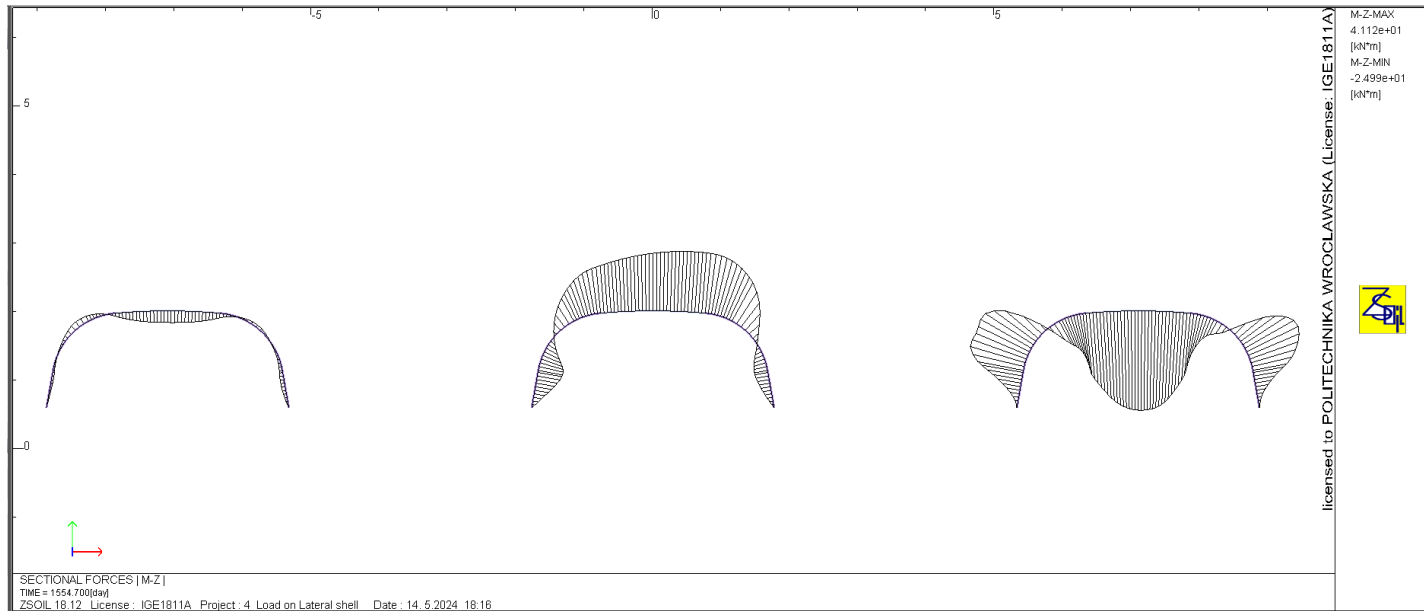


Figure 7.56: Bending moment distribution at failure load for ($S/D=1.0$)

7.4.3. Axial force

The analysis of the results axial forces provides profound insights into the behavior of both loaded lateral and unloaded central shells as influenced by varying S/D ratios. A consistent trend is observed where the axial forces at the crown of the loaded lateral shell decrease proportionally with decreasing S/D ratios, while they increase at both the crown and haunches of the unloaded central shell as the S/D ratio decreases. For instance, in Model $S/D=0.04$, axial forces at the crown of the loaded lateral shell decreased by 42% compared to the reference model, indicating a clear relationship between S/D ratio and axial force behavior. Conversely, axial forces increased at both the crown and haunches of the unloaded central shell across all S/D ratios. These findings emphasize the critical role of S/D ratios in influencing axial force distributions in multi-span shell configuration and provide valuable insights into load transfer and structural responses. The distribution of axial forces at the failure are shown in Figs 7.57 to 7.61

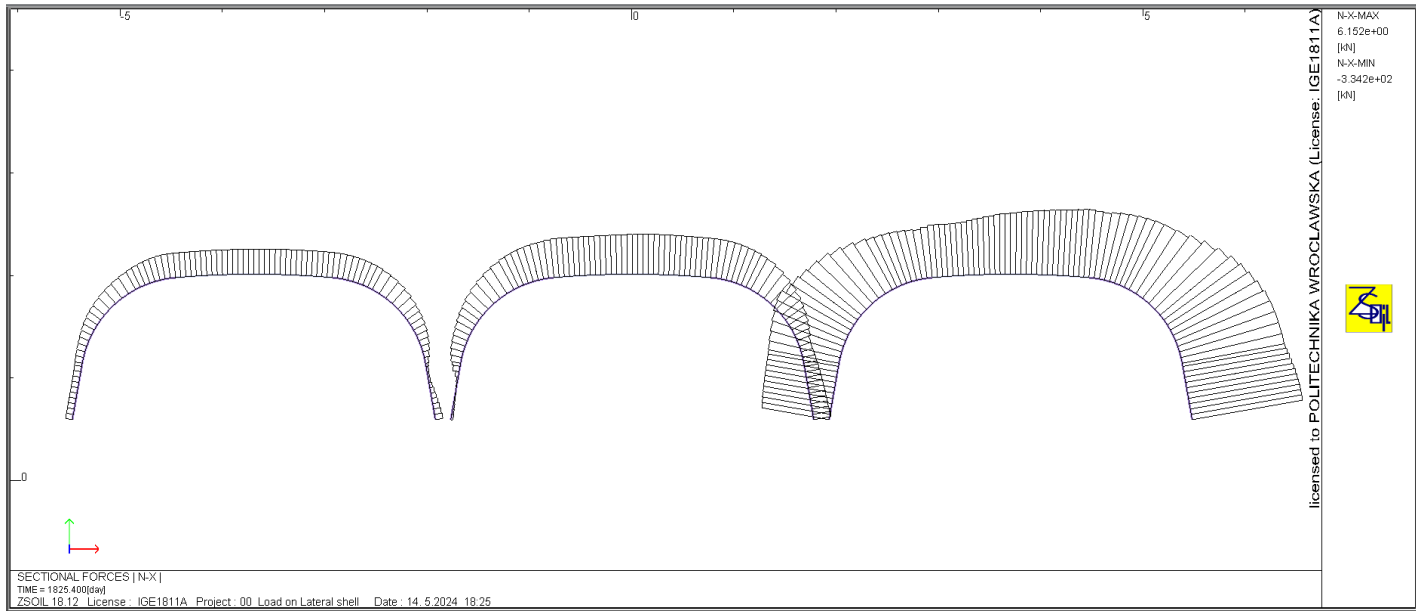


Figure 7.57: Axial force distribution at failure load for ($S/D=0.04$)

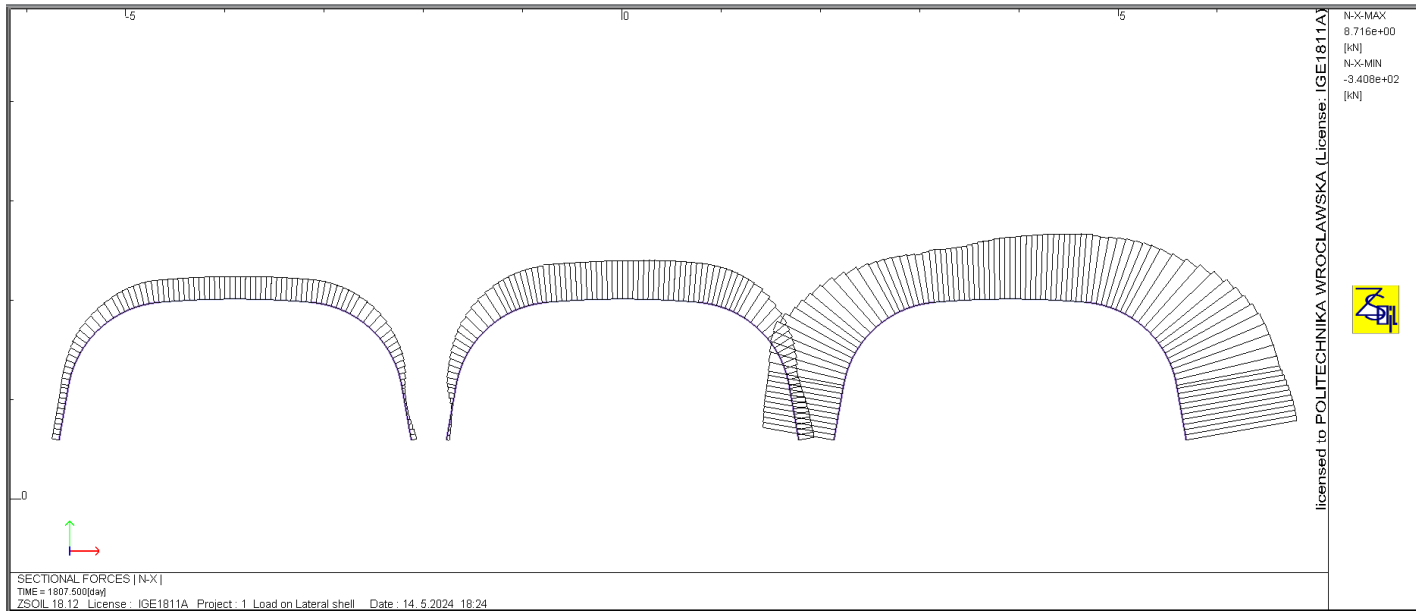


Figure 7.58: Axial force distribution at failure load for ($S/D=0.10$)

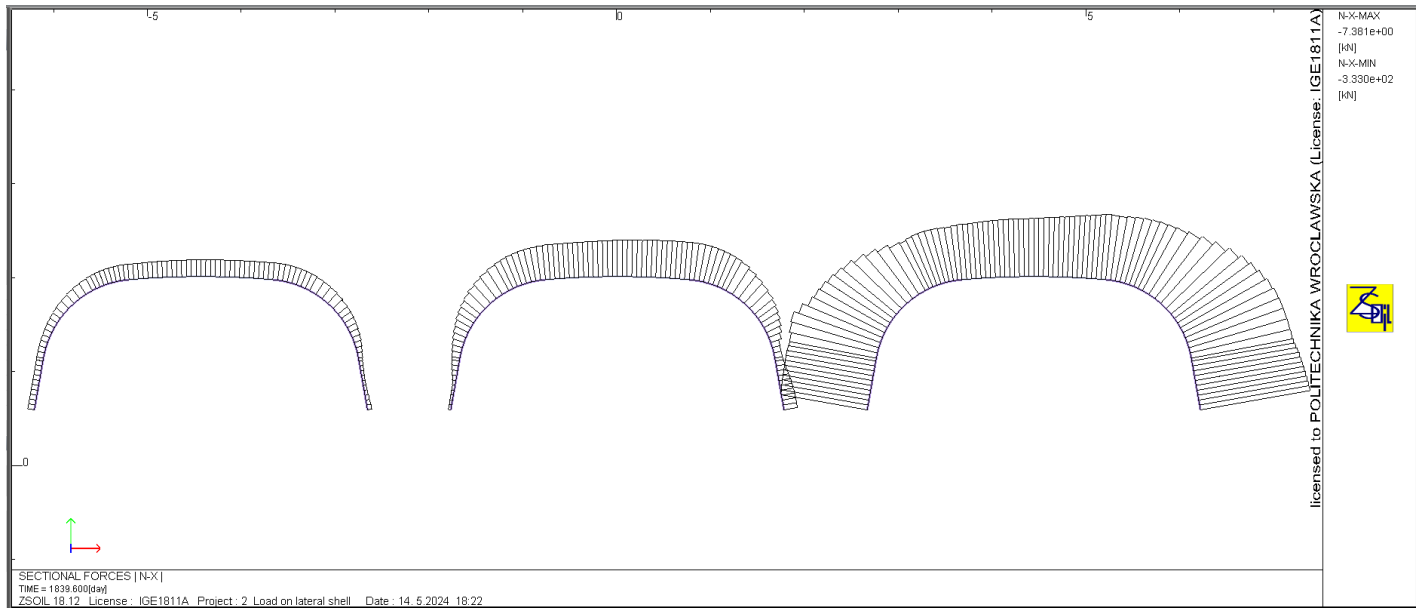


Figure 7.59: Axial force distribution at failure load for ($S/D=0.25$)

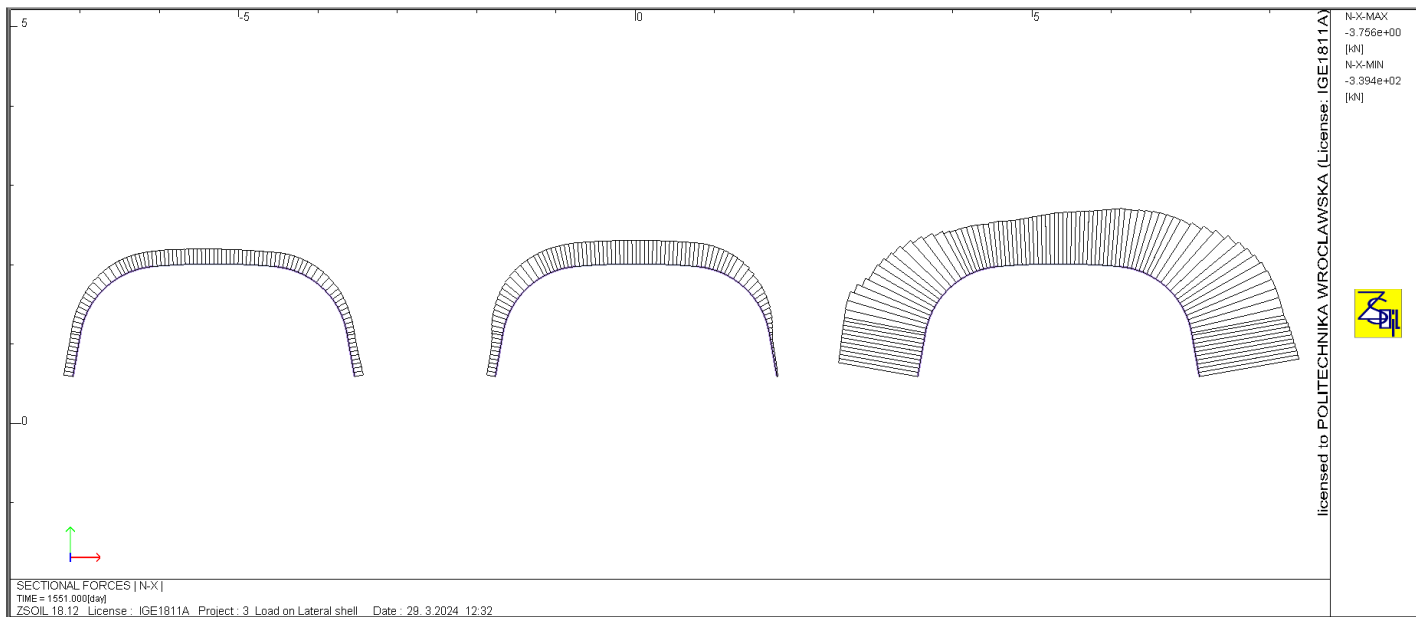


Figure 7.60: Axial force distribution at failure load for ($S/D=0.50$)

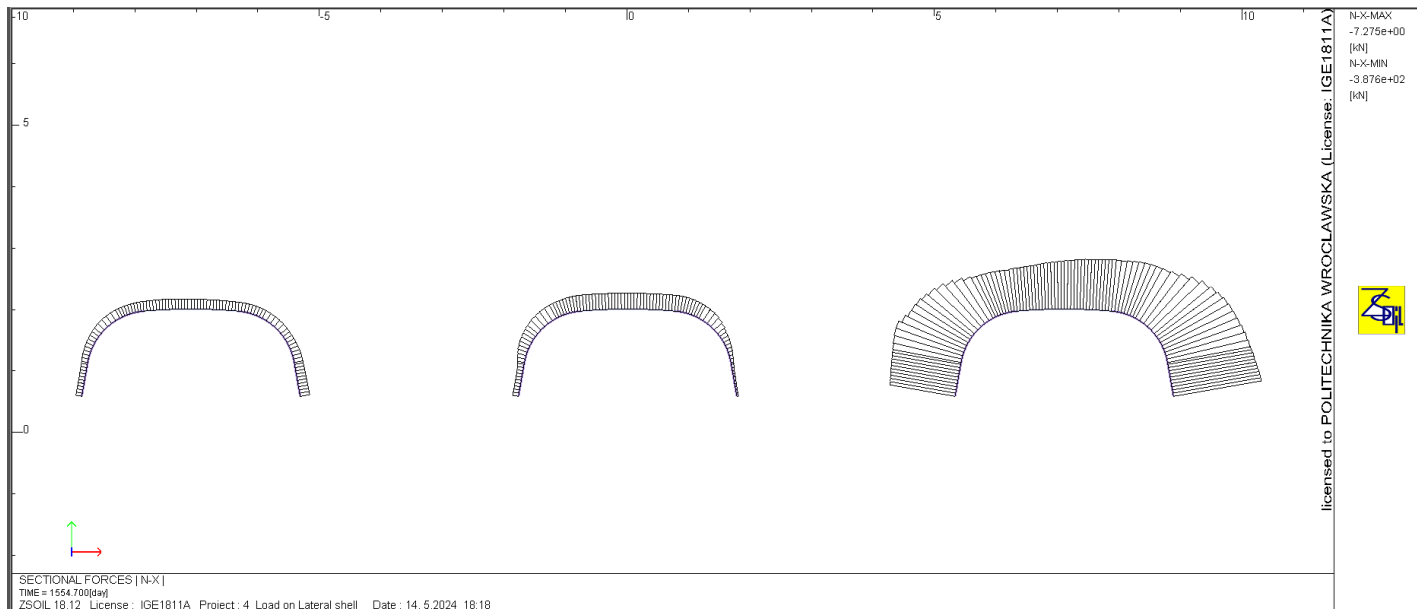


Figure 7.61: Axial force distribution at failure load for ($S/D=1.0$)

Similar to the loading scenario in Model-C, in Model-R, the load-bearing capacity of the shell increases as the S/D ratio increases (see Table 7.4). Comparing the influence of loading position on the behavior of the SSCS indicates that there is no significant difference in loading conditions between Model-C and Model-R. The maximum difference observed was less than 4%; for example, $S/D=0.04$, the bearing capacity increased by approximately 4% in Model-R.

Table 7.4: Comparison of bending moment and axial force of central and lateral shells for different S/D ratios under Model-R at peak load

Model	Load (kN)	Bending Moment (kNm/m)				Axial force (kN/m)			
		Central shell		Loaded Lateral shell		Central shell		Loaded Lateral shell	
		Crown	Haunch	Crown	Haunch	Crown	Haunch	Crown	Haunch
$S/D=0.04$	856	-20.93	-24.98	53.95	-23.99	-122.09	-43.14	-217.58	-328.20
$S/D=0.10$	896	-19.17	-24.79	55.19	-23.90	-120.98	-37.98	-233.68	-335.23
$S/D=0.25$	998	-18.19	-24.59	58.77	-23.62	-114.57	-32.49	-264.01	-393.73
$S/D=0.50$	1054	-16.99	19.35	60.09	-23.49	-92.85	-17.22	-272.66	-416.51
$S/D=1.00$	1174	-11.28	12.98	64.46	-22.94	-75.49	-15.18	-347.11	-480.26
Reference Model*	1206 kN*	–	–	66.32	-22.72	–	–	-372.85	-488.37

7.4.4. Failure mode of the SSCSs under model-R loading condition

The failure mechanism of the shells in the Model-R loading condition (load applied to one lateral shell) is summarized as follows:

When, $S/D=0.04$, the first yielding is observed around the shoulder of the loaded lateral shell, occurring when the load reaches 668 kN. The second yielding occurs around the haunch of the loaded lateral shell, reaching approximately 753 kN. As the loading increases towards the peak load, further yielding occurs around the shoulder and haunch of the central shell, with a load of approximately 850 kN, nearly reaching the peak load for this model. It should be noted that the unloaded lateral shell was also checked for yielding, but no yielding was observed. In this model, the unloaded lateral shell fails after forming plastic hinge around the bottom haunch of the shell, after the load reaches the peak in post failure of both central and loaded lateral shell.

When $S/D=0.10$, the first yielding is observed around the shoulder of the loaded lateral shell, occurring when the load reaches 698 kN. The second yielding occurs around the haunch of the loaded lateral shell, reaching approximately 807 kN. As the loading increases towards the peak load, further yielding occurs around the haunch and shoulder of the central shell, with a load of approximately 895 kN, nearly reaching the peak load for this model. Similar to $S/D=0.04$, no yielding was observed in the unloaded lateral shell. Compared with Model-00, the load which causes the first yielding is increased approximately by 5%.

When $S/D=0.25$, the first and second yielding are observed around the shoulder and haunch of the loaded lateral shell, occurring when the load reaches 783 kN and 998 kN, respectively. Once failure occurs in the loaded lateral shell, the load is transferred to the central shell, and yielding that causes a plastic hinge occurs around the haunch of the central shell, and then around the shoulder of the central shell. Compared with Model $S/D=0.04$, the load which causes the first yielding is increased by approximately 17%.

When $S/D=0.50$, yielding initially occurs at the shoulder and then at the haunch of the loaded lateral shell, at loads of 863 kN and 994 kN, respectively. Following the failure of the loaded lateral shell, plastic hinges emerge at the shoulder of the central shell as the load reaches its peak of 1054 kN.

When $S/D=1.0$, the first yielding, which causes the first plastic hinge, occurs at the shoulder of the loaded lateral shell once the load reaches 932 kN. This load is increased by 40% compared to the load which causes the first yielding in Model $S/D=0.04$. Once the loaded lateral shell yields and fails, a plastic hinge is observed around the shoulder of the central shell. However, the haunch of both central and lateral shell was not yielded. Moreover, compared with the reference model with a single span shell, the load which causes the first yield is only decreased by 5%. This indicates that the loaded lateral shell acts as an independent shell. Comparing the failure mechanisms across all models, it is evident that the load leading to the first formation of a plastic hinge at the shoulder of the lateral shell increases as the S/D ratio increases.

Table 7.5: Summary of critical location and failure mode for all models under loading position –Model-R

Models	Interaction values due to combined bending moment and axial force						
	Central shell			Load Lateral shell			Lateral shell
	Crown	Shoulder	Haunch	Crown	shoulder	Haunch	Haunch
Model 00 ($S/D=0.04$)	< 1	1.0	1.0	< 1	1.0	1.0	1.0
Model 01 ($S/D=0.10$)	< 1	1.0	1.0	< 1	1.0	1.0	< 1
Model 02 ($S/D=0.25$)	< 1	1.0	1.0	< 1	1.0	1.0	< 1
Model 03 ($S/D=0.5$)	< 1	1.0	< 1	< 1	1.0	1.0	< 1
Model 04 ($S/D=1.0$)	< 1	1.0	< 1	< 1	1.0	1.0	< 1

In line with the loading scenario outlined in Model-R, a notable observation emerges neither the lateral nor central shell crowns exhibited yielding under the applied failure load. Additionally, an interesting finding from Table 7.5 is evident in Model with $S/D=0.04$, where the haunch of the unloaded lateral shell undergoes complete plastic deformation. This observation underscores the significance of shell spacing on structural behavior. Despite the loading being applied to the lateral shell on the right side of the central shell, failure manifests in the lateral shell on the left side. This observation highlights the paramount influence of shell spacing on the structural response and serves as a crucial aspect in the analysis of the shells' behavior.

7.5. Behavior of multi-span SSCS under ultimate load (Model-LR)

In this loading scenario, the loading to failure is imposed on both lateral shells and the response of lateral shells and their effect on unloaded central shell is analyzed. The results are presented in the form of load-displacement curves at the crown and haunch section of the shells. Moreover, the bending moment and axial force distributions for both shells are presented at different S/D ratios.

7.5.1. Load displacement curve

The load-displacement curve obtained from the numerical simulation provides valuable insights into the mechanical behavior of the soil-steel structure under loading conditions until failure. Comparing the load-bearing capacity in Model-LR with the previous Model-C and Model-R, there was almost a doubling of the load-bearing capacity in Model-LR. The results are presented below in terms of the load-displacement curve at the crown of the loaded and unloaded shell, as well as at the haunches of the loaded and unloaded shell. Fig.7.62 illustrates the load-displacement curve for the unloaded central shell, highlighting a noticeable upward deflection pattern. This observed behavior corresponds to the deflection pattern noted at the crown of the unloaded shell in both Model-C and Model-R, indicating a consistent response across varied loading scenarios.

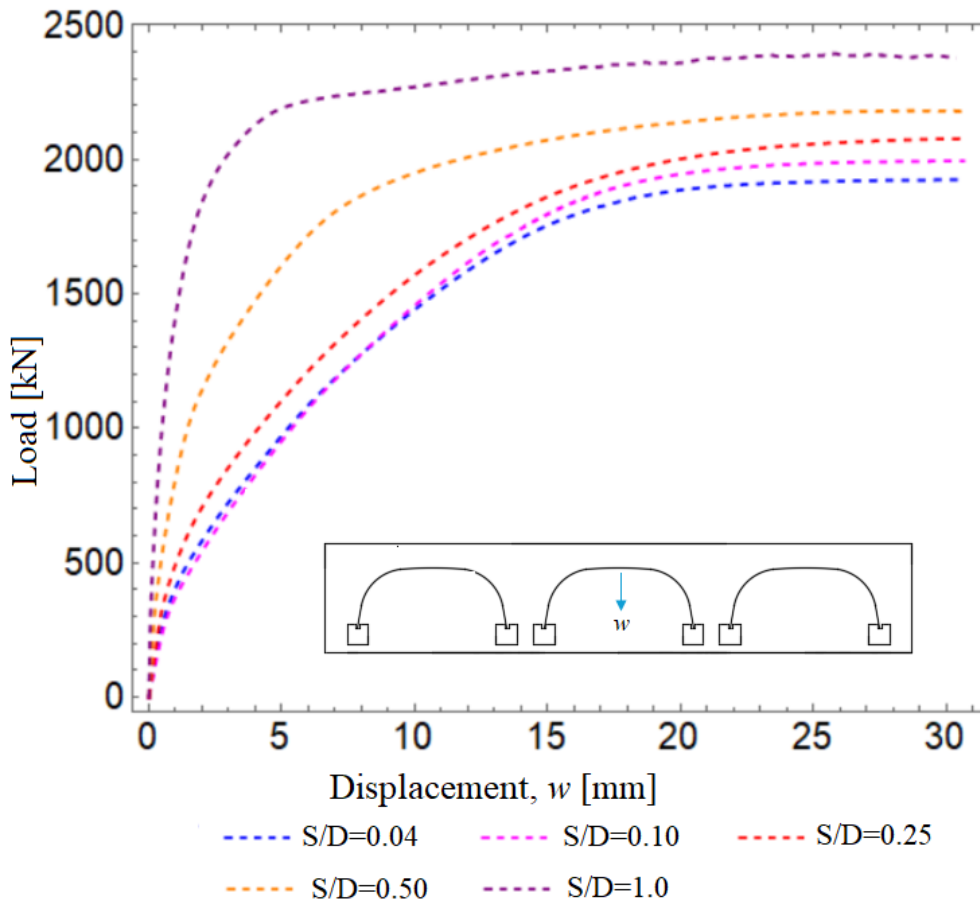


Figure 7.62: Load displacement curve at the crown of central shell.

The behavior of the shell, as illustrated in Fig. 7.63, demonstrates a gradual evolution in deflection corresponding to varying S/D (spacing-to-diameter) ratios. The load-displacement curve in Fig. 7.63 exhibits a smooth and linear increase in slope until reaching peak load across all models with different S/D ratios. This characteristic behavior can be attributed to the high stiffness of the composite structure, particularly noticeable when both lateral shells are under load. An important observation is that the lateral shells provide equal lateral support to the central shell in both directions when loaded, consequently reducing the lateral deflection of the central shell. As the S/D ratio increases, there is a corresponding increase in load-bearing capacity, indicative of the lateral shells beginning to independently handle external loads. This transition in load distribution contributes to the enhanced load-bearing capability of the structure.

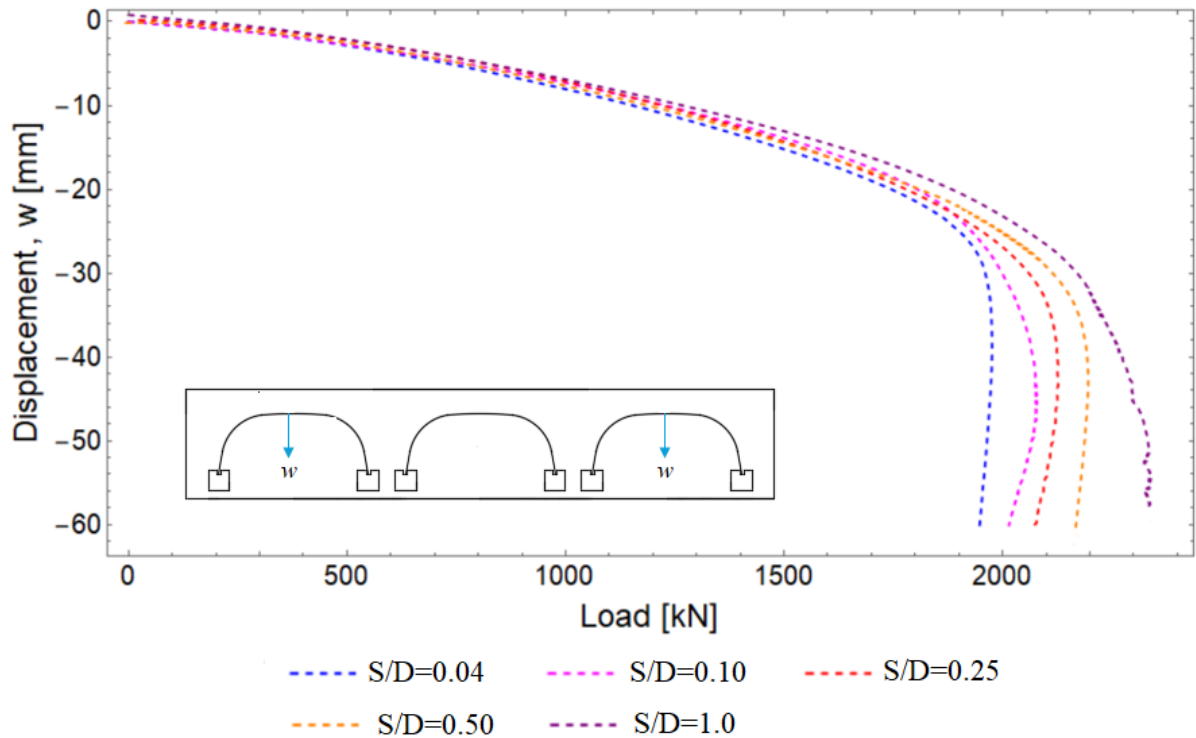


Figure 7.63: Load displacement curve at the crown of the loaded lateral shell.

As the S/D ratio decreases, there is a corresponding decrease in the load-bearing capacity of the structure. For instance, in the scenario where the shells are closely spaced with an S/D ratio of 0.04, a peak load of 1976 kN is observed. This peak load is approximately 17% lower compared to the model with a larger spacing between the shells, at $S/D=1.0$. The observed reduction in load-bearing capacity can be attributed to the reduced spacing, which limits the lateral support provided by the backfill. This limitation exposes the central shell to heightened vulnerability under load, leading to a decreased peak load capacity in the structure. The peak load of 2050 kN, 2103 kN, 2187 kN, and 2374 kN is observed in Model with $S/D=0.10$, $S/D=0.25$, $S/D=0.50$ and $S/D=1.0$ respectively. When compared with the reference model (single span model), the load-bearing capacity increased significantly by approximately 64%, 70%, 74%, 81%, and 97% in Mode $S/D=0.04$, $S/D=0.10$, $S/D=0.25$, $S/D=0.50$ and $S/D=1.0$, respectively.

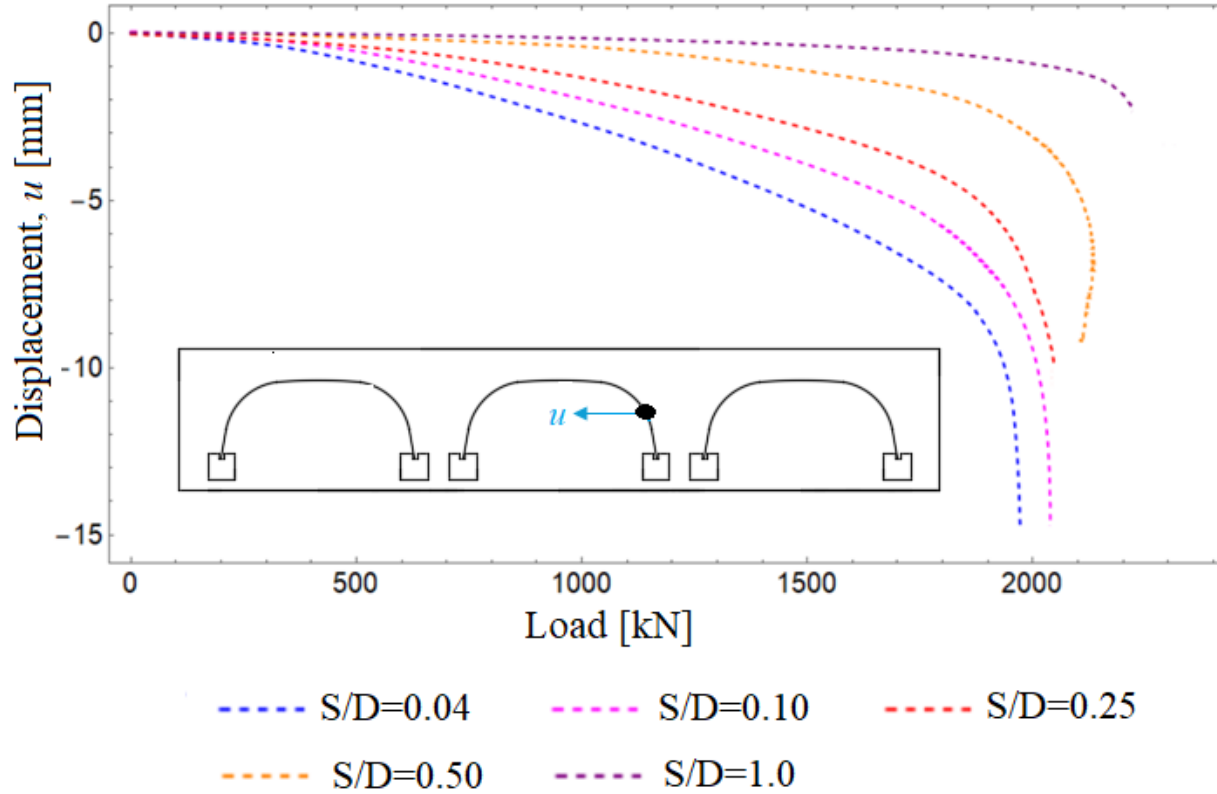


Figure 7.64: Load displacement curve at the haunch of central shell

The lateral displacement along the horizontal axis decreased as the S/D ratio increased at the haunch of the unloaded central shell, as depicted in Fig. 7.64. However, a greater lateral displacement is observed at the haunch of the loaded lateral shell compared to that of the haunch of the unloaded central shell, as shown in Fig. 7.65.

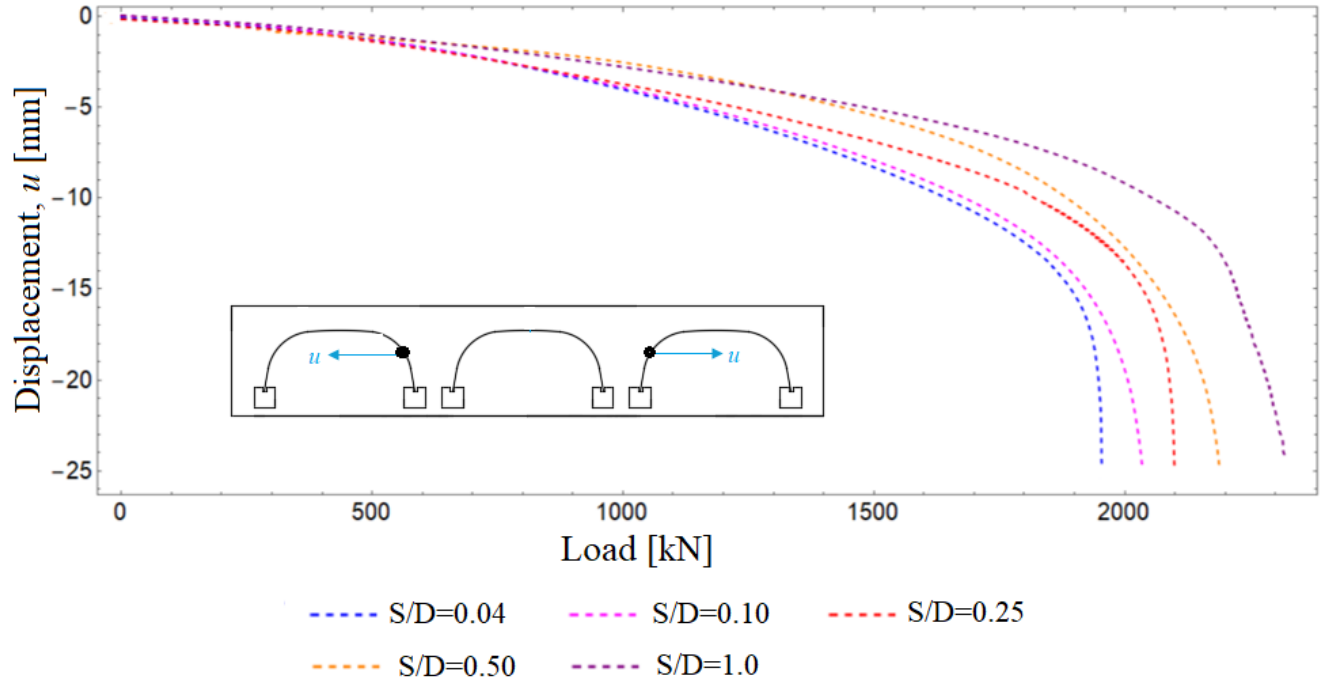


Figure 7.65: Load displacement curve at the haunch of the loaded lateral shell.

7.5.2. Bending moment

As the S/D ratios decrease, a noticeable decrease in the bending moment is observed at the crown of loaded lateral shells under peak load, whereas an increase is noted at the haunches. Concurrently, both the crown and haunch of the unloaded central shell experience an increase in bending moment as the S/D ratio decreases. These trends highlight the complex relationship between shell configurations, S/D ratios, and internal forces, emphasizing the need for comprehensive analysis and design considerations in multi-span structural systems. The distribution of bending moments for all considered S/D ratio models is shown in Figs 7.66 to 7.70.

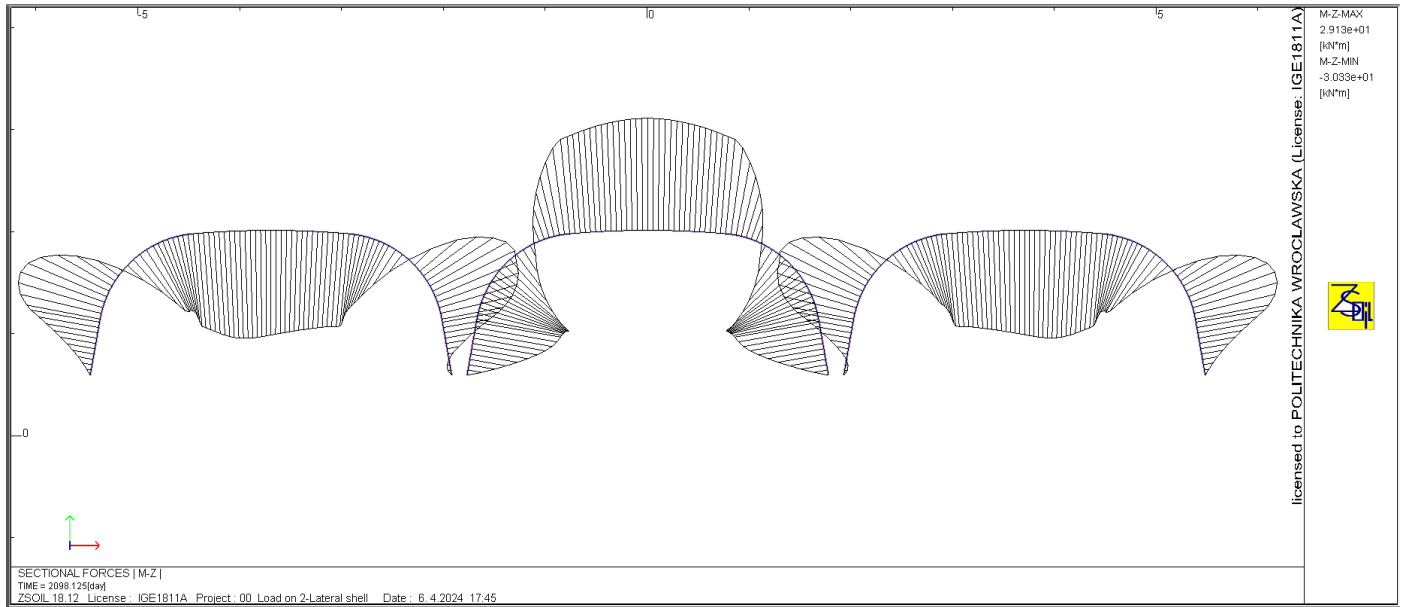


Figure 7.66: Bending moment distribution at failure load for ($S/D=0.04$)

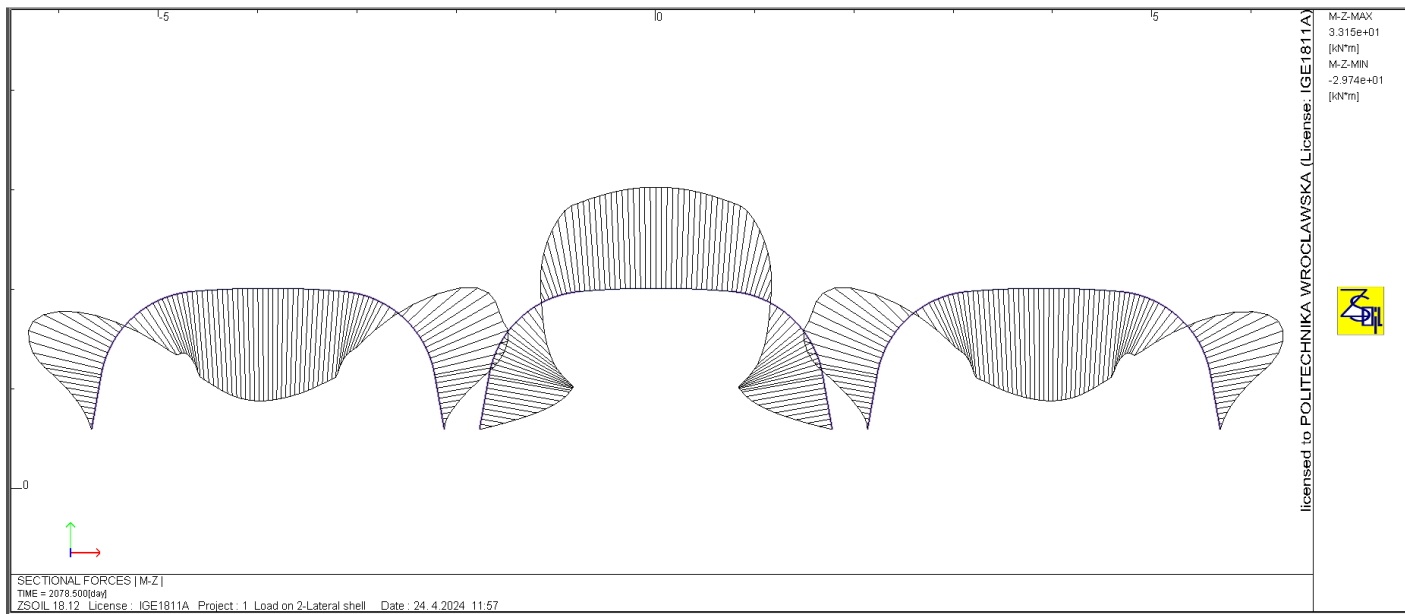


Figure 7.67: Bending moment distribution at failure load for ($S/D=0.10$)

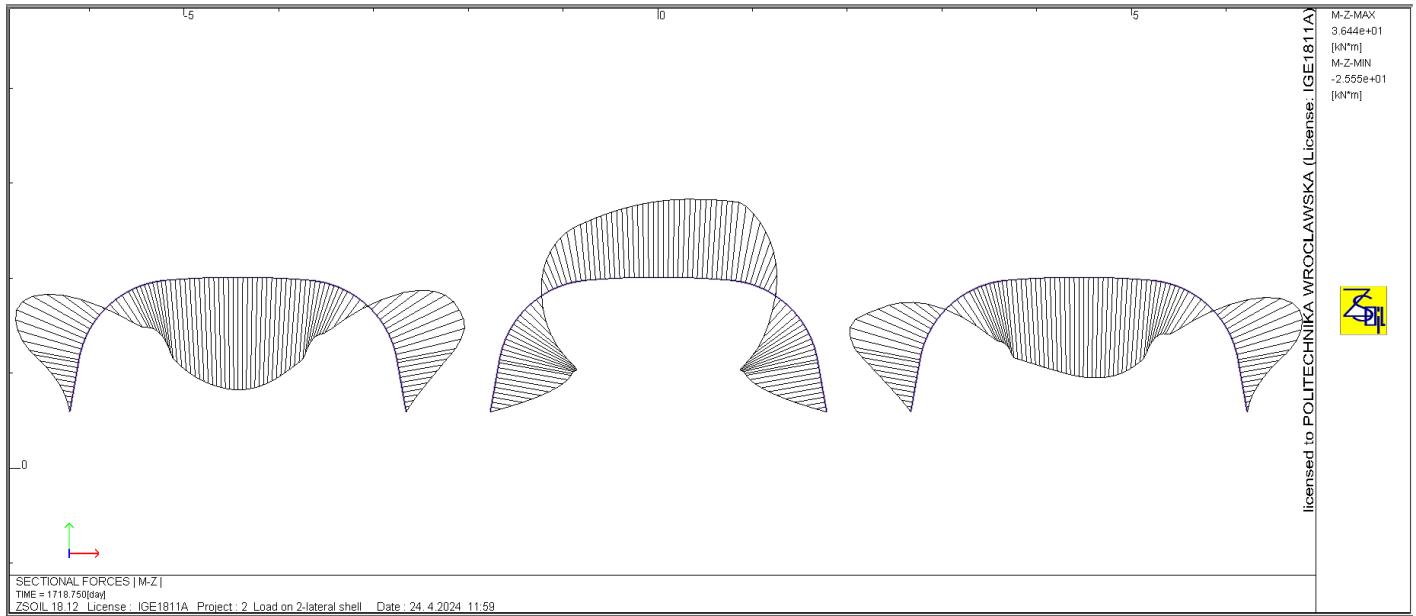


Figure 7.68: Bending moment distribution at failure load for (S/D=0.25)

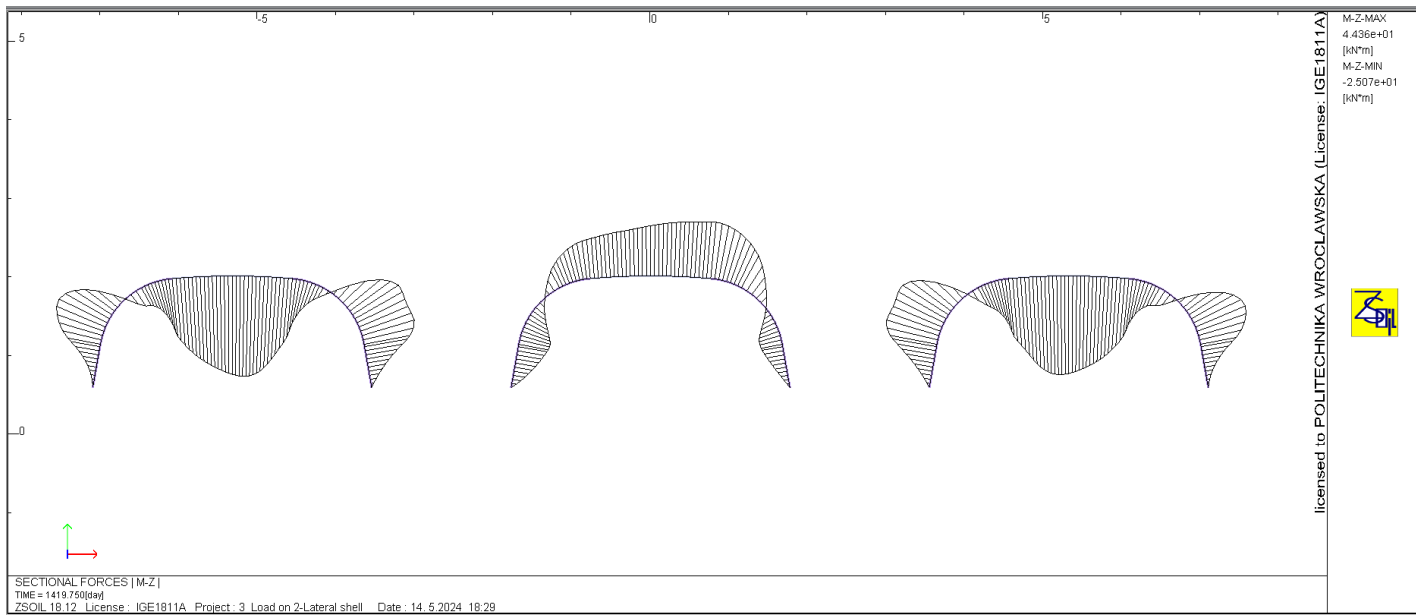


Figure 7.69: Bending moment distribution at failure load for (S/D=0.50)

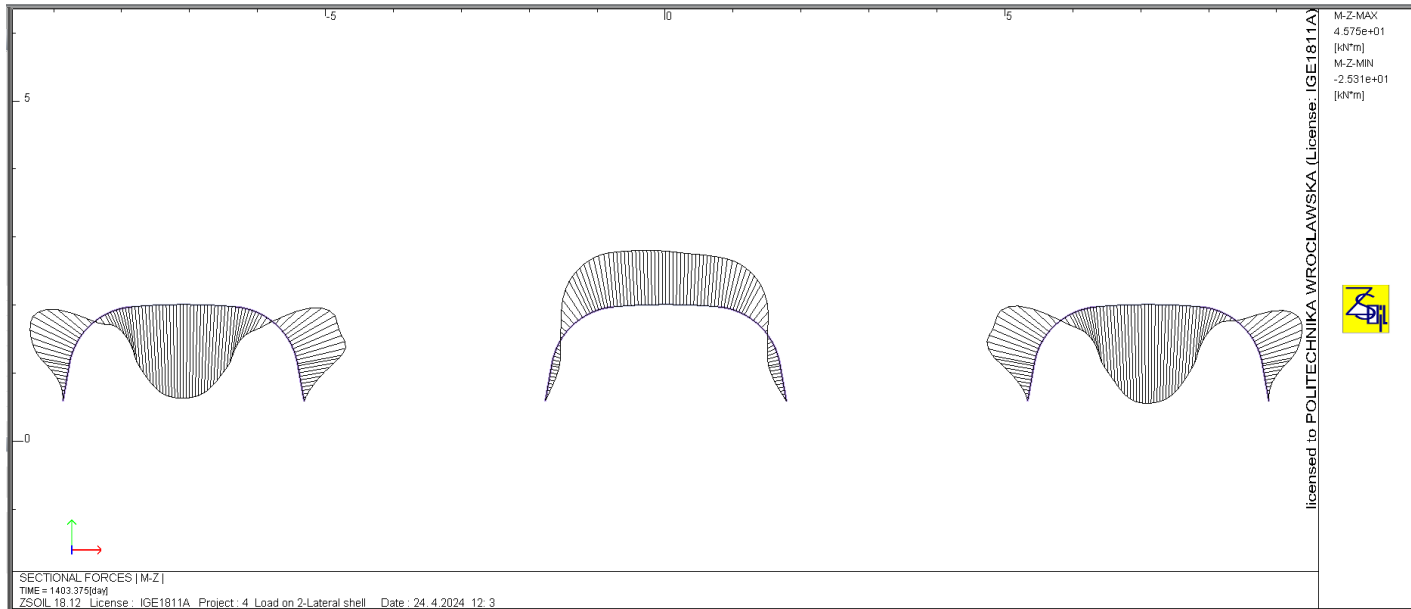


Figure 7.70: Bending moment distribution at failure load for ($S/D=1.0$)

7.5.3. Axial force

Similar to the loading positions in Model-C and Model-R, the axial force under peak load at the crown and haunch of the loaded lateral shell decreases as the S/D ratios decrease. Conversely, increments are observed at the crown and haunch of the unloaded central shell as the S/D ratios decrease. These trends highlight the varying load distributions and structural responses based on shell configurations and S/D ratios, emphasizing the importance of such considerations in analyzing and designing multi-shell systems. The distribution of axial forces at failure is shown in Figs 7.71 to 7.75.

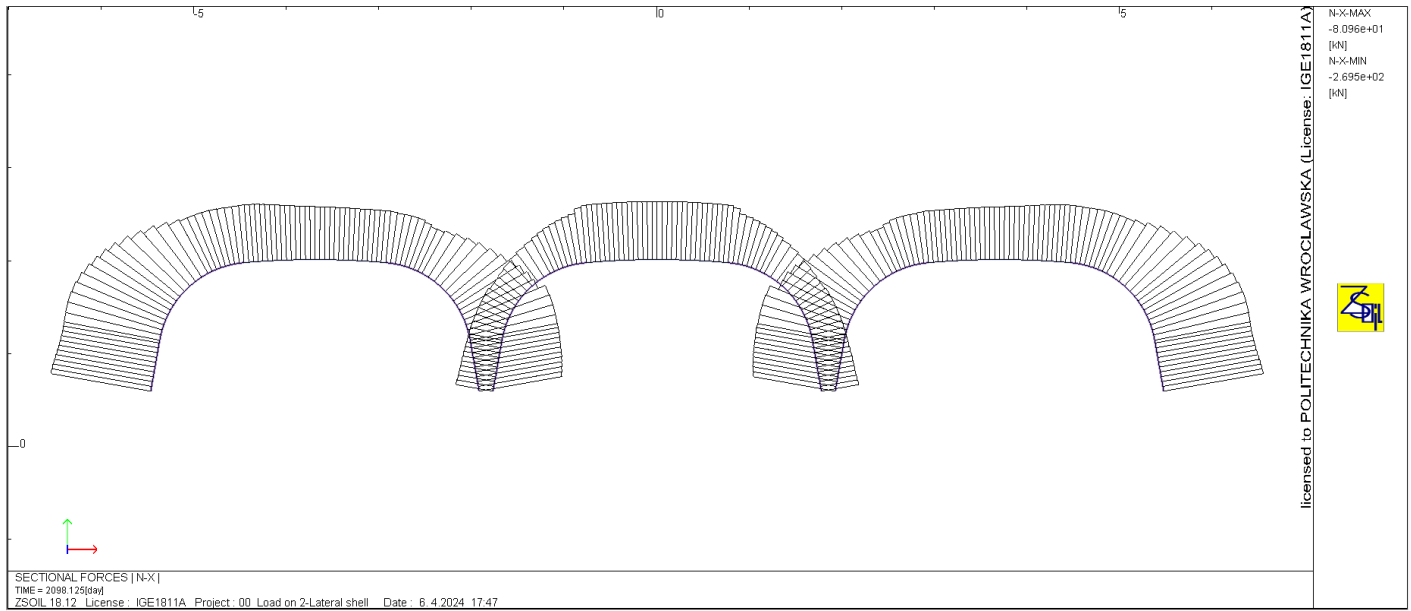


Figure 7.71: Axial force distribution at failure load for ($S/D=0.04$)

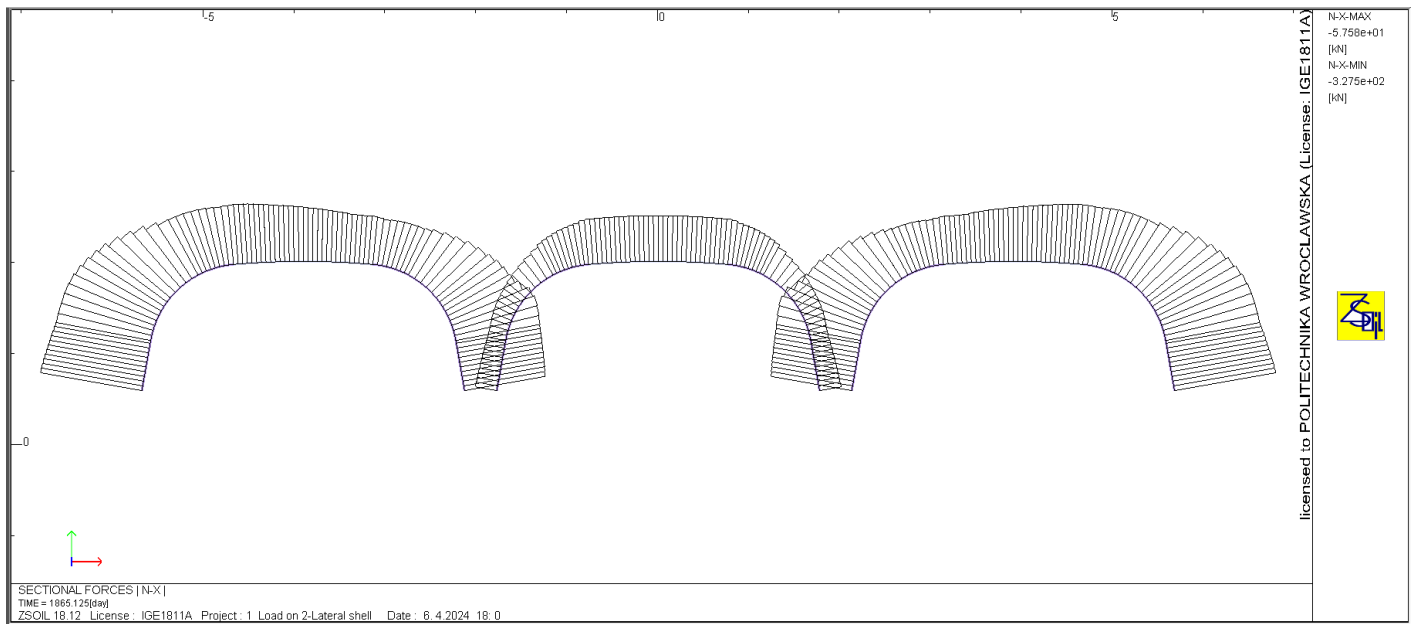


Figure 7.72: Axial force distribution at failure load for ($S/D=0.10$)

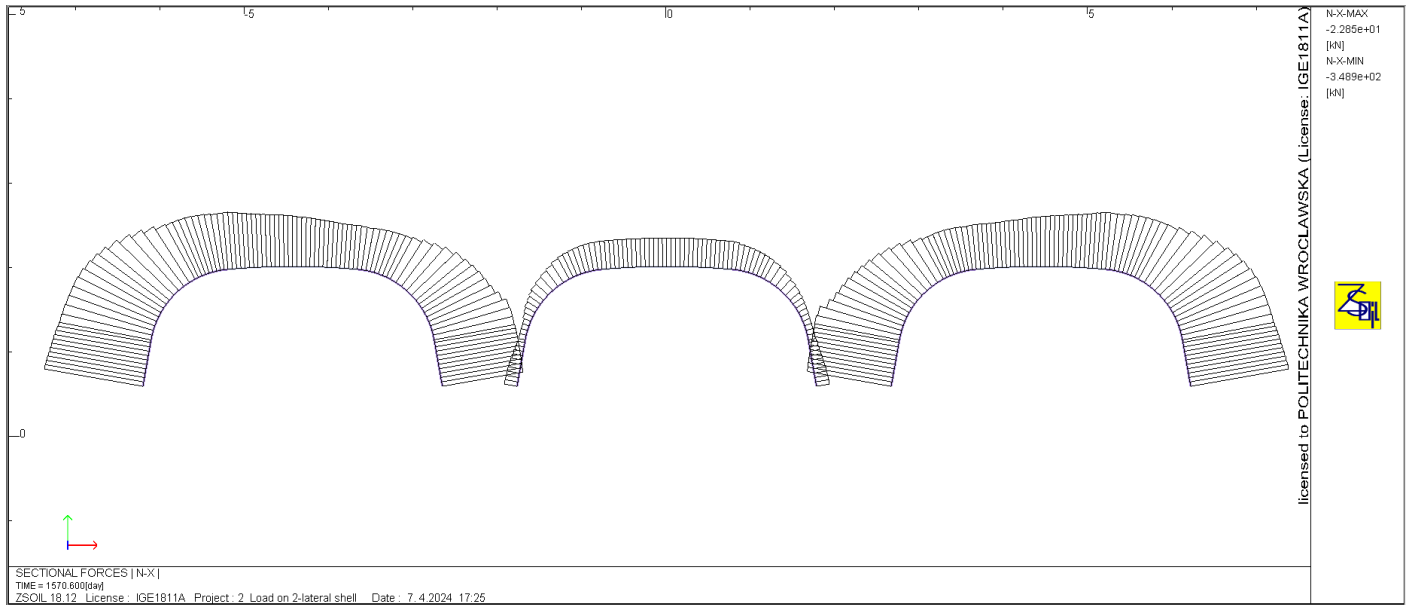


Figure 7.73: Axial force distribution at failure load for ($S/D=0.25$)

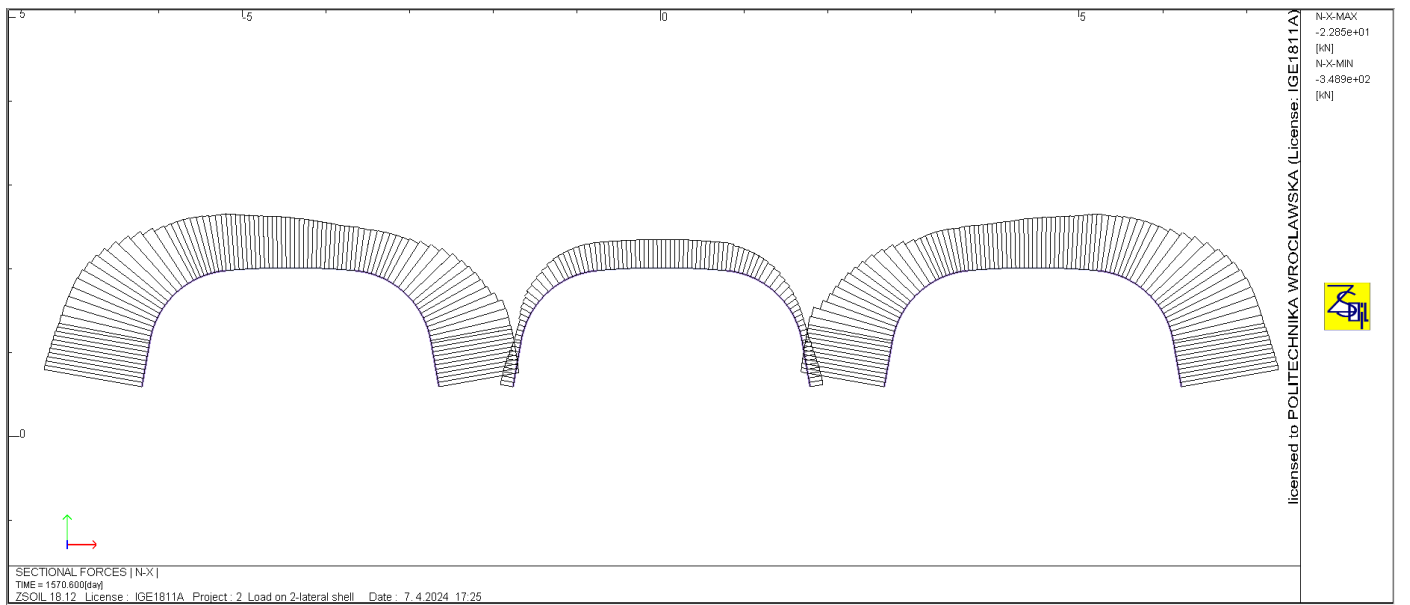


Figure 7.74: Axial force distribution at failure load for ($S/D=0.50$)

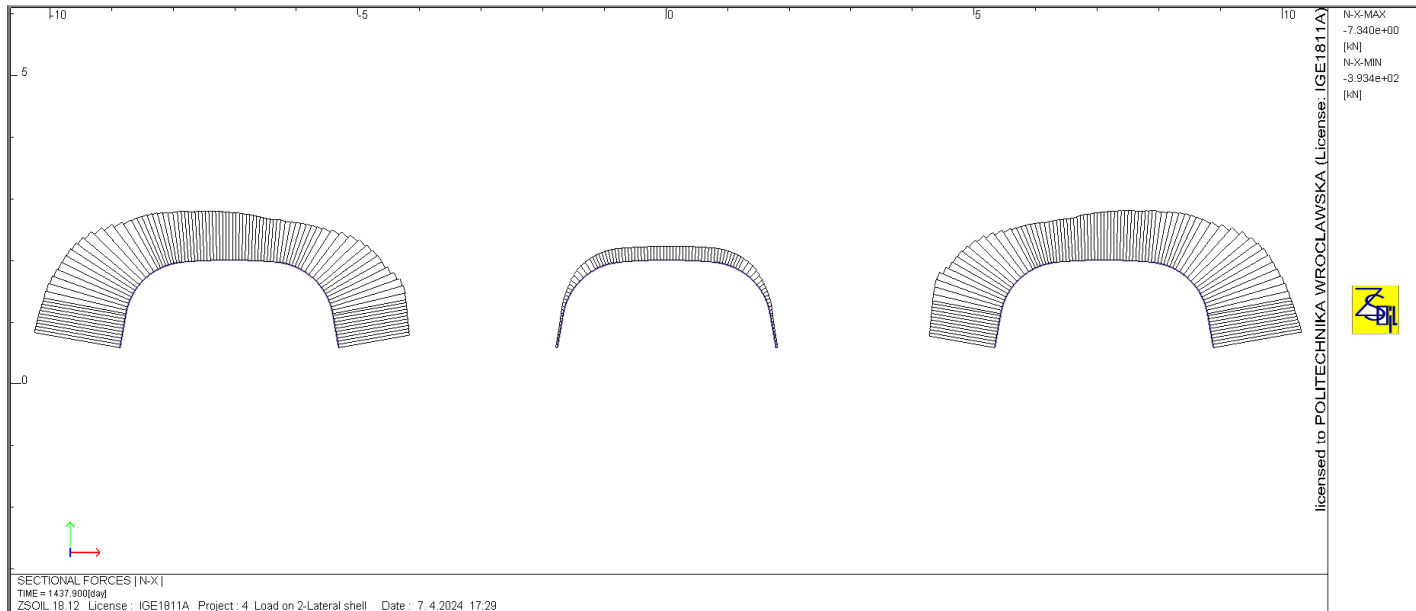


Figure 7.75: Axial force distribution at failure load for ($S/D=1.0$)

As depicted in Table 7.6, similar to Model-C and Model-R, the bearing capacity of the SSCS increases with the S/D ratio. However, in Case III, the load-bearing capacity is nearly doubled compared to the single-shell scenario. This can be attributed to the loading configuration in Case III, where both lateral shells are loaded. As the S/D ratio increases, both loaded lateral shells begin to act independently, leading to the doubling of the bearing capacity compared to the single-shell case.

Table 7.6: Comparison of bending moment and axial force of central and lateral shells for different S/D ratios under Model-LR at ultimate load

Model	Load (kN)	Bending Moment (kNm/m)				Axial force (kN/m)			
		Central shell		Loaded Lateral shell		Central shell		Loaded Lateral shell	
		Crown	Haunch	Crown	Haunch	Crown	Haunch	Crown	Haunch
$S/D=0.04$	1976	-31.37	24.99	56.57	-23.91	-185.53	-77.18	-256.87	-378.50
$S/D=0.10$	2050	-30.77	24.98	62.80	-23.39	-178.20	-64.40	-285.40	-419.28
$S/D=0.25$	2103	-29.04	24.94	62.88	-23.33	-129.78	-68.44	-293.18	-429.18
($S/D=0.50$)	2187	-26.13	22.39	64.56	-23.38	-101.11	-55.75	-293.89	-430.36
$S/D=1.00$	2374	-18.52	17.37	65.82	-22.81	-86.49	-15.38	-364.62	-483.12
Reference Model*	1206	–	–	66.32	-22.72	–	–	-372.85	-488.37

7.5.4. Failure mode of the SSCSs under Model-LR loading condition

In Model S/D=0.04, the bending moment capacity of the shell is reached first at the shoulder of both loaded lateral shells, with the load causing this yielding approximately 1819 kN. Comparing with S/D=0.04 of Model-C and Model-R, the load causing the first yielding increases by approximately more than 170%. The reason behind such a substantial increment is that, in Case III, both lateral shells are loaded, and the stiffness of the composite structure is increased by supporting unloaded central shells in both directions. However, in Model-C and Model-R, only one shell is loaded. The second yielding is observed at the shoulder of the unloaded central shell. Then, yielding is propagated to the haunch of both lateral shells and the central shell after the load reaches the peak load of 1976 kN.

In Model-S/D=0.10, the first yielding that causes a plastic hinge is observed around the shoulder of the loaded lateral shells at a load of 1821 kN. The second plastic hinge is formed at a similar position but on the central shell once the load reaches 2004 kN. Once failure is observed in both lateral and central shells, and the load reaches the peak of 2045 kN, more plastic hinges are formed around the haunch of the central and lateral shells. In this model, the load which causes the formation of the first plastic hinge is almost the same as in Model- S/D=0.04.

In Model-S/D=0.25, the first yielding that causes a plastic hinge is observed around the shoulder of the loaded lateral shells at a load of 1744 kN. The second plastic hinge is formed at a similar position but on the central shell once the load reaches 2075 kN. The third location of plastic hinge is also observed on the central shell around the haunch once the load approaches the ultimate load of 2103 kN. Then, additional plastic hinges are formed around the haunch of the lateral shells during post-failure.

In Model-S/D=0.50, the first yielding that causes a plastic hinge is observed around the shoulder of the loaded lateral shells at a load of 1859 kN. The second plastic hinge is formed around the haunch of the lateral shells once the load reaches 2075 kN. Once the loaded lateral shell fails at the peak load of 2127 kN, plastic hinges are observed around the shoulder and haunch of the central shell. From this model, it can be clearly seen that, unlike previous models, the failure in the central shell is observed once the loaded lateral shell fails, indicating a decrease in interaction between the shells.

In Model-S/D=1.0, the plastic hinges are formed first around the shoulder and the haunch of the loaded lateral shells at loads of 1960 kN and 2248 kN, respectively. Unlike in Case-I in this case, the failure of the unloaded central shell is observed when the load approaches the peak load of 2374 kN. This indicates that when both lateral shells are loaded to failure, they have an effect on the behavior of the unloaded central shell.

Table 7.7: Summary of critical location and failure mode for all models under loading position – Model-LR

Model	Interaction value due to combined bending moment and axial force					
	Central shell			Lateral shell		
	Crown	Shoulder	Haunch	Crown	Shoulder	Haunch
S/D=0.04	<1	1.0	1.0	<1	1.0	1.0
S/D=0.10	<1	1.0	1.0	<1	1.0	1.0
S/D=0.25	<1	1.0	1.0	<1	1.0	1.0
S/D=0.5	<1	1.0	<1	<1	1.0	1.0
S/D=1.0	<1	1.0	<1	<1	1.0	<1

Upon comparing the failure load across three loading conditions, there is a clear increase in the bearing capacity of the SSCS in Model-LR, nearly doubling compared to the first two cases as described in Fig. 7.76. Notably, when only one shell is loaded, whether it be the central or lateral shell as in Model-C and Model-R, the load-bearing capacity closely aligns with that of the reference model representing the single-span scenario, especially when the S/D ratio is 1. This underscores that when the shells are spaced at a distance equal to the span of the structure, the presence of lateral shells exerts minimal impact on the bearing capacity of the central shell, and vice versa.

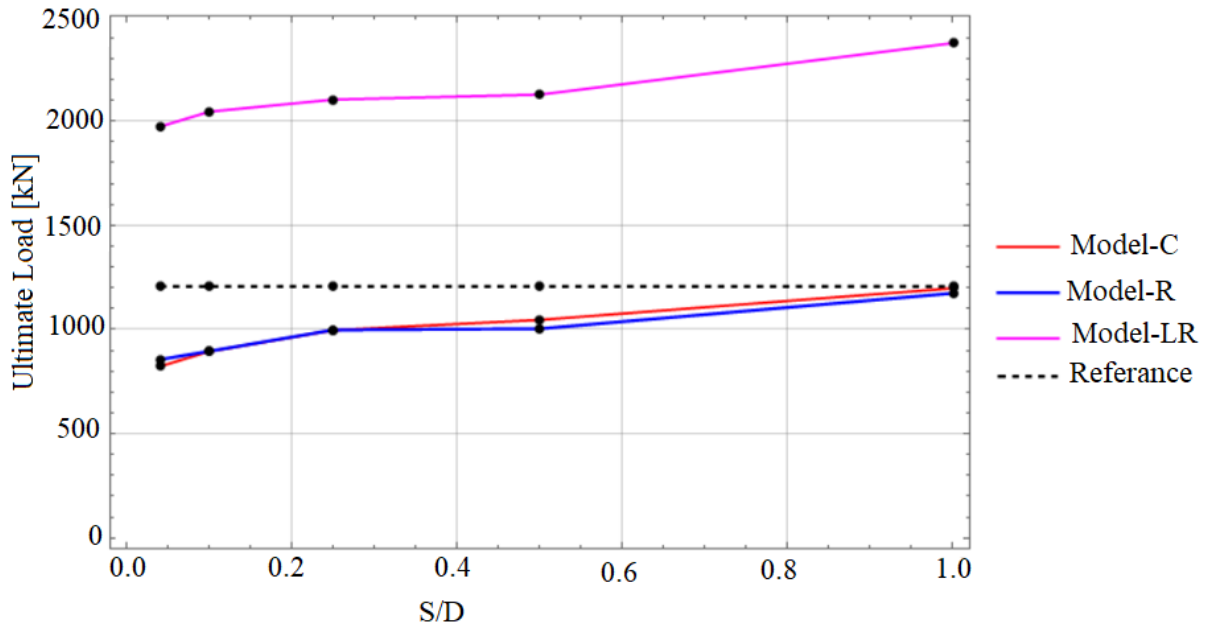


Figure 7.76: Comparing the failure load in three loading conditions.

7.6. Stability of multi-span soil-steel composite structures

The critical force due to global buckling can be estimated using the methodology presented by Pettersson [51]. According to [51] if the length of the reinforcement plate in the crown area is less than the length of the top radius plate itself, the critical normal force of the reinforced top plate can be increased using a diagram as illustrated in Chapter four, Figure 4.6, and by following the procedure described in section 4.4.1. However, in this model since the length of the stiffening rib at the crown section is equal to the length of the top radius, the critical force increment factor, γ will be unit. Thus, taking the values of $L=1540$ mm, $I_2= 13485$ mm⁴/mm, the critical force is 11504 kN/m. The values of induced maximum normal force in all three loading scenarios at different S/D ratio are significantly less than the critical forces, indicating that the shell is safe from global buckling.

However, it's important to note that local buckling, which incorporates out-of-plane deformation, cannot be directly investigated due to the limitations associated with the 2D approach adopted in the analysis. Generally, in the model, the maximum axial forces in all models of S/D ratio were found to be far less than the estimated critical force. This suggests that the structure is more likely to fail due to physical nonlinearity rather than buckling, which is related to geometric

nonlinearity. Thus, the failure mode of the multi-span SSCS is attributed to reaching the limit values of internal forces.

7.7. Summary

In this section, numerical analysis was employed to examine the influence of the spacing to span ratio on the bearing capacity and failure modes of multi-span box-type soil-steel composite structures under ultimate load conditions. The numerical analysis was based on 2D nonlinear finite element analysis validated with full-scale test of soil steel composite structure during both backfilling and under ultimate load. The relationship between the bearing capacity and S/D ratios for all three loading scenarios are identified and summarized. The main conclusions drawn from the numerical simulations conducted are as follows:

- During backfilling, the vertical displacement at the crown of the central shell decreases as the S/D ratios decrease. Conversely, the upward deflection of the crown of the central shell increases as the S/D ratios decrease. It is noteworthy that there is no significant difference in the crown's vertical displacement between the central and lateral shells.
- Based on the findings presented, it is evident that the load bearing capacity of multi-span SSCS experiences a significant decrease of approximately 32% under the condition of narrow spacing with S/D=0.04 in Model-C loading position. This reduction in load-carrying capacity is associated with a corresponding decrease in maximum axial force, specifically by 42% at the crown and 27% at the shoulder of the central shell. Furthermore, the bending moment undergoes changes, with a decrease of 19% at the crown and a 6% increase, particularly at the haunches.
- Comparing the influence of loading position on the behavior of the multi-span SSCS reveals that there is no significant difference between Model-C and Model-R. For instance, in Model S/D=1.0, Model-C demonstrates a 2% reduction in bearing capacity compared to Case-I. However, a significant difference arises when contrasting the loadbearing capacities of Model-C and Model-R with Model-LR. Notably, in Model-LR, the multi-span SSCS exhibits nearly double the bearing capacity observed in Model-C and Model-R.

- In all loading conditions, the failure of the shell starts around the shoulder of the loaded shell followed by the haunches of the same shell.
- The induced maximum normal force in all three loading positions at different S/D ratios are significantly less than the critical forces, indicating that the shell is safe from global buckling.

In the next chapter, the influence of spacing to span ratio is analyzed under quasi-static moving loads. The focus is on the behavior of the central shell when a vehicle crosses the structure, while varying the spacing between the central and lateral shells.

8. Effect of shell spacing on mechanical behavior of multi-span soil-steel composite structure under moving load

The analysis in this chapter shares similarities with the previous chapter (Chapter 7). However, while the focus of the previous chapter was on ultimate load, this chapter shifts its attention to the behavior of the structure under moving loads. Specifically, it examines the effect of lateral shells on the central shell at different spacings in a multi-span soil-steel composite structure subjected to quasi-static moving loads. Through finite element (FE) analysis, the displacements and internal forces of the central shell during consecutive truck passages over the structure are investigated. To calibrate input parameters, field measurements from a site in Niemcza, Poland, are utilized.

Extensive research has been carried out to understand the mechanical behavior of SSCSs under various loading conditions, e.g., under static load [78] [140], semi-static load [72] [73] [125] [141] dynamic load [14] [142] [143], and seismic excitation [13] [144] [145]. Furthermore, several attempts have been made in both field tests [54] [63] [82] and numerical simulation [45] [112] [146] to investigate the response of SSCSs under ultimate loading conditions.

The arrangement of spans in multi-span SSCS holds a critical role in dictating their mechanical behavior. This pivotal aspect, including the spacing between individual shells, profoundly influences the load distribution, stress propagation, and overall structural response. Example of multi-spans soil steel composite structure is shown in Fig.8.1.



a)



b)

Figure 8.1: Example of multi-span soil steel composite structure; a) open profile [6] b) closed profile [147]

Understanding the intricate interactions between shell spacing and mechanical behavior is paramount for the informed design and robust performance of these composite systems.

This chapter presents two-dimensional finite element analyses to investigate the influence of lateral shells on the mechanical behavior of the central shell at various inter-shell spacings within a multi-span SSCS when subjected to quasi-static moving loads. For the analysis, an experimentally validated computational model was developed using non-linear finite element method (FEM) and implemented in the ZSoil FEA numerical program.

8.1. The behavior of the structure under live load

The structure tested by Antoiszyn *et al* [8] was a single-span SSCS with a span of 5.0 m and a rise of 1.85 m, located near Niemcza, Poland. The flat steel shell, which resembles a circular arch, had a thickness of 23.0 mm.

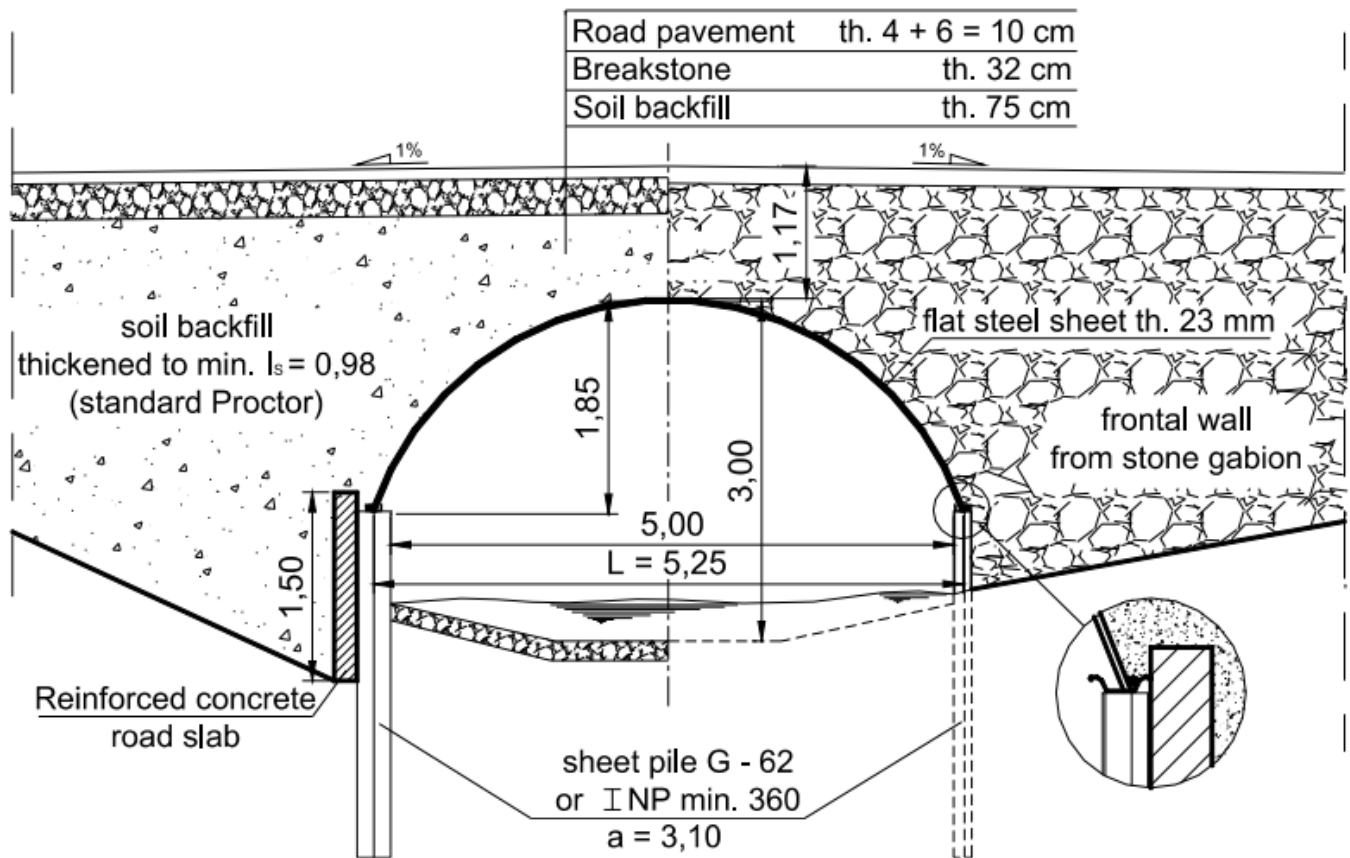


Figure 8.2: Cross section of the tested structure [8].

Fig. 8.2 illustrates the cross-section of the tested structure. The measuring base was adjusted according to the load schemes imposed by a truck and the configuration of the shell. Measurements were taken at ten reference points on the bottom surface of the shell, utilizing sensors placed in both longitudinal and transverse directions.

8.1.1. Testing procedure

The experimental test [8] is conducted by moving the dumper truckload on the bridge. During this experimental test, displacements and strain increments are recorded on the bottom of the shell under a moving truck. The loading arrangement is shown in Fig. 8.3. During the test, the truck crosses the bridge while moving to the left, then turns around and drives to the right. The driving was accomplished in a quasistatic approach, which indicates that the measurements were obtained while the truck was stationary as it slowly moved from one marker to the next. The following forces were transferred from the truck's axles to the structure: front axle ($P_1=54.0$ kN), middle axle ($P_2=129.0$ kN), and rear axle ($P_3=102.0$ kN).

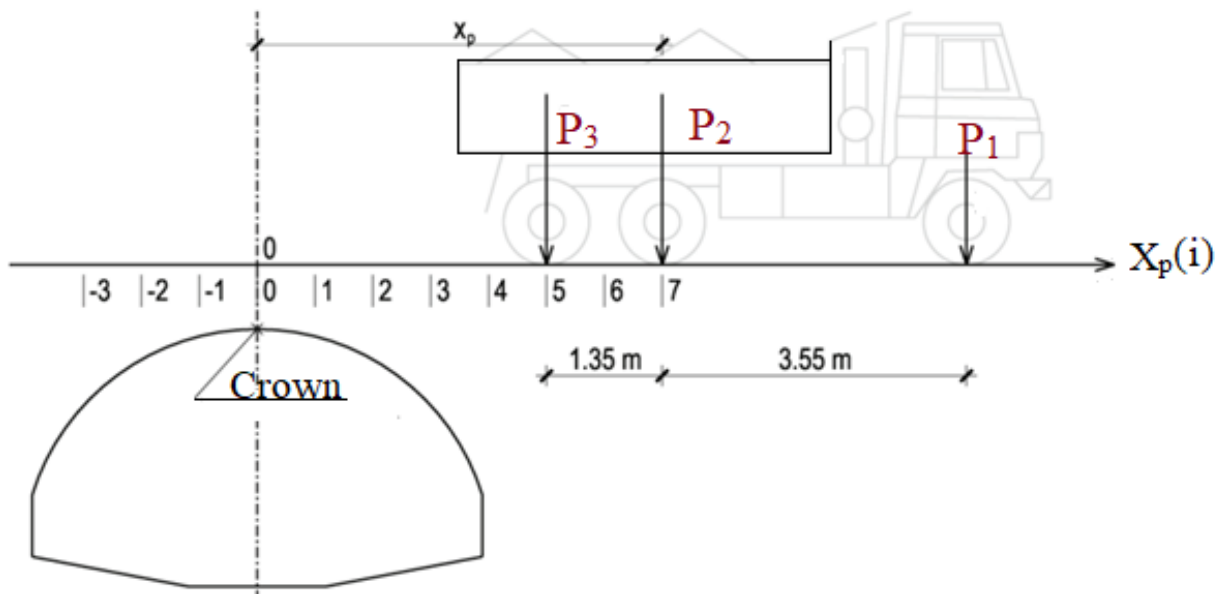


Figure 8.3: Loading arrangement, for test.

The markings with subsequent numbers i have been set along the road at intervals of every 0.675 m, where $i=0$ located on the axis symmetry of the structure Fig. 8.3. The measurement started when $i = 7$, i.e., when middle axle, P_2 is at distance 4.725 m from the axis of the structure. Then the truck crosses the structure, and the first travel will end once the P_2 reaches $i = -3$, i.e.,

when P_2 moves -2.025 m away from the central axis of the structure. Then truck return back without turning until P_2 back to initial starting point, $i=7$ by creating a loop. During this successive movement of truck over the bridge, the measurement was taken at bottom of crown of the shell as shown in Figs (8.4(a-b)).

The initial study report by [8] presents the results of field tests performed during two phases, namely before and after the pavement on the bridge. The field measurement on the unpaved bridge is considered in this thesis.

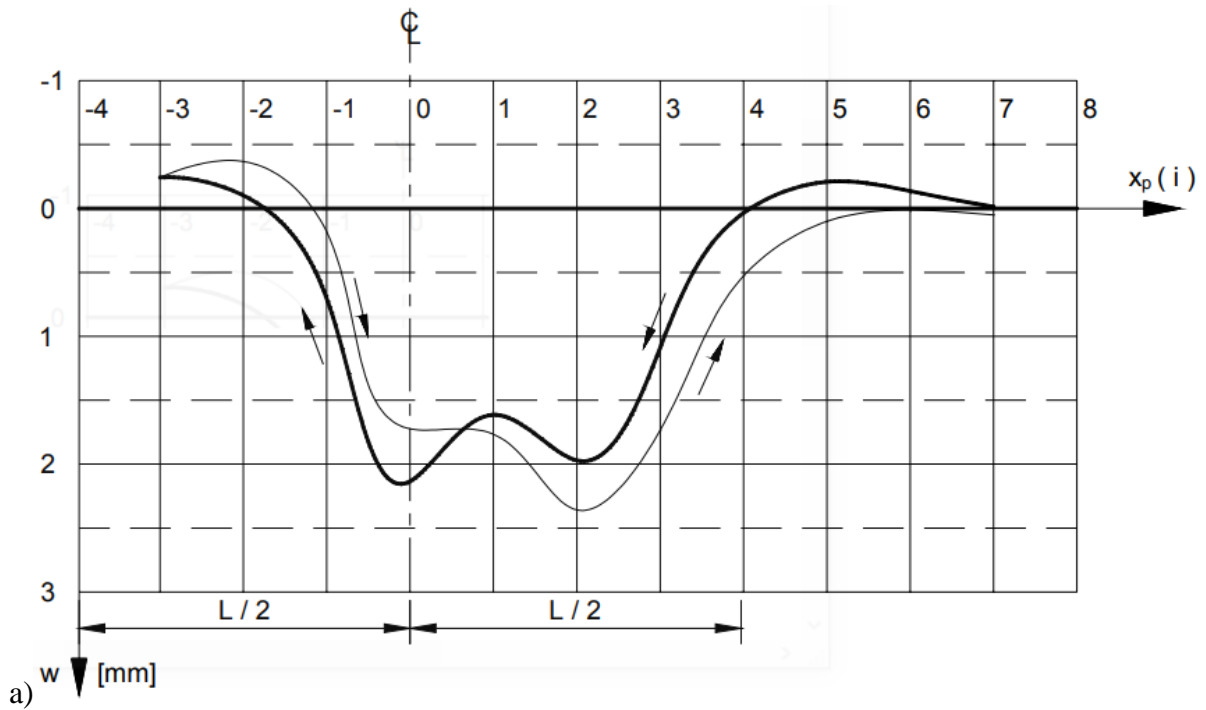
8.1.2. Testing results

On the horizontal axis of Fig. 8.3, the position (i number) of the truck as it travels along a designated movement track is described (moving along the bridge axis). It's important to note that the measuring cycle on the structure typically commenced when the truck was at position $i = 7$. At this initial position, the sensors indicated a minimum deflection as shown Fig. 8.3. Subsequently, the truck was driven back in the proper direction and stopped at predetermined positions to facilitate the automatic registration of the measurement results. In the field test [8], vertical displacements were meticulously measured perpendicular to the steel shell surface, with a particular focus on the crown of the structure. This measurement setup allowed to capture the response of the structure subjected truck load accurately. The results of these measurements, specifically the vertical displacements occurring at the crown.

A distinctive and significant characteristic observed in the field test is the consistent shift of extreme deflections in the direction of the truck's movement, particularly the first drive with reference to the return drive. This shift in extreme deflections is a key finding of the study. Particularly, the deflection extrema are prominently formed under the P_2 (middle) and P_3 (rear) axles when they are positioned over the crown of the shell. This observation indicates that the structural response, specifically the vertical displacements (See Fig. (8.4(a)), is most pronounced when these axles are in proximity to the crown. Moreover, these extrema align with the positions of specific truck axles further emphasize the direct relationship between the loading configuration and the structural response.

Fig. (8.4(b)) displays the curve representing the normal stress in the circumferential direction (σ_x) at the same point, crown of the shell. Similar to the displacement curve, the presence of shift of extreme value of stresses in the direction of the truck's movement.

To sum-up, the results obtained from measurement by [8], reveal an interesting behavior in the structural response of the soil steel composite structure under vehicular loading conditions. Specifically, the curves corresponding to the displacements and stress (See Figs. (8.4(a–b))) exhibit hysteresis loops, which indicate a unique and significant characteristic of the structural response. Hysteresis loops in structural response curves are of significant interest and importance in structural engineering and mechanics. They indicate that the response of the structure is history-dependent, meaning it not only depends on the current loading but also on its previous loading history. This behavior can be attributed to various factors, including material behavior, nonlinearities, and energy dissipation within the structure.



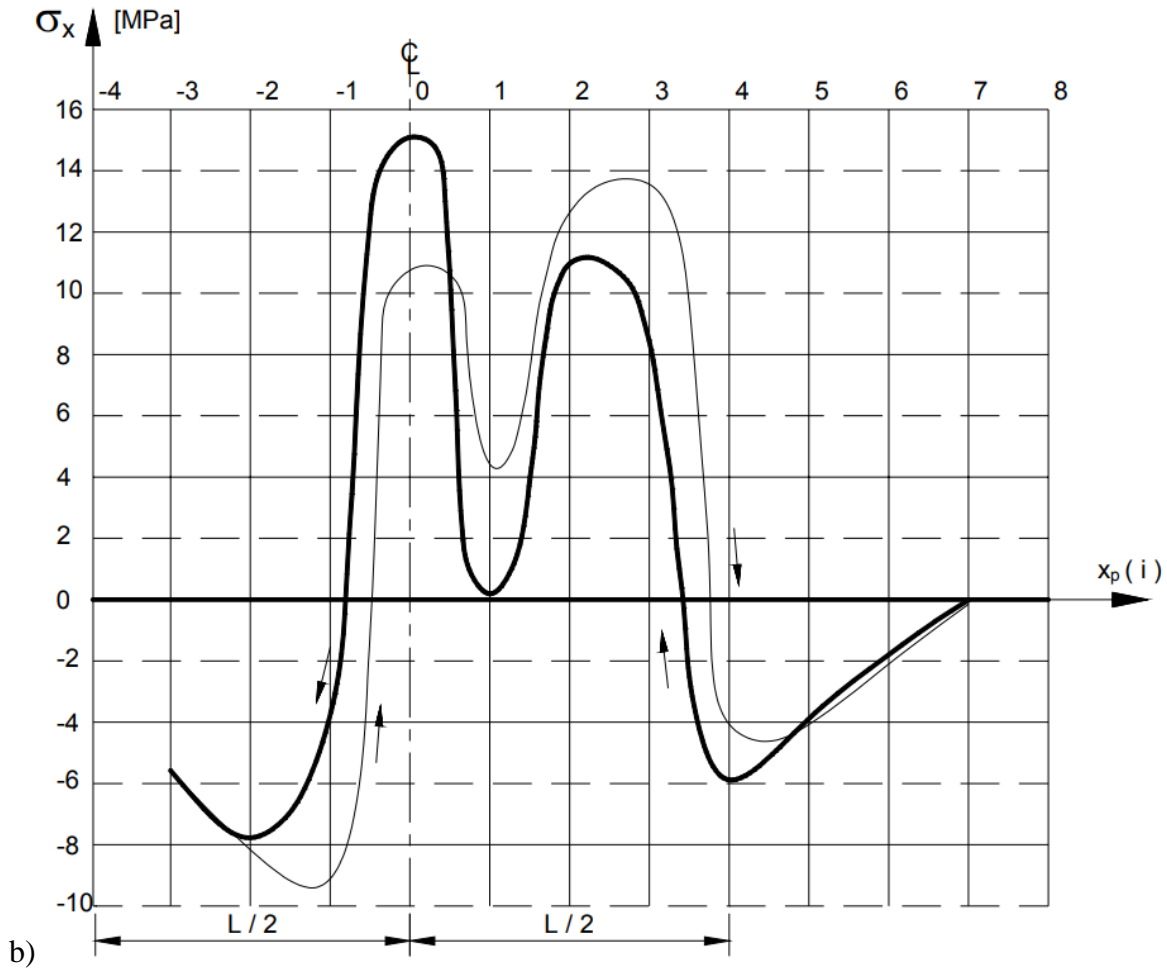


Figure 8.4: Results from the field measurement at the crown of the shell a) vertical displacement b) stress [8]

8.2. Formulation of computational model

The numerical analysis of the behavior of SSCSs subjected to quasi-static moving loads was performed using the ZSoil software program [124], based on the Finite Element Method (FEM). The structure was modeled as a 2D object in plane strain, utilizing beam elements for the shell structure and sheet piles, and solid elements for the backfill soil. The bottom boundary was fixed in all directions, while the vertical boundaries were restricted against horizontal displacements. In the numerical calculation, a plain strain analysis was assumed. For the backfill soil, an elastic-plastic constitutive model with the Mohr-Coulomb yield criterion was employed. The unassociated plastic flow rule was described by the ZSoil user manual and used to determine the dilatancy angle based on Eq(8.1) [124]:

$$\psi = \max (0.1\varphi, \varphi - 25^\circ), \quad (8.1)$$

where φ the internal angle of friction and ψ is the dilatancy angle.

The interface between shell and backing soil is generated in the model. A one-sided contact was assumed at the interface, i.e., separation of the backfill material from the shell is permitted if the shell moves away from the backfill material and subsequent contact renewal is permitted if the backfill and shell get closer again. The Coulomb condition was used to describe the behavior of the assumed interface. A non-associated plastic flow rule was used to govern a plastic slip, with the dilation angle set to $\psi = 0$. The Coulomb condition governs the value of maximum tangential stress in contact elements based on Eq (8.2):

$$|\tau_f| \leq a + \sigma \tan \delta, \quad (8.2)$$

Where adhesion $a = 0$, the angle of friction $\delta = 0.6 \varphi$ and $\varphi = 34^\circ$ is the internal friction angle of the backfill material adjacent to the interface. The dilation angle ψ , was assumed as zero. Elastic deformation moduli (normal and tangential stiffness) for interface elements were determined according to the ZSoil user manual [124] as follows:

$$K_n \approx K_t = \frac{E}{h} \quad (8.3)$$

Where E is its modulus of adjacent material, that is, the filling soil, and h is the depth of the very thin weak layer. Based on Eq (8.3), the value of normal and tangential stiffness adopted in the calculation was 1.5×10^7 kN/m. The parameters of backfill soil in a dense compaction state, i.e., density index $I_D = 0.8$ considered in the model. The shell and sheet pile are modeled as beam elements and linear elastic constitutive relations were assumed for both materials. Sheet piles of type G-62 were assumed and positioned at a distance of 3.1 m.

As this study aims to investigate the effect of spacing, six different models of different distances between shells have been created. Furthermore, a single-shell structure reference model is considered for calibration purposes. All the models mentioned, in terms of their geometry, are presented in Figs. (8.5(a – g)). The first model was prepared as a single shell, that is, without lateral shells, as shown in Fig. (8.5(g)). The displacement and stress from this model are used as a reference to understand the effect of the lateral shells on the central one at a different distance. The

quasi-static approach of moving truck was simulated as presented in previous works [46] [72] [73] [125] [148].

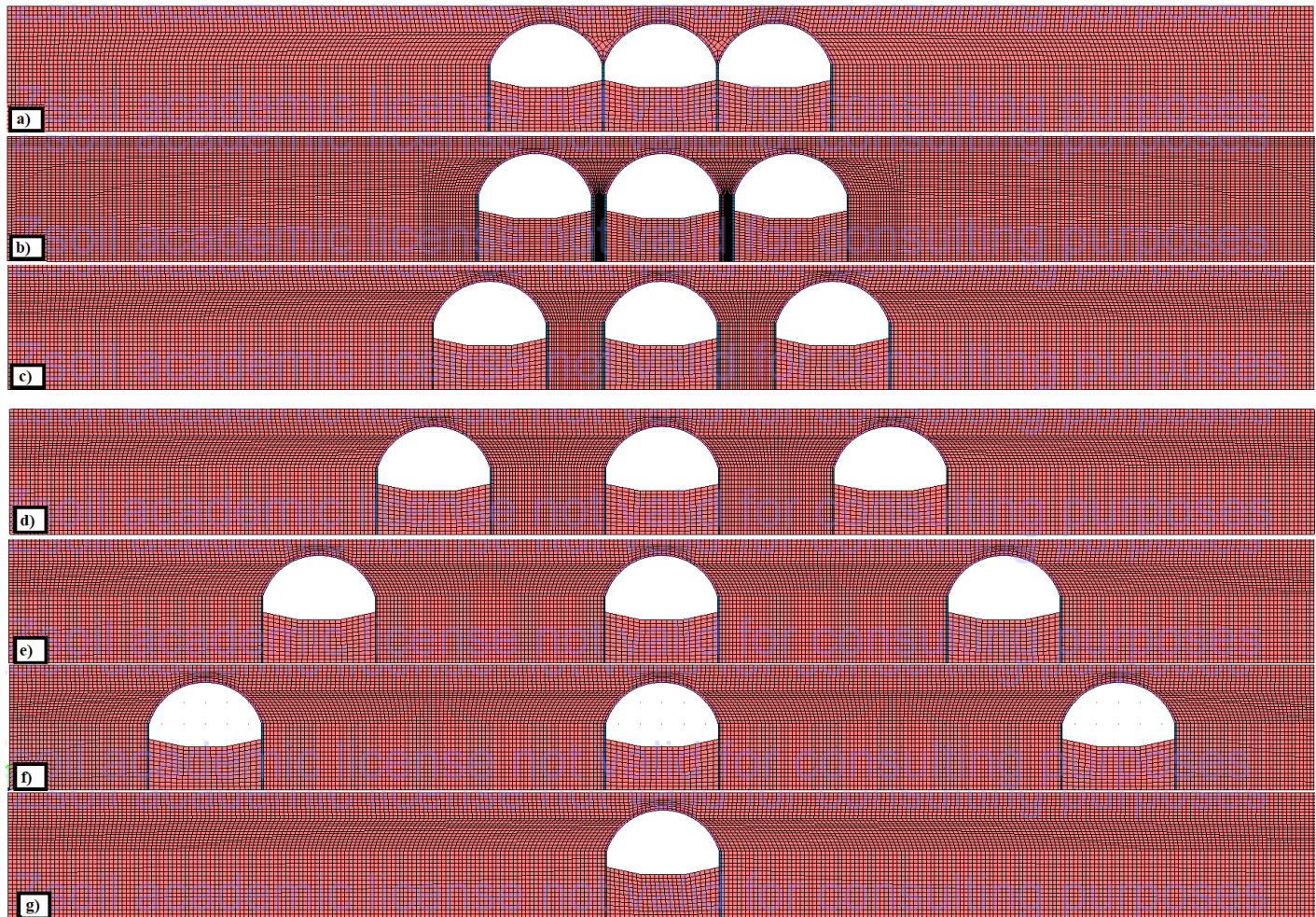


Figure 8.5: Geometry of numerical models: a) no space between the shells b) 0.6 m spacing c) half of the span spacing d) spacing equal to span e) twice of span spacing f) three-time span spacing g) infinite spacing or reference bridge.

8.2.1. Parametric analysis

A steel shell with a span of 5.25 m and a depth of 0.75 m cover was examined together with two lateral shells with five different spacings. These spacings are 0.0, 0.6, 2.625, 5.25, 10.5, and 15.75 m, corresponding to a spacing-to-span ratio (S/D) of 0.0, 0.114, 0.5, 1.0, 2.0, and 3.0, respectively. In the third model, 0.6 m of space was provided between the shells. This distance was the minimum distance recommended by [57] for short-span structures based on the type of profile and the span of the structure to be considered. The initial stress by the dead weight load was the first phase of the simulation. The simulation was then continued by applying the load

exerted by the truck at its starting position. The position of the truck load is labelled by the variable X . When $X = 0$ the truck load is at the center of the structure (see Fig. 8.6). Three hundred successive load locations were carried out during the truck movement between extreme positions ($X = -30.0$ m; $X = +30.0$ m). In the simulation, it was assumed that the forces of the truck axis were distributed on the width of the track in the transverse direction and at a distance of 0.5 m along the bridge, similar to the assumption proposed by [72]. The reduced load P were calculated based on Eq. (8.4) [149].

$$q = \frac{P}{b'} \quad (8.4)$$

where P is the value of the force transferred from the axle load ($(P_1 = 54.0$ kN, $P_2 = 129.0$ kN, and $P_3 = 102.0$ kN)) and b' the reduced width of the impact of truck.

Because of their 3D distribution, soil stresses decrease as depth increases. creating a similar effect in 2D is impossible. As a result, the impact width b' was calculated by proper calibration based on field measurement displacement. Accordingly, the reduced width $b' = 1.8$ m. and the corresponding distributed loads are $q_1 = 60.0$ kN/m, $q_2 = 143.3$ kN/m, and $q_3 = 113.3$ kN/m. Similar assumptions were considered by [11] [20].

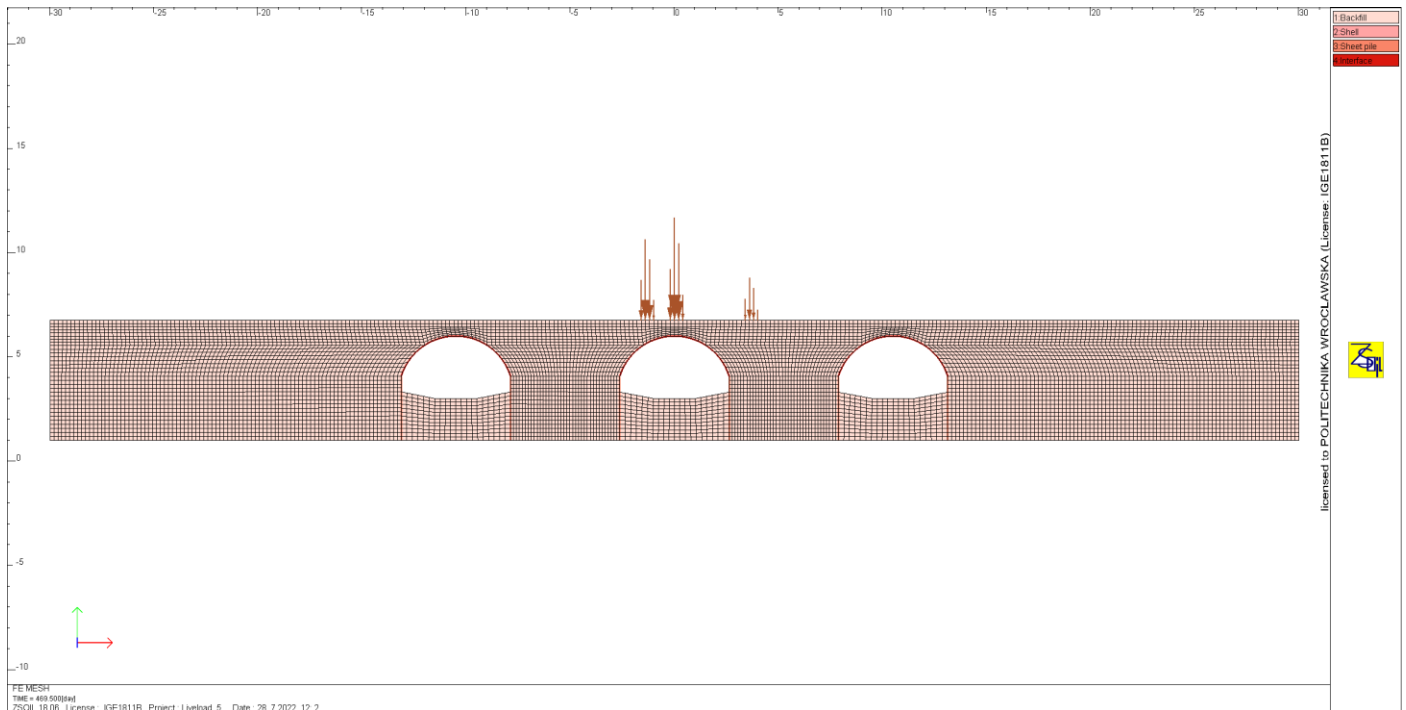


Figure 8.6: Equivalent nodal forces from truck loads.

The numerical analysis assumed four passes of the truck over the bridge, that is, two complete load cycles consisting of "forward" and "back" travel. The live load from the truck is added to the model after the soil fill has been laid, but before the road foundation and asphalt surface are laid. That means that in this model, the effect of road foundation and pavement was not taken into account. Based on the position of the lateral shells, seven different models were developed, including the reference model, Fig. (8.5(g)). The first model was prepared without lateral shells. The result of the simulation is described in the next section.

8.2.2. Validation of numerical model

8.2.2.1. Simulation results

Given the challenge of conducting experiments on multi-span SSCS with varying shell spacing, a decision has been made to employ field measurements on a single span SSCS as outlined in Section 8.1. The numerical model has been validated using thus field tests conducted on this particular structure subjected to quasi-static moving loads.

The measured displacement and stress at the bottom of the shell crown (at reference crown) in Fig (8.2(a)) sets the basis for the validation of the numerical model. Taking into account these measured displacements, a parametric analysis is conducted to calibrate the input parameters like modulus of elasticity, cohesion, friction angle, and interface stiffness, i.e., both normal and tangential. The main objective of this calibration is to fit the absolute maximum displacement and stresses during the first passage. Accordingly, the calibration of the FE model is successfully carried out using the results of measured displacement and stress, as shown in Fig (8.7) and Fig (8.8), respectively.

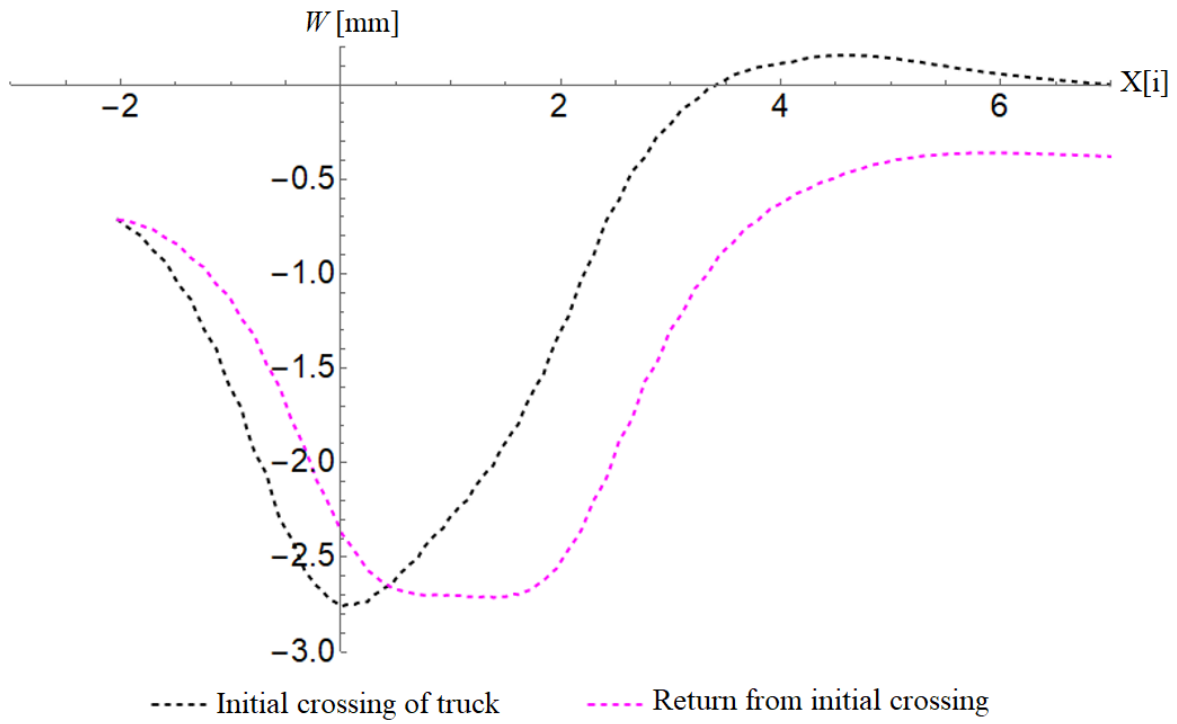


Figure 8.7: Vertical displacement curve at the crown of the shell during consecutive truck crossings.

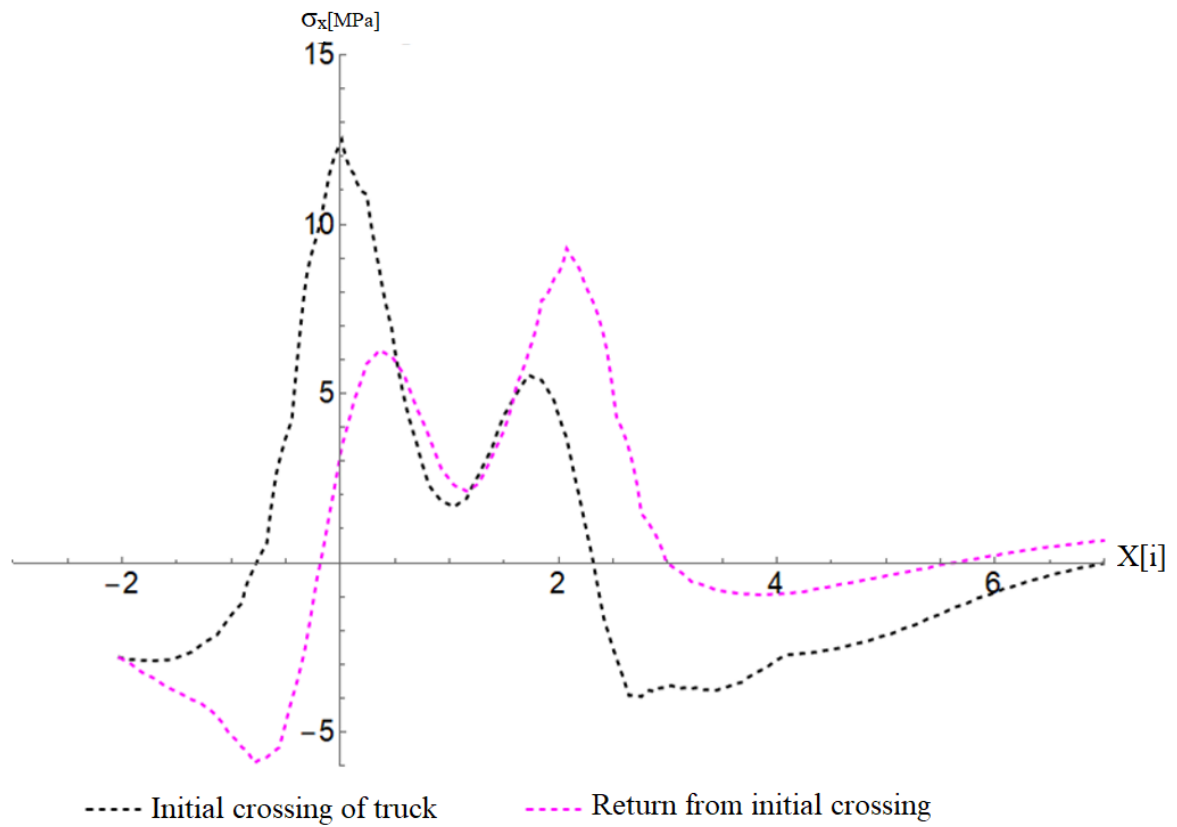


Figure 8.8: Circumferential stress at the crown of the shell during consecutive truck crossings.

The absolute maximum vertical displacement observed in the field test at the crown of the shell is approximately 2.4 mm [8] as shown Fig. (8.4(a)). While numerical simulation predicts an absolute maximum displacement of approximately 2.54 mm. These results demonstrate a close agreement between the field test and numerical simulation, with the simulation slightly overestimating the maximum vertical displacement. Nevertheless, it is important to note that the difference is less than 6 %. Furthermore, the finding from both the field test and numerical pertains to a consistent shift in the location of the maximum vertical displacement, occurring in the direction of the truck's movement. This phenomenon provides a clear indication that the structural response is asymmetrical and influenced by the position of the truck's axle during its passage over the structure. This highlights the effects of loading position on flexible soil steel composite structures.

The values of stress are underestimated but the course of the chart is in good agreement with the experimental one. This suggests that while the absolute values may differ, the trends and patterns of stress distribution are captured effectively by the numerical model. Similar to the vertical displacement, a significant finding in both the field test and numerical simulation is the consistent shift of extreme stress values in the direction of truck movement for consecutive truck passes. Thus, the results obtained numerically exhibit the same tendency as those identified experimentally.

The parameters for the material used in the numerical computations are shown in Table 8.1.

Table 8.1: The material parameters used in the computations.

	Steel sheet	Steel pile	Backfill soil
Young's modulus	205 GPa	205 GPa	150 MPa
Poisson ratio	0.3	0.3	0.25
Moment of Inertia	$1.01 \times 10^{-6} \text{ m}^4/\text{m}$	$9.833 \times 10^{-6} \text{ m}^4/\text{m}$	-
Sectional area	$1.91 \times 10^{-2} \text{ m}^2/\text{m}$	$2.07 \times 10^{-3} \text{ m}^2$	-
Unit weight	$78.6 \text{ KN}/\text{m}^3$	$78.6 \text{ kN}/\text{m}^3$	$19 \text{ kN}/\text{m}^3$
Cohesion	-	-	10 kPa
Friction angle	-	-	34 °
Dilatancy angle	-	-	9 °

In conclusion, the comparative analysis of field test and numerical simulation results for the vertical displacement and stress at the crown of the shell demonstrates a good level of agreement, providing validation for the numerical model.

8.3. Numerical results

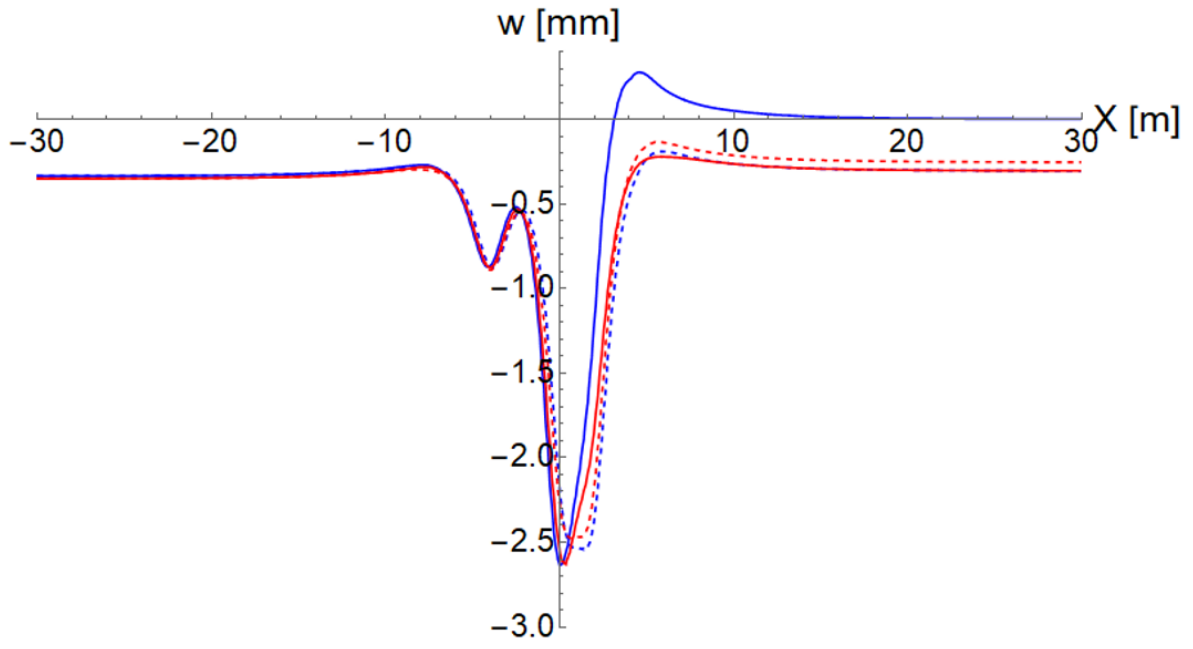
The Selected vertical and horizontal displacement, as well as the stress, σ_x results obtained from the six different models of the SSCSs are shown in Figs. (8.9–8.11). The graphs show the change in shell displacements and stress caused by the truck passage and the position of the lateral shells. The results of the displacements and stress at the crown of the central shell are presented. The graphs illustrate changes in central shell displacement produced by the trucks' initial and returning travels, as well as the position of the lateral shells. On the basis of these results, the effect of the position of the lateral shells on the deformation of the central shell is observed.

The stress at the crown of the central shell, presented here as a numerical simulation result, was calculated based on Eq. (8.5):

$$\sigma_x = \frac{(N-N_0)}{A} + \frac{(M-M_0)}{I} \cdot \frac{h}{2} \quad (8.5)$$

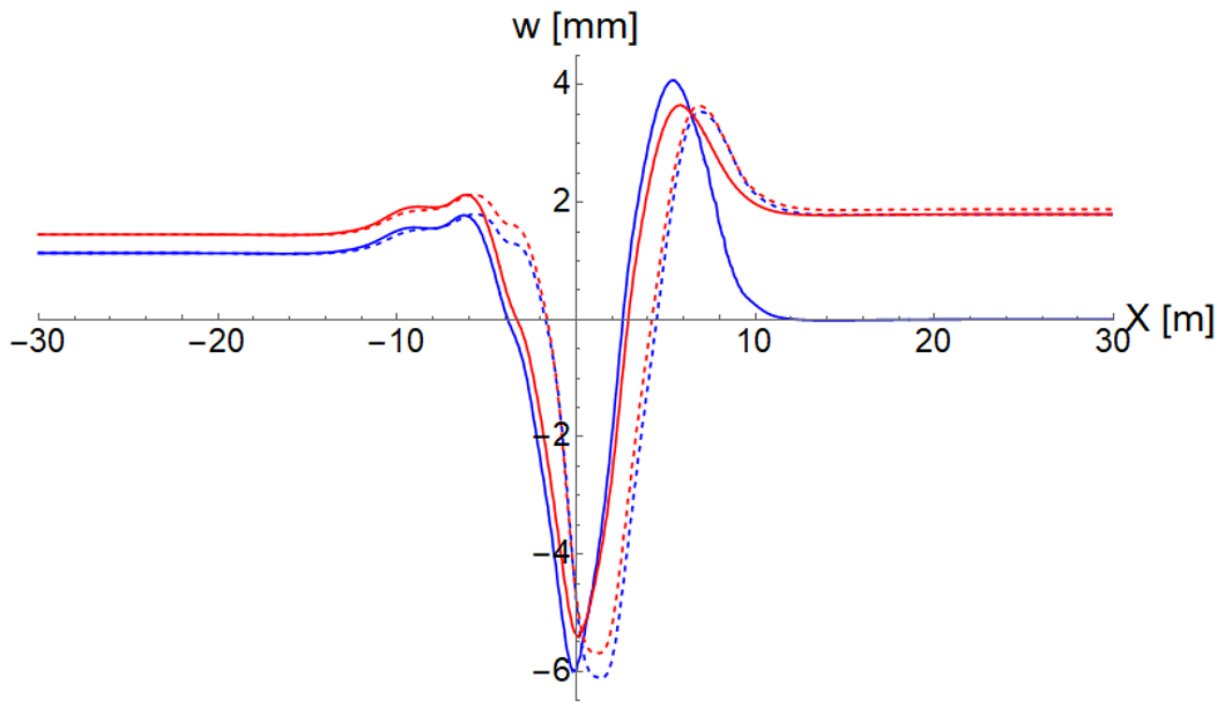
where N , M stands for the axial force and the bending moment, respectively, and N_0 and M_0 are the values of the axial force and moment for the calculated structure at the start of the test, I and A are moment of inertia and the cross section area respectively. while h is the thickness of the steel shell.

Under the scope of this numerical modeling, critical results pertaining to the vertical and horizontal displacements, as well as stress distributions, have been obtained at the crown of a soil-steel composite structure shell. The investigation centered on understanding how the bridge responds as a truck crosses it, both in backward and forward movements in quasi-static manner, without any turning. To create a robust modeling scenario, the truck completed four crossings in total by traversing the bridge twice in each direction. The visual representations in Figs. (8.9–8.11) illustrate these crossings, with the initial crossing of the truck from $x = L$ to $x = -L$ highlighted in blue, and the return from $x = -L$ to $x = L$ marked with dashed blue lines. Similarly, the second crossing from $x = L$ to $x = -L$ is depicted in red, and the return from $x = -L$ to $x = L$ is denoted with dashed red lines.



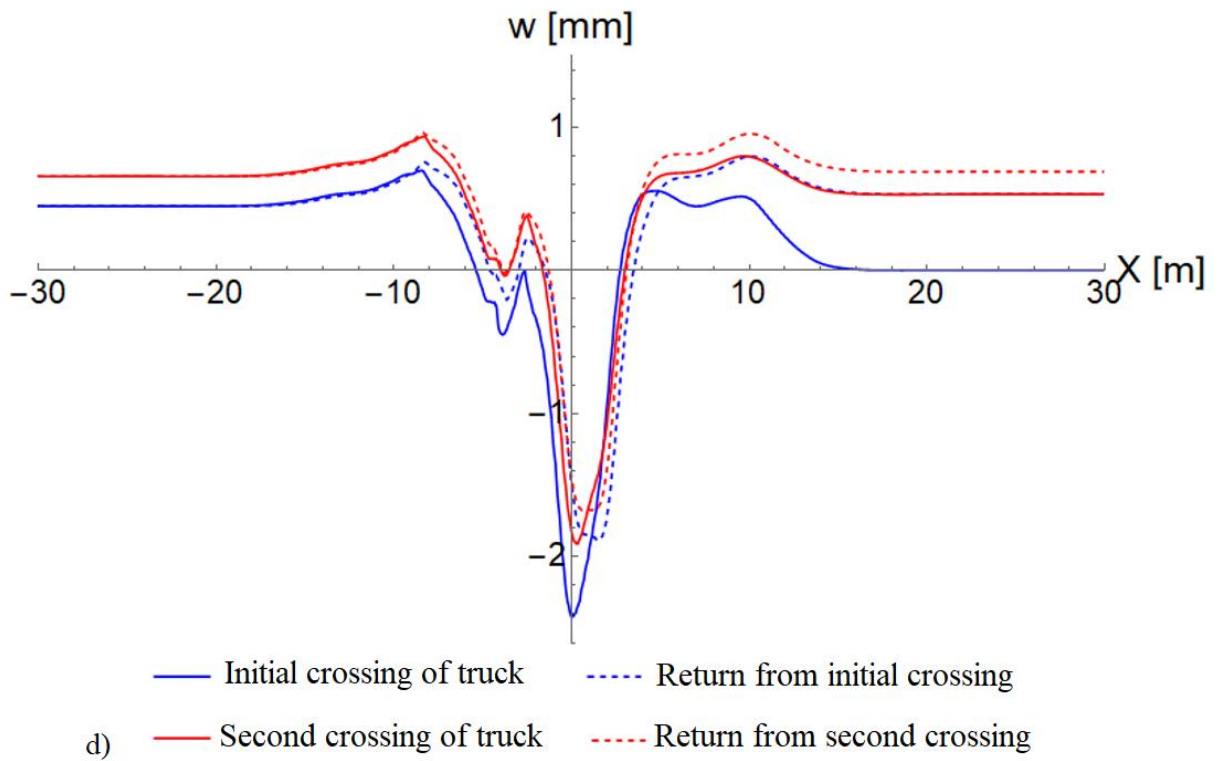
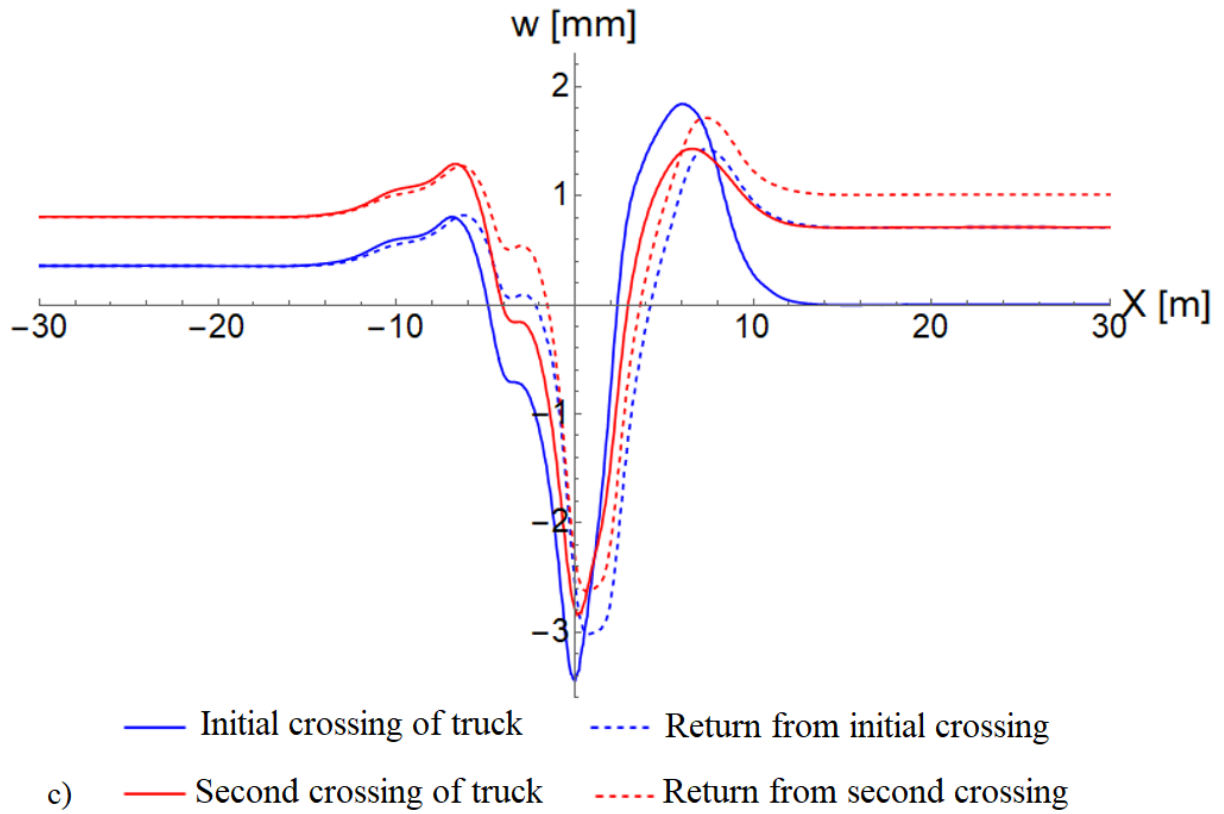
— Initial crossing of truck - - - Return from initial crossing
 — Second crossing of truck - - - Return from second crossing

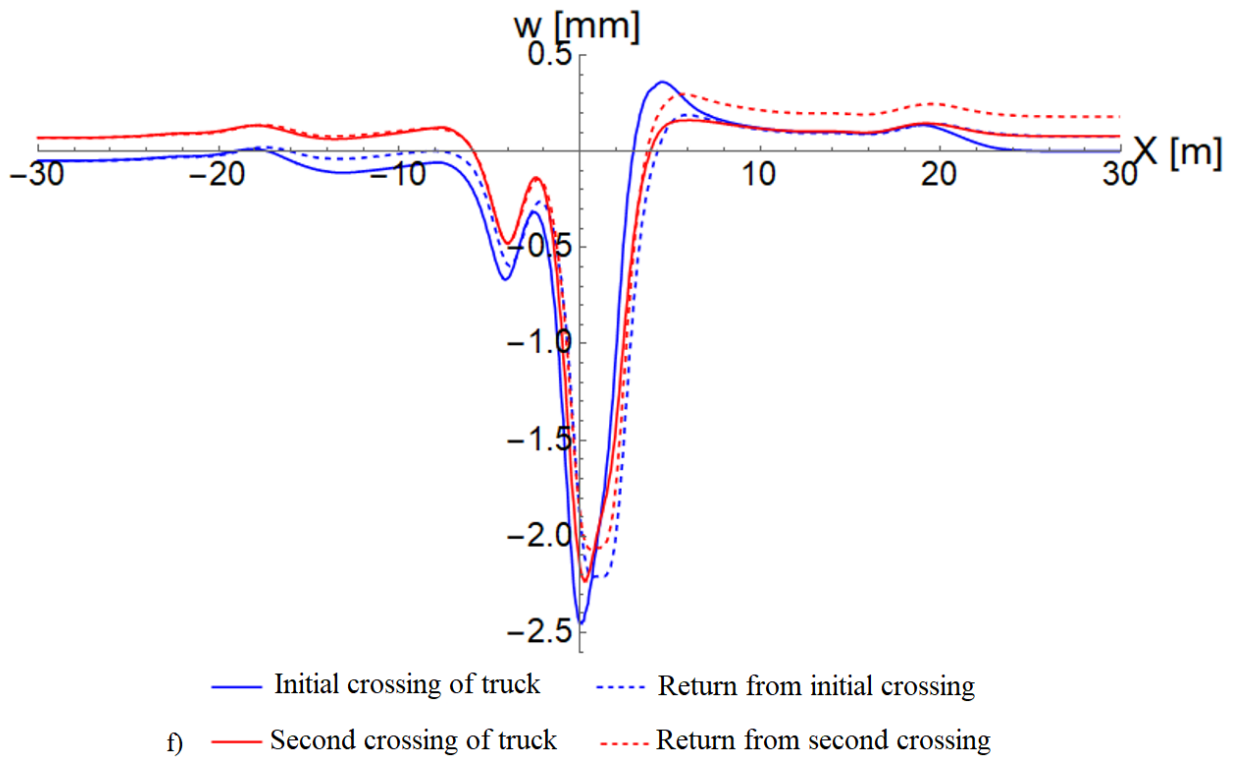
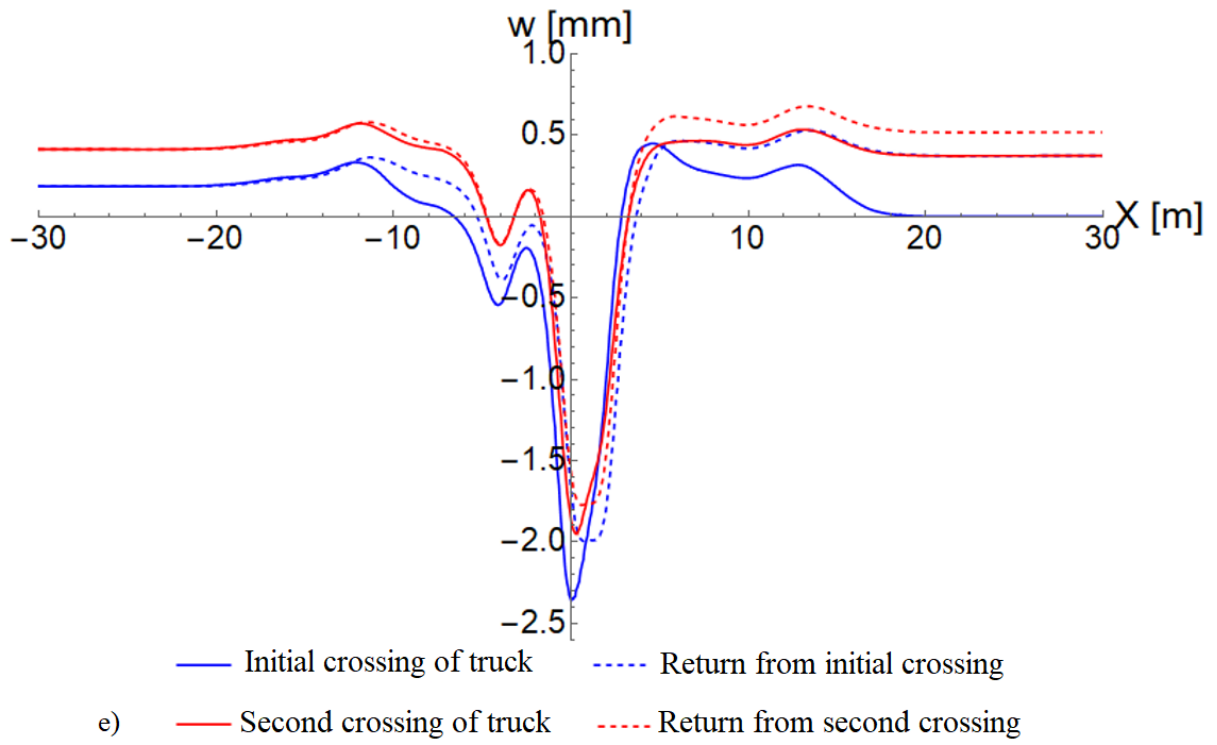
a)



— Initial crossing of truck - - - Return from initial crossing
 — Second crossing of truck - - - Return from second crossing

b)





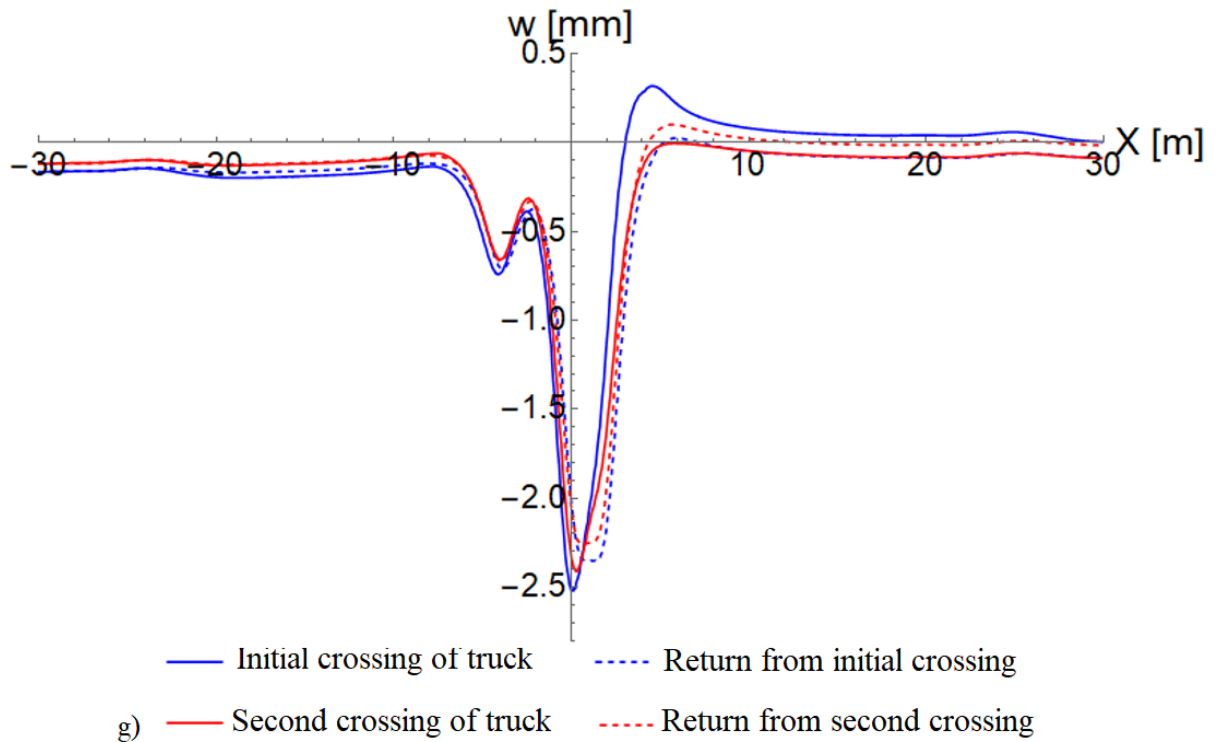
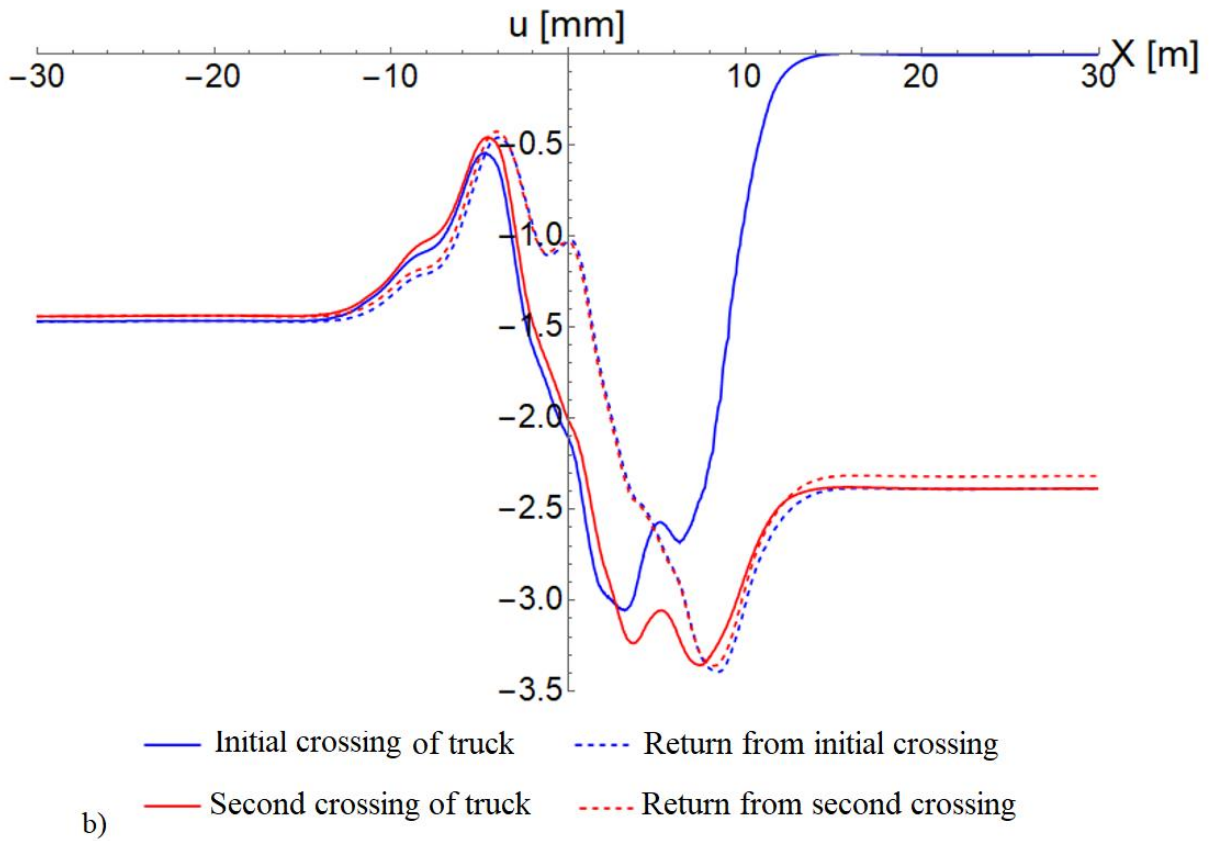
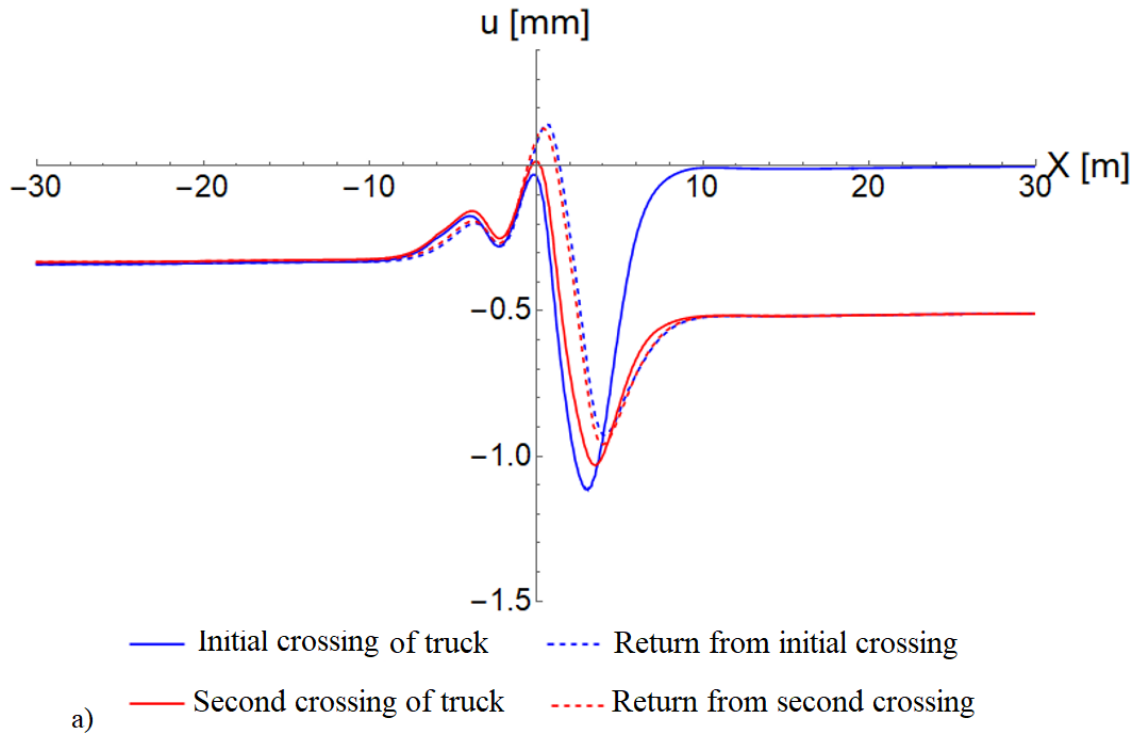
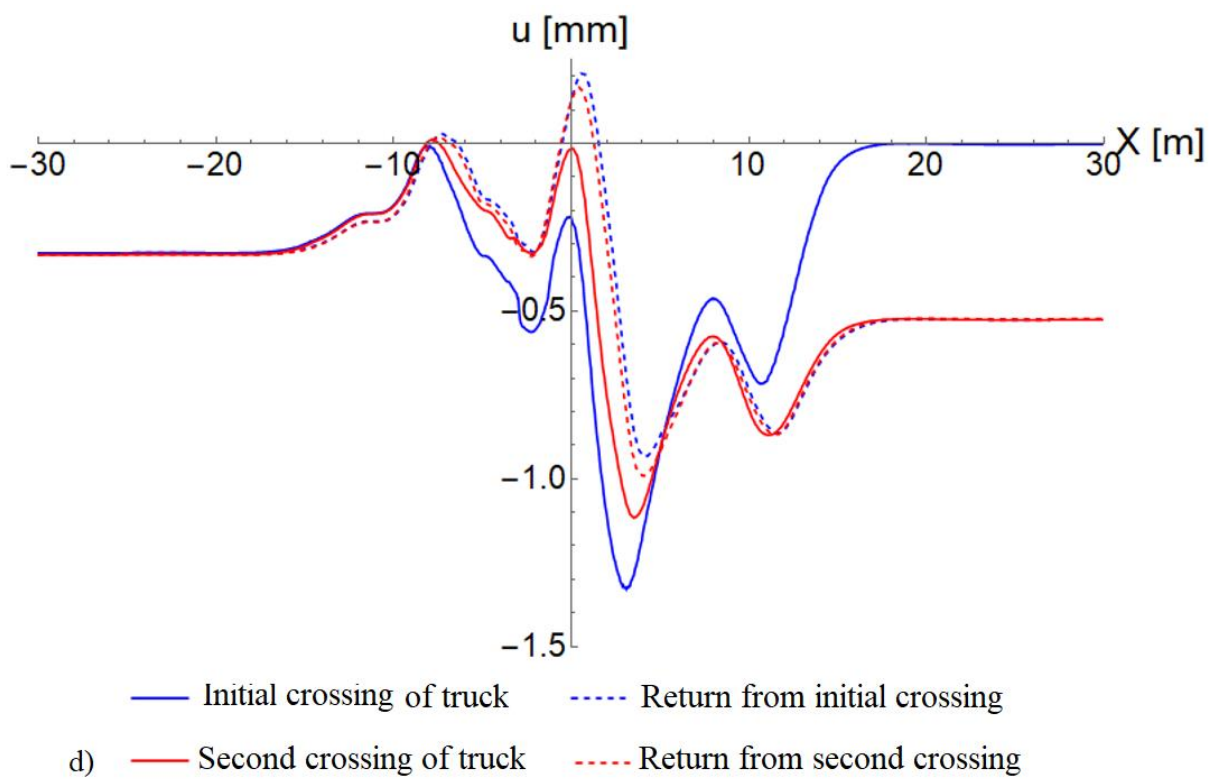
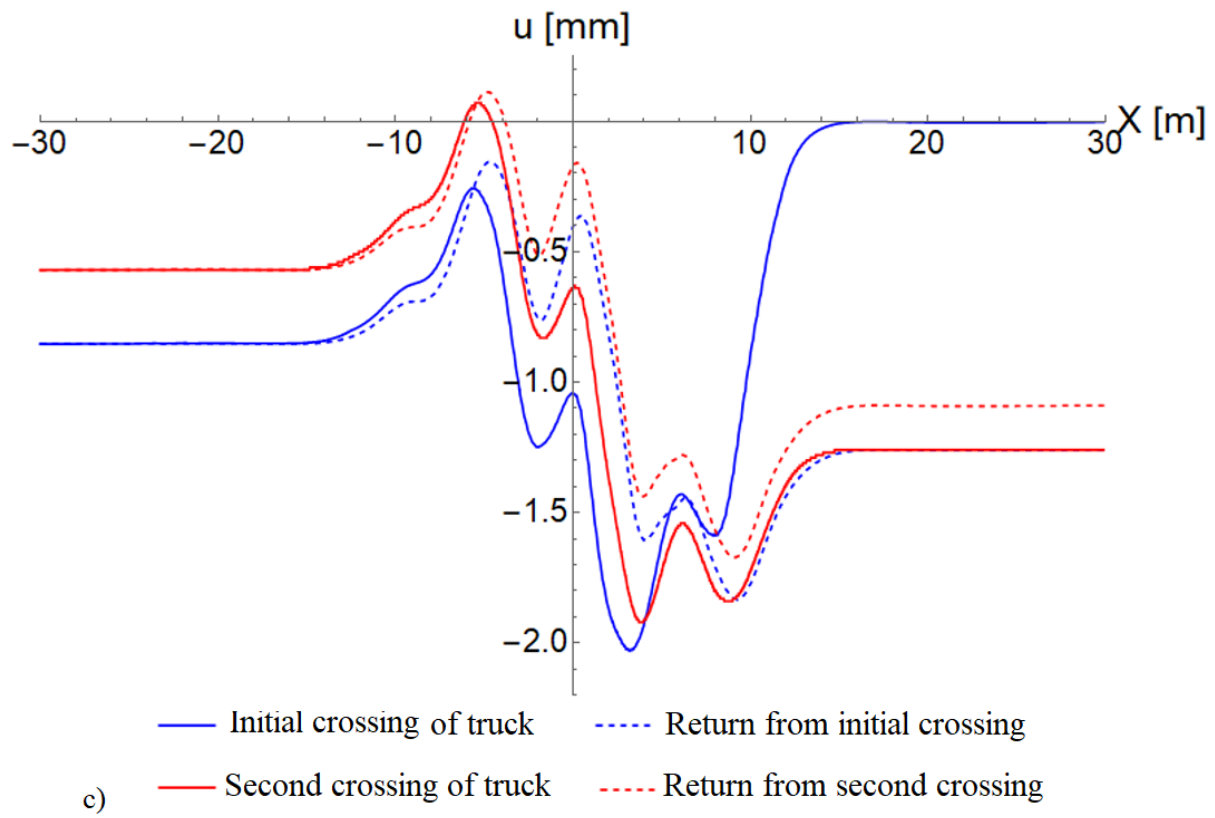
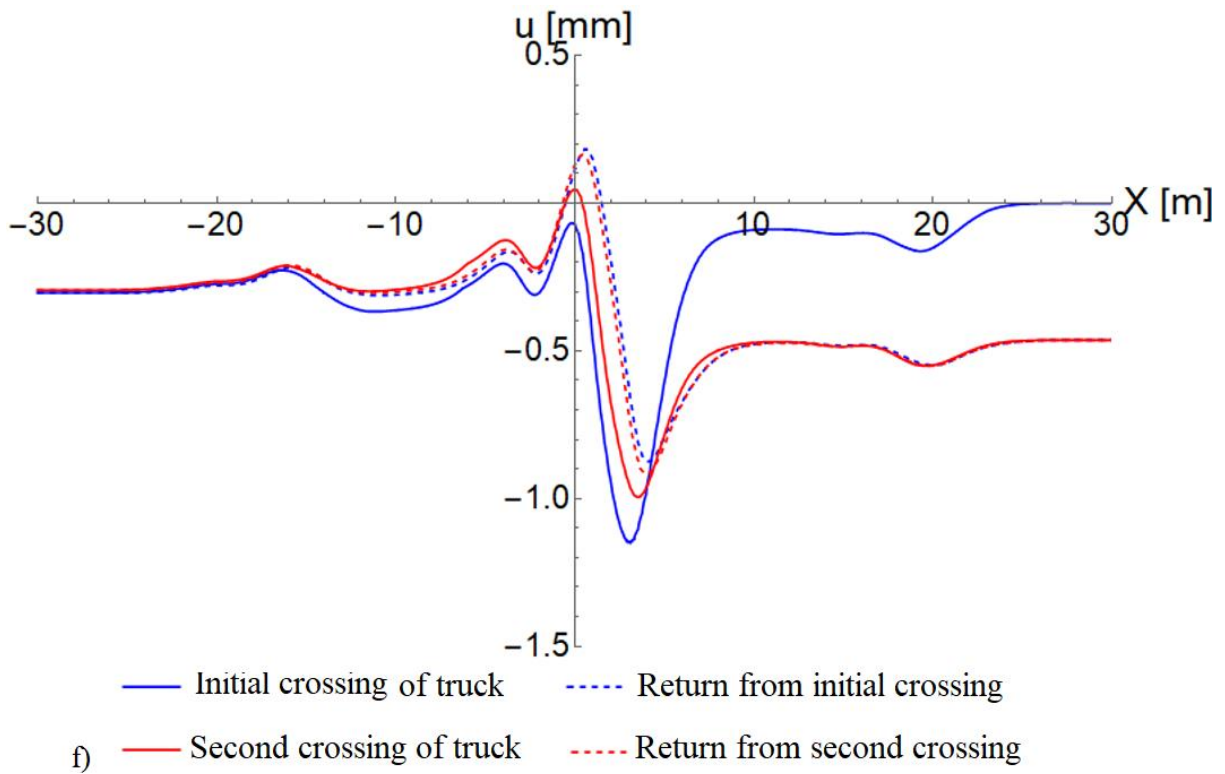
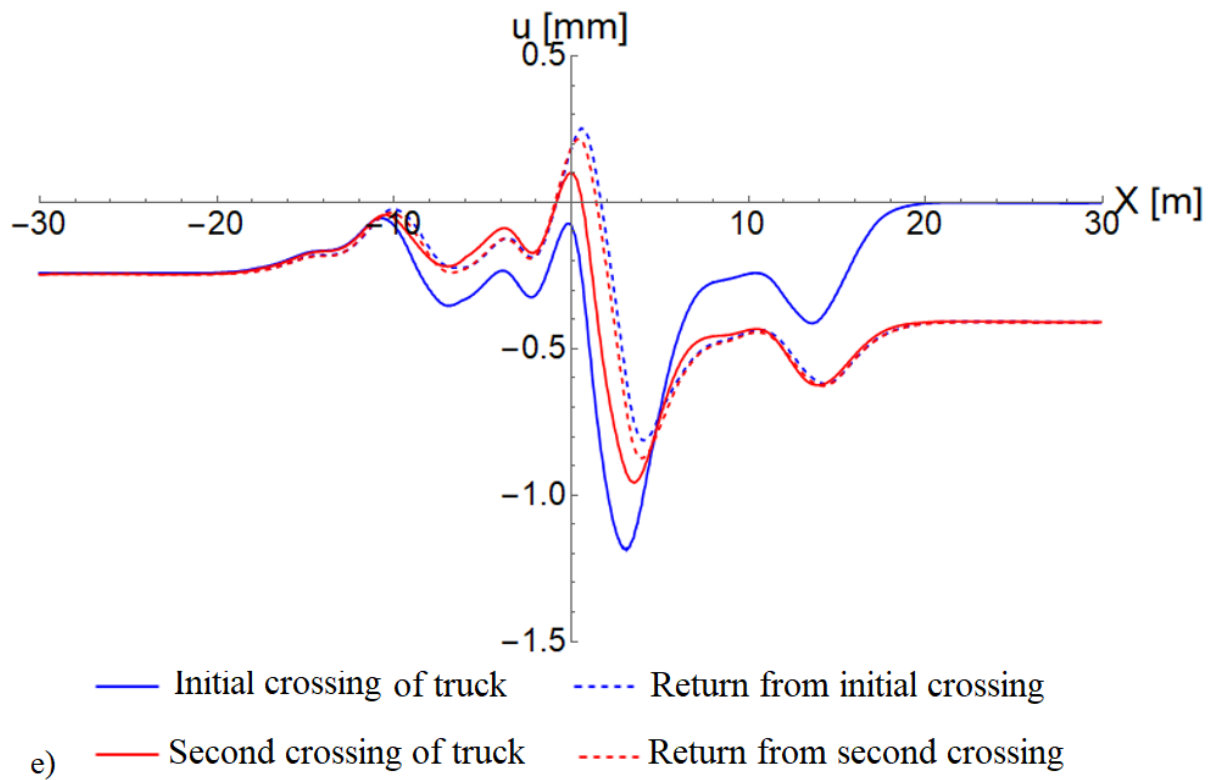


Figure 8.9: Vertical displacement at the crown of the central shell during consecutive truck crossings: (a) reference (b) central shell at 0.0m distance from lateral shell (c) at 0.6m (d) at 2.625m (e) at 5.25m (f) at 10.5 m (g) at 15.75 m

Notably, the analysis reveals that the values of the displacements and stress change as the direction of movement changes. These variations in displacement and stress are critical to understanding the bridge's dynamic behavior under the influence of the truck's movements. Furthermore, the results consistently show the creation of hysteresis loops, indicating that the bridge's response is not only dependent on the current loading but also on the previous loading history. The presence of hysteresis loops in the results highlights the importance of considering the bridge's past loading conditions when assessing its response. These findings represent essential contributions to bridge design and analysis, shedding light on the complex behavior of soil-steel composite structure under repetitive truck crossings.







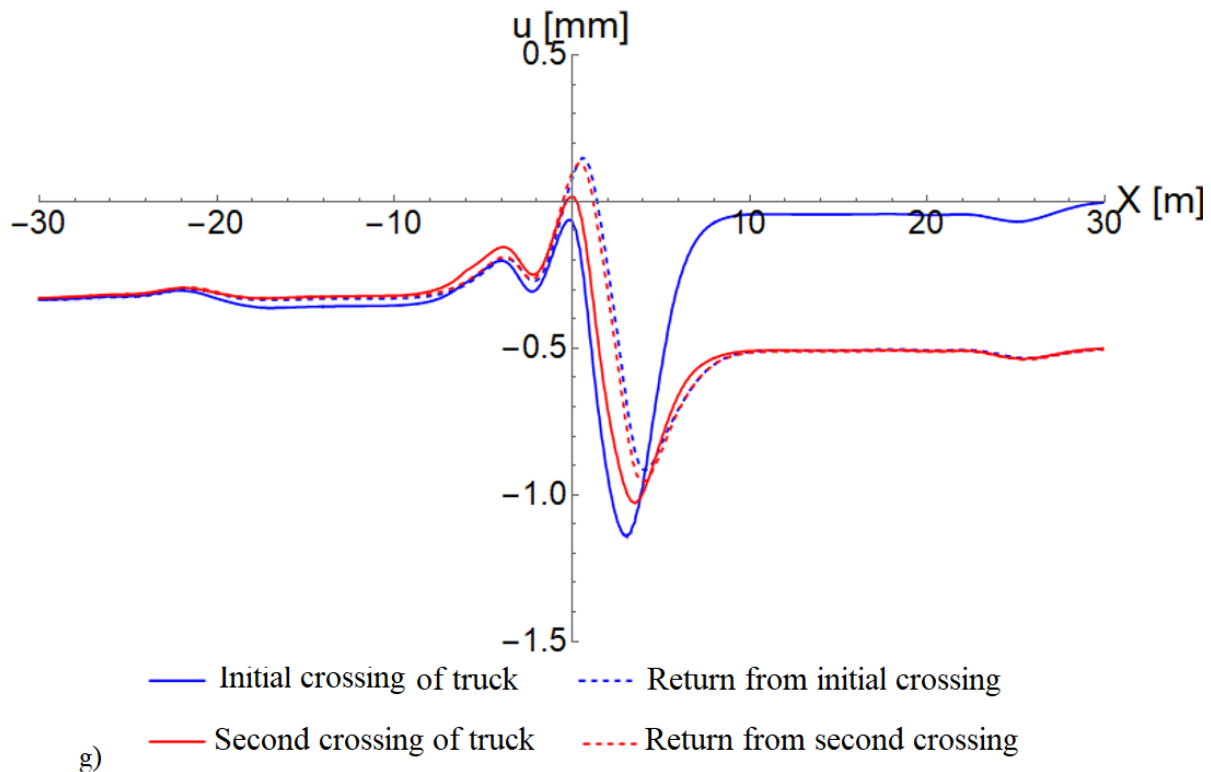
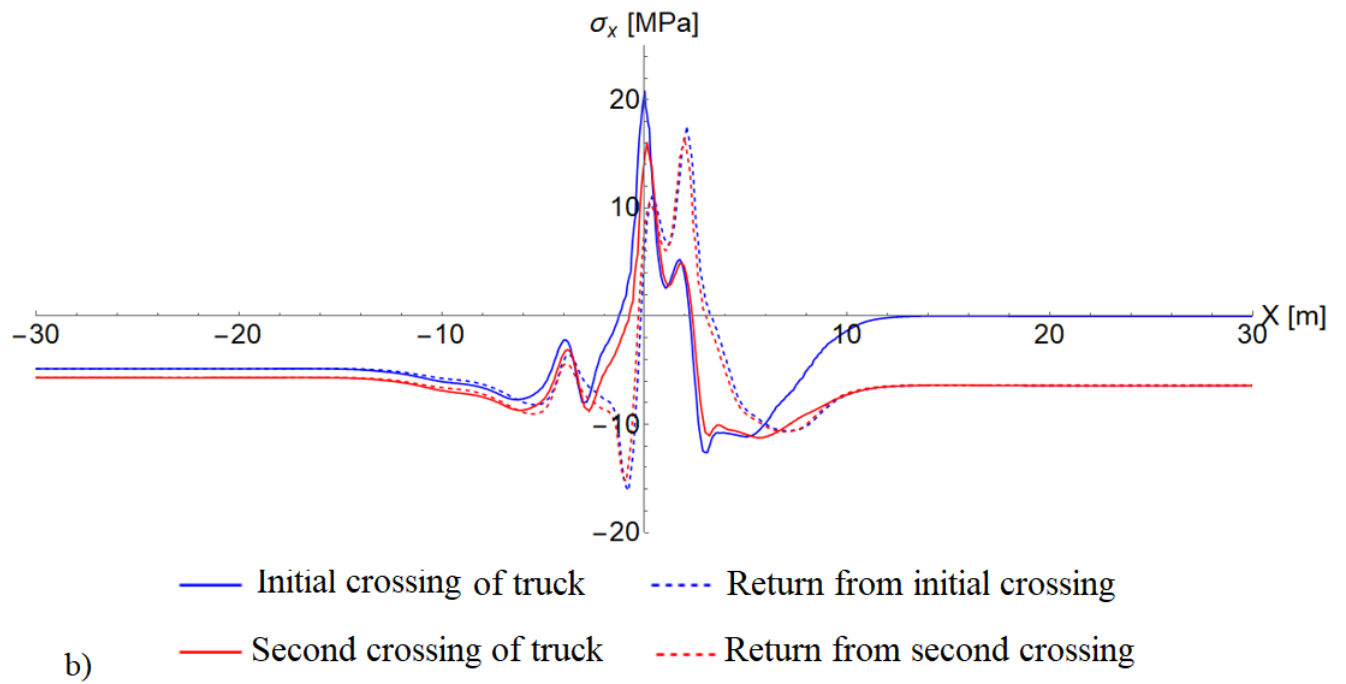
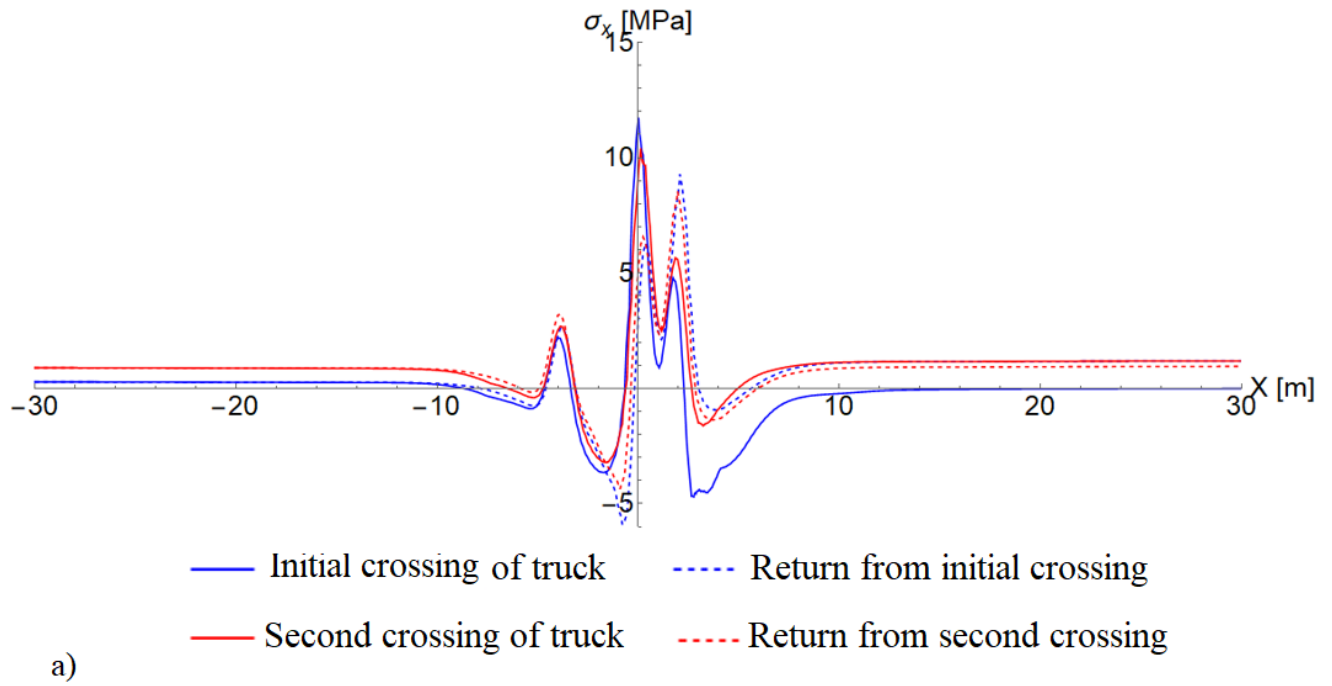
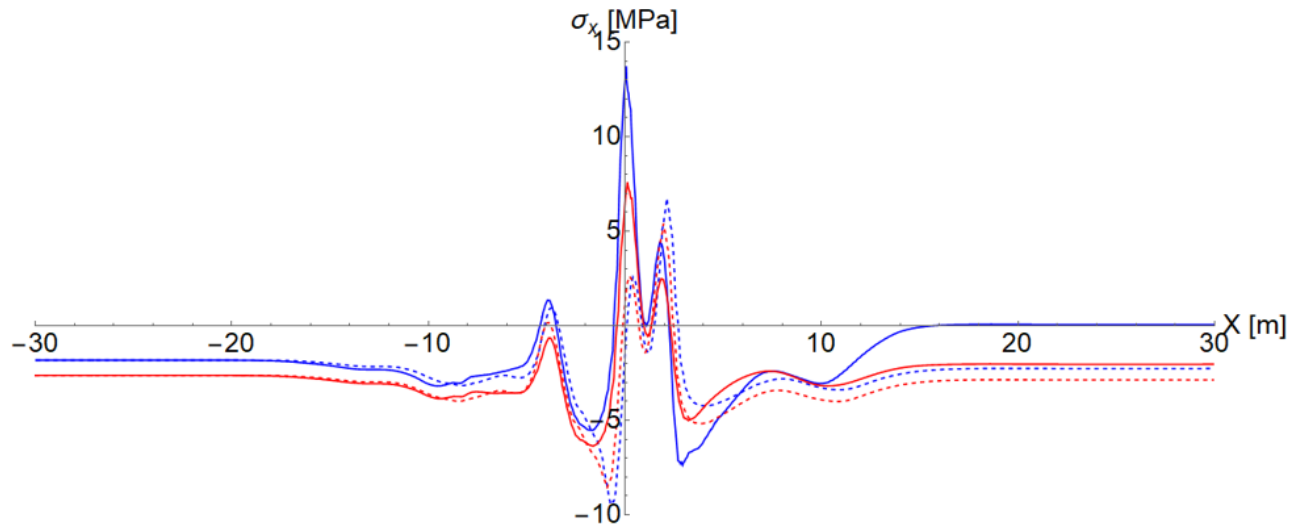


Figure 8.10: Horizontal displacement in the central shell crown during consecutive truck crossings: (a) reference, (b) central shell at 0.0m distance of 0.0 m from the lateral shell (c) at 0.6m (d) at 2.625m (e) at 5.25m (f) at 10.5 m (g) at 15.75 m.

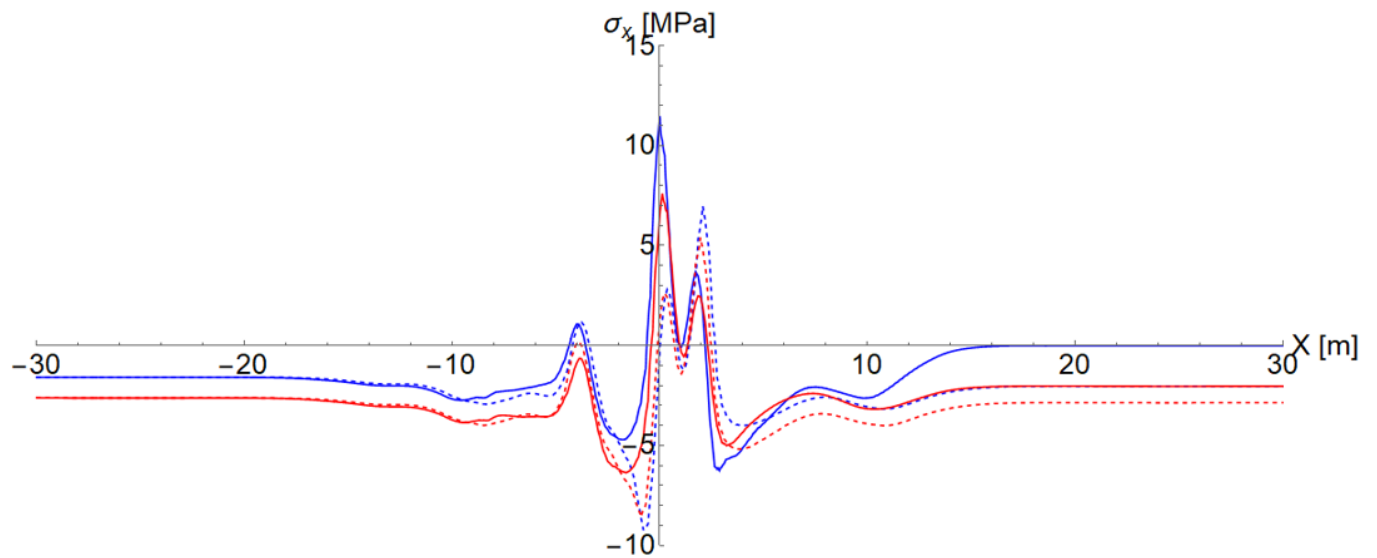
Also As illustrated in Figs. (8.9–8.11), the outcomes of the numerical simulations reveal a pronounced sensitivity to not only the direction of the movement of truck but also the position of the lateral shells. The results exhibit significant variations, both in terms of quantitative values and qualitative behavior, depending on the specific positioning of the lateral shells, the direction of the load, and the interaction with the structure. These findings highlight the complexity of the interactions within the shell of the multi-span soil-steel composite structure under different loading conditions. The position of the lateral shells plays a crucial role in distributing and transmitting the load across the bridge's span. Depending on the lateral shell configuration and load direction, the central shell's response can range from subtle variations in displacements and stress to more pronounced changes in structural behavior.





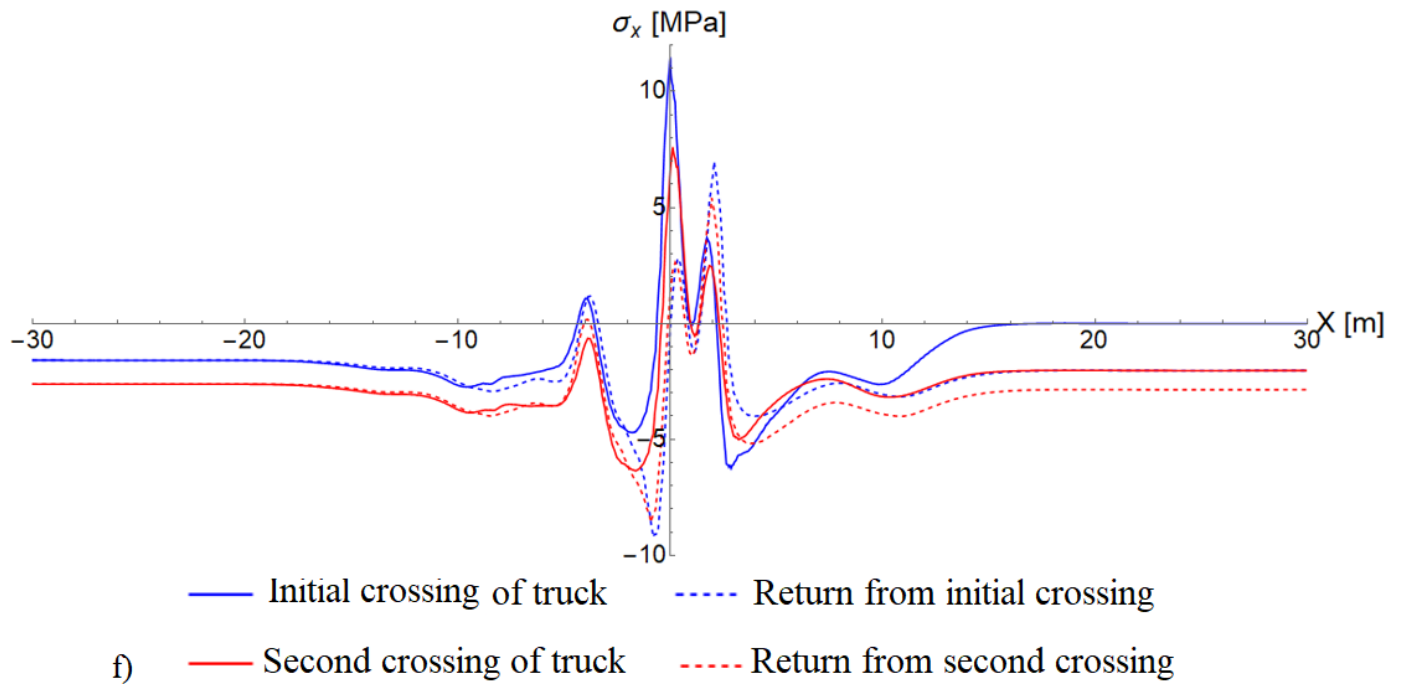
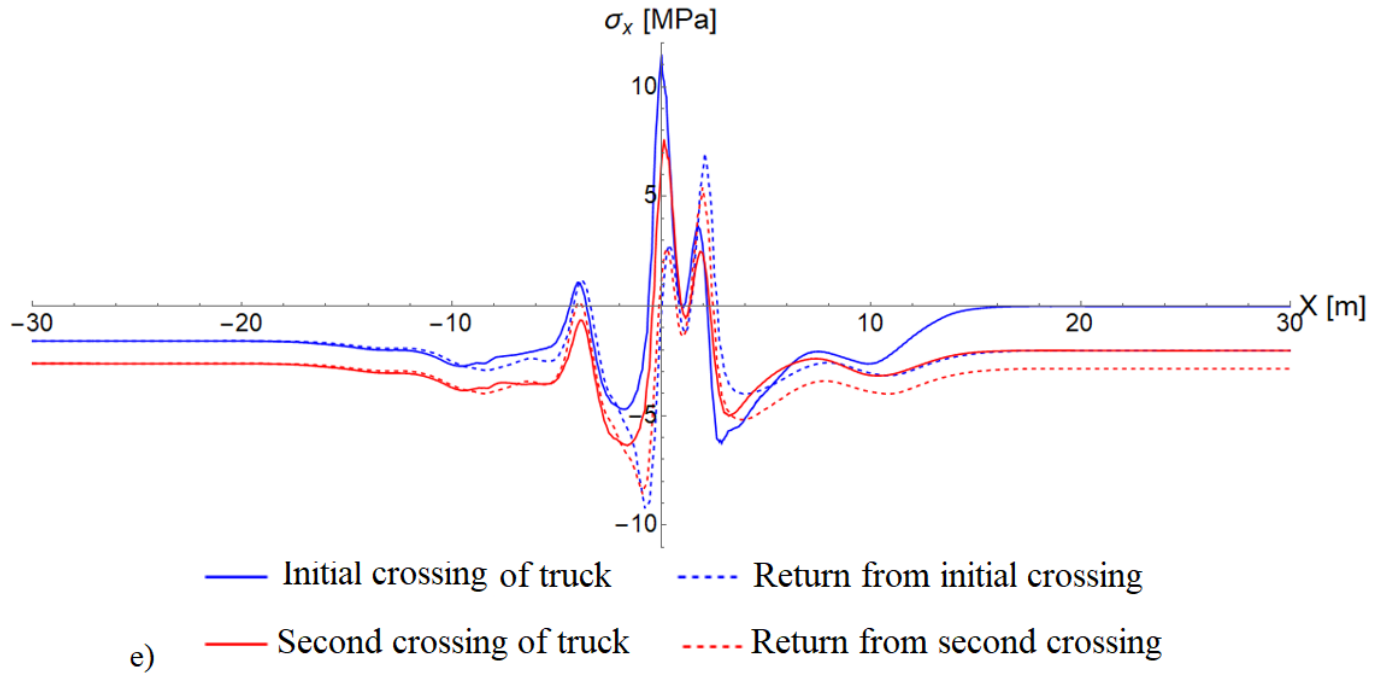
— Initial crossing of truck - - - Return from initial crossing

c) — Second crossing of truck - - - Return from second crossing



— Initial crossing of truck - - - Return from initial crossing

d) — Second crossing of truck - - - Return from second crossing



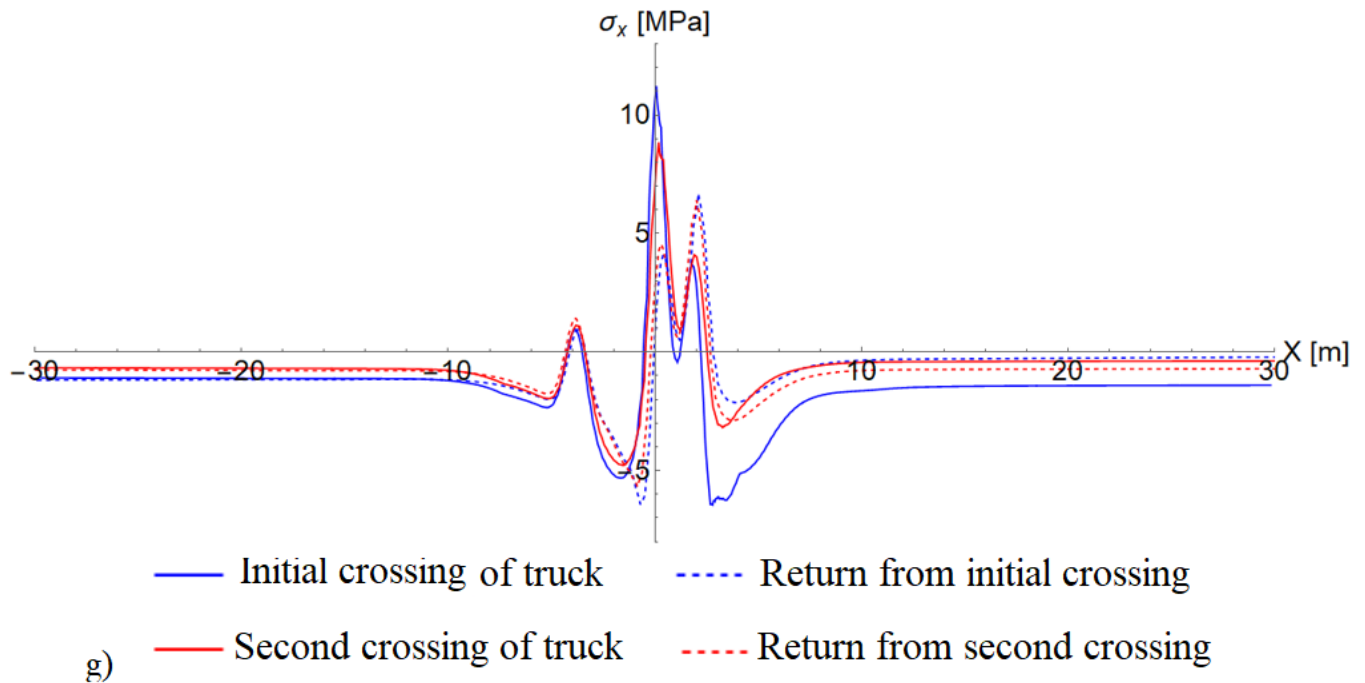


Figure 8.11: Stress in the crown of the central shell during consecutive truck crossings: (a) reference (b) central shell at 0.0m distance of 0.0 m from the lateral shell (c) at 0.6m (d) at 2.625m (e) at 5.25m (f) at 10.5 m (g) at 15.75 m

8.4. Discussions

A significant phenomenon observed in the simulations is the considerable uplift of the shell during successive truck crossings when the truck initially starts moving over the bridge. This uplift phenomenon is more pronounced when the lateral shells are in close proximity to the central shell as depicted in Figs. (8.9(a–g)), resulting in an upward tilt of the shell. As the truck advances toward the crown of the shell, this uplift of the shell gradually decreases, and the vertical displacement reaches its maximum when the truck aligns with the crown during consecutive load cycles, consistent across all simulations. Each subsequent load cycle, or truck pass, induces irreversible changes in the shell's behavior, particularly when the lateral shells exert lateral pressure on the central shell due to their proximity. This lateral pressure significantly impacts the structure's load-bearing capacity.

Notably, the simulations consistently yield closed hysteresis loops in the vertical displacement graphs for all scenarios, indicating the bridge's ability to maintain a consistent behavior under cyclic loading conditions. This alignment between simulated results and field measurements, as

observed in a single-span shell by [8], underscores the accuracy of the modeling approach and offers valuable insights into the dynamic response and stability of the soil-steel composite bridge.

Based on the analysis conducted, the maximum vertical displacement, w , that occurred in the central steel frame is within a range of -5.99 to 4.084 mm Fig. (8.9(b)) as compared to the in situ measurement without lateral frame, which ranges of -2.5 to 0.5 mm [8]. Maximum vertical displacement was observed during the first truck travel when the lateral shells were placed at a distance of 0.0 m from the enteral shell. However, significant reductions have been observed when the lateral cover was placed at a distance of 0.6 m (ranging from -3.452 to 1.842 mm). From these two simulation results, it can be concluded that providing a spacing of around 10% of the span of the structure has a significant impact on the reduction of vertical displacement. When the lateral supports are placed half of the span of the bridge (2.625 m) from the central support, the vertical displacement at the crown of the central support was almost similar to the reference support (no lateral shells), as shown in Fig. (8.9(a)) and Fig. (8.9(d)). As shown in Figs. (8.9(e–g)), the change in vertical displacement was almost constant.

The reduction in deformation as span spacing increases can be attributed to a variety of factors. For instance, backfill plays a crucial role in providing support, stability, and load distribution to this particular type of structure. Furthermore, it provides lateral support to the shell of SSCS, aiding in the resistance of the lateral forces and reducing deformation in the shell induced by vehicular loads. Consequently, a substantial portion of the load-bearing capacity and stiffness of SSCS is achieved through interaction with the backfill material. This indicates that as the spacing increases, the shell receives more support from the backfill, leading to increased stiffness of the composite structure and a more uniform distribution of the truck load across the spans. Consequently, this could result in reduced deflection at the central shell.

In all models Figs. (8.9(a–8g)), the maximum vertical displacement occurred during the first passage of the truck, and when the truck moves away from the structure, the deflection decreased but did not return to zero, i.e., the residual displacements remained. A similar phenomenon was observed in earlier studies [54] [146]. The extreme vertical deflection shift is observed in the direction of truck movement. This shift was basically due to the difference in the magnitude of the axle loads. The deflection extrema are formed under the P_2 (middle) and P_3 (rear) axles when they are in the crown of the shell. This means that the extreme deflections for the backward movement

and forward movement of the truck are not at the same position as observed in Figs (8.9(a–g)). A similar result was observed in the work of [8] and [72]. Understanding these characteristics is crucial for assessing the structural integrity of the shell under loads, such as those imposed by vehicular traffic. It provides insights into the points of maximum stress and deformation, which are essential considerations for structural design and analysis.

In contrast to vertical displacement, the maximum horizontal displacement in the range of -0.46 to -3.39 mm was observed during the second travel, i.e., the return of the truck from the first trip (the blue dashed line in Fig. (8.10(b))). However, it was observed when the lateral shells were placed at a 0.00 m distance from the central shell, as in the case of vertical displacement. Once the lateral shells were placed at 0.6 m from the central shell, the displacement decreased to a range of (0.1 to -2.03 mm) Fig. (8.10(c)). At 2.625 m (half of the span of the considered bridge), the displacement decreased, (0.2 to -1.33 mm). Compared to the reference, the increment is only 21%. Like the vertical displacement, the effect of lateral shells is not very significant when they are placed at a distance greater than half of the span of the structure. Consequently, the horizontal (absolute) displacements at spacings of 5.25 , 10.5 , and 15.75 m are 1.19 , 1.15 , and 1.14 mm, respectively.

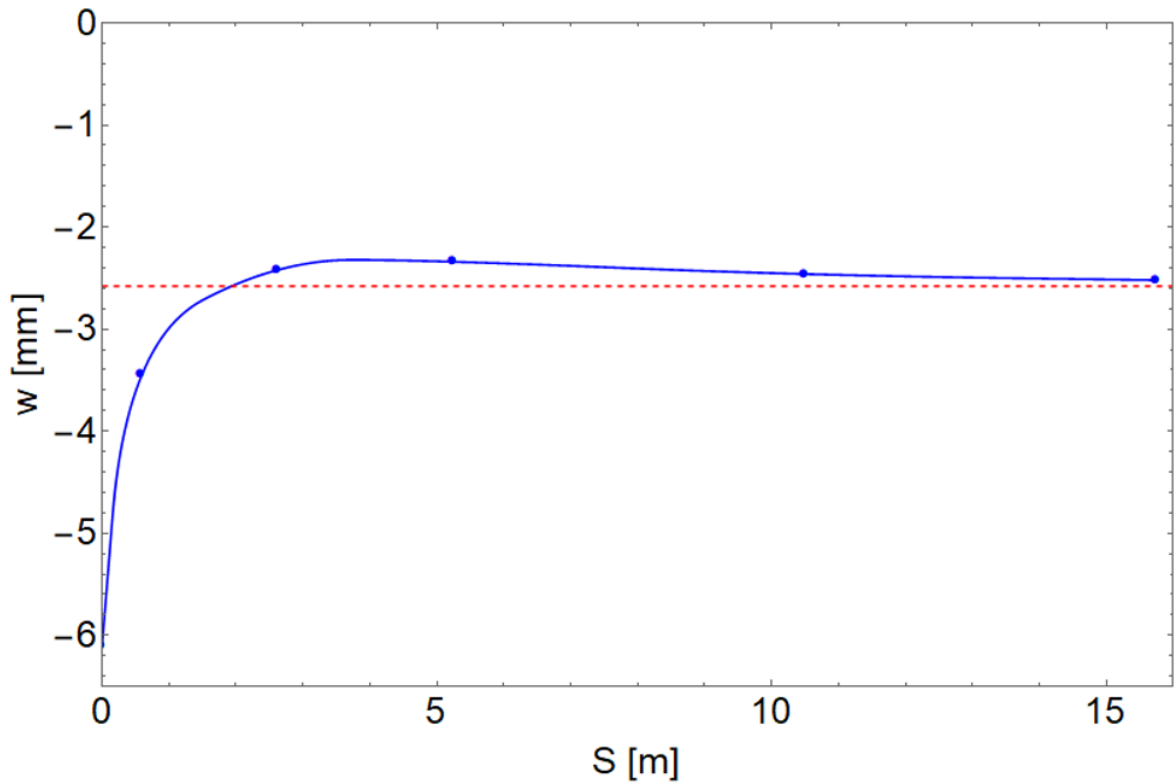
In other words, when the ratio between the spacing (S) and the span (D) of the structure ($S/D \geq 0.5$), the effect of the lateral shell on the displacements of the central shell is negligible, as shown in Figs. (8.12(a–b)). This indicates that the lateral shells have no such significant influence on the vertical displacement of the central shell under live load when they are spaced at a distance equal to or greater than half the span of the structure.

However, in contrast to vertical displacement, the residual displacement was extensive in horizontal displacement. In all models Figs. (8.10(a–g)) except the model without spacing, the absolute maximum horizontal displacement occurred during the first passage of the truck, and when the truck left the structure, the displacement decreased but did not return to zero, that is, the residual displacements remained. Compared to vertical displacement, residual displacements are very large. The extreme maxima are shifted in the direction of the truck movement as a vertical displacement.

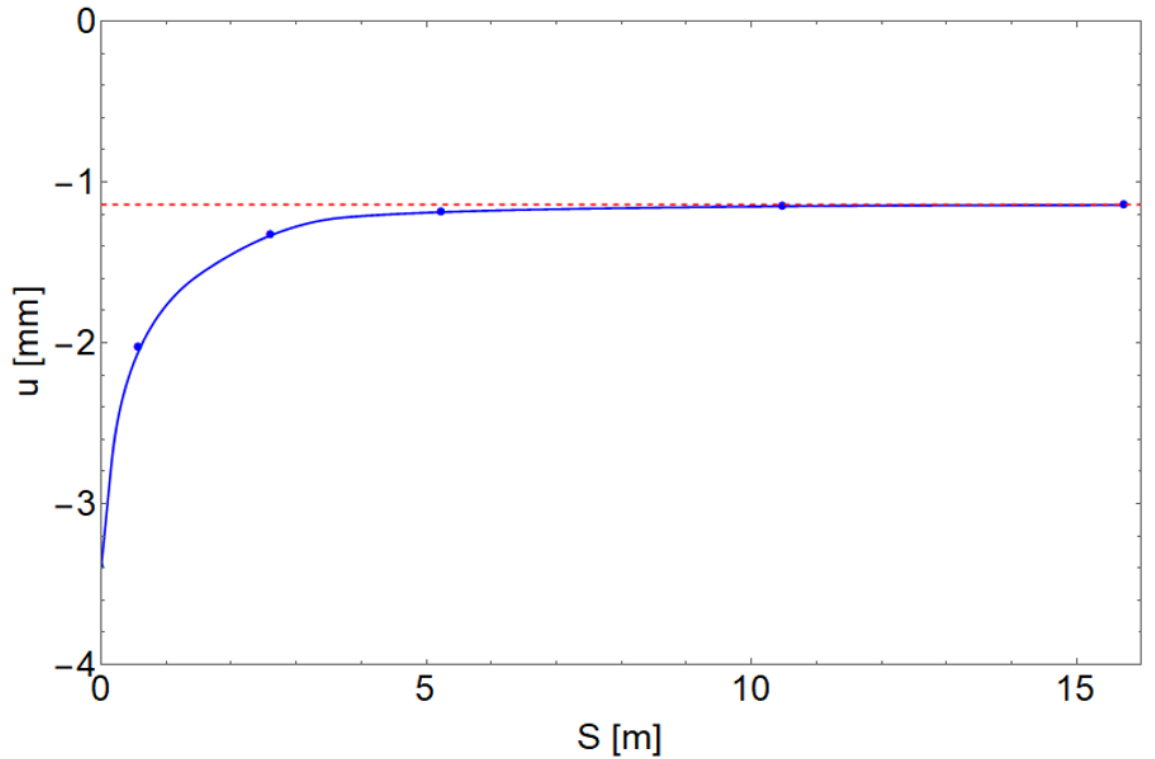
In both vertical and horizontal displacements, there is a significant difference in the displacements registered during the truck's passage over the structure, depending on the direction

of the crossing. This phenomenon, known as the hysteresis effect, had already been discovered in other soil-steel composite structure in the work [8] [46] [73] [125][148].

The results of the circumferential stress σ_x for models are presented on Figs. (8.11(a–g)). The maximum value of circumferential stress σ_x was observed when the lateral shell is placed at 0.0 m, as presented in Fig. (8.11(b)). From the graphs, the stress ranges from -12.607 to 20.855 MPa. The magnitude of stress is significantly increased compared to the in situ stress test [8], which was (-10.0 to 15.0 MPa).



a) —●— Vertical displacement at different spacing - - - - Reference displacement



b) — Horizontal displacement at different spacing - - - Reference displacement

Figure 8.12: Displacements at the crown of the central shell vs. shell spacing during truck crossings (a) vertical and (b) horizontal.

Similarly, to displacements, a significant reduction in stress (absolute) was observed when the lateral shells were placed at a spacing greater than half the span of the structure. The values of the extreme maxima (absolute) at 2.625, 5.24, 10.5, and 15.75 m spacing are 11.47, 10.51, 10.79, and 10.87 MPa, respectively, as shown in Fig. 8.13. The finding of [88] also concluded that in two span SSCS, stress significantly decreases as the spacing increases.

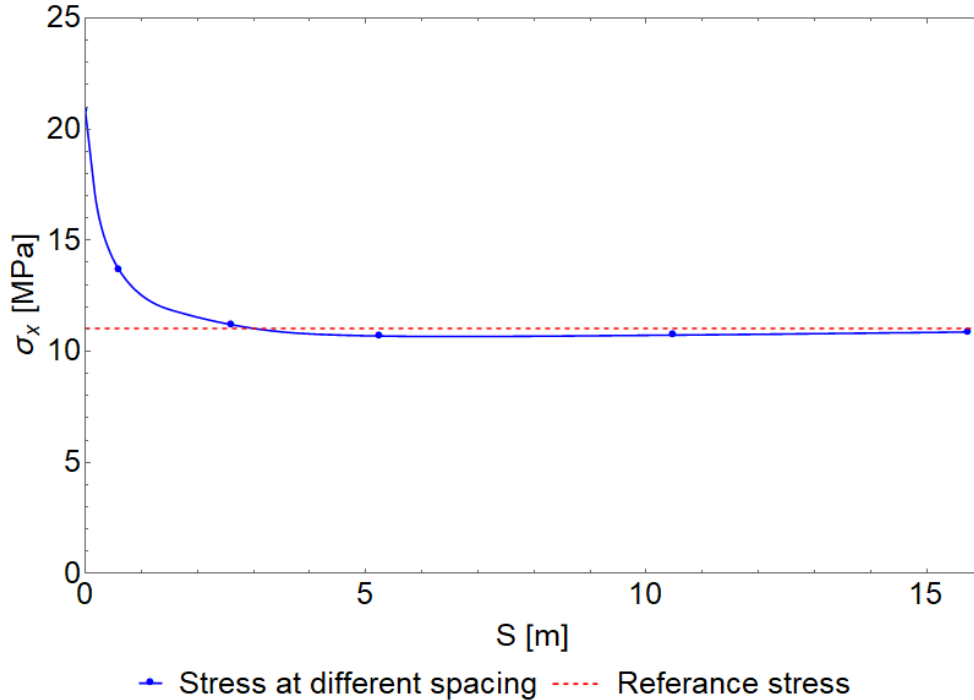


Figure 8.13: Stress at the Crown of the Central Shell vs. Shell Spacing During Truck Crossings

The relation between stress in the crown of the central shell and spacing (S) is shown in Fig. (8.13). From this figure, it can be clearly seen that the narrow spacing between the layers has a considerable effect on the induced circumferential stress (σ_x), since the adjacent and unloaded layer provides supports with lower stiffness to the side of the loaded layer. A similar conclusion was formulated by [150].

8.5. Summary

The effect of lateral shells at different positions on the mechanical behavior of the central shell under live load was investigated numerically. The constitutive model for the backfill soil was elastic-perfectly plastic and linear elastic for the shell as well as the sheet piles. The plastic slip along the soil-steel contact interface was described in terms of the Coulomb condition with the dilation angle value set to $\psi = 0$. The main conclusions drawn from the numerical simulations conducted are as follows:

- Vertical and horizontal displacement increase significantly when the S / D ratio is less than 0.5. Providing 0.6 m spacing, which is almost 10 % of the span of the structure, the displacements are substantially decreased almost by 50 % compared to the field test.

- Maximum stress in the central shell is observed when the lateral shells are placed at a 0.0 m distance. Similarly, to displacements, the stresses at the crown of the central shell are decreased by 35% by providing 0.6 m spacing.
- Extreme displacement and stress values change in the direction of truck movement. These characteristics is crucial for assessing the structural integrity of the shell under different loading conditions, such as those imposed by vehicular traffic. It provides insights into the points of maximum stress and deformation, which are essential considerations for structural design and analysis.
- The effect of non-zero residual displacements and stress, which remain in the structure after consecutive load cycles, is clearly visible and more evident in horizontal displacement compared to vertical displacements. The residual stress decreased as the S/D ratio decreased.
- The effect of the position of the lateral shells on the displacements and stress of the central shell is not significant when $S/D > 0.5$.
- Closely spaced conduits are considerably affected by each other because their support is stiffer than that of their other counterparts.
- The load carrying capacity of the multi-span SSCSs increases with the increase in spacing between the adjacent shells. It is recognized that the interaction between closely spaced SSCSs is affected by the spacing between them. However, for practical purposes, considering the minimum spacing based on factors such as the size and shape of the shell, as well as the depth of cover in the soil, is essential.

9. Summary and final conclusions

The main purpose of this work is to present the results of numerical analyses of the behavior of soil-steel composite structures under both service and ultimate loads, considering variable positions. The following subsections provide a summary of the analyses conducted and the conclusions drawn from them.

9.1. Evaluation of ultimate load: effects of stiffening ribs and geotextile

A model of a box-type SSCS with a span of 3.55 m was analyzed under four cases of reinforcement: Model-I (with a stiffening rib), Model-II (without a stiffening rib), Model-III (with a stiffening rib and geotextile), and Model-IV (without a stiffening rib but with geotextile). A computational model was developed for the analysis, and its parameters were validated against data obtained from real-scale tests[98]. Initially, the structure was analyzed during the construction stage and then under ultimate load.

The FE model accurately determined displacements within the shell during the construction stage. The maximum upward and downward vertical displacements of the shell during construction were less than 0.1% of the structure's rise, which complies with the requirements of the CHBDC [134] (CSA 2019) code limit of 2%.

Comparing the effect of stiffening rib reinforcement with geotextile reinforcement, it was observed that the bearing capacity is significantly increased with the stiffening rib. The failure mode for all four considered models of the soil-steel composite structure, at which the structure cannot carry more load, was determined as a bending failure of the shell. This conclusion aligns with findings from a previous study [63]. Furthermore, the analysis revealed that structures with stiffening ribs reach their load-carrying capacity due to the creation of a plastic hinge at the shell's shoulder and haunch. Conversely, structures without stiffening ribs experienced full plasticity in the crown and haunch sections of the shell under peak load.

In conclusion, this study underscores the importance of considering stiffening rib and geotextile reinforcement in soil-steel composite structures to enhance their load-bearing capacity and structural performance under ultimate load conditions. Understanding the behavior and failure mechanisms of SSCSs under ultimate load is crucial for optimizing their design and ensuring structural integrity in engineering applications.

9.2. Influence of geotextile soil reinforcement layout on the deformation of a model SSCSs

The conducted numerical analysis focuses on evaluating the performance of various geotextile arrangements in the soil cover over the crown of the SSCS under static loads. Initially, the effect during the construction stage is investigated, followed by the response under external static loads. Results show a significant reduction in maximum displacements and stresses when employing a single-layer geotextile, both during construction and under external static loads. Notably, the most substantial reduction in vertical displacement occurs when the geotextile is positioned at a shallower depth.

Subsequently, the influence of a double layer of geotextile is examined. It is found that vertical displacements in the crown are significantly reduced compared to using a single layer of geotextile reinforcement. Furthermore, analyzing the effect of the geotextile layer's position reveals that reinforcement is more effective when placed at a shallower depth, closer to the zone of influence of the load.

In conclusion, strategic placement of geotextiles plays a crucial role in minimizing displacements and stresses in soil-steel composite structures. Both single-layer and double-layer geotextile reinforcement show promising results, especially when positioned at shallower depths and closer to the load's zone of influence. These findings contribute to enhancing the mechanical behavior and load-carrying capacity of SSCSs under static load conditions.

9.3. Behavior of multi-span SSCS under ultimate load: effect of shell spacing

The numerical analysis was utilized to investigate the impact of spacing-to-span ratio on the bearing capacity and failure modes of multi-span soil-steel composite structures under ultimate load conditions. The influence of three different loading positions was examined: first, with the load applied on the top of the central structure; second, with the load applied on the top of the shell on the right side; and third, with the load applied on the top of both lateral shells on the right and left sides.

The findings indicate a significant decrease in the load-bearing capacity of multi-span SSCS under conditions of narrow spacing. This decrease in capacity correlates with a reduction in maximum axial force and bending moments at the crown. Comparing the effects of loading

position on the behavior of the multi-span SSCS reveals no significant difference between loading only the central shell and loading only one lateral shell. However, a notable difference emerges when both lateral shells are loaded simultaneously, leading to nearly double the observed bearing capacity.

Moreover, in all loading conditions, the failure of the shell initiates around the shoulder of the loaded shell and progresses to the haunches of the same shell. These findings provide insights into the structural behavior and failure mechanisms of multi-span SSCS under different loading configurations and emphasize the importance of spacing considerations in optimizing load-bearing capacity.

9.4. Behavior of multi-span SSCS under moving load: effect of shell spacing

The study focused on analysing how the lateral shells affect the central shell at various spacing intervals in a multi-span soil-steel composite structure subjected to quasi-static moving loads. Investigating the displacements and internal forces experienced by the central shell during a loading cycle comprising consecutive truck passages over the structure. The analysis revealed a significant increase in both vertical and horizontal displacements when the ratio between shell spacing and span length was less than 0.5. The maximum stress was observed when the shells were assumed to be adjacent to each other, i.e., without any spacing. In this scenario, the stress nearly doubled compared to the reference case of a single-span structure. Moreover, the extreme deflections and stress were observed to shift in the direction of the vehicle movement.

Conversely, the impact of the lateral shell on the central shell's performance under moving load was nearly negligible when the spacing-to-span ratio was greater than 0.5. This finding underscores the critical role of spacing considerations in minimizing stress concentrations and optimizing the structural response of multi-span SSCSs under quasi-static moving loads.

References

- [1] K. Terzaghi, *Theoretical soil mechanics*. New York: John Wiler and Sons, 1943. doi: 10.1002/9780470172766.
- [2] M. A. M. Al-Naddaf, “Investigation of soil arching under different modes of soil movement and surface loading,” University of Kansas, 2019.
- [3] Z. Getzler, A. Komornik, and A. Mazurik, “Model study on arching above buried structures,” *J. Soil Mech. Found. Div.*, vol. 94, no. 5, pp. 1123–1141, 1968.
- [4] J. Han, F. Wang, M. Al-Naddaf, and C. Xu, “Progressive development of two-dimensional soil arching with displacement,” *Int. J. Geomech.*, vol. 17, no. 12, p. 4017112, 2017, doi: [https://doi.org/10.1061/\(ASCE\)GM.1943-5622.0001025](https://doi.org/10.1061/(ASCE)GM.1943-5622.0001025).
- [5] Gonzalo Ramos Schneider and Lars Pettersson, “Soil steel composite bridges An international survey of full scale tests and comparison with the Pettersson-Sundquist design method,” 2014.
- [6] ViaCon Poland, “Catalogues English,” 2022. <https://viacon.pl/en/download> (accessed Feb. 11, 2022).
- [7] D. Beben, *Soil-Steel Bridges; Design, Maintenance and Durability*. Opole, Poland: Springer Nature, 2020. doi: <https://doi.org/10.1007/978-3-030-34788-8>.
- [8] G. Antoniszyn, C. Machelski, and B. Michalski, “Live load effects on a soil-steel bridge founded on elastic supports,” *Stud. Geotech. Mech.*, vol. Vol. 28, no. nr 2-4, pp. 65–82, 2006.
- [9] S. Alzabeebee, D. N. Chapman, and A. Faramarzi, “Innovative approach to determine the minimum wall thickness of flexible buried pipes,” *Geomech. Eng*, vol. 15, no. 2, pp. 755–767, 2018, doi: <https://doi.org/10.12989/gae.2018.15.2.755>.
- [10] M. G. Katona, “Influence of soil models on structural performance of buried culverts,” *Int. J. Geomech.*, vol. 17, no. 1, p. 4016031, 2017, doi: 10.1061/(ASCE)GM.1943-5622.0000684.
- [11] P. Kolisoja and A. Kalliainen, “Modelling of plastic culvert and road embankment interaction in 3D,” *Procedia Eng.*, vol. 143, pp. 427–434, 2016, doi: 10.1016/j.proeng.2016.06.05.
- [12] S. L. Gassman, A. J. Schroeder, and R. P. Ray, “Field performance of high density polyethylene culvert pipe,” *J. Transp. Eng.*, vol. 131, no. 2, pp. 160–167, 2005, doi: [https://doi.org/10.1061/\(ASCE\)0733-947X\(2005\)131:2\(160\)](https://doi.org/10.1061/(ASCE)0733-947X(2005)131:2(160)).
- [13] T. Maleska, J. Nowacka, and D. Beben, “Application of EPS geofoam to a soil–steel bridge to reduce seismic excitations,” *Geosci.*, vol. 9, no. 10, 2019, doi: 10.3390/geosciences9100448.
- [14] P. Mellat, A. Andersson, L. Pettersson, and R. Karoumi, “Dynamic behaviour of a short span soil–steel composite bridge for high-speed railways – Field measurements and FE-analysis,” *Eng. Struct.*, vol. 69, pp. 49–61, Jun. 2014, doi:

10.1016/J.ENGSTRUCT.2014.03.004.

- [15] A. Sanaeiha, M. Rahimian, and M. S. Marefat, "Field Test of a Large-Span Soil–Steel Bridge Stiffened by Concrete Rings during Backfilling," *J. Bridg. Eng.*, vol. 22, no. 10, p. 06017002, 2017, doi: 10.1061/(asce)be.1943-5592.0001102.
- [16] L. Pettersson, "Full Scale Tests and Structural Evaluation of Soil Steel Flexible Culverts with low Height of Cover.," KTH Royal Institute of Technology, 2007. [Online]. Available: [http://digilib.unila.ac.id/11478/16/16.BAB II.pdf](http://digilib.unila.ac.id/11478/16/16.BAB%20II.pdf)
- [17] H.-J. Sun, Y.-L. Guo, C.-B. Wen, J.-Q. Zuo, Q. Zhao, and Z.-G. Liu, "The strength design of deeply buried circular corrugated steel arches with considering only soil radial restraining," *Thin-Walled Struct.*, vol. 183, p. 110422, 2023.
- [18] H. Fang, P. Tan, X. Du, B. Li, K. Yang, and Y. Zhang, "Numerical and experimental investigation of the effect of traffic load on the mechanical characteristics of HDPE double-wall corrugated pipe," *Appl. Sci.*, vol. 10, no. 2, p. 627, 2020, doi: <https://doi.org/10.3390/app10020627>.
- [19] V. Kovalchuk, J. Luchko, I. Bondarenko, R. Markul, and B. Parneta, "Research and analysis of the stressed-strained state of metal corrugated structures of railroad tracks," *Eastern-European J. Enterp. Technol.*, vol. 6, no. 7, pp. 4–9, 2016, doi: DOI: 10.15587/1729-4061.2016.84236.
- [20] I. D. Moore, "Buried pipes and culverts," in *Geotechnical and geoenvironmental engineering handbook*, Springer, 2001, pp. 541–567.
- [21] J. Kang, F. Parker, and C. H. Yoo, "Soil–structure interaction for deeply buried corrugated steel pipes Part I: Embankment installation," *Eng. Struct.*, vol. 30, no. 2, pp. 384–392, Feb. 2008, doi: 10.1016/J.ENGSTRUCT.2007.04.014.
- [22] N. Nguyen-Minh, N. Tran-Van, T. Bui-Xuan, and T. Nguyen-Thoi, "Static analysis of corrugated panels using homogenization models and a cell-based smoothed mindlin plate element (CS-MIN3)," *Front. Struct. Civ. Eng.*, vol. 13, no. 2, pp. 251–272, 2019, doi: 10.1007/s11709-017-0456-0.
- [23] F. De'nan, H. Hasan, M. H. Osman, and S. Saad, "Torsional behavior of triangular web profile (TRIWP) steel section by experimental study," *Front. Struct. Civ. Eng.*, vol. 10, no. 4, pp. 409–419, 2016, doi: 10.1007/s11709-016-0358-6.
- [24] Lars Pettersson and Håkan Sundquist, "Design of soil steel composite bridges," *Arch. Civ. Mech. Eng.*, no. 5, pp. 1–82, 2014.
- [25] A. Wysokowski, "Durability of flexible steel corrugated shell structures-theory and practice," *Arch. Inst. Civ. Eng.*, pp. 347–360, 2017, doi: 10.21008/j.1897-4007.2017.23.32.
- [26] C. Machelski, *Modelowanie mostowych konstrukcji gruntowo-powłokowych (Modeling of bridge ground-shell structures)*. Wrocław, Poland: Lower Silesian Educational Publishing House, 2008.
- [27] L. MacDonald, "Numerical modelling of vehicle loads on buried orthotropic steel shell

- structures,” Dalhousie University, 2010.
- [28] C. Machelski, P. Tomala, B. Kunecki, L. Korusiewicz, K. Williams, and M. M. El-Sharnouby, “Ultracor - 1-st realization in Europe, design, erection, testing,” *Arch. Inst. Civ. Eng.*, no. 23, pp. 188–197, 2017, doi: 10.21008/j.1897-4007.2017.23.18.
- [29] M. El-sharnouby, S. G. Engineer, A. I. Limited, L. Janusz, V. Group, and J. Newhook, “Performance of the Largest Steel Buried Bridge,” in *Structures Session*, 2019, pp. 1–13.
- [30] Z. “Zee” Manko and D. Beben, “Tests During Three Stages of Construction of a Road Bridge with a Flexible Load-Carrying Structure Made of Super Cor Type Steel Corrugated Plates Interacting with Soil,” *J. Bridg. Eng.*, vol. 10, no. 5, pp. 604–621, 2005, doi: 10.1061/(asce)1084-0702(2005)10:5(604).
- [31] B. B. · A. M. Bridges, *Bridges Analysis, Design, Structural Health Monitoring, and Rehabilitation*, Second. Winnipeg, MB, Canada: Springer, 2015. doi: 10.1007/978-3-319-17843-1.
- [32] P. Tomala and C. Machelski, “Budowa obiektu gruntowo-powłokowego z zastosowaniem blachy UltraCor (Construction of a ground-coating facility using UltraCor sheet metal),” *Arch. Inst. Inżynierii Lądowej*, 2017.
- [33] T. Maleska and D. Beben, “Numerical analysis of a soil-steel bridge during backfilling using various shell models,” *Eng. Struct.*, vol. 196, no. January, p. 109358, 2019, doi: 10.1016/j.engstruct.2019.109358.
- [34] C. E. de Normalisation, “Concrete-Part 1: Specification, performance, production and conformity,” *EN206-1, 22 CEN*, vol. 69, p. 23, 2000.
- [35] K. M. El-Sawy, “Three-dimensional modeling of soil-steel culverts under the effect of truckloads,” *Thin-walled Struct.*, vol. 41, no. 8, pp. 747–768, 2003, doi: [https://doi.org/10.1016/S0263-8231\(03\)00022-3](https://doi.org/10.1016/S0263-8231(03)00022-3).
- [36] A. Wysokowski, M. Mońka, and J. Howis, “Foundation of flexible steel structures-developmental trends,” *Arch. Inst. Inżynierii Lądowej*, 2017.
- [37] B. Kunecki, “Laboratory Test of the Fire Protection Layer Used in the Soil-steel Tunnel in Poland,” in *Transportation Research Board 92nd Annual Meeting*, 2013, pp. 13–3015.
- [38] ARMTEC, “BRIDGE PLATE Deep Corrugated Plate pushes the span of structural plate products to over 20 metres,” 2020. [Online]. Available: <https://armtec.com/>
- [39] D. Beben, “The role of backfill quality on corrugated steel plate culvert behaviour,” *Balt. J. Road Bridg. Eng.*, vol. 12, no. 1, pp. 1–11, 2017, doi: 10.3846/bjrbe.2017.01.
- [40] L. Pettersson, E. B. Flener, and H. Sundquist, “Design of Soil–Steel Composite Bridges,” *Struct. Eng. Int.*, vol. 25, no. 2, pp. 159–172, 2015, doi: 10.2749/101686614x14043795570499.
- [41] H. El Naggar, A. Campbell, and I. Ezzeldin, “Effect of the Employed Material Model on the Predicted Behaviour of Corrugated Metal Pipes,” *Transp. Res. Rec.*, vol. 2675, no. 10, pp. 1364–1372, 2021.

- [42] K. Kim and C. H. Yoo, “Design loading on deeply buried box culverts,” *J. Geotech. Geoenvironmental Eng.*, vol. 131, no. 1, pp. 20–27, 2005, doi: 10.1061/(ASCE)1090-0241(2005)131:1(20).
- [43] J. M. Duncan, “Behavior and design of long-span metal culverts,” *J. Geotech. Eng. Div.*, vol. 105, no. 3, pp. 399–418, 1979.
- [44] R. Khademi Zahedi, P. Alimouri, H. Khademi Zahedi, and M. Shishesaz, “Investigating peak stresses in fitting and repair patches of buried polyethylene gas pipes,” *Front. Struct. Civ. Eng.*, vol. 14, no. 1, pp. 147–168, 2020, doi: 10.1007/s11709-019-0587-6.
- [45] A. Wadi, L. Pettersson, and R. Karoumi, “On Predicting the Ultimate Capacity of a Large-Span Soil–Steel Composite Bridge,” *Int. J. Geosynth. Gr. Eng.*, vol. 6, no. 4, pp. 1–13, 2020, doi: 10.1007/s40891-020-00232-z.
- [46] D. Łydzba, A. Różański, M. Sobótka, D. Stefaniuk, G. Chudy, and T. Wróblewski, “Mechanical behavior of soil-steel structure subjected to live loads and different water conditions,” *Arch. Inst. Inżynierii Lądowej*, 2017.
- [47] Czesław Machelski, “Classification of soil-steel structures due to shell deformation changes during backfilling Abstract:,” *Transp. Overv.*, vol. 41, pp. 1–10, 2016, doi: 10.35117/A_ENG_16_09_01.
- [48] C. Machelski, A. Czerepak, and O. Basar, “Stiffness of Corrugated Steel Plate on Buried in Surrounding Soil as an Ecological Bridge Structure,” *Ce/Papers*, vol. 3, no. 5–6, pp. 316–323, 2019, doi: 10.1002/cepa.1206.
- [49] E. B. Flener, “Soil-Steel Interaction of Long-Span Box Culverts—Performance during Backfilling,” *J. Geotech. Geoenvironmental Eng.*, vol. 136, no. 6, pp. 823–832, 2010, doi: 10.1061/(asce)gt.1943-5606.0000287.
- [50] M. Mumot, “Balastowanie powłok mostów gruntowo-powłokowych (Ballasting of coatings of ground-shell bridges),” *Transp. Overv.*, no. 3, pp. 16–18, 2015.
- [51] B. Liu, “Effect of Parameters on Soil-Structure Interaction of a Buried Corrugated Steel Arch Bridge,” *Open Civ. Eng. J.*, vol. 5, no. 1, pp. 154–162, 2011, doi: 10.2174/1874149501105010154.
- [52] T. Maleska and D. Beben, “The impact of backfill quality on soil-steel composite bridge response under seismic excitation,” *IOP Conf. Ser. Mater. Sci. Eng.*, vol. 419, no. 1, 2018, doi: 10.1088/1757-899X/419/1/012040.
- [53] H. L. White and J. P. Layer, “The corrugated metal conduit as a compression ring,” in *Highway Research Board Proceedings*, 1960, vol. 39.
- [54] E. B. Flener, “Response of Long-Span Box Type Soil-Steel Composite Structures during Ultimate Loading Tests,” *J. Bridg. Eng.*, vol. 14, no. 6, pp. 496–506, 2009, doi: 10.1061/(asce)be.1943-5592.0000031.
- [55] L. AASHTO., “AASHTO LRFD bridge design specifications,” *Am. Assoc. State Highw. Transp. Off. Washington, DC, USA*, 2017.

- [56] CAN/CSA-S6-06, “Canadian Highway Bridge Design Code,” in *A National Standard of Canada*, Canada standard association, 2010.
- [57] L. Pettersson and H. Sundquist, *Design of soil steel composite bridges*. KTH Royal Institute of Technology, 2014.
- [58] AASHTO M145-91, “Standard Practice for Classification of Soils and Soil-Aggregate Mixtures for Highway Construction Purposes,” *Standard Specifications for Transportation Materials and Methods of Sampling and Testing*, 2012.
- [59] D. 2-98 ASTM, “Standard practice for classification of soils for engineering purposes (unified soil classification system).” West Conshohocken, PA, 2011.
- [60] A. Wadi and L. Pettersson, “Recent research on flexible culverts in sloping terrain,” *Arch. Inst. Inżynierii Lądowej*, no. April, pp. 293–299, 2017, doi: 10.21008/j.1897-4007.2017.23.27.
- [61] A. Wadi, L. Pettersson, and R. Karoumi, “Flexible culverts in sloping terrain: Numerical simulation of soil loading effects,” *Eng. Struct.*, vol. 101, pp. 111–124, 2015, doi: 10.1016/j.engstruct.2015.07.004.
- [62] A. Wadi, “Flexible culverts in sloping terrain: Research advances and application [Licentiate thesis],” no. December, 2015.
- [63] C. Regier, N. A. Hoult, and I. D. Moore, “Laboratory study on the behavior of a horizontal-ellipse culvert during service and ultimate load testing,” *J. Bridg. Eng.*, vol. 22, no. 3, p. 4016131, 2017.
- [64] M. Esmaceli, J. A. Zakeri, and P. H. Abdulrazagh, “Minimum depth of soil cover above long-span soil-steel railway bridges,” *Int. J. Adv. Struct. Eng.*, vol. 5, no. 1, pp. 1–17, 2013, doi: 10.1186/2008-6695-5-7.
- [65] L. Korusiewicz, “Testing of a large-span soil-shell structure without stiffeners during backfilling process,” *Roads Bridg. - Drog. i Most.*, vol. 14, no. 3, pp. 203–218, 2015, doi: 10.7409/rabd.015.014.
- [66] E. B. Flener, R. Karoumi, and H. Sundquist, “Field testing of a long-span arch steel culvert during backfilling and in service,” *Struct. Infrastruct. Eng.*, vol. 1, no. 3, pp. 181–188, 2005, doi: 10.1080/00222930500030929.
- [67] L. Korusiewicz and B. Kunecki, “Behaviour of the steel box-type culvert during backfilling,” *Arch. Civ. Mech. Eng.*, vol. 11, no. 3, pp. 637–650, 2011, doi: 10.1016/s1644-9665(12)60106-x.
- [68] R. B. Seed and C.-Y. Ou, *Measurements and analyses of compaction effects on a long-span culvert*, no. 1087. 1986.
- [69] Z. “Zee” Manko and D. Beben, “Research on Steel Shell of a Road Bridge Made of Corrugated Plates during Backfilling,” *J. Bridg. Eng.*, vol. 10, no. 5, pp. 592–603, 2005, doi: 10.1061/(asce)1084-0702(2005)10:5(592).
- [70] K. Embaby, M. H. El Naggar, and M. El Sharnouby, “Performance of large-span arched

- soil–steel structures under soil loading,” *Thin-Walled Struct.*, vol. 172, no. December 2021, p. 108884, 2022, doi: 10.1016/j.tws.2022.108884.
- [71] H. Yokota and D. M. Frangopol, *Bridge Maintenance, Safety, Management, Life-cycle Sustainability and Innovations: Proceedings of the Tenth International Conference on Bridge Maintenance, Safety and Management (IABMAS 2020), June 28-July 2, 2020, Sapporo, Japan*. CRC Press, 2021.
- [72] M. Sobótka, “NUMERICAL SIMULATION OF HYSTERETIC LIVE LOAD EFFECT IN A SOIL-STEEL BRIDGE,” *Stud. Geotech. Mech.*, vol. 36, no. 1, pp. 104–110, 2014, doi: 10.2478/sgem-2014-0012.
- [73] M. Sobótka and C. Machelski, “Hysteretic live load effect in soil-steel structure,” *Eng. Trans.*, vol. 64, no. 4, pp. 493–499, 2016.
- [74] C. Machelski, “Dependence of deformation of soil-shell structure on the direction of load passage,” *Roads Bridg. i Most.*, vol. 13, no. 3, pp. 223–233, 2014, doi: 10.7409/rabdim.014.015.
- [75] S. G. Czesław Machelski, Maciej Sobótka, “Displacements of shell in soil-steel bridge subjected to moving load : determination using strain gauge measurements and numerical simulation,” *Stud. Geotech. Mech.*, vol. 44, no. 1, pp. 1–12, 2021, doi: 10.2478/sgem-2021-0028.
- [76] C. Machelski and M. Mumot, “Corrugated shell displacements during the passage of a vehicle along a soil-steel structure,” *Stud. Geotech. Mech.*, vol. 38, no. 4, pp. 25–32, 2016, doi: 10.1515/sgem-2016-0028.
- [77] C. Machelski, P. Tomala, and M. Mońka, “Research on the interface elements in soil-steel structures based on the in situ test,” *Mod. Trends Res. Steel, Alum. Compos. Struct.*, no. Figure 2, pp. 106–112, 2021, doi: 10.1201/9781003132134-10.
- [78] J. Nowacka, D. Beben, and T. Maleska, “Analysis of soil-steel bridge with EPS geofoam under static loads,” in *Bridge Maintenance, Safety, Management, Life-Cycle Sustainability and Innovations*, CRC Press, 2021, pp. 1816–1823.
- [79] C. H. B. D. Code, “CAN/CSA-S6-14;,” “Canadian Standards Association International,” Canada, 2014.
- [80] I. D. Moore and B. Taleb, “Metal culvert response to live loading: Performance of three-dimensional analysis,” *Transp. Res. Rec.*, vol. 1656, no. 1, pp. 37–44, 1999, doi: 10.3141/1656-05.
- [81] D. Beben and A. Stryczek, “Numerical analysis of corrugated steel plate bridge with reinforced concrete relieving slab,” *J. Civ. Eng. Manag.*, vol. 22, no. 5, pp. 585–596, 2016, doi: 10.3846/13923730.2014.914092.
- [82] R. W. I. Brachman, I. D. Moore, and A. C. Mak, “Ultimate limit state of deep-corrugated large-span box culvert,” *Transp. Res. Rec.*, vol. 2201, no. 1, pp. 55–61, 2010, doi: 10.3141/2201-07.
- [83] A. Wadi, L. Pettersson, and R. Karoumi, “FEM simulation of a full-scale loading-to-

- failure test of a corrugated steel culvert,” *Steel Compos. Struct.*, vol. 27, no. 2, pp. 217–227, 2018, doi: 10.12989/scs.2018.27.2.217.
- [84] A. C. Lougheed, *Limit states testing of a buried deep-corrugated large-span box culvert*. Queen’s University Kingston, Ontario, Canada, 2008.
- [85] X. Bao, X. Wu, J. Shen, S. Wu, X. Chen, and H. Cui, “Performance Analysis of Multiple Steel Corrugated Pipe Arch Culvert under Construction and Periodic Vehicle Load,” *Appl. Sci.*, vol. 13, no. 16, p. 9441, 2023, doi: <https://doi.org/10.3390/app13169441>.
- [86] Y. Sawamura, K. Kishida, and M. Kimura, “Centrifuge model test and FEM analysis of dynamic interactive behavior between embankments and installed culverts in multiarch culvert embankments,” *Int. J. Geomech.*, vol. 15, no. 3, p. 4014050, 2015, doi: [https://doi.org/10.1061/\(ASCE\)GM.1943-5622.0000361](https://doi.org/10.1061/(ASCE)GM.1943-5622.0000361).
- [87] J. Hwang, M. Kikumoto, K. Kishida, and M. Kimura, “Dynamic stability of multi-arch culvert tunnel using 3-D FEM,” *Tunn. Undergr. Sp. Technol. Inc. Trenchless Technol. Res.*, vol. 21, no. 3, p. 384, 2006, doi: <http://dx.doi.org/10.1016/j.tust.2005.12.195>.
- [88] M. W. Aleksander Urbanski, Karol Ryz, Przemyslaw Milczarek, “Design of a railway overpass of soil-shell sheets. Analytical and numerical approach,” *Tech. Journal. Environ.*, no. 27, 2012.
- [89] C. Xu, C. Liang, and P. Shen, “Experimental and theoretical studies on the ultimate bearing capacity of geogrid-reinforced sand,” *Geotext. Geomembranes*, vol. 47, no. 3, pp. 417–428, 2019, doi: <https://doi.org/10.1016/j.geotextmem.2019.01.003>.
- [90] S. F. Bartlett, B. N. Lingwall, and J. Vaslestad, “Methods of protecting buried pipelines and culverts in transportation infrastructure using EPS geof foam,” *Geotext. Geomembranes*, vol. 43, no. 5, pp. 450–461, 2015.
- [91] M. Y. Fattah, W. H. Hassan, and S. E. Rasheed, “Behavior of flexible buried pipes under geocell reinforced subbase subjected to repeated loading,” *Int. J. Geotech. Earthq. Eng.*, vol. 9, no. 1, pp. 22–41, 2018.
- [92] N. R. EL-Sakhawy, H. Arafat, and A. Abd Allah, “Application of geogrids in a soil-steel culvert,” *Proc. XVII ECSMGE-2019, Reykjavik, Icel.*, 2019.
- [93] T. Maleska, A. Wysokowski, and D. Bęben, “Impact of Reinforcement Layer in Soil-Steel Culvert on Laboratory and Numerical Tests,” in *International Scientific Conference Environmental Challenges in Civil Engineering, 2022*, pp. 139–148.
- [94] A. Wysokowski, “Influence of single-layer geotextile reinforcement on load capacity of buried steel box structure based on laboratory full-scale tests,” *Thin-Walled Struct.*, vol. 159, p. 107312, 2021.
- [95] R. J. Bathurst and M. A. Knight, “Analysis of geocell reinforced-soil covers over large span conduits,” *Comput. Geotech.*, vol. 22, no. 3–4, pp. 205–219, 1998, doi: 10.1016/S0266-352X(98)00008-1.
- [96] J. Vaslestad, L. Janusz, B. Bednarek, and Ł. Mielnik, “Instrumented full-scale test with geogird above the crown of corrugated steel box culvert,” in *Proceedings of the Seventh*

International Conference On Geosynthetics, Geosynthetics State of the Art Recent Developments, 2002, pp. 1153–1155.

- [97] J. K. Jeyapalan and R. L. Lytton, “Stress reduction in flexible culverts due to overlays of geofabrics,” in *Proc. of 2nd International Conf. of Geotextiles, Las Vegas, USA*, 1982, pp. 701–706.
- [98] A. Wysokowski, “Full scale tests of various buried flexible structures under failure load,” *Sci. Rep.*, vol. 12, no. 1, pp. 1–14, 2022, doi: <https://doi.org/10.1038/s41598-022-04969-7>.
- [99] L. Korusiewicz and B. Kunecki, “Behaviour of the steel box-type culvert during backfilling,” *Arch. Civ. Mech. Eng.*, vol. 11, no. 3, pp. 637–650, 2011, doi: [10.1016/s1644-9665\(12\)60106-x](https://doi.org/10.1016/s1644-9665(12)60106-x).
- [100] Polish Standards of bridge load – PN - 85/S10030, “Bridge structures Loads,” Warsaw, 2013.
- [101] M. Abambres and M. R. Arruda, “Finite element analysis of steel structures—a review of useful guidelines,” *Int. J. Struct. Integr.*, vol. 7, no. 4, pp. 490–515, 2016, doi: <https://doi.org/10.1108/IJSI-07-2015-0020>.
- [102] A. Jennings, *Structures: from theory to practice*. CRC Press, 2018. doi: <https://doi.org/10.1201/9781315275017>.
- [103] A. C. Ugural and S. K. Fenster, *Advanced strength and applied elasticity*. Pearson education, 2003.
- [104] M. B. Wong, *Plastic analysis and design of steel structures*. Butterworth-Heinemann, 2011.
- [105] J. Chakrabarty, *Theory of plasticity*, Third edit. Elsevier, 2012.
- [106] R. M. Jones, *Deformation theory of plasticity*. Bull Ridge Corporation, 2009.
- [107] ABS, “Nonlinear Finite Element Analysis of Marine and Offshore Structures,” Texas, 2021.
- [108] E. H. Gaylord, C. N. Gaylord, and J. E. Stallmeyer, *Design of steel structures*, First. Springer-science and business media, B.V, 1992.
- [109] Tomasz Wierzbicki, “Structural Mechanics,” Massachusetts Institute of Technology, 2013.
- [110] H. P. Gavin, “Plastic Design of a Fixed-Fixed Beam-Column,” 2015.
- [111] D. Beben, “Field performance of corrugated steel plate road culvert under normal live-load conditions,” *J. Perform. Constr. Facil.*, vol. 27, no. 6, pp. 807–817, 2013, doi: [https://doi.org/10.1061/\(ASCE\)CF.1943-5509.0000389](https://doi.org/10.1061/(ASCE)CF.1943-5509.0000389).
- [112] K. Embaby, M. H. El Naggar, and M. El-Sharnouby, “Ultimate capacity of large-span soil-steel structures,” *Tunn. Undergr. Sp. Technol.*, vol. 132, p. 104887, 2023.
- [113] P. G. Cranston, M. C. Richie, and L. C. M. Vieira, “Stability of Buried Corrugated Metal Pipe,” *Orlando, Florida, USA*, 2016.

- [114] S. P. Timoshenko and J. M. Gere, *Theory of elastic stability*. Courier Corporation, 2009.
- [115] B. Kunecki, “Behaviour of orthotropic buried arch shells under static and dynamic live load,” PhD thesis. Report, 2006.
- [116] G. G. Meyerhof and L. D. Baikie, “Strength of steel culvert sheets bearing against compacted sand backfill,” *Highw. Res. Rec.*, no. 30, 1963.
- [117] R. J. Krizek, R. A. Parmelee, J. N. Kay, and H. A. Elnaggar, “Structural analysis and design of pipe culverts,” *NCHRP Rep.*, no. 116, 1971.
- [118] R. Cichocki, I. Moore, and K. Williams, “Steel buried structures: Condition of Ontario structures and review of deterioration mechanisms and rehabilitation approaches,” *Can. J. Civ. Eng.*, vol. 48, no. 2, pp. 159–172, 2021, doi: <https://doi.org/10.1139/cjce-2019-0580>.
- [119] A. Wadi, “Soil-Steel Composite Bridges: Research advances and application,” Kungliga tekniska högskolan, 2019.
- [120] S. Safari *et al.*, “Diagnostic load testing and assessment of a corroded corrugated metal pipe culvert before rehabilitation,” *Struct. Infrastruct. Eng.*, pp. 1–10, 2023.
- [121] A. M. Legese, A. Rózański, and M. Sobótka, “Effect of shell spacing on mechanical behavior of multi-span soil-steel composite structure,” *Heliyon*, vol. 10, no. 1, p. e23376, 2023, doi: <https://doi.org/10.1016/j.heliyon.2023.e23376>.
- [122] K. Williams, S. MacKinnon, and J. Newhook, “New and innovative developments for design and installation of deep corrugated buried flexible steel structures,” in *The 2nd European conference on buried flexible structures*, 2012, no. 12, pp. 265–274.
- [123] A. M. Legese, M. Sobótka, C. Machelski, and A. Rózański, “Behaviour of soil-steel composite structures during construction and service: a review,” *Arch. Civ. Eng.*, vol. 69, no. 4, pp. 263–292, 2023, doi: <http://dx.doi.org/10.24425/ace.2023.147659>.
- [124] T. Zimmermann, A. Truty, A. Urbanski, and K. Podles, “ZSoil user manual,” *Zace Serv. Switz.*, 2016.
- [125] C. Machelski, M. Sobótka, and S. Grosel, “Displacements of shell in soil-steel bridge subjected to moving load: determination using strain gauge measurements and numerical simulation,” *Stud. Geotech. Mech.*, vol. 44, no. 1, 2022, doi: [doi:10.2478/sgem-2021-0028](https://doi.org/10.2478/sgem-2021-0028).
- [126] C. Machelski and L. Janusz, “Application of Results of Tests in Developing a Two-Dimensional Model for Soil–Steel Railway Bridges,” *Transp. Res. Rec.*, vol. 2656, no. 1, pp. 53–60, 2017, doi: <https://doi.org/10.3141/2656-06>.
- [127] R. W. I. Brachman, T. M. Elshimi, A. C. Mak, and I. D. Moore, “Testing and analysis of a deep-corrugated large-span box culvert prior to burial,” *J. Bridg. Eng.*, vol. 17, no. 1, pp. 81–88, 2012, doi: [https://doi.org/10.1061/\(ASCE\)BE.1943-5592.0000202](https://doi.org/10.1061/(ASCE)BE.1943-5592.0000202).
- [128] Y. Liu, I. D. Moore, N. A. Hoult, and H. Lan, “Numerical Investigation of the Structural Behavior of Corrugated Steel Culverts under Surface Load Tests Using Three-Dimensional Finite-Element Analyses,” *J. Pipeline Syst. Eng. Pract.*, vol. 14, no. 2, p.

- 4023002, 2023, doi: <https://doi.org/10.1061/JPSEA2.PSENG-1412>.
- [129] R. B. Seed and J. M. Duncan, “FE analyses: compaction-induced stresses and deformations,” *J. Geotech. Eng.*, vol. 112, no. 1, pp. 23–43, 1986, doi: 10.1061/(ASCE)0733-9410(1986)112:1(23).
- [130] T. M. Elshimi and I. D. Moore, “Modeling the effects of backfilling and soil compaction beside shallow buried pipes,” *J. Pipeline Syst. Eng. Pract.*, vol. 4, no. 4, p. 4013004, 2013, doi: [http://dx.doi.org/10.1061/\(ASCE\)PS.1949-1204.0000136](http://dx.doi.org/10.1061/(ASCE)PS.1949-1204.0000136).
- [131] T. J. McGrath, E. T. Selig, M. C. Webb, and G. V. Zoladz, “Pipe interaction with the backfill envelope,” University of Massachusetts at Amherst. Transportation Center, 1999.
- [132] A. Wadi, L. Pettersson, and R. Karoumi, “Flexible culverts in sloping terrain: Numerical simulation of avalanche load effects,” *Cold Reg. Sci. Technol.*, vol. 124, pp. 95–109, 2016, doi: 10.1016/j.coldregions.2016.01.003.
- [133] I. Ezzeldin and H. El Naggar, “Numerical Modelling of Induced Stresses in Buried Corrugated Metal Structures due to Compaction Efforts,” *Transp. Geotech.*, vol. 32, p. 100706, 2022, doi: 10.1016/j.trgeo.2021.100706.
- [134] C. S. Association, “CHBDC (Canadian Highway Bridge Design Code),” *CAN/CSA-S6-14*, 2019.
- [135] K. Embaby, “Performance and Ultimate Limit State of Large-Span Soil-Steel Structures,” The University of Western Ontario, 2022.
- [136] H. Dai *et al.*, “Behavior Study of Shallowly Buried Large-Span Steel Culverts by Inclusion of Geotextile Reinforcements,” *Indian Geotech. J.*, pp. 1–10, 2024, doi: <https://doi.org/10.1007/s40098-024-00918-5>.
- [137] Y. Zhang, B. Liu, and L. Meng, “Structural behavior and soil arching state of underground corrugated steel utility tunnel,” *J. Constr. Steel Res.*, vol. 203, p. 107798, 2023, doi: <https://doi.org/10.1016/j.jcsr.2023.107798>.
- [138] J. M. Duncan, R. B. Seed, and R. H. Drawsky, *Design of corrugated metal box culverts*, no. 1008. Transportation Research Board, 1985.
- [139] Y. F. Girges, “Three-dimensional analysis of composite soil-steel structures,” University of Windsor, 1993.
- [140] E. Bayoglu Flener, “Testing the response of box-type soil-steel structures under static service loads,” *J. Bridg. Eng.*, vol. 15, no. 1, pp. 90–97, 2010, doi: [https://doi.org/10.1061/\(ASCE\)BE.1943-5592.0000004](https://doi.org/10.1061/(ASCE)BE.1943-5592.0000004).
- [141] M. Sobótka and D. Łydzba, “Shape optimization of soil-steel structure by simulated annealing,” *Procedia Eng.*, vol. 91, no. December 2014, pp. 304–309, 2014, doi: 10.1016/j.proeng.2014.12.065.
- [142] E. Bayoğlu Flener and R. Karoumi, “Dynamic testing of a soil–steel composite railway bridge,” *Eng. Struct.*, vol. 31, no. 12, pp. 2803–2811, Dec. 2009, doi: 10.1016/J.ENGSTRUCT.2009.07.028.

- [143] D. Beben, “Experimental study on the dynamic impacts of service train loads on a corrugated steel plate culvert,” *J. Bridg. Eng.*, vol. 18, no. 4, pp. 339–346, 2013, doi: 10.1061/(ASCE)BE.1943-5592.0000395.
- [144] A. Mahgoub and H. El Naggar, “Assessment of the seismic provisions of the CHBDC for CSP culverts,” in *International Conference GeoOttawa*, 2017, pp. 1–4.
- [145] T. Maleska and D. Beben, “Behaviour of corrugated steel plate bridge with high soil cover under seismic excitation,” *MATEC Web Conf.*, vol. 174, 2018, doi: 10.1051/mateconf/201817404003.
- [146] T. M. Elshimi, “Three-dimensional nonlinear analysis of deep-corrugated steel culverts.” Queen’s University, 2011.
- [147] NCSPA, “2022 Project of the Year Winner – Special Application: Columbia Ridge Landfill Railroad,” *National Corrugated Steel Pipe Association*, 2024. <https://ncspa.org/about-the-ncspa/>
- [148] M. Sobótka and D. Łydźba, “Live load effect in soil-steel flexible culvert: role of apparent cohesion of backfill,” *Eur. J. Environ. Civ. Eng.*, vol. 8189, 2019, doi: 10.1080/19648189.2019.1670264.
- [149] L. Czesław Machelski and Janusz, “The vehicle impact on the corrugated steel shell in soil-steel structures,” *Transp. Overv.*, pp. 18–29, 2017, doi: 10.35117/A_ENG_17_09_03.
- [150] H. N. Kung, H.S. and Lau, “The Effect of Spacing on the Performance of Soil-Steel Structures,” University of Windsor, 1985.

Abstract

Numerical modelling of soil-steel composite structures behavior under ultimate loads

Soil-steel composite structures (SSCSs) employ a construction technology where a flexible shell interacts synergistically with surrounding backfill. Typically composed of corrugated steel plates (CSPs) joined by high-strength screws, the mechanical behavior of SSCSs is inherently complex due to the intricate interaction between the backfill and the CSP, resulting in significantly non-linear structural characteristics.

This research presents the outcomes of numerical modelling to examine SSCS behavior under ultimate and moving loads. The study considers both single-span and multi-span structures, investigating the impact of geotextile reinforcement and stiffening ribs, as well as the effects of spacing between structures on bearing capacity and failure modes. A displacement-imposing approach is utilized to evaluate the ultimate bearing capacity with kinematic forcing ensuring numerical convergence for more precise determination of maximum load capacity.

Analysis of geotextile layer positioning indicates that reinforcement is most effective when placed at shallower depths, closer to the load's zone of influence. These insights are valuable for designers aiming to optimize geotextile placement to enhance SSCS performance. Furthermore, a double layer of geotextile significantly improves bearing capacity compared to a single layer. The addition of stiffening ribs around the crown of the shell also notably increases bearing capacity.

The investigation into shell spacing in multi-span SSCSs reveals that narrow spacing between shells significantly diminishes load-bearing capacity. Computational results identify the primary cause of failure as reaching the limit values of internal forces due to steel strength. Analysis of the effects of lateral shells on a central shell at varying spacings under quasi-static moving loads shows that both vertical and horizontal displacements increase substantially when the shell spacing-to-span length ratio is below 0.5. Maximum stress is observed when shells are placed directly adjacent to each other without spacing. Extreme deflections and stress shift in the direction of truck movement. However, the influence of lateral shells on the central shell's performance under moving loads is negligible when the spacing-to-span ratio exceeds 0.5.

Streszczenie

Modelowanie numeryczne zachowania podatnych konstrukcji gruntowo-powłokowych pod obciążeniem granicznym

Podatne konstrukcje gruntowo-powłokowe stanowią technologię budowy obiektów mostowych, w której sprężysta powłoka współdziała synergicznie z otaczającą ją zasypką gruntową. Powłoki wykonywane są zazwyczaj z arkuszy blach falistych połączonych ze sobą śrubami o wysokiej wytrzymałości. Mechaniczne zachowanie konstrukcji gruntowo-powłokowych jest ze swej natury złożone ze względu na skomplikowaną interakcję między powłoką i zasypką. Efektem tego, charakterystyka mechanicznego zachowania się tego typu obiektów jest istotnie nieliniowa.

W rozprawie przedstawiono wyniki modelowania numerycznego zachowania się konstrukcji gruntowo-powłokowych pod obciążeniami granicznymi (niszczącymi) i ruchomymi. W przeprowadzonych badaniach rozpatrywano wpływ zbrojenia gruntu geosyntetykami i zastosowania żeber usztywniających powłokę na ich nośność i sztywność. Uwzględniono zarówno konstrukcje jednoprzęsłowe, jak i wieloprzęsłowe, dla których rozważano także wpływ rozstawu między powłokami na nośność i sposób zniszczenia pod obciążeniem granicznym. Do oceny nośności granicznej zastosowano podejście, w którym obciążenie zadano w postaci wymuszenia kinematycznego. Pozwoliło to na określenie maksymalnego obciążenia przy zachowaniu stabilności numerycznej rozwiązania.

Analiza umiejscowienia warstwy geosyntetyku w zasypce gruntowej wskazuje, że wzmocnienie takie jest najbardziej skuteczne, gdy geosyntetyk znajduje się jak najbliżej górnej powierzchni obiektu, na której przykładane są obciążenia. Spostrzeżenie to może być wykorzystane w praktyce projektowej do optymalizacji rozmieszczenia zbrojenia zasypki w celu zwiększenia nośności konstrukcji. Pokazano ponadto, że podwójna warstwa geosyntetyku znacznie poprawia nośność obiektu. Jeśli chodzi o analizę efektywności żeber usztywniających, wykazano, że ich zastosowanie w górnej części powłoki również znacznie zwiększa nośność konstrukcji.

Badanie wpływu rozstawu między powłokami w wieloprzęsłowych konstrukcjach podatnych wykazało, że zastosowanie małych odstępów istotnie zmniejsza nośność. Wyniki obliczeń

wskazują, że konstrukcja niszczy się wskutek osiągnięcia wartości granicznych sił wewnętrznych w powłoce, wynikających z wytrzymałości stali. Analiza wpływu powłok bocznych na powłokę centralną w różnych odstępach pod działaniem quasi-statycznych obciążeń ruchomych pokazuje, że zarówno przemieszczenia pionowe, jak i poziome znacznie wzrastają, gdy stosunek rozstawu między powłokami do długości przęsła jest mniejszy niż 0,5. Maksymalne naprężenia obserwuje się, gdy powłoki są umieszczone bezpośrednio obok siebie bez odstępów. Ekstremalne ugięcia i naprężenia przesuwają się w kierunku ruchu ciężarówki. Wpływ powłok bocznych na pracę powłoki centralnej pod obciążeniem ruchomym jest pomijalny, gdy stosunek rozstawu do rozpiętości przekracza 0,5.